Additive manufacturing of Ni-rich nitinol for superelastic properties for stent application

A thesis submitted in fulfilment of the requirements for the degree of

Doctor of Philosophy (PhD)

from Dublin City University

School of Mechanical and Manufacturing Engineering

By

Neha Agarwal

B.E. , M.Sc.

13th August 2025

Supervisors: Prof. Dermot Brabazon, Dublin City University

Dr. Muhannad Ahmed Obeidi, Dublin City University

Declaration

I hereby certify that this material, which I now submit for assessment on the programme of study leading to the award of Doctor of Philosophy (Ph.D) is entirely my own work, and that I have exercised reasonable care to ensure that the work is original, and does not to the best of my knowledge breach any law of copyright, and has not been taken from the work of others save and to the extent that such work has been cited and acknowledged within the text of my work.

Signed: Neha Agarwal ID No.: 21268600 Date: 13/08/2025

Acknowledgements

First and foremost, I would like to express my deepest gratitude to my amazing supervisor, **Prof. Dermot Brabazon**. His support, encouragement, and wealth of knowledge has guided me every step of the way during this research journey. His thoughtful insights and honest feedback constantly challenged me to think critically and improve, and I consider myself incredibly fortunate to have worked under his mentorship. Thank you for believing in me and for the opportunity to be part of such a fascinating project.

I am also sincerely thankful to **Dr. Muhannad Ahmed Obeidi**, for his guidance, support, unmatched technical expertise and mentorship throughout this work. His approachable nature and constructive advice helped me navigate the complexities of this research, and I truly appreciate the time and effort he invested in helping me grow.

I would like to extend my appreciation to **I-Form, the Advanced Manufacturing Research Centre**, and **Dublin City University (DCU)** for providing the infrastructure, resources, and financial support that made this research possible. I express my sincere gratitude to the generous support provided by **Fort Wayne Metals, Ireland**. I would also like to extend my gratitude to **Ms. Joan Kelly** and the staff from Nano Research Facility for their continuous support during this journey.

I would like to also thank all my office colleagues and friends in DCU for their in numerous discussions. Our many discussions—whether technical or just to unwind—were a great source of motivation, and their support helped me stay focused during the tough phases.

To my husband **Kshitiz**, **family and friends**, thank you for being my constant pillars of strength. Your love, patience, and belief in me—even when I doubted myself—have carried me through. I'm especially thankful for the times you listened, celebrated small victories, and reminded me of how far I've come.

This thesis is the result of many minds, generous hearts, and unwavering support. I'm deeply grateful to each and every person who played a part in this journey. Any mistakes or shortcomings in this work are my own.

TABLE OF CONTENTS

LIST OF FIGURES

LIST OF TABLES

List of Publications

Agarwal, N.; Ryan Murphy, J.; Hashemi, T.S.; Mossop, T.; O'Neill, D.; Power, J.; Shayegh, A.; Brabazon, D. Effect of Heat Treatment Time and Temperature on the Microstructure and Shape Memory Properties of Nitinol Wires. *Materials* **2023**, *16*, 6480. https://doi.org/10.3390/ma16196480

Agarwal, N., Monu, M. C., Selvam, K. T., Obeidi, M. A., & Brabazon, D. (2023). Study of the effects of laser power and scanning speed on the microstructural morphologies and physical properties of L-PBF produced Ni52. 39Ti47. 61. *Journal of Materials Research and Technology*, *27*, 8334-8343. https://doi.org/10.1016/j.jmrt.2023.11.146

Agarwal, N., Gallagher, K. A., Carton, J. G., Brabazon, D., & Obeidi, M. A. (2024). Influence of processing parameters on the corrosion resistance of additively manufactured nitinol parts for biomedical applications. *Results in Materials*, 100536. https://doi.org/10.1016/j.rinma.2024.100536

Agarwal, N., Bourke D., Obeidi, M. A., & Brabazon, D. (2024). Influence of laser powder bed fusion and ageing heat treatment parameters on the phase structure and physical behavior of Ni-rich nitinol parts, *Journal of Materials Research and Technology*, *30*, 4527-4541. https://doi.org/10.1016/j.jmrt.2024.04.198

Agarwal, N., Bahramyan, M., Healy, P., Obeidi, M. A., & Brabazon, D. (2025). Control of surface finish and mechanical properties of nitinol stents fabricated via laser powder bed fusion, *Journal of Materials Research and Technology, 37, 1808-1821, https://doi.org/10.1016/j.jmrt.2025.06.128*

Conference Proceedings

Agarwal, N., Perumal G. Obeidi, M. A., & Brabazon, D. (2024). Investigating the effect of the addition of WC into NiTi for stent application, *Materials Research Proceedings*, *41*, 249-256. https://doi.org/10.21741/9781644903131-28

Agarwal N., Asal K., Faraoni A., Pola A., Obeidi M.A., Brabazon D., Effect of solution heat treatment of nitinol (Ni55%-Ti45%) manufactured via L-PBF, *Shape Memory Proceedings*, *3-4*. https://doi.org/10.31399/asm.cp.smst2024p0003

List of Oral Presentations

Neha Agarwal, Karthikeyan Tamil Selvam, Muhannad Ahmed Obeidi, Dermot Brabazon, "Heat Treatment of Nitinol Manufactured via L-PBF For Biomedical Application", Conference presentation at 23rd International Conference on Advances in Materials and Processing Technologie - AMPT2022, 10-14 October, Portorož, Slovenia

Neha Agarwal, Karthikeyan Tamil Selvam, Muhannad Ahmed Obeidi, Dermot Brabazon, "Effects of printing parameters on phase transformation and mechanical properties of nitinol for biomedical implant manufacturing using Laser Powder Bed Fusion", Conference presentation at International ESAFORM Conference 2023, 19-21 April, Krakow, Poland

Neha Agarwal, Muhannad Ahmed Obeidi, Dermot Brabazon, "Effects of printing parameters on phase transformation temperature and mechanical properties of nitinol for medical device manufacturing using Laser Powder Bed Fusion", AMSCDT Student Conference presentation, 18-19th July 2023, University of Sheffield, Sheffield, UK

Neha Agarwal, Gopinath Perumal, Muhannad Ahmed Obeidi, Dermot Brabazon, "Investigating the effect of the addition of WC into NiTi for stent application", Conference presentation at International ESAFORM Conference 2024, 24-26 April, Toulouse, France

Neha Agarwal, Karim Asal, Andrea Faraoni, Annalisa Pola, Muhannad Ahmed Obeidi, Dermot Brabazon, "Effect of solution heat treatment of nitinol (Ni55%-Ti45%) manufactured via L-PBF", Conference presentation at Shape Memory and Superelasticity Technologies 2024, 6-10 May, Cascais, Portugal

List of Poster Presentations

Agarwal, N., Ahmed Obeidi, M., Brabazon, D., "Effects of heat treatment of nitinol cuboids manufactured via L-PBF for biomedical application", AMSCDT Student Conference, 11-12th July, Dublin City University, Dublin, Ireland.

Agarwal, N., Ahmed Obeidi, M., Brabazon, D., "Heat treatment of additively manufactured nitinol parts", I-FORM Gathering, 7-8th December 2022, Athlone, Ireland.

Agarwal, N., Bourke D., Ahmed Obeidi, M., Brabazon, D., "Influence of laser powder bed fusion and ageing heat treatment parameters on the phase structure and physical behaviour of Ni-rich nitinol parts", SMST Ireland 2025, 22nd May, Galway, Ireland.

ABSTRACT

Neha Agarwal

Additive manufacturing of Ni-rich nitinol for superelastic properties for stent application

Nitinol, an alloy of nickel and titanium, has emerged as a promising material for biomedical applications, due to its exceptional superelasticity and shape memory effect. These unique properties allow stents to expand and contract in response to physiological conditions, providing superior performance compared to conventional metallic stents. However, traditional manufacturing techniques, such as machining and laser cutting, present significant challenges in processing nitinol due to its high work hardening rate, poor machinability, and complex phase transformation behavior. These limitations have driven the adoption of Laser Powder Bed Fusion (L-PBF) that enables the fabrication of intricate and patient-specific stent designs with greater precision and structural complexity.

Nitinol parts produced using this method often suffer from inherent defects such as high residual stresses, microstructural inhomogeneities, porosity, and poor surface finish due to the rapid solidification and localized heat accumulation during the printing process. These factors can significantly degrade mechanical performance, reducing the fatigue resistance, superelastic behavior, and functional longevity of the stent. Therefore, post-processing treatments are essential to achieve optimal functional properties. Heat treatments, including solution annealing and ageing, play a critical role in reducing residual stresses, refining the microstructure, and tuning the phase transformation temperatures which enable setting the superelastic response required for stent applications. Similarly, surface modification techniques such as electropolishing are necessary to reduce surface roughness and improve corrosion resistance, minimizing the risk of nickel ion leaching in the human body and ultimately enhancing the biocompatibility of the stent.

Optimizing process parameters in L-PBF, with effective post-processing strategies, is important to tailor the mechanical performance, surface characteristics, and biocompatibility of Ni-rich nitinol for medical applications. This study investigates the effects of L-PBF process parameters, ageing heat treatment, and electropolishing on the functional properties of Ni-rich nitinol. The goal is to enable nitinol metal additive manufacturing for next-generation stent production.

Chapter 1

1 Introduction

Biomedical devices, particularly stents have seen a significant growth in the healthcare industry in the recent years accounting for 8.6 billion USD in 2021 with an estimated growth of 4% between the years 2022 and 2028 [1]. The advancement of medical devices, particularly cardiovascular stents, is attributed to innovations in manufacturing and material technologies within emerging markets, together with the global expansion of the healthcare infrastructure and the rising demand driven by an ageing population. In recent times, patients have experienced improvised performance and efficiency with reduced complications due to the technological advancement in stent production. Metallic stents with different materials and production techniques have seen their utilization in the medical industry [2]. However, these stents are produced of standard dimensions in terms of diameters and length which might not be suitable for adult population (senior citizens) or children [3,4]. This raises the emerging concern of the need to produce bespoke metallic stents.

Additive manufacturing technology has the potential to produce stents and also as a technology aid in providing benefits towards the environmental and sustainability of the value chain of part production [5–7]. With this technique, production of sustainable and optimized products with improved resource efficiency and reduced carbon footprint can be achieved. Design freedom is another important aspect which additive manufacturing provides in terms of its relative ease of manufacturing of complex parts or part designs which are not possible via other methods [8]. Additive manufacturing has some challenges such as retained residual stresses [9] and higher surface roughness [10].

Another challenge faced is the compatibility of the material of biomedical devices such as stents. The property of superelasticity of nitinol – an alloy of nickel and titanium, makes it a suitable choice for stents which has good recoverability capability after releasing the load subjected on it [11]. Nitinol (NiTi) possesses unique properties and features such as high corrosion resistance, good biocompatibility, high wear resistance and excellent damping capacity [12–14]. These features in addition to the shape memory behavior and superelasticity characteristics making them suitable for various industries including biomedicine, actuation systems, aerospace industry as well as automation

systems [15]. However, a detailed evaluation of nitinol's functional properties and surface finish is essential when characterizing it for stent applications.

To combat the challenges present in the parts produced by the additive manufacturing process, a detailed study and analysis is vital for improving the part properties and surface finish of the part. A better understanding of the role of the printing parameters on the produced parts is necessary, which provides a deeper insight into the properties of the part. Assessment of the properties such as phase transformation temperatures, hardness, phase type and density could be altered by varying the printing properties. Further alteration of the resultant properties to achieve targeted results could be possible with the help of post processing techniques such as heat treatment for properties and electropolishing for achieving better surface finish.

Post processing technique such as the heat treatment process is a common technique for altering the properties of the NiTi parts produced by the additive manufacturing technique. The process leads to releasing of the inherent residual stresses, effectively enhancing the thermomechanical properties by controlling the change in physical properties. In a controllable manner, microstructural formation could be tailored in the material by changing the heat treatment parameters. For several applications, the combination of the additive manufacturing and the heat treatment process helps in achieving the required properties of the fabricated NiTi parts.

In this doctoral research thesis, the effect of the laser powder bed fusion (L-PBF) manufacturing process parameters on the phase transformation temperatures, density, hardness and microstructures of NiTi parts was evaluated. To improve these functional properties, the effects of ageing heat treatment was also investigated. The biocompatibility of the produced parts was assessed in comparison to Ti6Al4V alloy in biological environments of Hanks and Ringers solution at an elevated temperature of 37°C, which is the human body temperature.

1.1 Aims and Objectives

This thesis investigates the physical properties and surface finish of NiTi components fabricated via L-PBF, encompassing both bulk samples and geometrically complex structures such as stents, with emphasis on the influence of the manufacturing process

and subsequent post-processing. Deeper investigations were conducted through the following objectives:

1. Investigate the possibility of the ageing heat treatment to alter the physical properties of nitinol wires to understand the effect on the phase transformation temperatures, hardness, and recovery strain.
2. Assess the influence of ageing heat treatment on L-PBF produced NiTi parts to alter the physical characteristics to achieve the targeted properties.
3. Assess the effects of printing parameters of L-PBF produced NiTi parts on phase transformation temperatures, hardness, density, chemical composition and formed microstructures.
4. Assess the effects of printing parameters of NiTi parts on the corrosion resistance in comparison to Ti6Al4V parts for biocompatibility.
5. Assess the influence of electropolishing to improve the surface quality of nitinol stents produced via L-PBF according to a Box Behnken DoE.

1.2 Thesis Outline

This thesis is compiled with published original research articles which contribute to literature. It has been organized in the following way:

Chapter	Title of the paper	Status	Journal Details
3	Effect of Heat Treatment Time and Temperature on the Microstructure and Shape Memory Properties of Nitinol Wires	Published	*Materials* **2023**, *16*(19), 6480; https://doi.org/10.3390/ma16196480
4	Influence of laser powder bed fusion and ageing heat treatment parameters on the phase structure and physical behavior of Ni-rich nitinol parts	Published	Journal of Materials Research and Technology, 2024 May-June;30:4527-41. https://doi.org/10.1016/j.jmrt.2024.04.198
5	Study of the effects of laser power and scanning	Published	Journal of Materials Research and Technology. 2023 Nov 1;27:8334-

	speed on the microstructural morphologies and physical properties of L-PBF produced $Ni_{52.39}Ti_{47.61}$		43; https://doi.org/10.1016/j.jmrt.2023.11.146
6	Influence of processing parameters on the corrosion resistance of additively manufactured nitinol parts for biomedical applications	Published	Results in Materials. 2024 Jan 20:100536; https://doi.org/10.1016/j.rinma.2024.100536
7	Control of surface finish and mechanical properties of nitinol stents fabricated via laser powder bed fusion	Published	Journal of Materials Research and Technology, Jul-Aug 2025, 37, 1808-1821; https://doi.org/10.1016/j.jmrt.2025.06.128

The thesis comprises six chapters and a summary of the content of each chapter has been outlined as follows:

- **Chapter 1** outlines the identified research gap addressed in this study, highlights the underlying need for investigation, and defines the primary objectives of the thesis
- **Chapter 2** comprises the existing knowledge in the field of additive manufacturing of nitinol. It highlights the possible need of post-processing of the produced parts and suggests the possible ways to mitigate these challenges which is addressed as original research work.
- **Chapter 3** studies the influence of heat treatment on the properties of nitinol wires before diving into additively manufactured nitinol parts. It shows the treatment effect on the phase transformation temperatures, hardness, and recovery strain.

- **Chapter 4** examines the combined effects of the printing parameters and ageing heat treatment on the resulting phases, grain size and volume fraction of the phases along with the hardness values of the Ni-rich nitinol parts produced by L-PBF.
- **Chapter 5** focuses on the effect of printing parameters such as laser power and scanning speed on the grain formation, transformation temperatures, density and hardness of the Ni-rich nitinol parts produced via L-PBF.
- **Chapter 6** determines the optimised printing parameters of Ni-rich nitinol parts which are additively manufactured to show the best corrosion resistance in the bodily environment.
- **Chapter 7** verifies the influence of electropolishing as a post-processing technique to improve the surface quality of the Ni-rich nitinol stents processed using a Box-Behnken design.
- **Chapter 8** summarises the main findings of this research study and recommends the scope of future research in the field.

Chapter 2

2 Literature Review

2.1 Nitinol as a biomedical material

Shape memory and superelastic alloys have been extensively used in medicine in a broad range of applications due to their exceptional properties. Nitinol is also known for its biocompatibility. The advancement of nitinol in biomedical applications has been facilitated by the combination of these unique properties of nitinol [16]. Such applications include orthopaedic implants, cardiovascular devices, surgical instruments as well as orthodontic devices, as shown in **Figure 2-1**.

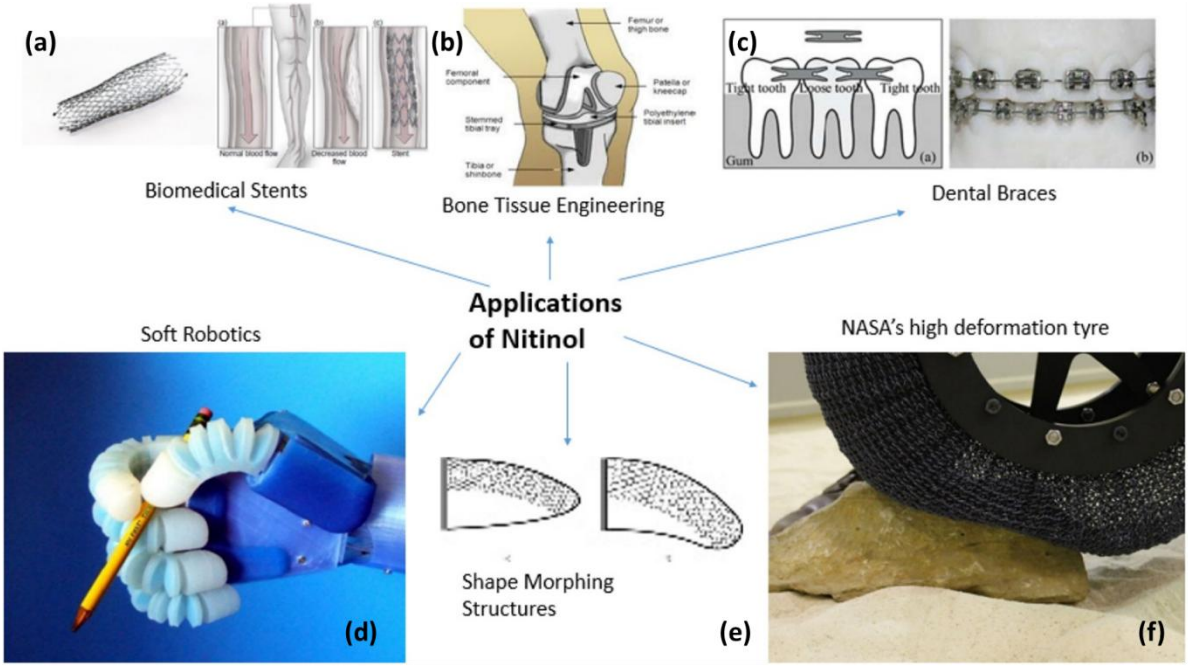

Figure 2-1: Biomedical applications of nitinol: (a) stents, (b) bone tissue engineering, (c) dental braces, (d) soft robotics, (e) shape morphing structures and (f) tyres [17].

2.1.1 Superelasticity of NiTi in biomedical applications

Several studies conducted on NiTi demonstrated the superelastic property of NiTi which opened possibility of usage of NiTi in various applications [12,13,16,18,19]. By setting the phase change temperature well below body temperature, this eliminates the requirement of a heat source and provides a cost-efficient way of utilizing NiTi [16,20,21].

2.1.2 Biocompatibility of NiTi in biomedical applications

Nitinol is used as a favourable material for biomedical applications due to its excellent biocompatibility. The term biocompatibility refers to a material's ability to survive in the mild biological environment without producing any allergic reactions to the biological system. Several factors contribute to the biocompatibility of NiTi such as:

- Corrosion resistance: promotes the prevention of the release of harmful ions in the biological environment.
- Biological inertness: no adverse effects when in contact with biological tissues.
- Tissue compatibility: being compatible with the various tissues of the human body.
- Surface properties: enhanced interaction with biological tissues with modifications like surface coatings or treatments.
- Conformability: flexibility to undergo significant deformation and returning to original shape without any permanent deformation.
- Stability: higher durability and reliability as an implant material.

2.2 Other applications of nitinol

2.2.1 Aerospace applications

Complex geometries with reduced costs and light weight parts of the aerospace industry could be produced with the help of the additive manufacturing technique as shown in **Figure 2-2**. Parts can be produced sustainably in low volumes to meet the demand in a cost-efficient manner by using metal additive manufacturing.

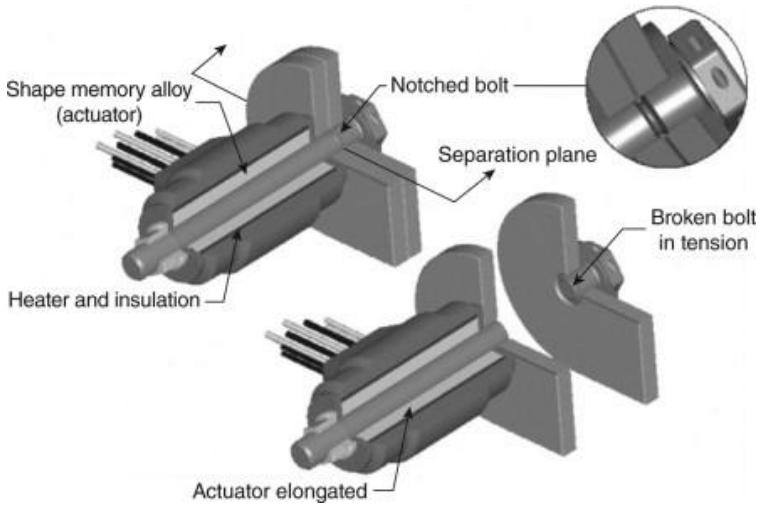

Figure 2-2: Nitinol used an actuator in the aerospace industry [22]**.**

2.2.2 Automation applications

Nitinol and the additive manufacturing technique offers the possibility to create robotic arms with enhanced expansions and contractions of the nitinol filaments. This can be enabled without placing any additional actuators while utilizing the shape memory effect of NiTi. Customised spare parts for the automotive industry could be manufactured while maintaining the functionality of the parts as shown in **Figure 2-3**.

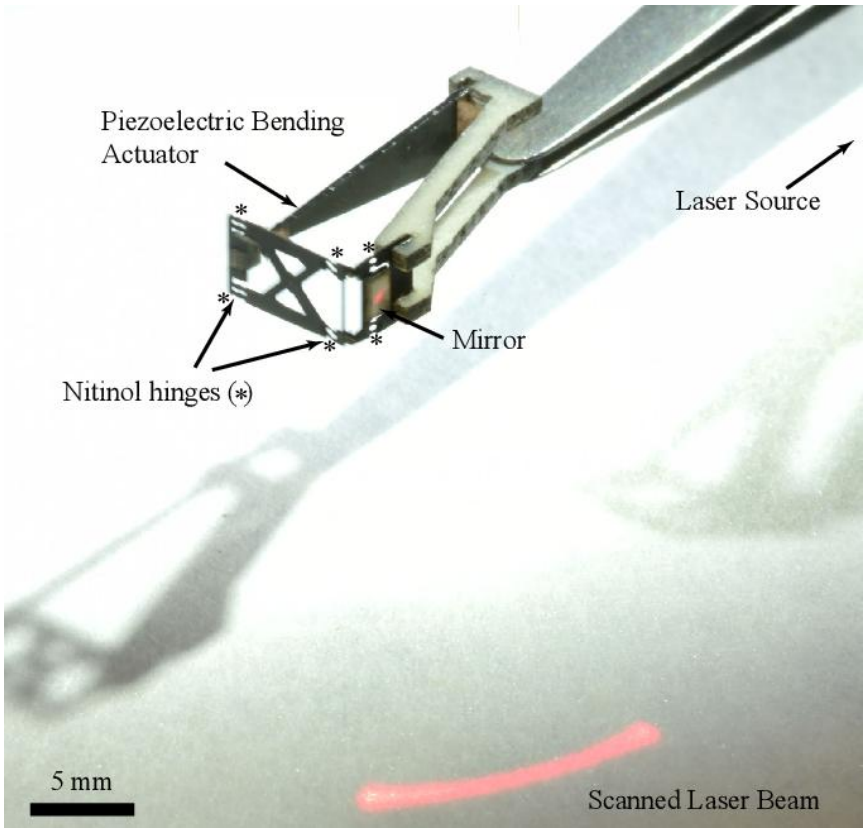

Figure 2-3: Four-bar nitinol linkage driven by a piezoelectric actuator, orienting a mirror to steer a laser beam [23]**.**

2.2.3 Consumer goods

Consumer good sectors are also facilitated by additive manufacturing by the ability to follow trend of customisation and offers design freedom to produce enhanced products. Consumer goods such as jewellery can be customised by offering designers to fully explore the possibilities with additive manufacturing enabling the production of personalised items as shown in **Figure 2-4**. Fully functional printed parts are produced while maintaining high quality in shorter periods of times and complex shapes.

Figure 2-4: Customised jewellery made from nitinol which opens up when heated [24].

2.3 Traditional ways of manufacturing NiTi stent

Over several decades varied forms of traditional methods of NiTi stent manufacturing have been explored covering conventional techniques such as laser cutting, machining, and mechanical forming. Laser cutting, is the most used technique among the other well-established methods for fabrication of NiTi stents. Intricate stent geometries can be produced using lasers. Stent fabrication is most performed via the laser cutting of tube profiles to realise the final stent geometry. Critically controlled dimensional accuracy can be achieved and maintained with the help of laser cutting, an essential requirement for medical applications [25,26]. Mechanical forming of the stent by expanding the cut-out pattern and then crimped to the size of the targeted vessels is the next step. Following which, is the radial expansion which ensures the stents functionality during the placement of the stent in the human body as shown in **Figure 2-5**.

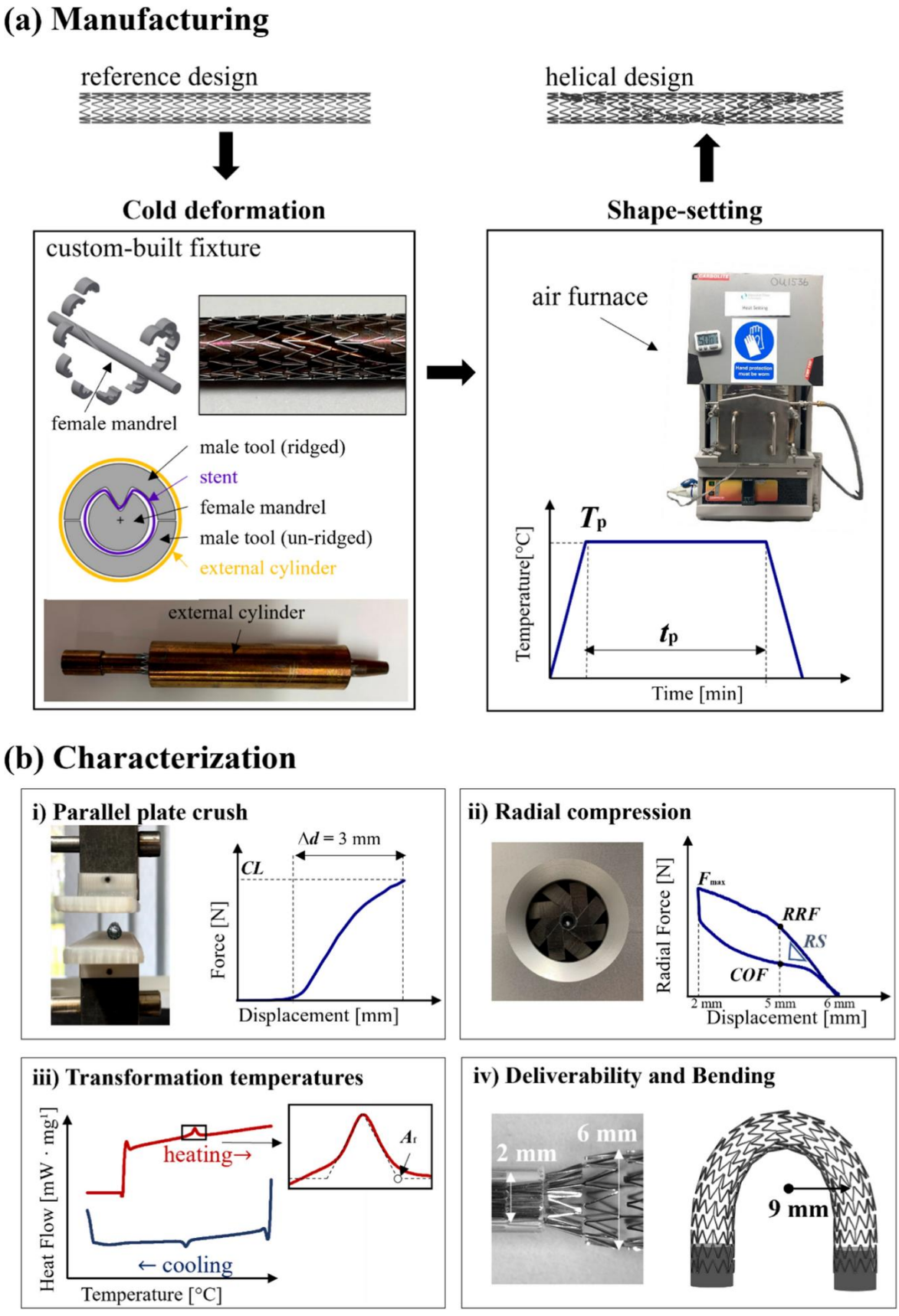

Figure 2-5: Schematic of stent (a) manufacturing process and (b) characterization tests [27].

Several multi-components of the stents are joined together with the help of other processes such as laser welding or resistance welding. These processes maintain the integrity and structure of the stent, thereby ensuring the superelastic properties of the stents [28]. Another post-processing needed for stent manufacturing is the heat treatment process. To help with the optimization of the phase transformation temperatures, this heat treatment step is crucial for NiTi stents. The combination of these techniques has been highly effective to control and maintain the mechanical properties and long-term durability of the produced stents. However, it possess the drawback of a lack of design freedom, high material wastage, high costs of the material used, and long production time [29,30].

Due to the challenges of high production time and limitation in the design freedom, newer technologies like additive manufacturing (AM) are currently being explored to improve the production efficiency. Nonetheless, the traditional way of manufacturing NiTi stents is the current industry standard because of their compatibility with the regulatory standards and reliability.

2.4 Design considerations for stents

Designing stents from nitinol fabricated through additive manufacturing (AM) involves a complex interplay of material science, mechanical engineering, and biomedical requirements to achieve optimal performance in vascular applications. Key design considerations encompass geometry, material composition, mechanical behaviour, surface characteristics, manufacturing precision, and regulatory compliance.

Stent geometry is a critical factor, as it influences the mechanical properties and clinical performance of the stent. The choice between open-cell and closed-cell designs significantly affects flexibility and radial strength as shown in **Figure 2-6**. Open-cell designs provide greater flexibility and are beneficial in tortuous vessels, allowing the stent to conform better to the natural anatomy. In contrast, closed-cell designs offer uniform radial strength and better scaffolding of the vessel wall, which can be advantageous in straight arteries or where consistent support is needed [31]. Additionally, strut thickness and width need to be carefully balanced. Thinner struts reduce the risk of disturbing blood flow, which can help minimize restenosis (re-narrowing of the artery) but may compromise mechanical strength. Stent length and diameter must also match the

target vessel dimensions accurately to avoid malposition, which can lead to complications such as thrombosis [32].

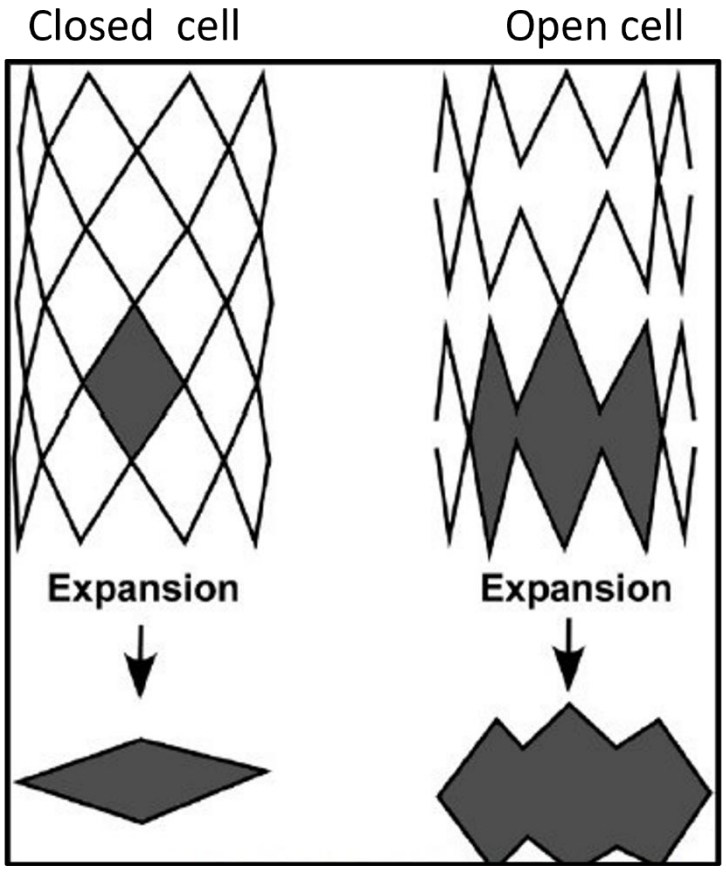

Figure 2-6: With the closed cell design, cell geometry connects consistently throughout forming complete and bridging cells. With expansion, the individual cells do not merge to form larger open areas. With open cell design, cell geometry does not connect consistently throughout, forming incomplete and non-bridged cells. With expansion, the individual cells merge to form larger open areas [31].

Material selection and composition play a pivotal role in achieving the desired superelasticity and biocompatibility [33]. Nitinol is chosen for its unique shape memory and superelastic properties, allowing the stent to self-expand upon deployment. The nickel content must be carefully controlled to balance superelastic behaviour and minimize toxic ion release, which could trigger allergic reactions or inflammatory responses. The alloy's phase transformation behaviour, dictated by its nickel-titanium ratio, directly influences its performance under physiological conditions.

Mechanical performance requirements include radial force, elastic recoil, fatigue resistance, and flexibility. A stent must exert enough radial force to keep the artery open

while maintaining minimal elastic recoil to prevent restenosis. Fatigue resistance is critical because the stent endures cyclic loading due to pulsatile blood flow. The design must ensure that the stent can withstand these repeated stresses without structural failure over the lifetime of the implant [34].

Surface finish and coatings are also important as they affect blood compatibility and healing response. A smooth surface reduces platelet adhesion, lowering the risk of thrombus formation. Many stents incorporate drug-eluting coatings to release antiproliferative drugs, which prevent excessive tissue growth (neointimal hyperplasia) that could block the artery. Additionally, polymer or ceramic coatings can enhance biocompatibility and control drug release kinetics.

From a manufacturing perspective L-PBF, must deliver high dimensional accuracy and precision in creating the complex geometry of stents. Process parameters, such as laser power, scan speed, and layer thickness, influence the final microstructure and mechanical properties of the stent. Managing residual stresses and thermal distortions is crucial to maintain structural integrity. Post-processing treatments, including heat treatment and surface finishing, help refine the stent's microstructure and restore its superelastic properties. Achieving a stable TiO_2 layer on the stent surface improves corrosion resistance, a vital property for long-term implantation in the bloodstream.

The radiopacity of stents is necessary for real-time imaging during placement. Nitinol on its own may not be sufficiently radiopaque, so alloying with elements like tantalum or platinum can improve visibility under fluoroscopy, aiding in accurate deployment [35]. Since nitinol stents are typically self-expanding, the design must support controlled expansion and deployment mechanisms that minimize vessel trauma. This includes ensuring the stent can be crimped into a compact delivery profile and expand uniformly without inducing plastic deformation.

Finally, compliance with regulatory standards such as ISO 25539-2 (for cardiovascular implants) and ASTM F2063 (for nitinol components) is essential. These standards guide material testing, design validation, and biocompatibility assessments, providing a framework for safe and effective stent design. By adhering to these guidelines, manufacturers can ensure that their stents meet the stringent safety and performance criteria required for clinical use.

2.5 Properties of nitinol (NiTi)

Nitinol, a shape memory alloy of titanium and nickel, is becoming a popular material of choice for the medical implant industry. It can be deformed and then return repeatedly to the original shape which makes it ideally suitable to be useful as stents [36]. The complex geometry of these implants means that only a small number of processing routes are available for their manufacture. The dimensions available such as length, diameter, and variations of these are quite limited due to the limits of capabilities from conventionally manufactured techniques. Standardized manufacturing of stents makes it difficult to match the manufactured stents with the individual differences of the real blood vessels of each different human body. This individualisation could be provided using additive manufacturing [37]. Approximately 50.5% atomic Ni is required for the martensite start temperature to be at room temperature or below. Compositions of nitinol with this atomic percentage or above will therefore be in the austenite phase at room temperature which is the standard phase used for stent application. However, nickel rich nitinol can also presents some potential problems such as an allergic response within the human body when it comes in contact with the bodily fluids for long periods of time [38].

Nitinol has the unique properties of superelasticity and shape memory effect. It is well established that NiTi alloy has two prominent phases of austenite and martensite. The martensite phase has a defined monoclinic structure and the austenite phase has body centred cubic BCC crystal [39]. The most intriguing property of NiTi is its reversible phase transformation between austenite (A) to martensite (M). The alloy elemental composition greatly affects the phase transformation temperature in the range of 10 – 50°C [40]. The phase change in the Ni-Ti system does not occur at a certain temperature but over a range of temperatures as shown in the phase diagram in **Figure 2-7**. Hamilton et al. [41] also studied the effect of age hardening at 400 and 500 °C for 1 – 5 hrs and observed the formation of favourable precipitates of Ni_4Ti_3, Ni_3Ti_2 and Ni_3Ti, in terms of improved mechanical properties. Also, the researchers reported that an increase in age hardening temperature decreases phase transformation temperature.

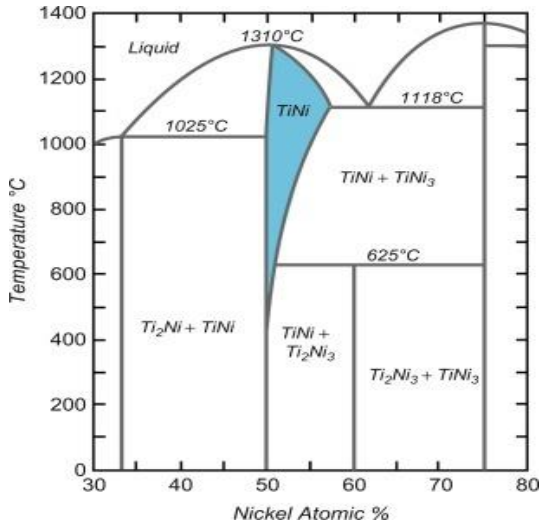

Figure 2-7: Nickel-titanium phase diagram [42]

The phase transformation is also highly dependent on the effects of the stress that is applied on NiTi. Residual stresses prior to the cold work as well as the precipitation for excess nickel in solution can generate stresses which can significantly affect the transformation [43]. Around 8% recovery strain has been reported in the literature as shown in **Figure 2-8** [44]. Advancements of additive manufacturing technique has gained great deal of attention and research in the last decade, especially in the field of the customised medical industry. Customisation has made significant advances in the medical industry and is the need of the hour to combat with the individual requirements of the human body which can be fulfilled by the additive manufacturing technique. The combination of the additive manufacturing technique and the superelastic property of nitinol could potentially revolutionize the medical industry.

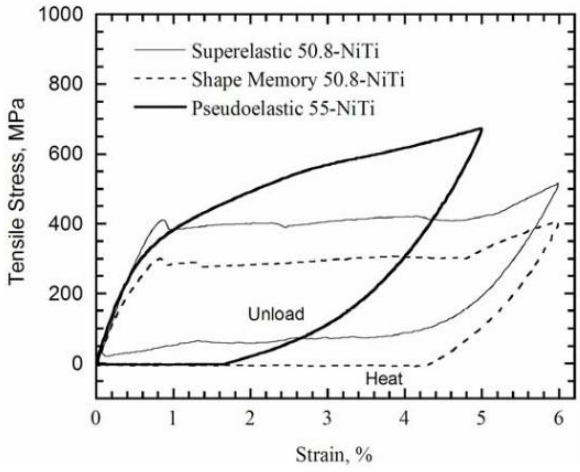

Figure 2-8: Superelastic (SE), shape memory (SM) and pseudoelastic (PSE) stress-strain response in NiTi alloys [44].

2.5.1 Superelastic NiTi

Superelasticity or pseudoelasticity has been described as phenomenon which occurs for shape memory alloys to demonstrate their ability to recover from deformation into its original shape upon unloading. Usually for NiTi, the superelastic effect occurs at a higher temperature than the Af temperature [12,45]. A typical stress-strain curve exhibiting the loading-unloading condition of a superelastic material has been presented in **Figure 2-9**. In the **Figure 2-9**, point A depicts the material which is above the Af temperature and is in the austenitic phase. When the sample is subjected to a load, the structure gets deformed and changed, resulting in a change of the structure to a detwinned martensitic structure, as depicted by point D in the figure. This reaction is called as martensitic transformation. Upon unloading of the sample, the material recovers from its deformed state to return to an austenitic structure.

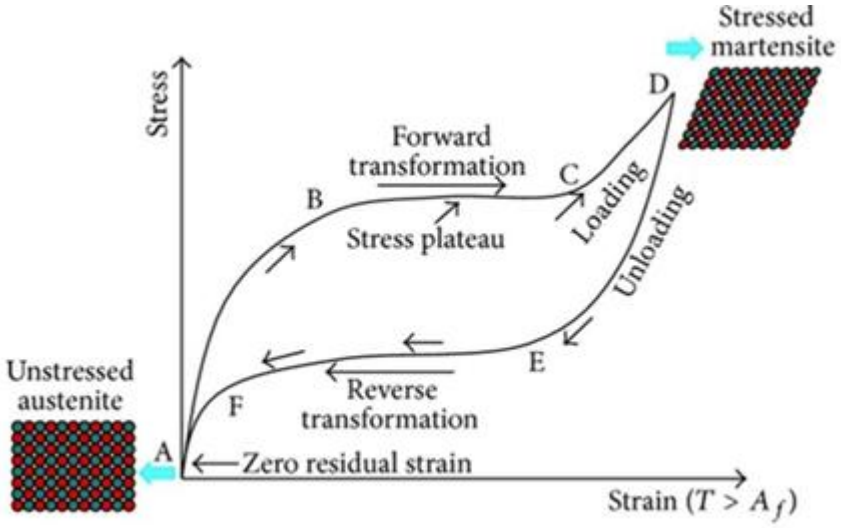

Figure 2-9: Schematic stress – strain curve of superelastic effect of SMAs [46].

2.5.2 Shape memory NiTi

One of the main characteristics of SMA is the shape memory effect (SME). **Figure 2-10** (a) provides a schematic picture of the phase transformation as a function of temperature and stress, and **Figure 2-10** (b) shows the behaviour of the phase transformation as a function of deformation, temperature, and stress. The SME is a phenomenon in which a material can undergo a reverse transformation to return to its original shape when heated above A_f after being distorted in its martensitic phase below M_f. For simplicity, a NiTi component with a twinned martensite structure at an initial temperature $T < M_f$ is considered. The martensite phase changes from twinned to detwinned by reorienting and

detwinning the lattice structure, thereby accommodating the applied load. This process is known as "detwinning" and is achieved by applying a high enough load to distort the material. The material remains deformed and maintains its detwinned state even after the load is removed because the twin borders migrate to support the load. When the material is heated to a temperature greater than A_f, a reverse transition turns it into austenite. The non-elastic deformation is recovered by the heating-induced reverse transformation. The applied stress has altered the martensitic structure; therefore, the austenite phase transition generates a large transformation strain with the same amplitude as the applied load but in the opposite direction, completely restoring the original shape and properties. Ultimately, the material cools and the structure realign to its original twinned martensite form. In conclusion, heat application and martensitic transformation combine to produce this process, which is initiated by heating and culminates in the structure's transition from detwinned martensite to austenite [12,40,47,48].

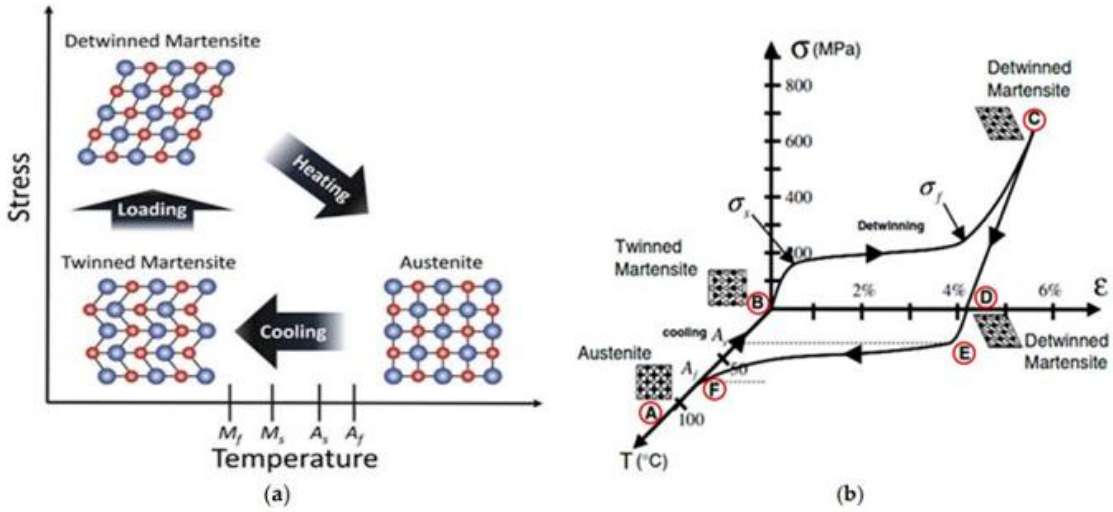

Figure 2-10: (a) Representation of phase transformation in shape memory NiTi and (b) stress-strain-temperature graph showing phase transformation in NiTi [40].

2.6 Additive manufacturing process for nitinol

Additive manufacturing (AM), commonly known as 3D printing is the technological advancement in the industry to manufacture lighter, stronger parts and systems. It uses data computer-aided-design (CAD) software or 3D object scanners to direct hardware to deposit material, layer upon layer, in precise geometric shapes. Additive manufacturing has the potential to combat with the industry challenges by improving the production processes to produce complex geometries. As the name suggests, it's an additive

technique which joins the material to form an object. This is completely in contrast to the traditional methods, which often removes material through milling, machining, carving, shaping or other means. The technological advancement in the field of additive manufacturing has enabled wider uptake of commercial applications; particularly for the rapid prototyping and production of high-valued products which would be difficult to produce traditionally otherwise. Several prototypes can be printed in a single batch without running the actual production cycle, to ensure that specifications have been met. Another biggest advantage of AM is the possibility of customisation which offers design freedom and innovation without additional costs and time constraints as opposed to the traditional production techniques. Also, AM offers several environmental benefits compared to traditional manufacturing especially waste reduction and energy savings. Some of the other benefits of AM includes material waste reduction, part flexibility, shorter run cycles, production flexibility and supply chain improvements. Along with the benefits, there are several challenges as well attached to additive manufacturing. A certain level of post-processing of the produced part is required by the additive manufacturing technique to achieve the desired surface finish as well as dimensional accuracy. Pre-alloyed material is required of high quality which adds to the cost of the raw material. Additionally, it's not an efficient way of high-volume part production.

Nitinol's properties are found to be very sensitive by the elemental composition of Ni and Ti in the NiTi matrix [49,50]. However, the additive manufacturing technique especially L-PBF significantly alters the composition of Ni and Ti from the starting material composition [51–55]. During processing, nickel evaporates because of the higher temperatures in the melt pool which reaches more than 3500 °C [56] leading to melting of nickel [57] before titanium [58]. Rapid cooling of the melt pool at a rate of 10^2 - 10^7 K/sec for a typical L-PBF process further leads to the restricting of the NiTi matrix [56,59]. Such dramatic variations during processing of nitinol have a strong influence on the mechanical as well as physical properties of the fabricated NiTi parts.

However, it has also been reported that NiTi parts fabricated using the L-PBF technique exhibits the unique properties of nitinol with better flexibility and resilience making them suitable for biomedical implants. These parts could be manufactured with higher precision even with complex geometries to better fit the patient's anatomy. These fabricated parts possess higher density and good mechanical properties offering longer

durability of the implants. Not only this, but these implants also promote osseointegration with the surrounding tissues by matching the surface properties of the biological system.

2.6.1 Laser powder bed fusion technique (L-PBF)

A commonly known additive manufacturing technique is the laser powder bed fusion (L-PBF) technique, also known as Selective Laser Melting (SLM), which uses a high-power laser to melt the metallic powder to create 3 dimensional parts. The laser parameters are the most important control parameters which influence the properties, shape, and quality of the final part. Optimization of the processing parameters such as the laser power (P), scanning speed (S), scanning strategy, hatch space (h), layer thickness and powder particle size are a few parameters which is necessary to produce high quality parts as shown in **Figure 2-11**. Depending on these parameters, the melt pool characteristics are determined which is critical for the fabrication of the parts. Rapid solidification of the melt pool also controls the functional properties of the part depending on the issues related to the melt pool stability such as lack of fusion, non-melting of the particles, generation of microcracks and pores and defects in the part. Another challenge led by the instability of the solidification process is the residual thermal stress inherent in the part causing delamination and warpage.

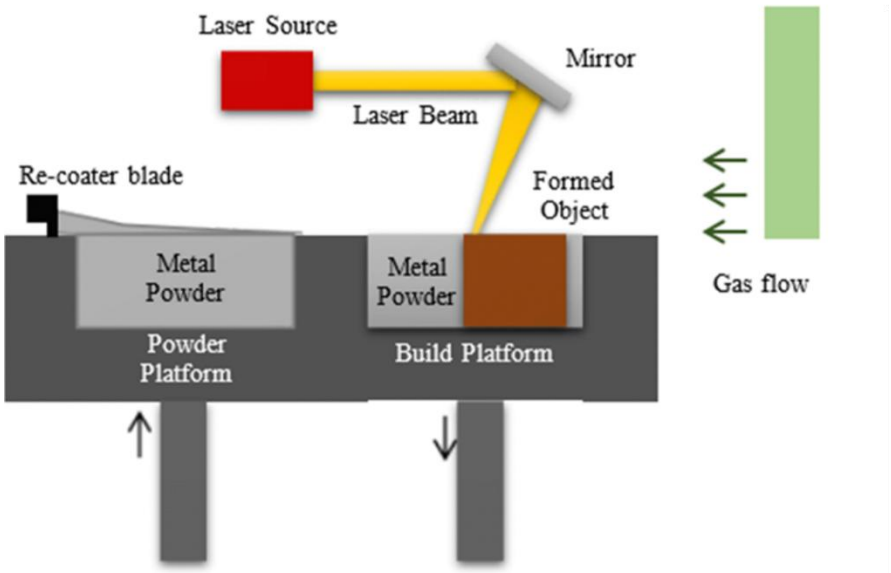

Figure 2-11: Schematic representation of the L-PBF process [60].

Laser power is the input power from the laser which is primarily required to melt and fuse the NiTi powder with higher laser power resulting in faster melting and quicker build

times. It also affects the depth of fusion or depth of penetration into the material resulting in control of the density and structural integrity of the NiTi part. Another critical factor for successful printing of NiTi part is the control of the hatch spacing. It determines the overlapping of the adjacent laser scans. This overlapping plays an important role in controlling the part density by minimizing the risks of defects like pores. It also controls the heat accumulation during processing which helps in reducing the residual stresses and possibility of warpage. Scanning speed of the laser determines how fast the laser moves over the powder bed during each scan which controls the depth of the melt pool. Higher scan speed induces faster solidification rates which could result in formation of cracks and poor bonding between the layers. Lower scan speeds results in deeper melt pool resulting in over melting of the powder. Scan speed has a strong influence on the heat affected zone of the melt pool thereby controlling the thermal gradients and reducing the risk of thermal distortion. Another controlling parameter is the layer thickness which is usually dependent on the particle size of the powder feedstock as well as the smallest feature size in the design model. Layer thickness also controls the build times as each layer needs to be deposited with precise thickness as specified which needs to be done with the help of the re-coater blade of the machine. Typically, the layer thickness ranges between 30 and 120 μm.

Along with the laser processing parameters, particle size and the distribution of the powder is also a critical parameter which influences the quality of the part produced. For successful processing of the part, the powder feedstock should meet the standard requirements as a raw material for the L-PBF process. The selectively melting process of the powder depending on the digital CAD model enables precise building of the part by layer-by-layer deposition which melts the powder and solidifies it rapidly in each layer. After building of the part, post-processing treatments such as heat treatment, electropolishing or even mechanical polishing may be needed to achieve the desired material properties as well as the surface finish of the nitinol part. There is ongoing research being conducted to optimize the processing parameters to achieve the required surface finish, targeted mechanical properties, and dimensional accuracy according to the intended application.

2.6.2 Effect on properties of the NiTi part

The laser powder bed fusion process directly influences and controls the properties of the produced component. This is particularly true for NiTi due to its higher sensitivity to the

varying phase transformation temperature which governs its unique properties such as shape memory effect and superelasticity [61,62]. Input laser energy density is a combination of the processing parameters such as laser power, scanning speed, hatch spacing and layer thickness and is given by equation (1).

$$VED\ \left(\frac{J}{mm3}\right) = \frac{laserpower\ (w)}{scanning\ speed\ \left(\frac{mm}{s}\right) * hatch\ spacing\ (\mu m) * layer\ thickness\ (\mu m)} \quad (1)$$

Laser input energy is influenced by the material characteristics, the desired application, and the machine parameters. Nitinol processing is affected by it specific thermal and optical properties which varies the laser absorptivity. Particularly for nitinol, the laser absorption coefficient, thermal conductivity and melting temperature determines the response to the input laser energy. The strength, hardness and other mechanical properties are directly proportional to the input energy of the fabricated parts. Higher energy density can improvise the density of the part but also result in over melting of the material. Porosity in the part can negatively affect the mechanical properties of the NiTi part. Several studies have reported that finer microstructures results in denser parts with minimized porosity [63–67]. Not only the processing parameters of the L-PBF process governs the properties of the NiTi part, but also the environment of the machine during the processing. An inert environment is usually maintained with an oxygen level below 20 ppm to prevent any oxidation during processing. This control is necessary to avoid the adverse effects of oxidation on the fabricated NiTi part. Several oxides such as Ti4Ni2Ox leads to increased brittleness of the part produced, thereby reducing the mechanical properties needed for its intended application [64,68,69]. Higher energy densities could lead to larger melt pools which may involve impurities leading to the formation of intermetallic phases. These intermetallic phases could alter the phase transformation temperatures and the mechanical response. Larger melt pools could also lead to the entrapment of the gas bubbles generating higher number of pores [70]. As reported by Obeidi et. al. [71], the range of VED that can be used for the fabrication of NiTi via L-PBF could range from 11 to 110 J/mm^3. This wide range of VED helps in different mechanical response from the fabricated parts and varying functional properties.

Adhesion between subsequent layers can be enhanced by using pre-heating for the substrates or of the powder bed itself. The thermal gradient at the bottom of the NiTi component can be decreased with the help of substrate heating enhancing the sintering

process. The warpage effect between the first few layers and the build platform could be reduced by substrate heating which reduces the chances of build failure [72,73]. Post processing such as heat treatments also can be employed to improve the functional properties of the produced part [74–78].

2.6.3 Effect on microstructures of NiTi

The microstructural formation of nitinol processed via L-PBF technique is greatly influenced by the variations in the processing parameters and the powder feedstock characteristics. The feedstock is selectively melted, and rapid solidification leads to the formation of the microstructures governed by the particle size and composition of the feedstock. The input energy which is a combination of the processing parameters such as laser power, scan speed, layer thickness and hatch spacing, influences the temperature distribution and the solidification process. The desired characteristics of the NiTi part produced via L-PBF is achieved by controlling the layer thickness as thinner layer thickness subsequently leads to finer microstructures. This in turn improves the resolution of the produced part. Further, the grain size and orientation of the microstructures can also be influenced by the scanning strategy employed during L-PBF process. Post processing techniques such as heat treatments can reduce the residual stresses and refines the microstructures necessary for shape memory and superelastic properties. Cooling rates during the solidification process controls the microstructures by rapid cooling leading to finer grains and slow cooling generating coarser grains.

Achieving the required microstructural size, orientation and texture is necessary to improve and achieve the targeted properties of the NiTi part. This can be achieved by varying and optimizing the process parameters of the L-PBF process [49,52,79–81]. Shen et. al. [82] investigated and reported the influence of energy density on the microstructure, precipitates, chemical composition and the transformation temperatures. It was found that the Ni_3Ti precipitates were formed at the boundary and centre of the melt pool with spherical $NiTi_2$ and Ni_2Ti_4O precipitates in the NiTi matrix as shown in **Figure 2-12**. Shi et. al. [83] found that the superelasticity of L-PBF produced NiTi part was dependent on the crystallographic orientation with (0 0 1) texture exhibiting the highest recoverable strain as shown in **Figure 2-13**. It was also reported that the microstructures affect the mechanical properties and wear which guides the tribological design and application of the produced part.

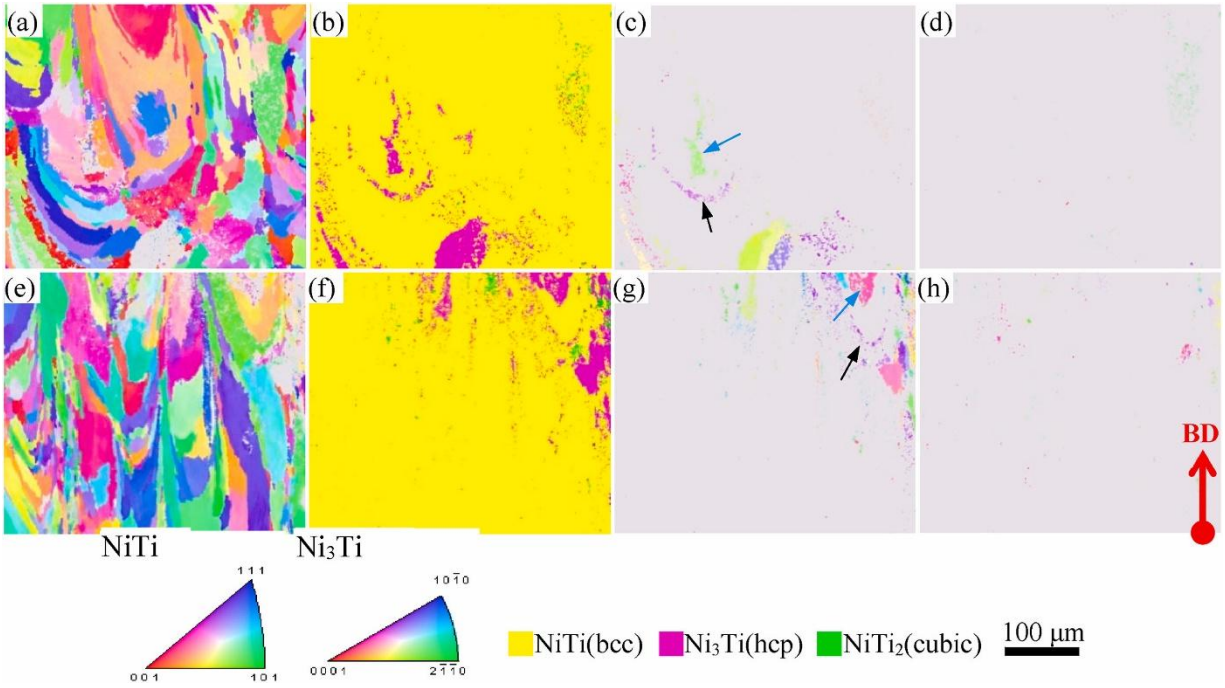

Figure 2-12: EBSD-reconstructed OIM and phase distribution in XZ planes (a–d) and YZ planes (e–h) of MP-700@79. (a), (e): OIM based on IPF of B2 phase; (b), (f): phase distribution; (c), (g): OIM based on IPF of Ni_3Ti phase; (d), (h): OIM based on IPF of $NiTi_2$ [82].

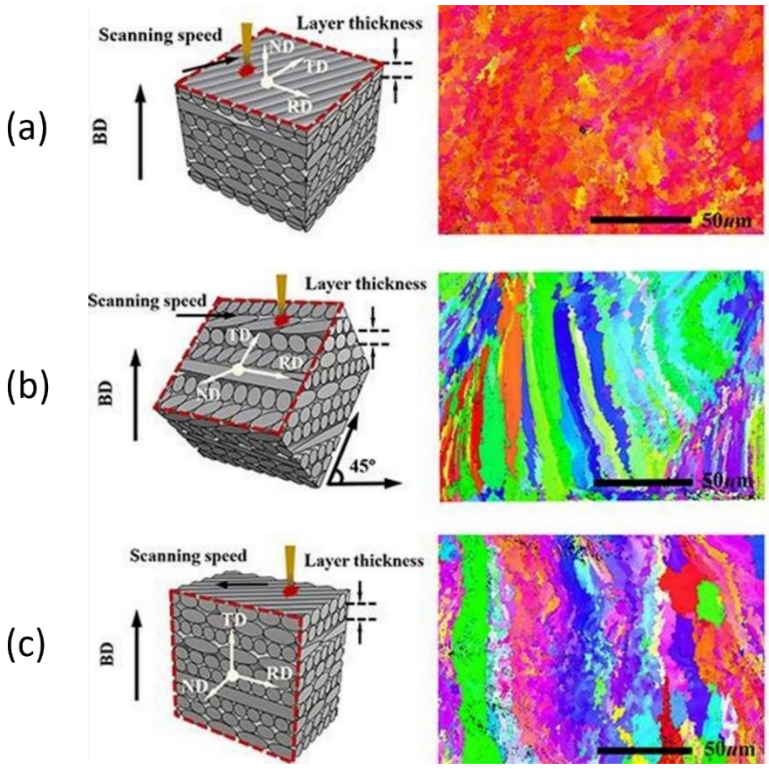

Figure 2-13: Orientation maps and phase distribution maps taken at (a) 0°, (b) 45° and (c) 90° to the build direction [83].

The critical processing parameters like the laser power and scanning speed govern the microstructure formation and orientation [84,85]. Ni evaporation is governed by the input energy which impacts the phase transformation temperature [86]. The complex process of re-melting and solidification during the L-PBF process affects the microstructures. Several studies have reported that longer grains are formed in the build direction due to the re-melting and subsequent bonding of the underlying layers [87,88]. This helps in avoiding pore formation in these layers and prevents failures of the L-PBF process. As reported by Chmielewska et. al. [89], re-melting of the layers helps in improving the density of the samples and also controls the orientation of the grains formed while varying the microhardness of the produced NiTi parts. Wang et. al. [90] found that the grain growth was dependent on the scanning angles and could be deflected according to the scanning angles utilised. Columnar grains were formed and an increase in the rotation angles resulted in the improvement of the grain orientation and texture. Saghaian et. al. [91] reported that the possibility of tailoring the microstructure ranging from highly textured microstructures in the [1 1 1] or [0 0 1] directions with the help of the L-PBF process. This was achieved by lowering the hatch space and achieving equiaxed solidification resulting in island grains with random orientations.

2.6.4 Effect on phase transformation temperatures of NiTi

Shape memory properties and superelastic behaviour of the NiTi parts are highly dependent on the phase transformation temperature of nitinol. Transformation temperatures determine the transition between the austenite and martensite phase of the NiTi parts. L-PBF process can also influence the transformation temperature of nitinol due to the thermal history comprising of localized heating and rapid cooling. The parameters of the process impact the resulting microstructures and phase characteristics. Any variation in the laser power, scan speed or laser spot size, changes the temperature reached during process and the solidification process, thereby affecting the phase transformation temperature. The cooling rate of each layer controls the formation of the microstructure and consequently, the phase transformation temperature. Studies have shown that post-processing treatments such as annealing helps in relieving the residual stress and affect the transformation temperature. Optimization of these transformation temperatures with the processing parameters crucially affects the materials properties of the NiTi parts produced with shape memory and superelastic properties.

Several studies have reported the influence of the laser input energy on the phase transformation temperatures during the L-PBF process [71,79,92–96]. Ren et. al. [97] has reported that the phase transformation temperature decreases in NiTi when the laser power is increased. This study also reported that with increase in the laser power led to an increase in the phase transformation temperature which corresponded to a simultaneous increase in the Ni content in the alloy. Wen et. al. [98] reported that the phase transformation temperature is also dependent on the Ni content of the NiTi part. A lower Ni content exhibited shape memory effect when compared to a relatively higher Ni content which showed superelastic property. The Ni content was related with the phase transformation temperature as well with a decrease in the Ni content increasing the phase transformation temperature. Post processing such as ageing heat treatment also affects the transformation temperatures as reported by Liu et. al. [39]. The transformation temperature increased with an increase in the holding time during ageing however it decreased with increasing ageing temperature after an initial increase.

2.7 Challenges of additive manufacturing technique for nitinol

Shape memory alloy, nitinol has been found to be difficult to machine and process due to its high hardness, requiring a higher amount of force to process leading to high wear and tear as well as failure [99]. In contrast to the traditional processing methods of nitinol, several challenges have also been reported while processing NiTi with the help of additive manufacturing techniques, especially L-PBF. The main issues that have been found are summarized below:

- Controlling and maintaining a uniform composition of the alloy needed for suitable phase transformation characteristics.
- Fabricating fully dense samples due to higher defect possibilities leading to pores.
- Understanding the effect of printing parameters influences the quality of the produced parts.
- Achieving the targeted mechanical and functional properties by controlling the input laser energy density.
- Influence of the oxygen content on the fabricated parts due to higher affinity of Ti to be oxidized.
- Supply of high-quality nitinol feedstock.

- Inheritance of unwanted residual stresses resulting in higher material's yield strength.
- Delamination between the layers due to non-precise control of the temperature during the process.
- Occurrence of warpage and cracking due to the temperature variations of the process.
- Achieving very high rough or irregular surfaces requiring further post processing to achieve better surface finish.

2.7.1 Residual stresses and cracking risks

During the L-PBF manufacturing of nitinol stents, inheritance of residual stresses and cracking risks are inevitable. Due to the rapid cooling and heating cycles of the L-PBF process leading to thermal gradients which subsequently results in the arise of residual stresses in the parts produced. This also alters the phase change between austenite and martensite phase [37]. These residual stresses adversely affect the performance of the stents by causing dimensional distortions and reducing the superelastic and shape memory effect. These stresses can also initiate cracks which in turn affects the durability of the medical device [100].

The thermal distribution and gradient during the L-PBF processing of NiTi stents results in the formation of residual stresses. Several researchers have reported that a thermal treatment can remove these residual stresses which leads to homogenisation of the phases. This increases the fatigue resistance and the durability of the nitinol stents [101,102].

Presence of defects, pores and micro-cracks which are formed during the processing of nitinol via L-PBF often enhances the cracking risks. Higher concentrations of stresses along the grain boundaries formed by the high cooling rates and the thermal gradient results in solidification cracks. These stressed areas often facilitate the crack initiation process, thereby reducing the fatigue life [56]. In order to mitigate these cracks, surface quality can be improved by post-processing methods to reduce the surface roughness and eliminate the micro-defects on the surface of the nitinol stents.

In addition to this, nickel content of the NiTi matrix also influences the cracking risks and the residual stresses. Higher nickel content stabilizes the austenite phase at body temperature, however, it could also contribute to cracking under mechanical loading-

unloading cycle [103]. By optimizing the surface finish parameters and the thermal treatment process, residual stresses and cracking can be minimized to increase the longevity of the stents.

2.7.2 Control of Ni content

The nickel Ni content in the NiTi matrix significantly controls the superelastic functionality, biocompatibility, and corrosion resistance of the nitinol stents. To establish stable austenitic phase at body temperature of 37 °C to exhibit superelastic behaviour of nitinol stents, the Ni content should be typically maintained between 50.8 and 51.5 atomic percentage [104]. The martensitic phase transformation temperatures are significantly affected by even a slight change in the Ni content which affects the shape memory effect and fatigue life of the stents. It has been reported by Pelton et. al. [105] that a 0.1at.% change in the Ni content can alter the transformation temperatures by 10 °C.

It has been seen that compositional homogeneity is a significant challenge due to the rapid thermal cycles in case of additive manufacturing particularly L-PBF. These cycles segregate the elements and leads to the formation of higher concentrations of Ni-rich or Ti-rich regions generating internal stresses and initiating cracks [49]. To ensure compositional homogeneity, process parameters such as laser power, scan speed and hatch space must be optimised to help in uniform melting and mixing of the powder. Pre-alloyed powders of nitinol with a controlled particle size distribution can be employed to enhance the uniformity in the composition during the L-PBF process.

Thermal treatments can also be used to enhance homogeneity in the composition of the NiTi matrix. Solution heat treatment at higher temperatures of 700 to 900 °C for longer times can help in dissolving the precipitates which leads to uniform distribution of Ni in the NiTi matrix. This in turn stabilizes the austenite phase and ensures higher corrosion resistance, increasing the life cycle of the nitinol stents [106]. Careful measurements must be made to ensure that the Ni content is in the recommended range with the help of inductively coupled plasma mass spectrometry (ICP-MS) and energy-dispersive X-ray spectroscopy (EDS) to prevent nickel ion release in the human body and increasing the reliability of the medical device.

2.7.3 Porosity, surface roughness and surface finish

Porosity, surface roughness and surface quality are several challenges that affect other factors such as biocompatibility and mechanical performance of nitinol stents fabricated via L-PBF. Several factors during the L-PBF such as gas entrapment, incomplete or partial melting of the powder particles and rapid thermal cycling of heating and cooling usually result in the occurrence of porosity. These pores or voids leads to the reduction of fatigue life and steepens the risk of crack initiation under repetitive loading conditions which the stents undergo [107]. Minimizing the porosity levels is crucial and can be achieved by optimizing the laser process parameters such as laser power, scan speed and hatch space to ensure melt pool dynamics enhancing better part production [108].

Another critical challenge inherited by the L-PBF process is surface roughness typically resulting from the staircase effect, partially melted particles, and balling phenomena. Corrosion resistance is reduced when the surface roughness is high for the fabricated part exposing more attack sites for corrosion and nickel ion release, risking infections in the human body [109]. Postprocessing methods must be employed to reduce the surface roughness by removing unwanted particles through techniques likes electropolishing, chemical etching and laser polishing.

Surface finish can be enhanced by removing the support structures and smoothing the surface to maintain the dimensional accuracy of the stents. Mechanical performance could be compromised if the surface has defects due to the inadequate removal of support structures. Surface quality plays a significant role in enhancing the functional properties of the nitinol stents.

2.7.4 Cost and scalability concerns

Ni-rich nitinol stents produced via the L-PBF process often possess concerns such as cost and scalability issues influencing their commercial viability and widespread adoption as a manufacturing technique. High material costs of nitinol to produce superelastic stents in comparison to stainless steel or cobalt-chromium alloys is the most critical challenge for the commercialisation of the L-PBF process. In addition to this, the L-PBF process itself requires energy consumption, expensive machinery and labour-intensive processing [110]. To produce high quality parts without failures, to increase cost-efficiency for the produced parts, optimisation of the laser process parameters and the powder quality is necessary.

Scalability remains another significant challenge. Although L-PBF offers design flexibility to produce bespoke stents, scaling up to meet the production demands is not easy. Several factors such as precise quality of the process including powder quality, material composition or the consumables needed along with the machine specifications could lead to differences in the parts produced [61]. It is also difficult to achieve high throughput with customisation which could lead in inconsistencies due to batch-to-batch variations effecting the reliability and costs of the stents.

Several strategies are being explored to combat with these challenges. Hybrid manufacturing combining both additive and subtractive manufacturing are paving way to help reduce production costs and time while maintaining benefits of both the techniques [111]. Design flexibility of AM and production efficiency of traditional techniques could be leveraged to create pathway for more cost-effective and scalable manufacturing of these biomedical devices. Automation of the post-processing techniques could help reduce labour costs and increase efficiency for mass production.

2.7.5 Regulatory and compliance issues for medical devices

In terms of medical devices, regulatory and compliance issues should be considered with utmost importance when producing nitinol stents using L-PBF process. The medical device industry is highly regulated to ensure the safety, efficacy, and quality of products. However, the additive manufacturing characteristics add to the complexity in meeting the regulatory requirements. Regulatory bodies such as the U.S. Food and Drug Administration (FDA), European Medicines Agency (EMA), and other global regulatory authorities have established stringent guidelines for the approval of medical devices, which include comprehensive pre-market approval (PMA) processes, clinical testing, and ongoing post-market surveillance. A list of all the standards has been tabulated in **Table 2-1** [112,113].

Medical devices possess concerns regarding the quality and safety of the product after being manufactured by the L-PBF method. This method introduce inconsistencies like porosity and defects, makes material quality difficult to control, higher surface roughness affecting the overall performance of the device.

Authorities are required to check manufacturers who can provide high reproducibility and reliability of the device manufacturing, ensuring the manufacturing standards of each individual unit for safety. Stringent quality control must be opted by the manufacturers

to have precise control over the material and the process for achieving highest repeatability across different production runs.

Although AM utilises the design flexibility to produce stents, this becomes a challenge for the regulatory body. Further scrutiny is needed for complex designs and are facilitated by the comprehensive design history file and risk management files to document the device's design. Stents produce via L-PBF undergo high standard of mechanical as well as biocompatibility tests along with clinical tests to ensure safety and efficacy of the medical device. Robust tracking must be in place ensuring traceability of the entire production batch to help trace back the device to specific batch, material source and even design changes. This will ensure the traceability throughput its lifecycle in case of emergency.

Table 2-1: List of standards for manufacturing of self-expanding nitinol stents.

Area	Standard / Guidance
Biocompatibility	ISO 10993 series
Vascular Stents	ISO 25539-2
Fatigue Testing	ASTM F2477
Radial Force Testing	ASTM F3067
Corrosion	ASTM F2129
Drug-Eluting Stents	ASTM F2743, F2394 (as applicable)
Risk Management	ISO 14971
Sterilization Validation	ISO 11135 / 11137

Standardization of L-PBF as a manufacturing technique for medical devices is still underway. Although several regulatory bodies have issues guidance for AM in medical device production, its full integration is still a slow process [114]. Consequently, manufacturers must often engage in pre-submission consultations with regulatory bodies to ensure they meet all necessary requirements and avoid delays in approval.

2.8 Post-processing of L-PBF produced nitinol parts

Although L-PBF has enabled the possibility of producing intricate and complex structures such as stents with its design freedom property, the parts produced via this technique often need to undergo further treatment to enhance the mechanical properties, surface finish and the performance of the stents itself. Post processing usually helps in

addressing issues like surface roughness, porosity, residual stresses and microstructural inhomogeneity leading to improved functionality of the stents.

One of the most common post-processing steps is thermal treatment. Two different types of thermal treatments, namely, ageing and solution heat treatment could be utilised to help relive residual stresses, lead to formation or dissolving the precipitates and alter the phase transformation temperatures. This results in tailoring the properties of the NiTi parts produced via L-PBF [115].

Another challenge which needs attention is the surface quality of the NiTi parts produced via L-PBF. Typically, parts produced using L-PBF exhibit high surface roughness which could possibly smoothened with the help of either electropolishing or laser polishing techniques. These techniques remove the residual powder particles, thereby, improving the appearance as well as biocompatibility of the stents.

2.8.1 Heat treatment of nitinol

Even with all the advantages of AM technologies, there are still some challenges that it possesses. Defects such as high surface roughness, different porosity levels, residual stress, and heterogeneous microstructures are frequently seen in as-built AM samples [116]. It is crucial to control and prevent nickel evaporation and assess how process parameters affect processing temperatures when it comes to the NiTi components that are additively built. Therefore, it is imperative to optimize these NiTi production-related factors using AM. This can be done by modifying process parameters or by applying post-processing methods such heat treatments and electropolishing. Several investigations have demonstrated the critical significance that distinct precipitate types play in altering the transformation behaviour of these alloys. The aforementioned precipitates are formed when heat treatments are applied to NiTi alloys, causing modifications in microstructure and internal tensions. For instance, in Ni-rich NiTi alloys, the emergence of Ni-rich precipitates causes the matrix's Ni content to drop, bringing the composition of the matrix closer to that of equiatomic NiTi and raising the transformation temperatures. As a result, a drop in the transformation temperatures is implied by an increase in the concentration of Ni in the matrix [117–120]. Because of this, applying heat treatments to NiTi alloys can produce varying transformation temperatures, which makes this technique appropriate for simulating the component's post-production attributes.

2.8.1.1 Effect of ageing treatment of NiTi

Ageing heat treatment parameters are typically defined as the heating temperature and the holding times at that temperature. Several effects of ageing heat treatments include stabilization of the resulting properties of the part by minimizing the stress-induced phase transformations to enhance the performance of the parts. Ageing temperatures and times for nitinol can be chosen depending on the desired properties, however, the typical range is from 350 to 575 °C [121]. Specific mechanical, thermal or metallurgical properties can be achieved through controlled exposure of nitinol to ageing temperatures and times. Mechanical properties such as hardness, strength and toughness can be enhanced by the heat treatment process by the occurrence of precipitation and the hardening process. However, careful consideration should be conducted to achieve the targeted properties without having adverse effects on the other properties. Optimization of the ageing parameters are required to achieve targeted properties which is highly dependent on the composition of the part, the intended application as well as the controlled process of the heat treatment. Overall stability of the part is improved by facilitating the reduction in the internal stresses due to the manufacturing process or previous mechanical treatments. Ageing heat treatment also contributes to the formation of corrosion resistant phases of nitinol, enhancing the durability of the parts in corrosive environments.

2.8.1.2 Effect of solution treatment of NiTi

Another type of heat treatment used for certain alloys, including nitinol is the solution heat treatment. For nitinol, solution heat treatment is beneficial to homogenize the alloy and to dissolve any undesirable phases or precipitates into the NiTi matrix, which may have been formed during the previous processing of the material, typically done between the temperature range of 950 to 1050 °C [103]. This process helps in achieving a uniform distribution of the alloyed elements and recover the ability to be ductile after any cold working had been done on it. Unlike ageing, the temperature and times used for this process is generally above the critical temperature of the alloy to achieve stable solid solution of the nitinol. Since solution heat treatment temperature is above the austenitic finish temperature of the material, its coverts any metastable phases and martensitic phases into stable austenitic phases. This process also leads to the recrystallization of NiTi with the formation of new strain-free grains. Typically, a subsequent quenching step is performed to rapidly cool the material in the desired solid-state solution. Microstructural changes are a result of this heat treatment process owing to the

dissolution of the precipitates and the transformation of the phases. This process is usually needed to carefully tailor the properties of the material to achieve the targeted material characteristics of nitinol parts for the intended applications.

2.8.2 Surface finish of NiTi

The surface finish and quality of NiTi parts is an important factor in determining the functionality like corrosion resistance and biocompatibility for medical devices specially stents. With unique properties of nitinol such as superelasticity and shape memory effect, surface related issues including higher roughness and defects are susceptible leading to reduced corrosion resistance, higher fatigue and adverse biological responses. Surface roughness is inherited due to the manufacturing process such as laser cutting, milling or even L-PBF. Factors including thermal changes during processing, layer-by-layer deposition and remaining powder particles typically contribute to increase the roughness. Highly rough surfaces have adverse effects in the human body causing platelet aggregation and increased thrombosis risks [122].

Post-processing techniques needs to be employed to reduce the surface roughness by smoothening it by removing the unmelted adhered particles or the micro-defects on the surface. Different approaches like chemical etching, laser polishing and electropolishing have been made to improve the surface finish of stents. Electropolishing has been the most widely opted techniques that not only enhances the appearance of the surface but also forms a stable TiO_2 oxide layer which supports corrosion resistance and biocompatibility [106]. This stable layer prevents the release of nickel ions in the human body reducing the possibility of allergic reactions [103]. Laser polishing has also gained importance as a polishing technique to improve the surface smoothness while maintain the integrity of the stent geometry. As discussed by Pelton et. al. [123], the average surface roughness of nitinol was found to be lesser than 0.1μm which was beneficial in increasing the fatigue life. In another study from Martinez et. al. [124], it has been reported that the average surface roughness of nitinol samples produced via L-PBF decreased from around 8 μm to less than 2 μm after electropolishing making it a suitable technique to improve the surface finish. This is turn also improves the corrosion resistance of the parts produced.

Achieving a better surface finish is required to improve the ability of the stents to withstand the cyclic loading which it undergoes in the human body. Moreover, a well-

finished surface enhances the wettability property, thereby promoting the biological response [19].

2.9 Mechanical performance of L-PBF Ni-rich nitinol stents

The mechanical performance of medical devices such as stents produced via L-PBF is crucial to ensure the reliable functioning, fatigue resistance and longevity of the device. Although L-PBF offers a single step process for the fabrication of nitinol stents with design freedom, however, its mechanical performance could be compromised. In comparison to stents produced via traditional methods, microstructural variations could lead to residual stresses, porosity and grain structure due to the L-PBF process. These changes could impact the functional properties including radial force and flexibility. Due to the pumping action of the heart which exerts cyclic loading on the stent device, could significantly reduce the fatigue life and performance of the stents due to the inherited residual stress.

Superelastic property of nitinol stents is crucial for their proper functioning in the human body to expand and contract because of the temperature change which can be influenced by the thermal history of nitinol during L-PBF. Post processing such as thermal treatment is thus necessary to enhance the superelastic behaviour. Appropriate thermal treatment can modify the microstructure of the stent, necessary for achieving the desired radial force and reliability [103].

Surface finish also plays an important role in determining the mechanical performance of the nitinol stents produced by L-PBF. Highly rough surface could lead to higher stresses which reduces the fatigue life and strength of the stents. Such surface defects could be removed with the help of electropolishing or laser polishing to improve the functional properties of the stents. Studies have demonstrated that such treatments not only improve surface finish but also enhance mechanical strength and long-term durability [106].

2.9.1 Corrosion behavior of NiTi

Nitinol, a combination of nickel and titanium, has an overall good corrosion resistance in the environment that it is exposed to. However, its corrosion behavior is strongly influenced by the composition of nitinol, its surface quality, and the environment to which it has been exposed to. This corrosion resistance property of nitinol makes it suitable for several applications in the fields of medical components as well as aerospace

industry. Nitinol could form a titanium oxide (TiO_2) and nickel oxide (NiO) layer as passivation layer on its surface which acts as a barrier against further oxidation. These oxide layers not only prevent the surface of nitinol being exposed to harmful environments but also TiO_2 oxide layer enhances the biocompatibility of the part by adding its ability to withstand the harsh environments. Certain chloride ions or harmful conditions can breach the oxide layer which could attack the underlying nitinol part. This leads to higher susceptibility of the nitinol part to localized pitting corrosion. Such pitting corrosion can be avoided with the help of surface treatments like additional passivation or coatings to improve the corrosion resistance of the nitinol part. The stability of the passivation layer also plays a vital role in preventing the part from corrosion in the environment that it is subjected to. However, depending on the pH, temperature and the combination of ions present in the environment, corrosion resistance of the part is also influenced strongly. Several tests have been conducted to determine the long-term stability of a nitinol part in bodily fluids, saline solutions, or other corrosive environments. Various factors influence the corrosion behavior of nitinol and its parts which require careful consideration and control. Appropriate measures should be made to protect the parts against corrosion depending on the intended application, subjected condition, and any other stress conditions that the part may be subjected to. Regular maintenance and inspection should be done to mitigate any failures due to the corrosion of the nitinol part.

2.9.2 Tensile and compressive properties

Thorough tensile and compressive investigations must be made for the nitinol stent samples fabricated using the L-PBF technique to ensure that they can withstand the mechanical demands during deployment and in-vivo conditions. It is essential for the stents to respond to the pulling forces without undergoing any permanent deformation or fracture. The Ni content and the post-processing techniques like heat treatment influences the ultimate tensile strength (UTS) which typically ranges from 800 to 1600 MPa for nitinol. The UTS can be further enhanced by stabilizing the austenitic phase of nitinol by increasing the Ni content till a certain extent. Additionally, AM nitinol can achieve 10–20% elongation, making it comparable to wrought nitinol when subjected to appropriate heat treatment [125].

Compressive properties exhibit the ability of nitinol to respond to the pushing forces which is between 1200 to 1500 MPa typically for nitinol. A higher fraction of austenitic

phases and homogeneous microstructures achieved through post-processing helps in enhancing the compressive strength. The typical elastic modulus of nitinol is dependent on the phase: austenite phase has a modulus of 40-75 GPa whereas the martensitic phase of nitinol has a range of 18 – 40 GPa [126]. The lower modulus of nitinol for medical applications is usually lower than 60 GPa which is significantly lower than that of stainless steel (~200 GPa) [109]. This offers better flexibility, thereby reducing the risk of arterial damage [127].

The mechanical characteristics of the nitinol stents are greatly influenced by several factors such as the Ni content. A higher Ni content (50.8–51.5 at.%) promotes the presence of the austenitic phase at body temperature, enhancing both tensile strength and superelastic properties [128]. Additionally, heat treatment plays a vital role in improving ductility and eliminating internal stresses introduced during the LPBF process. Aging at temperatures between 400–500°C is particularly effective in enhancing superelasticity by controlling the formation of precipitates [129]. The parameters used during additive manufacturing—such as laser power, scan speed, and layer thickness—also significantly impact the grain structure and porosity of nitinol, thereby influencing its tensile and compressive properties. Optimizing these parameters can result in a homogeneous microstructure with minimal defects, ensuring superior mechanical performance.

2.9.3 Fatigue resistance and durability of stents

Fatigue resistance and durability are critical factors in the performance and longevity of nitinol stents, especially considering the cyclic mechanical stresses they undergo in vivo due to pulsatile blood flow and vessel movements. The unique superelastic property of nitinol enables the product to undergo repeated loading cycles and the phase transformation allows to absorb energy [109]. Fatigue resistance is controlled by the microstructures formed, pores and defects and surface finish of the nitinol stents formed during the L-PBF process. Texture, grain size and distribution play a significant role in enhancing the fatigue life of the medical device [100].

Additively manufactured nitinol parts are very sensitive to the oxygen and impurity content affecting the fatigue and fracture properties. Higher oxygen content often forms TiO_2 and oxide inclusions leading to crack initiation sites which decreases the fatigue life of the part. Oxide inclusions acts as stress concentrations resulting in early crack

propagation at these locations, thereby reducing the fatigue resistance [130]. Formation of heterogeneous microstructures due to the presence of impurities such as carbon or nitrogen forms TiC or TiN phases which promotes brittleness and lowers the ductility. According to the ASTM F2063 standard [113], for ideal fatigue life, the oxygen content should be lower than 0.05 wt% (500 ppm). It has been reported that for every 0.01 wt% increase in oxygen can drop fatigue strength by 5-15%, depending on the L-PBF process and the geometry of the part.

Surface finish along with the nickel content in the nitinol matrix plays a pivotal role in determining the fatigue behaviour and durability of the nitinol stents. The optimal nickel content ensures a stable austenitic phase required for the proper functioning of the nitinol stents in the human body and also influences the fatigue life by maintaining the superelastic property. Designs with controlled strut thickness and pattern significantly influences the stress distribution and subsequently, the fatigue life and durability of the medical device [128].

2.9.4 Radial force, flexibility and deployment behavior

Radial force is an important property for the functionality of nitinol stent in maintaining the vessel patency and accommodating the dynamic environment of blood vessels. It is the force needed by the device to exert outward pressure against the blood vessel wall to prevent failure. Nitinol stents exhibit a lower radial force than stainless steel or Co-Cr stents which could be a limitation for its usage in heavily calcified lesions. Therefore, NiTi stents are most appropriate for tortuous vessels, where superelasticity and fatigue resistance are most critical. The unique superelastic property and stress induced martensitic transformation of nitinol stents control the radial force to maintain pressure even under large deformations [131].

Another essential property for nitinol stents is flexibility enabling them to withstand continuous cyclic loading-unloading without causing kinking. For the nitinol stents with lower elastic modulus than 75 GPa compared to that of stainless steel (>200 GPa) to adapt to the vascular environment, higher flexibility is required [132]. High recoverability of around 8% for nitinol without permanent deformation helps in achieving greater flexibility. This property is useful during crimping and deployment of the stents in the human body to enable the small diameter during crimping and its total recovery after deployment. Post processing can further refine the flexibility by promoting

a homogeneous austenitic phase distribution and enhancing the mechanical performance [39].

Nitinol stents expand on its own when released from the catheter providing a reliable deployment mechanism. Self-expanding nitinol stents reduce the risk of vessel injury and minimizes the need of high pressure ballons for deployment [115]. Finite Element Analysis (FEA) studies have shown that optimized strut designs support to minimize the local stresses without compromising the structural integrity of the stents.

2.9.5 Comparative analysis with conventional stents

Traditionally stents were manufactured from stainless steel (316L) and cobalt-chromium alloys. In the recent times, nitinol has gained popularity as a material of choice for the manufacturing of stents. One of the most prominent advantages of nitinol stents is the unique superelastic behaviour which exhibits large recoverability after loading, a property that is absent in conventional metallic stents. On the other hand, conventional stents rely on their plastic deformation to maintain vessel patency, which can lead to higher risks of fracture, particularly in tortuous or dynamic vessels [18].

Another superiority exhibited by nitinol is its higher corrosion resistance than other materials. The formation of the titanium oxide layer acting as passivation layer provides excellent protection against pitting and crevice corrosion, significantly outperforming the chromium oxide layers on stainless steel and cobalt-chromium alloys [106]. This prevents the metal ion release in the body reducing the risks inflammatory responses and hypersensitivity. Stainless steel stents can release iron, chromium, and nickel ions, which have been associated with local inflammation and restenosis [14]. In comparison, surface treatments like electropolishing on nitinol further enhance its corrosion resistance, ensuring long-term stability and reducing nickel ion leaching to non-toxic levels.

In terms of flexibility, nitinol stents have a distinct advantage due to their lower elastic modulus (30–75 GPa) compared to stainless steel (~200 GPa) and cobalt-chromium (~230 GPa) as shown in **Table 2-2** [133–135]. This lower modulus allows nitinol stents to conform better to complex and tortuous vascular anatomies without causing vessel trauma or kinking, which is particularly important in superficial femoral and coronary artery applications. The self-expanding nature of Nitinol stents also facilitates deployment in challenging anatomies without the need for high balloon pressures, reducing the risk of vessel injury during placement [115]. In contrast, conventional

balloon-expandable stents often struggle with elastic recoil and require higher deployment pressures, increasing the risk of complications.

Table 2-2: Comparison of the physical properties of nitinol, stainless steel and cobalt-chromium alloy stents.

Property	Nitinol	316L Stainless Steel	Cobalt-Chromium (CoCr)
Elastic Modulus (E)	30–75 GPa (phase-dependent)	~190–210 GPa	~220–240 GPa
Ultimate Tensile Strength	800–1600 MPa	~500–700 MPa	~1000–1500 MPa
Yield Strength	~195–700 MPa	~200–400 MPa	~600–1000 MPa
Elongation at Break	10–15% (functional)	30–50%	20–40%
Density	~6.45 g/cm³	~8.0 g/cm³	~9.0 g/cm³
Fatigue Resistance	Excellent (superelasticity)	Moderate	High
MRI Compatibility	Good (non-ferromagnetic)	Acceptable	May be limited (partially magnetic)
Radial Force (in stents)	Lower than CoCr	Moderate	High

2.10 Characterization techniques

2.10.1 Density measurements using Archimedes' principle

Density measurements were conducted using an analytical and precision balance, Sartorius Entris II Essential Line BCE124Ie1S as shown in **Figure 2-14**, with a precision of four decimal places. Samples were measured using the Archimedes principle [136] stated as in the equation (1).

$$\rho = \rho(a) + \frac{W(a) * [\rho(fl) - \rho(a)]}{W(a) - W(fl)} \quad (1)$$

Where $W(a)$ is the weight of solid in air, $W(fl)$is the weight of solid in liquid, $\rho(fl)$is density of liquid which was ethanol (0.789 g/cm^3), $\rho(a)$is the density of air under standard conditions (0.0012 g/cm^3). As stated by the principle, a body immersed in fluid indicates the loss in weight equal to the weight of the displaced fluid. This method requires a fluid that does not react with the sample being measured. It requires the sample

to be measured in air and then immersed in the fluid with known density. In this study, ethanol was used as the fluid. Each sample was measured 3 times to ensure the reliability and to minimize the errors according to the standard ASTM B962-13 [137] and the average was reported.

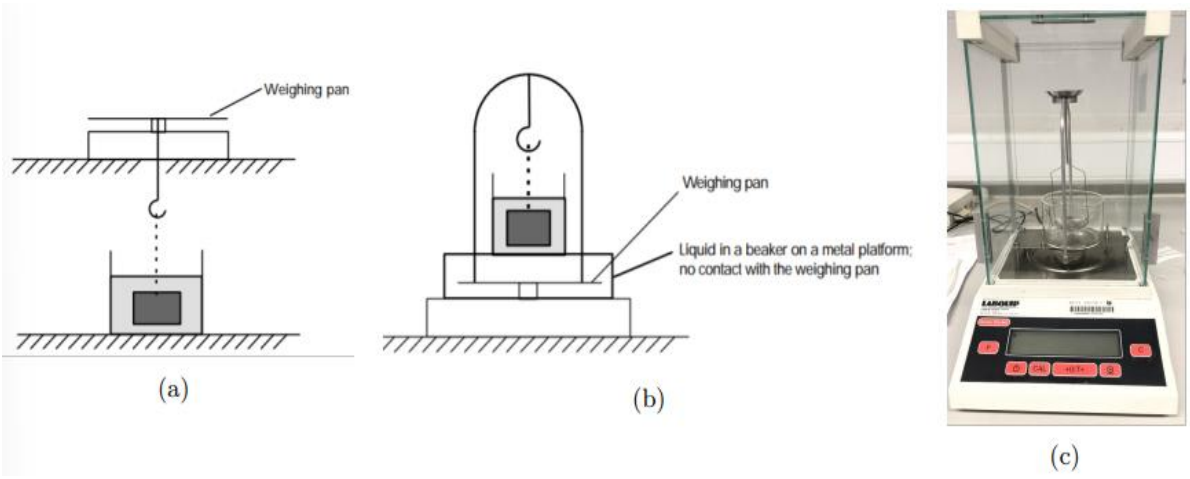

Figure 2-14: Buoyancy method of density measurement. (a) below balance weighing [138], (b) balance with hanging plummet and bridge to hold container for liquid [138], (c) balance in DCU for density measurements.

2.10.2 Microhardness tests using Vickers hardness

Hardness of a material is commonly measured by the Vickers microhardness tests. This technique works on very low force levels and are usually very useful for small samples. Since the hardness values are independent of the size of the indenter, therefore, can be used on thin or small samples. Samples are indented with a pyramidal indenter and makes a square indent on the sample. The lengths of the diagonals are measured which gives a measure of the material's resistance to deform. The Vickers microhardness is calculated by the equations (2) and (3) as follows:

$$HV = F\frac{2\sin(\frac{136^\circ}{2})}{d^2} \qquad (2)$$

$$HV = \frac{1.8544\,F}{d^2} \qquad (3)$$

where F is the force applied in kilogram-force, and d is the mean of the diagonal lengths d_1 and d_2 as shown in **Figure 2-15**. Samples were prepared so that they were completely

flat which was achieved by metallurgical preparations of the samples by grinding and polishing them.

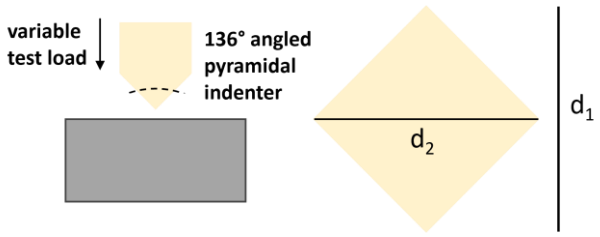

Figure 2-15: Vickers microhardness test with pyramidal indenter.

A Leitz MiniLoad 2® equipment was employed for measuring the Vickers microhardness. Samples were indented with a load of 981mN with a holding time of 20 seconds for each indent. Five random selections were made on the samples surface and the average was reported. The tests were carried out under standard laboratory conditions.

2.10.3 Crystallographic studies using X-Ray Diffraction technique

A Bruker D8 X-ray diffractometer was employed for the crystallographic studies equipped with a Cu Kα source of a wavelength of 1.5406Å. The samples under examination were scanned for a 2theta angle ranging between 10 and 100 degrees. A locked coupled setting with an increment of 0.01° and 8s/step was used for the scans.

2.10.4 Microstructural and elemental compositional characterisation

Surface morphology and topology was analysed using a scanning electron microscope (SEM) Zeiss EVO LS15 at a high voltage of 20 kV. This SEM machine is a thermionic emission SEM with variable pressure option, and a maximum magnification of 300,000 x with a 5-axis stage. It is also equipped with INCA, Oxford Instruments energy dispersive X-ray spectroscope (EDX) to analyse the chemical composition of the samples under investigation.

2.10.5 Temperature transformation studies using Differential Scanning Calorimetry (DSC)

A TA Instruments Discovery DSC 2500, New Castle, DE, USA was employed to perform the transformation temperature measurements. To conduct the measurements, the sample weight and the weight of the sample pans play a critical role and must be measured accurately. Pure aluminium pans with lids are used as sample pans. A Mettler AE200 Analytical balance is used for the mass measurements. A TRIOS software is used for measuring the changes in the thermal parameters of the sample. NiTi samples were

measured in a temperature range of 0°C to 150°C with a ramp up rate of -10°C/min. Around 20mg of sample weights were used for the measurement of the phase transformation temperatures. Liquid nitrogen was used as a cooling medium.

2.10.6 Corrosion testing

The electrochemical corrosion tests were conducted using the Gamry system Interface100 from Gamry Instruments, USA. In a lab setup, the accelerated corrosion tests are performed to see the effect of oxidation and reduction reactions involved in the corrosion process. The setup involves a three-electrode setup with the specimen being a working electrode with a defined exposed surface area; a $AgCl_2$ as the reference electrode and a graphite rod as the counter electrode. Bodily fluids such as Hank's solution and Ringers solution were used as the electrolyte. The setup was placed onto a heating plate to maintain the body-like temperature of the electrolyte at 37°C. Open circuit potential program was performed to help the electrodes to stabilize in the electrolyte environment for an hour before electrochemical impedance spectroscopy as well as before potentiodynamic polarization measurements. Electrochemical impedance spectroscopic measurements were conducted to analyse the anti-corrosion behaviour of the additively manufactured NiTi samples when they are immersed in the respective electrolyte. Potentiodynamic polarization measurements were done on the samples to investigate the corrosion behaviour of the samples at a constant scanning rate of 0.167 mVs^{-1}. The measurements were conducted in the range of -0.3V to 0.3V and the electrochemical parameters were determined using the Tafel curve fitting analysis from the Gamry Analyst software.

2.11 Summary of existing knowledge

Nitinol, a close to equi-atomic alloy of nickel and titanium, has acquired considerable attention in the biomedical field—particularly in the fabrication of vascular stents—owing to its unique shape memory effect and superelasticity. Facilitating full recovery of the original shape of the stent after deformation with minimal invasive delivery and deployment, these properties of nitinol play an important role. These properties make nitinol a more suitable material candidate, compared to alternatives such as stainless steel and cobalt-chromium alloys, by providing improved functional advantages particularly in dynamic environments like the cardiovascular system. However, poor machinability of nitinol, uncontrolled phase transformations and work hardening makes the processing of nitinol difficult. The traditional techniques of processing nitinol such as laser cutting,

wire drawing and machining also exhibits challenges which in turn hinders the ability to achieve geometric complexity and customization of nitinol stents.

To address to the machining challenges of nitinol, additive manufacturing (AM), especially Laser Powder Bed Fusion (L-PBF), has emerged as a transformative technique to fabricate nitinol stents with greater design freedom, precision and patient-specific customization. L-PBF grants the ability to produce intricate geometries with tailored porosity by using selective melting of metal layer-by-layer making it advantageous for biomedical implants. Although there are several advantages of L-PBF processing of nitinol, there exists several drawbacks as well. Residual stresses, inhomogeneity in microstructures formed and changes in phase transformation behaviour are often results of thermal gradients and rapid solidification of the L-PBF process. These adversely affect the mechanical and functional properties of nitinol parts. Post-processing techniques such as heat treatment and surface finishing techniques are required to meet the biomedical standards for better functionality and biocompatibility.

2.11.1 Research gaps

The existing literature has recognised the importance of process parameter optimization and post-processing techniques to enhance the properties of the nitinol parts produced via L-PBF. Still there is a lack of comprehensive understanding of how process parameters of L-PBF influence the functional properties of Ni-rich nitinol, especially in context of stent applications affecting its phase transformation characteristics, mechanical response and long-term biological performance. Similarly, post-processing techniques such as heat treatment and surface finishing have not been fully optimized to mitigate the adverse effects introduced during L-PBF processing. Consequently, there exists a need for a systematic study that not only investigates the effects of printing parameters and post-processing treatments on Ni-rich nitinol but also studies integrating process–structure–property relationships linking these factors to performance criteria essential for stent applications.

The research gaps and the methods employed and presented within this thesis to address these are summarized below.

- It was hypothesised that heat treatments could be applied in order to control the phase change temperatures and mechanical response of standard commercial

nitinol wire. In this case, to establish a foundation for thermal treatment strategies, Chapter 3 presents an examination of the effects of ageing heat treatments on conventionally manufactured nitinol wires. Such wires are used for the manufacture of stents and catheters. The effect of heat treatment temperature and time on phase transformation temperatures, hardness, and recovery strain were analysed, offering a baseline for comparing subsequent results from additively manufactured counterparts.

- It was hypothesized that the process parameters within the metal L-PBF, combined with control of the post process heat treatment parameters, can be used to control the microstructure and physical properties of nitinol printed parts. Chapter 6 presents this analysis of the combined effects of L-PBF process parameters and direct ageing heat treatment on phase characteristics, grain size and hardness. This study bridges the gap to understand the interplay between L-PBF parameters and thermal treatment in determining the performance of Ni-rich nitinol parts. The findings confirms that this synergistic approach can significantly improve the functional properties of the nitinol parts, specifically for biomedical applications.
- It was hypothesized that the process parameters within the metal L-PBF process can be used to control the resulting material microstructure and behaviour. In Chapter 4, the impact of laser power and scan speed on the material's density, grain morphology, hardness and phase transformation temperatures has been evaluated. This study provides valuable insights on how the final microstructures, density and phase transformation behaviour can be tuned using the optimized printing conditions to achieve desired mechanical integrity and functional performance.
- It was hypothesized that the process parameters within the metal L-PBF process can be used to control the corrosion characteristics of nitinol printed parts. Chapter 5 entirely focuses on finding the optimized L-PBF parameters that result in higher corrosion resistance, owing to the importance of biocompatibility and long-term performance in bodily environments for an extended period of time. This chapter identifies the printing parameters that yield optimal corrosion resistance, using electrochemical testing in simulated body fluids at elevated temperatures of 37 °C. It provides new insights into how microstructural features

and surface conditions, influenced by L-PBF settings, can impact the corrosion behaviour of Ni-rich nitinol.

- It was hypothesized that the surface finish of L-PBF printed stents can be improved via optimisation of the electropolishing process. Chapter 7 presents an examination of the influence of the electropolishing post processing technique on improving the surface quality. The effect of the electropolishing parameters of voltage, time and flow rate were examined. The results and discussion in this chapter helps to addresses the gap in understanding of the interplay between the printing parameters and electropolishing process parameters to improve the resulting surface properties for medical-grade nitinol stents.

In summary, this literature review reveals that while additive manufacturing of nitinol via L-PBF holds great promise for biomedical applications, particularly for vascular stents, substantial challenges remain. These include limited understanding of process-property relationships, lack of optimized post-processing techniques, and insufficient data on long-term biological performance. This thesis aims to fill these gaps through a structured investigation, contributing to the development of clinically viable, high-performance nitinol stents.

Chapter 3: Effect of Heat Treatment Time and Temperature on the Microstructure and Shape Memory Properties of Nitinol Wires

Publication Status: Published

Agarwal, N.; Ryan Murphy, J.; Hashemi, T.S.; Mossop, T.; O'Neill, D.; Power, J.; Shayegh, A.; Brabazon, D. Effect of Heat Treatment Time and Temperature on the Microstructure and Shape Memory Properties of Nitinol Wires. *Materials* **2023**, *16*, 6480. https://doi.org/10.3390/ma16196480

3 Abstract

In this study, the effect of heat treatment parameters on the optimized performance of Ni-rich nickel–titanium wires (NiTi/Nitinol) were investigated that were intended for application as actuators across various industries. In this instance, the maximum recovery strain and actuation angle achievable by a nitinol wire were employed as indicators of optimal performance. Nitinol wires were heat treated at different temperatures, 400–500 °C, and times, 30–120 min, to study the effects of these heat treatment parameters on the actuation performance and properties of the nitinol wires. Assessment covered changes in density, hardness, phase transition temperatures, microstructure, and alloy composition resulting from these heat treatments. DSC analysis revealed a decrease in the austenite transformation temperature, which transitioned from 42.8 °C to 24.39 °C with an increase in heat treatment temperature from 400 °C to 500 °C and was attributed to the formation of Ni_4Ti_3 precipitates. Increasing the heat treatment time led to an increase in the austenite transformation temperature. A negative correlation between the hardness of the heat-treated samples and the heat treatment temperature was found. This trend can be attributed to the formation and growth of Ni_4Ti_3 precipitates, which in turn affect the matrix properties. A novel approach involving image analysis was utilized as a simple yet robust analysis method for measurement of recovery strain for the wires as they underwent actuation. It was found that increasing heat treatment temperature from 400 °C to 500 °C above 30 min raised recovery strain from 0.001 to 0.01, thereby maximizing the shape memory effect.

3.1 Introduction

Nitinol is an intermetallic phase of the nickel–titanium alloy with near-equiatomic composition. It has two main crystal phases: a high-temperature austenitic phase with BCC crystal structure, and a low-temperature martensitic phase with a monoclinic lattice structure [139]. The transformation from austenite to twinned martensite on cooling is a diffusionless process meaning that it can occur at very low temperatures as depicted in **Figure *3-1***. As there is no diffusion of atoms, the only change that takes place is in the crystal structure of the material, as depicted in **Figure *3-1***, allowing what is known as the shape memory effect (SME) to occur [140]. When stress is applied to nitinol in the twinned martensite phase, provided the stress is sufficiently high to induce a phase transformation yet remains below the elastic limit, slip will not take place. Instead, a temporary phase change from twinned martensite to detwinned martensite will be

observed [141]. This means that during the phase change, no atomic bonds are broken and thus the phase change is reversible, allowing the nitinol to recover its original shape when heated to the high-temperature austenite phase. The nitinol then remains in this shape as it cools and transforms back to twinned martensite [142].

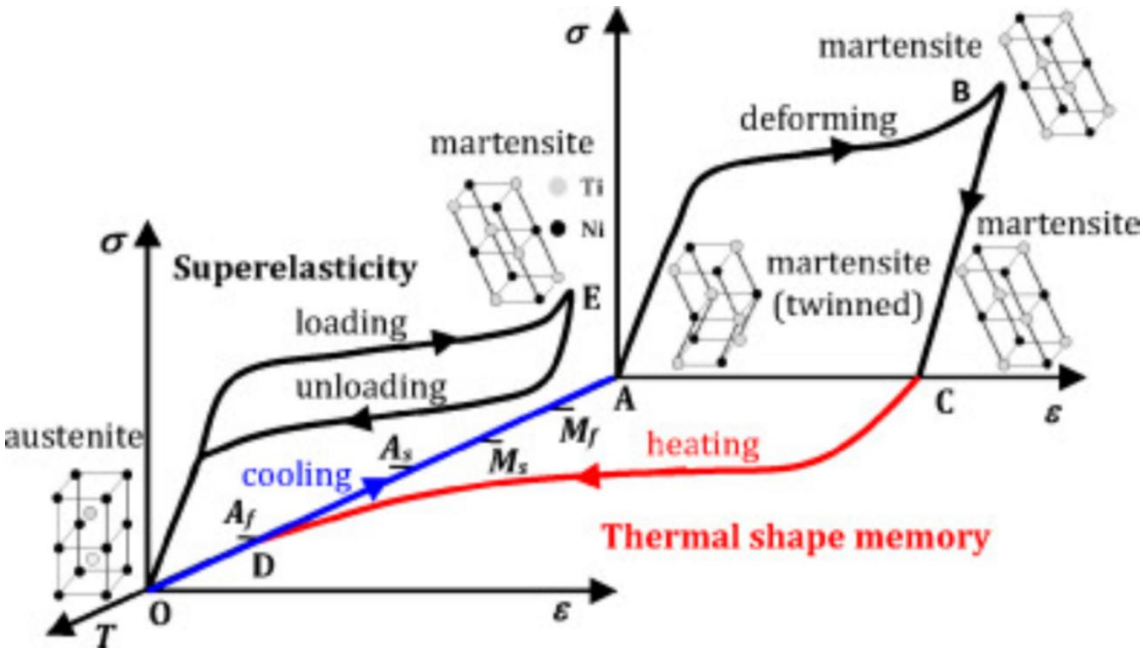

Figure 3-1: The illustration of the shape memory effect in NiTi alloy is depicted through stress, strain, and temperature variations, as adapted from Yuebin Guo et. al [99].

A process known as shape setting determines the shape that nitinol will return to, the 'remembered' shape, once the trained part is heated above the austenite finish (A_f) temperature. The most common method of shape setting nitinol is by heat treatment [39,117,143]. The nitinol is held in the desired shape with a mandrel or fixture while it is heat treated at a controlled temperature and time and is then quenched. When the nitinol is removed from the mandrel after quenching, it retains its shape that is the austenitic or "remembered" shape [144]. Another method of shape setting is over-straining that involves cold working nitinol to the point at which full recovery of the previous shape on heating is not possible. This process can be repeated until the previous austenitic shape is sufficiently removed. This procedure is time-consuming and is typically not as repeatable as heat treatment shape setting [145].

The three most important factors in the heat treatment method of shape setting nitinol are the heat treatment temperature, time spent at this temperature, and the raw material

condition. Shorter times and lower temperatures result in the material retaining the properties of the high-strength, cold-worked state, but will result in more spring back and less accurate shape setting. Longer times and higher temperatures can result in annealing; however, it also results in shapes that are more exact and have less spring back [105]. The existing literature shows that heat treating nitinol between 400 and 500 °C increases the SME [139,146,147]. This is due to the formation of metastable Ni_4Ti_3 precipitates on heat treatment of the samples and also due to the substantial density of reorganized dislocations that remain within the samples [148]. The Ni_4Ti_3 precipitates is dominantly present in the {111}B2 family of planes of the NiTi matrix [149]. This is the crystallographic orientation relationship between the Ni_4Ti_3 precipitate and the B2 phase. Each of the parent phase has four {111}B2 planes with two of these variants having the same plane leading to eight variants of the Ni_4Ti_3 precipitates. These precipitates have varying size vastly depending on the heat treatment temperatures and times. The precipitate formation in the ageing temperatures generally have affinity of nucleating and grow near the grain boundaries [150]. It was shown in the work of Sadiq et al. [151] that changes in distribution of the Ni_4Ti_3 precipitates governs the SME as it prevents plastic deformation by restricting the movement of dislocations and increasing the critical stress magnitude [151]. From this work, it was also noted that heat treatments at temperatures above 400 °C show the highest extent of the SME.

Several research studies have demonstrated that the nickel (Ni) content within NiTi based alloys and the presence of precipitates, such as $NiTi_2$, Ni_3Ti_2, and Ni_4Ti_3, play a significant role in influencing the alloy's phase transition temperature. Additionally, the incorporation of alloying elements not only impacts the phase transition temperature but also affects the resultant phase transition products and the pathway of the phase transition [152]. In NiTi binary alloys, a typical one-step phase transition directly from B2 to B19' is observed. However, the introduction of iron (Fe) results in a two-step phase transition, progressing from B2 to R and then to B19'. Notably, the degree of separation between these two transition steps becomes more pronounced with higher levels of Fe incorporation. The NiTi-Cu alloy system offers less sensitivity of the alloy's phase transition temperature due to compositional variations, facilitating enhanced control over memory performance. The addition of copper (Cu) imparts the alloy with a high phase transition temperature, exceeding room temperature, enabling the realization of shape memory effects even at ambient conditions. These favourable attributes position NiTi-

Cu alloy as a highly promising choice for practical applications in shape memory alloys. Additionally, incorporating palladium (Pd) into a NiTi alloy can substitute for nickel (Ni) atoms, resulting in an initial decrease in the alloy's phase transition temperature. However, as the quantity of added Pd increases, the phase transition temperature gradually rises with the Pd content [153]. The critical influence of nickel (Ni) content and precipitates on the phase transition temperature of NiTi-based alloys, as well as the profound impact of alloying elements on both the temperature and the characteristics of phase transitions, offers opportunities for tailoring shape memory alloys to suit various practical applications. Many different methods have been presented in the literature to determine the efficacy of heat treatment parameters on the SME of nitinol. In a study conducted by Lahoz and Puertolas [154], NiTi wire with A_f temperature of 29.2 °C was heat treated at 660 °C for 30 min and then quenched in water. Stress–strain and deformation–temperature curves of the NiTi wire were then obtained using a thermomechanical analyzer (TMA). Several different studies used a low-friction linear variable displacement transducer (LVDT) to measure the displacement of a nitinol part. In Lou and Abel [155], NiTi wire with an A_f temperature of 80 °C, heat treated at 550 °C for 20 min, was held stationary at one end by a support structure, while the other end was attached to the central slider of a LVDT that measured the horizontal displacement produced by SME. In Speicher et al. [156], nitinol helical springs and Belleville washers are tested using a cylindrical damper as a tension/compression device, and a LVDT was used to measure the vertical displacement during actuation of the nitinol component. In recent years, there has been a growing interest in harnessing the potential of shape memory alloys (SMAs) like nitinol to enhance structural behaviours. Nitinol, with its remarkable tensile strain recovery properties, offers the ability to generate and withstand substantial stresses and strains, making it a standout candidate for applications requiring high mechanical energy density. This feature enables more compact structural designs compared to other actuator systems and adaptive materials. Furthermore, nitinol's attributes, such as its robust tensile strength, corrosion resistance, and biocompatibility, have solidified its popularity in various fields, particularly in biomedical applications [157]. Moreover, nitinol-based single-stage bellows, shaped using the rubber bulge method, have been investigated for their compressive behaviour. These structures hold potential in energy absorption applications, providing adjustability in energy absorption and crushing forces based on their bellows' shapes. Additionally, nitinol-based bellows can be reused due to their recovery function, making them a promising choice for energy

absorption devices [125,127]. In a separate development, researchers have introduced a novel class of superelastic NiTi honeycomb structures. A unique brazing technique was employed to create nitinol based cellular structures with low relative densities. These structures exhibited impressive specific strength, high specific stiffness, and enhanced shape recovery when subjected to compression loading, outperforming monolithic shape memory alloys. This breakthrough opens the door to a wide range of engineered topologies with customizable properties and enhanced thermomechanical response [158]. These applications underscore the versatility and promise of nitinol in various fields, from seismic engineering to biomedical devices and advanced structural materials. While these studies also investigate the effect of heat treatment parameters on the SME of nitinol, there are still several gaps in our understanding of the process and material behaviour. Achieving optimal energy consumption and SME performance for NiTi involves selecting a temperature that closely aligns with the operational environment, avoiding being too close to prevent unintended actuation. Previous investigations have shown that the initial A_f temperature of the wires were above room temperature; the A_f temperature further increased after heat treatments. There are, however, many potential applications for NiTi closer to room temperature so by selecting NiTi with a starting A_f slightly below room temperature, after heat treatment, it becomes possible to establish the resulting A_f temperature at an appropriate level above room temperature. Studies to date have also only examined a very limited range of heat treatment times and temperatures [159]. Finally, mechanical device methods of displacement and strain measurement used in past studies are known to have errors due to inherent friction and strain accommodation within the connecting mechanical elements [160]. The study involved an extensive exploration of various temperatures and durations applied to nitinol wire with initial A_f temperatures below room temperature. The purpose was to determine the most effective heat treatment parameters to enhance shape memory effect (SME) control. Additionally, a strain recovery measurement was conducted using an image analysis methodology.

3.2 Materials and Methods

In this study, a DoE with two parameters at three levels was used to heat treat the nitinol wires in order to determine the optimum heat treatment parameters for maximum shape memory response. Wire samples of length 400 mm were heat treated and shape set as straight wires in a box furnace for 30, 60, and 90 min at 400 °C, 450 °C, and 500 °C. For

each of these parameters, two samples were tested in order to validate results and calculate the repeatability. These samples underwent characterization through metallography, density, hardness, and DSC measurements. These analyses were performed to investigate the influence of the heat treatment parameters on the material properties, as depicted in **Figure 3-2**. Finally, the shape memory effect (SME) of the samples was tested by angular displacement and recovery strain experiments to determine the optimum heat treatment parameters for SME in nitinol wires. Note that throughout this study n = 2 and error bars shown are 95% confidence intervals.

3.2.1 Heat treatment of nitinol wires

The nitinol (NiTi) wire used for this study was provided by Fort Wayne Metals, Castlebar, Co. Mayo, Ireland, with a chemical composition of 55 wt.% Ni and 45 wt.% Ti. The wire supplied had a diameter of 0.468 mm with austenite finish temperature (A_f) of 13.7 °C with a lightly oxide surface finish. For heat treating the wires, a Nabertherm N60/85HA chamber furnace was used. This furnace has an operating temperature range of 30 to 850 °C and its inner chamber's dimensions are 350 × 500 × 350 mm. This furnace is heated from the bottom, sides, and the top and uses recirculating air flow to maintain temperature uniformity within 10 K according to DIN 17052-1 [161]. A summary of the examined heat treatment temperatures and times is shown in **Table 3-1**. For each specific time and temperature configuration, a 150 mm wire length was subjected to the heat treatment process. In total, nine wires were heat treated in this study. All the samples were heat treated individually to have stability at the respective temperature, thereby avoiding opening of the furnace to add/remove samples. The samples were air cooled outside the furnace upon completion of each heat treatment process.

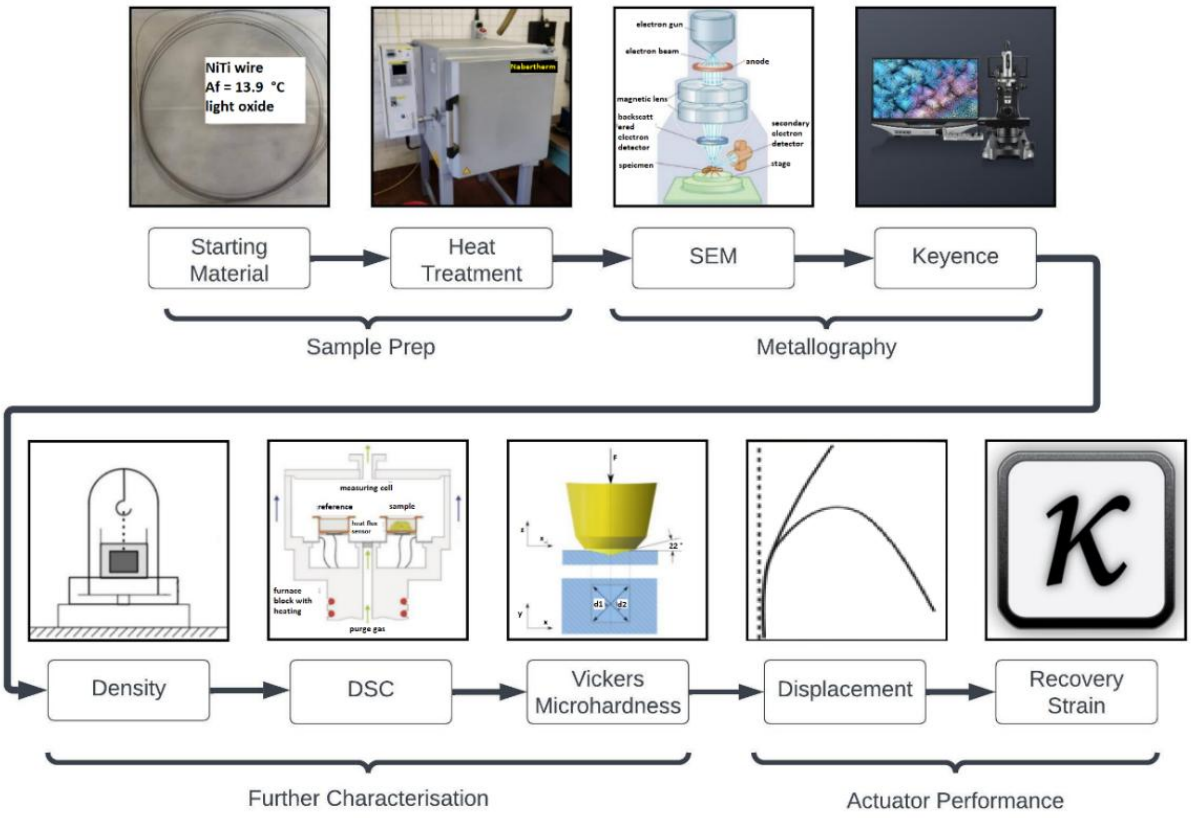

Figure 3-2: Process diagram showing the implemented experimental procedure.

Table 3-1: Heat treatment process parameters applied to the nitinol wires.

Sample Number	Temperature (°C)	Time (min)
1	As-received	As-received
2	400	30
3	400	60
4	400	120
5	450	30
6	450	60
7	450	120
8	500	30
9	500	60
10	500	120

3.2.2 Metallography

Metallographic analysis of the surface morphology and topology was conducted using a SEM (Zeiss EVO LS15) at an accelerating voltage of 20 kV. The Zeiss EVO LS15 is a thermionic emission SEM with variable pressure option, and a maximum magnification of 300,000× with a 5-axis stage. The thin wires were mounted on conductive stubs and placed inside the SEM chamber for analysis. As the NiTi wires are conductive, no additional sample preparation was required. An Oxford Instrument EDX (Energy Dispersive X-ray) was used for composition analysis. This analysis helped in identifying change in the Ni content as an effect of the variation in the heat treatment process parameters. As titanium is a highly oxidizing element [162], in order to study the microstructure, samples were etched with a Kroll's reagent (HF based acid) to provide a better contrast between chemically different features of the material. Nitinol is a particularly unreactive metal in part due to the formation of an insoluble titanium oxide layer. Unlike with primarily titanium-based alloys, this etching procedure is particularly sensitive to alloy segregation, as the chemical reactivity of nickel is significantly different from that of titanium. This creates a challenge for determining the etching time for this metal. The etching times were found to be different for the as-received and heat-treated samples. The etching times used for the samples ranged between 2–5 s. There were no significant differences observed in the microstructures after etching.

3.2.3 Density

The most widely used method for calculating the density of solids is the buoyancy method, which is based on the Archimedean principle. This principle states that a body immersed in a fluid indicates an apparent loss in weight equal to the weight of the fluid it displaces. Ethanol was used as the fluid medium for density measurement in this study [163]. Density measurements were conducted on the nitinol wires, which were heat treated. Three measurements for each sample were recorded with averages and confidence intervals reported in this study.

3.2.4 Differential Scanning Calorimetry

Differential Scanning Calorimetric analysis was performed using a TA Instruments® Discovery DSC2500, New Castle, DE, USA. DSC analysis was performed on all the heat treated samples as well on the as-received wire to study the phase transformation temperatures. The crucibles used for this experiment were made of pure aluminium,

which is suitable for solid and powder samples that do not decompose or boil at temperatures between −170 °C to 600 °C [164]. The tests were conducted in the temperature range of 0 °C to 150 °C with a ramp up rate of 10 °C/min. The austenite and martensite start and peak and finish temperatures were evaluated. TZero aluminium pan with TZero lids and a sample mass of around 20 mg were used to carry out the tests. Liquid nitrogen was used as the cooling medium.

3.2.5 Vickers Hardness

Vickers microhardness was recorded using a Leitz MiniLoad 2® equipment (Spectrographiv, Leeds, UK) by applying a force of 981 mN onto the surface of the samples with a holding time of 20 s [165]. Vickers hardness measurements were performed on all heat-treated samples, with each sample undergoing five measurements at randomly selected locations on its surface. The resulting average Vickers hardness values were then recorded and reported. For ease of the microhardness measurements with these thin wires, the wires were mounted in epoxy resin and grinded till the required surface finish was attained.

3.2.6 Displacement experiment of heat-treated nitinol wires

The 150 mm long heat-treated wires were deformed into ‘U’ shapes by bending the wires 180° around a 6 mm diameter mandrel while both the ends were held together. This bending process was carried out with careful attention to prevent kinks in the wire. Such kinks could potentially cause a form of irreversible deformation due to elevated internal stresses compared to the surrounding wire. This deformation, if present, might diminish the overall shape memory effect. The wire was then released and secured to a reference sheet. A controlled heating was then applied to raise the temperature of the wire above the austenite finish temperature. A photograph of the wire, normal to the surface, of each sample after heating was taken, and for the measurement of deformation, an image analysis utilizing ImageJ software (V 1.8.0) was employed [166]. A schematic representation of this entire process is visually outlined in **Figure 3-3**.

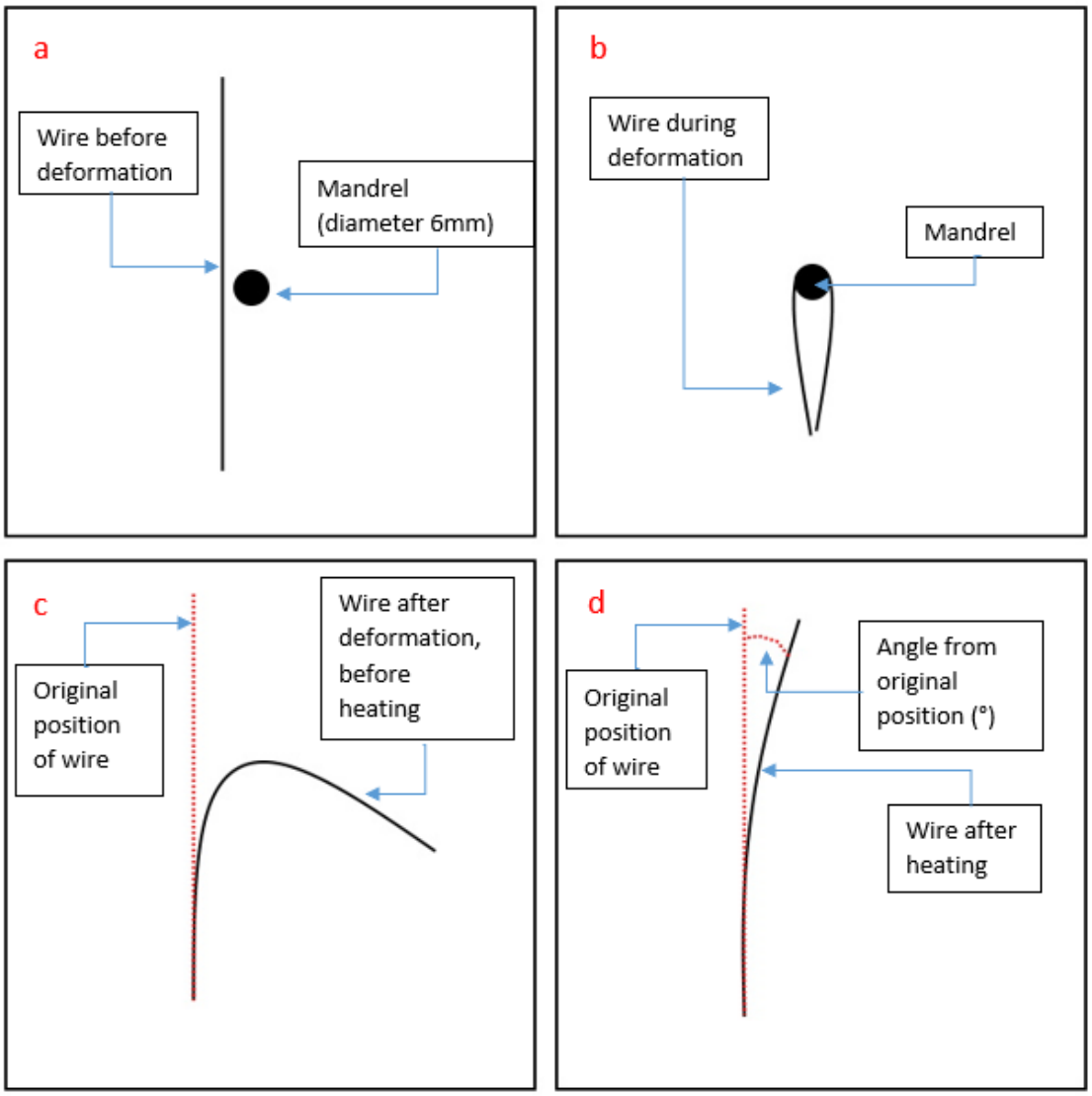

Figure 3-3: Schematic of the method used for the displacement and recovery strain experiments. (a) Wire and mandrel before deformation, (b) deformation of the wire around mandrel, (c) wire after it has been released from the mandrel, and (d) wire after controlled heating.

3.2.7 Recovery strain of heat-treated nitinol wires

Images were captured before and after bending for all of the heat-treated nitinol wires. ImageJ software was used to calculate the radius of curvature before and after the wires were heated above the A_f temperature. The radius of curvature was calculated using a developed ImageJ macro. Utilizing the initial radius of curvature (denoted by R), the bending stress equation was used to find the strain (denoted by ε) in the maximum bent section of the wire. The stress (denoted by σ) over the point of maximum stress equals the Young's modulus (denoted by E) divided by the radius of curvature as in equation 4.

$$\frac{\sigma}{y} = \frac{E}{R} \qquad (4)$$

Since, it is known that strain equals the Young's modulus by the stress as shown in equation 5.

$$\sigma = E \,.\, \varepsilon \qquad (5)$$

The combination of these two equations suggests that the strain within the sections of wire which is measured equals the point of maximum stress by the radius of curvature as shown in equation 6. The point of maximum stress is relative to the neutral axis. The neutral axis within the wires is the centre point in the wires. The point of maximum stress is equal to the radius of these wires. strain was calculated before and after the wires were exposed to the heat source. Recovery strain was calculated by subtracting the strain after recovery from the strain measured before recovery.

$$\varepsilon = \frac{y}{R} \qquad (6)$$

3.3 Results

3.3.1 Effect of heat treatment on density

Density measurements are conducted to evaluate the impact of heat treatment and its duration on the material's properties and characteristics. This allowed a comprehensive understanding of how changes in heat treatment conditions affect density and, by extension, the alloy's performance. While the density of the as-received nitinol was found to be close to the expected nitinol density of 6.45 g/cm^3 [167], differences in the resultant density were recorded for samples produced at the different processing parameters, see **Figure 3-4**. A slight decrease in density compared to the non-heat-treated samples was observed in the samples heat treated at 400 °C for 30 min (sample 2). Among the various heat treatment conditions, the sample treated at 400 °C for 60 min (sample 3) exhibited the highest density, with a value of 6.85 g/cm^3 , while the sample subjected to heat treatment at 450 °C for 30 min (sample 5) demonstrated the lowest density of 5.95 g/cm^3 . A decrease in density relative to the non-heated samples was observed for samples processed at all other heat treatment conditions. The density for the other heat treatment

conditions was on average 6.25 g/cm^3 . The density for the sample heat treated at 500 °C for 30 min (sample 8) was the closest to that of the as-received nitinol wire. Both samples, as received and heat treated, were also found to have the lowest standard deviation. It was observed that the heat treatment time had relatively little effect on the density value at 500 °C. Apart from one heat treatment condition, the heat treatments led to a decrease in the density relative to that of the as-received nitinol wire, which is consistent with previous research findings [168].

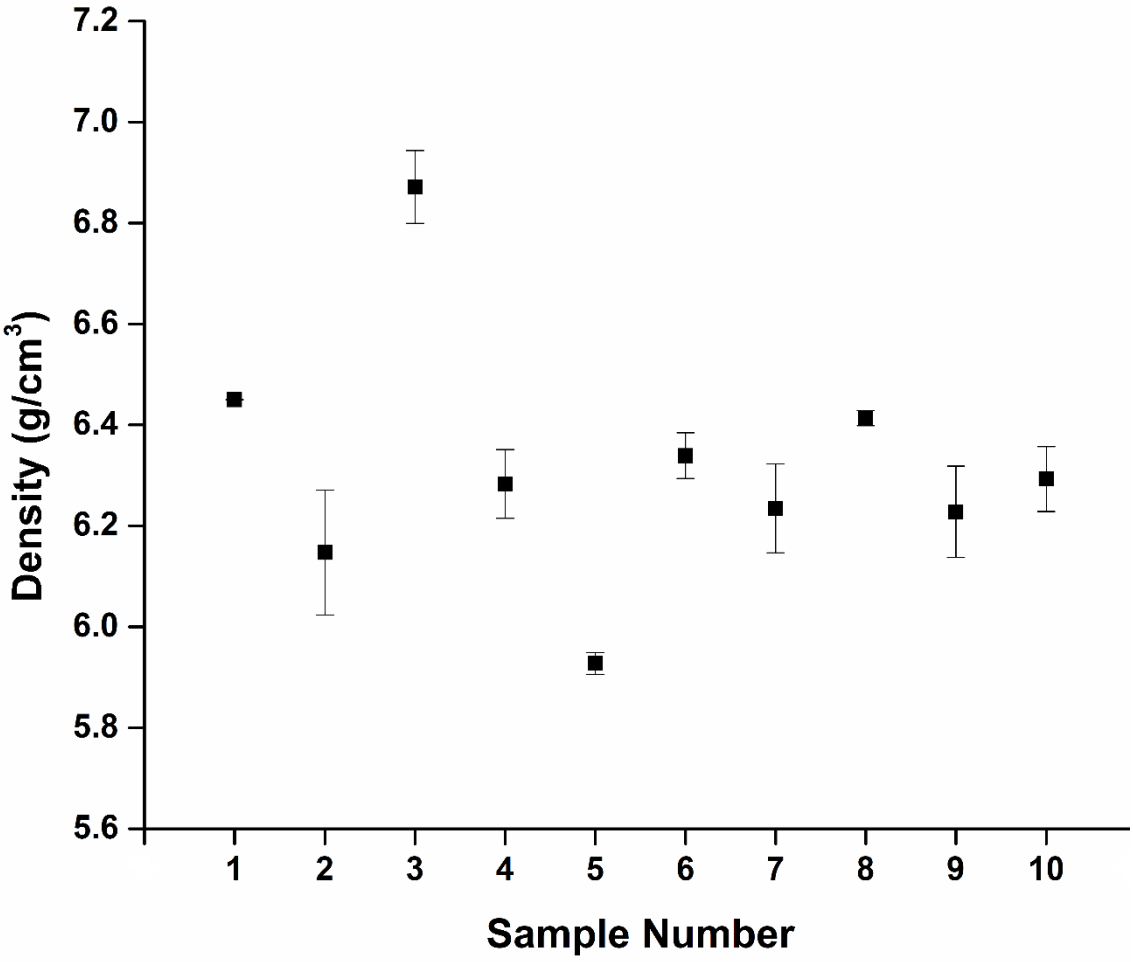

Figure 3-4: Density measurements of all heat-treated nitinol samples, n=3.

3.3.2 Effect of heat treatment on microstructure

The EDS results of the as-received wire showed a uniform distribution of Ni and Ti. Results of further EDS tests at different locations and areas confirmed that the surface of these samples contained a uniform composition of about 55 wt.% Ni and 45 wt.% Ti as shown in **Figure 3-5**. The composition was found to be very close to that reported by the manufacturer. The chemical composition of the heat-treated wires has been tabulated in

Table 3-2. Other observed elements were C and O but were insignificant to be mentioned.

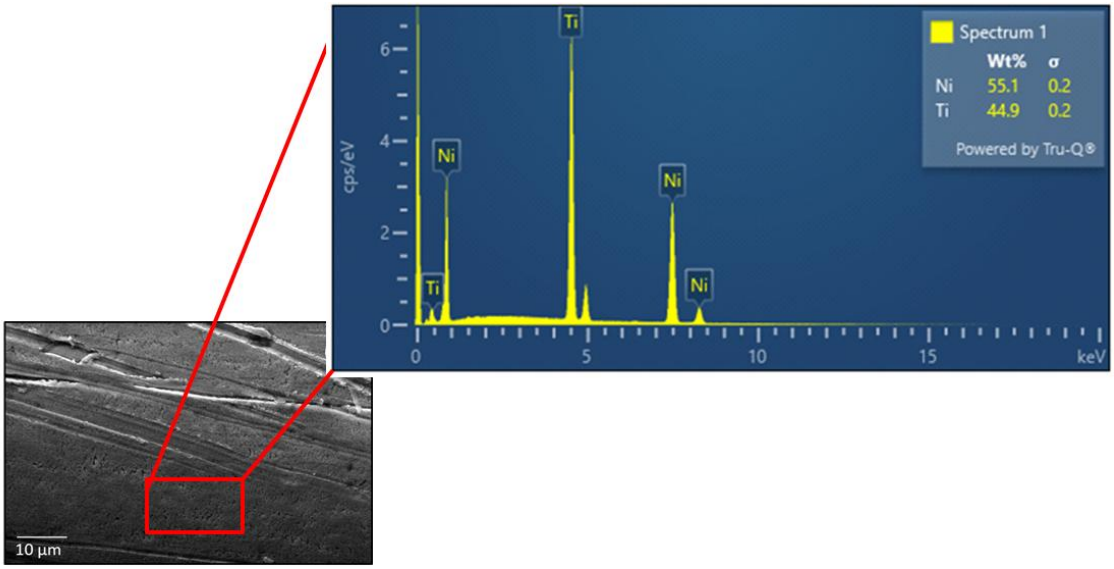

Figure 3-5: SEM image and EDX mapping of the surface of the as-received wire.

Table 3-2: Chemical composition of as-received and heat-treated nitinol wires.

Sample Number	Ni (at. %)	Ti (at.%)
1	49.9	50.1
2	49.3	50.7
3	49.5	50.5
4	49.4	50.6
5	47.9	52.1
6	48.8	51.2
7	49.1	50.9
8	48	52
9	47.5	52.5
10	46	54

3.3.3 Effect of heat treatment on the phase transformation temperatures

The phase change, including the austenite finish, temperatures (A_f) were measured using DSC, see **Figure 3-6** with the as-received wire with an austenitic finish (A_f) of 13.70 °C. These results show that there was a decrease in the A_f temperatures with increasing heat treatment temperature. The lowest A_f temperature for a specific temperature group was

higher than the highest A_f temperature found in the next lower temperature treated group. On the other hand, there was an increase in A_f temperature with time for samples heated at 400 °C, a decrease in A_f temperature with time at 500 °C, and relatively little effect of time at 450 °C on the A_f temperature. From the DSC curves, the phase change peaks become sharper with both heat treatment temperature and time with the broadest peak at 400 °C for 30 min and the sharpest at 500 °C for 120 min. The trend of sharpening of the peak was observed for in all samples annealed for longer times and higher temperatures.

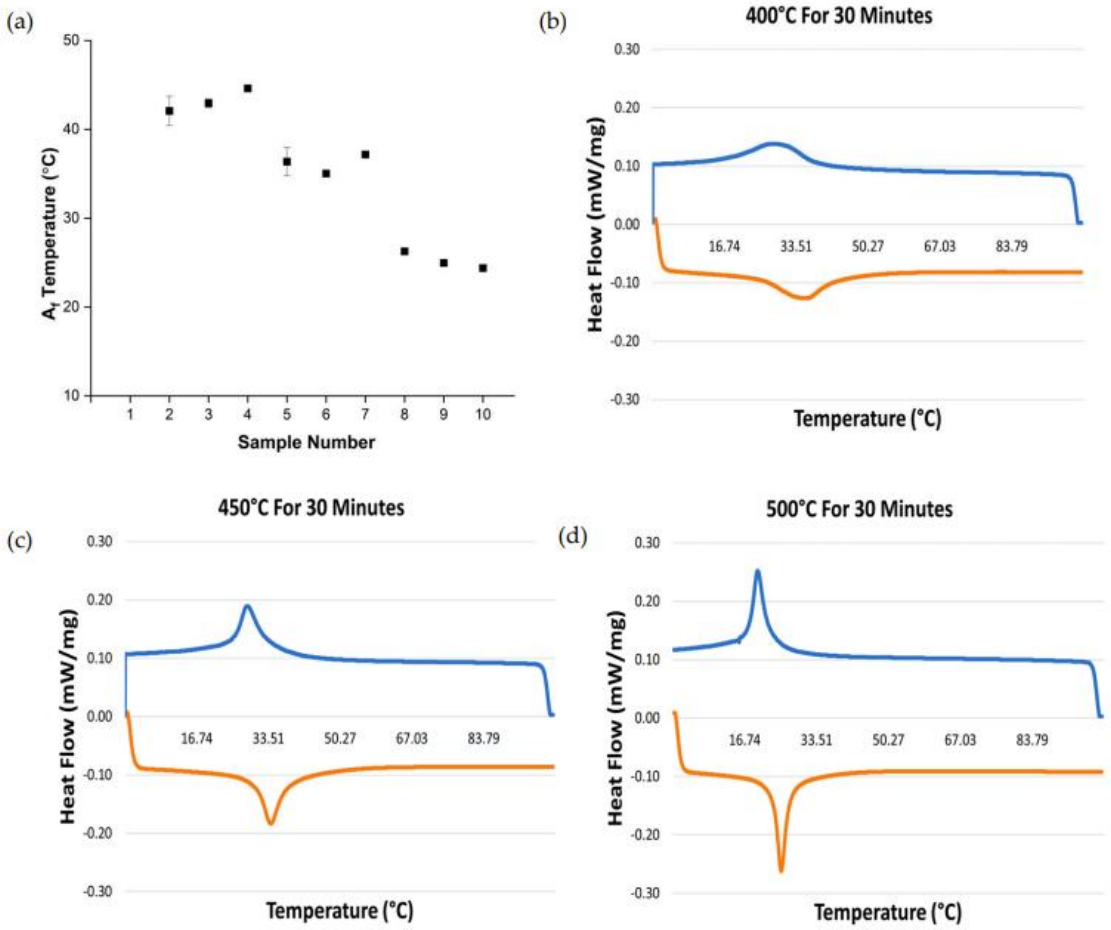

Figure 3-6: (a) The A_f phase transformation temperatures of the wire samples (n=2), and DSC heating curves (orange lines) and cooling curves (blue lines) of samples treated (b) at 400°C for 30 minutes, (c) at 450°C for 30 minutes, and (d) at 500°C for 30 minutes.

3.3.4 Effect on hardness due to the heat treatment process

Figure 3-7 presents the results from the Vickers microhardness indentation tests. The measured hardness for all the heat-treated samples in this study were found to be lower

than the measured hardness of the as-received nitinol wire. For the samples treated at 400 °C (samples 2, 3, and 4), there was an initial decrease in the hardness values between the samples treated at 30 min (sample 2) and those at 60 min (sample 3), and a subsequent increase in the hardness values from the 60 min samples (sample 3) to the 120 min (sample 4) heat-treated samples. For the samples treated at 450 °C (samples 5, 6, and 7), there was a general trend that showed a decrease in the hardness of the samples as the heat treatment time increased [162,169]. Increasing heat treatment temperature also resulted in a reduction in average hardness. The trend of results of this work in terms of hardness matched well with those recorded previously [170].

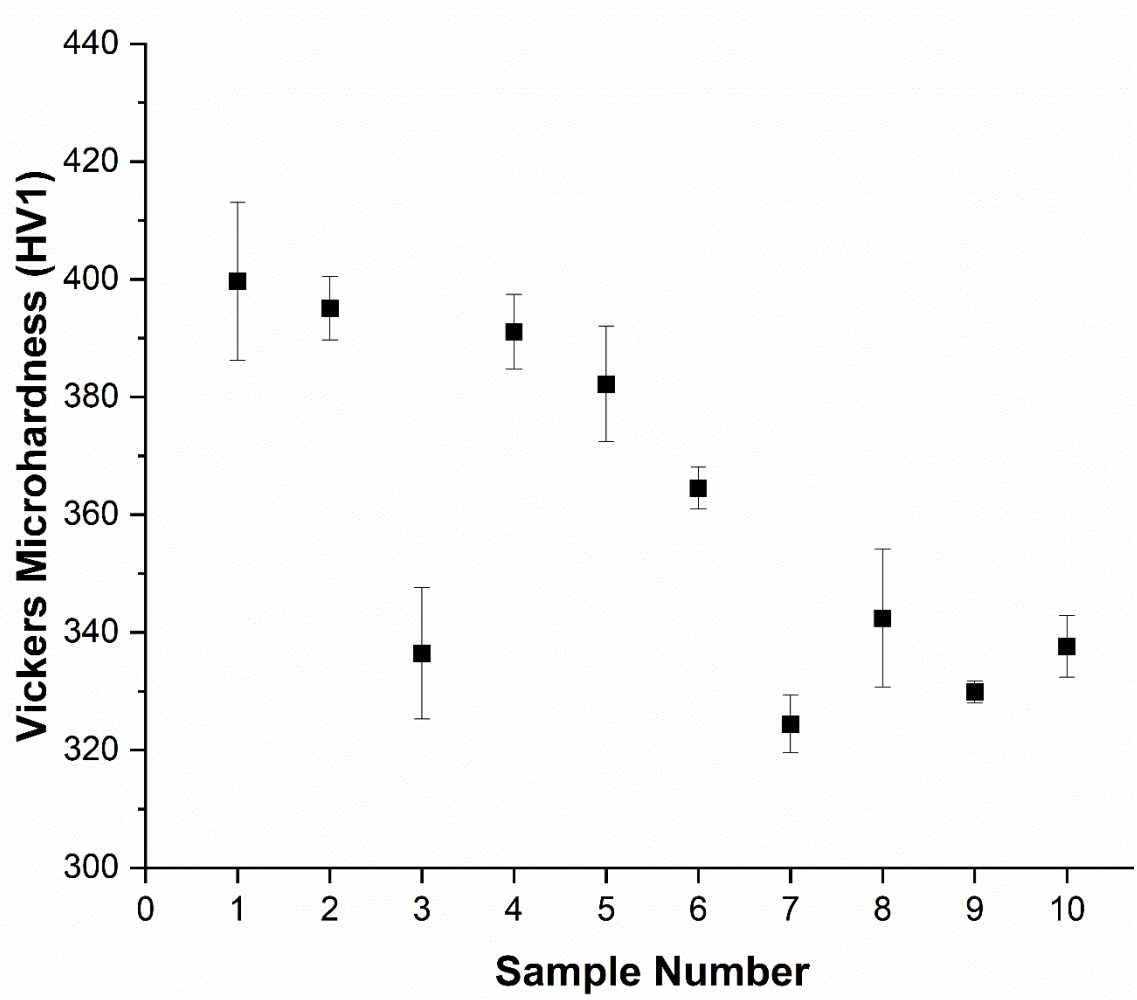

Figure 3-7: Vickers microhardness test results for as-received and heat-treated samples, n = 5.

3.3.5 Loss of actuation angle for the nitinol wires

The results in **Figure 3-8** show that the largest deviations from the straight wire occurred in samples heat treated at 400 °C for 30 (sample 2) and 60 min (sample 3) with angles of 18.80° and 18.16° degrees, respectively. Increasing the heat treatment time to 120 min at 400 °C resulted in a reduction of this angle to 10.61°.

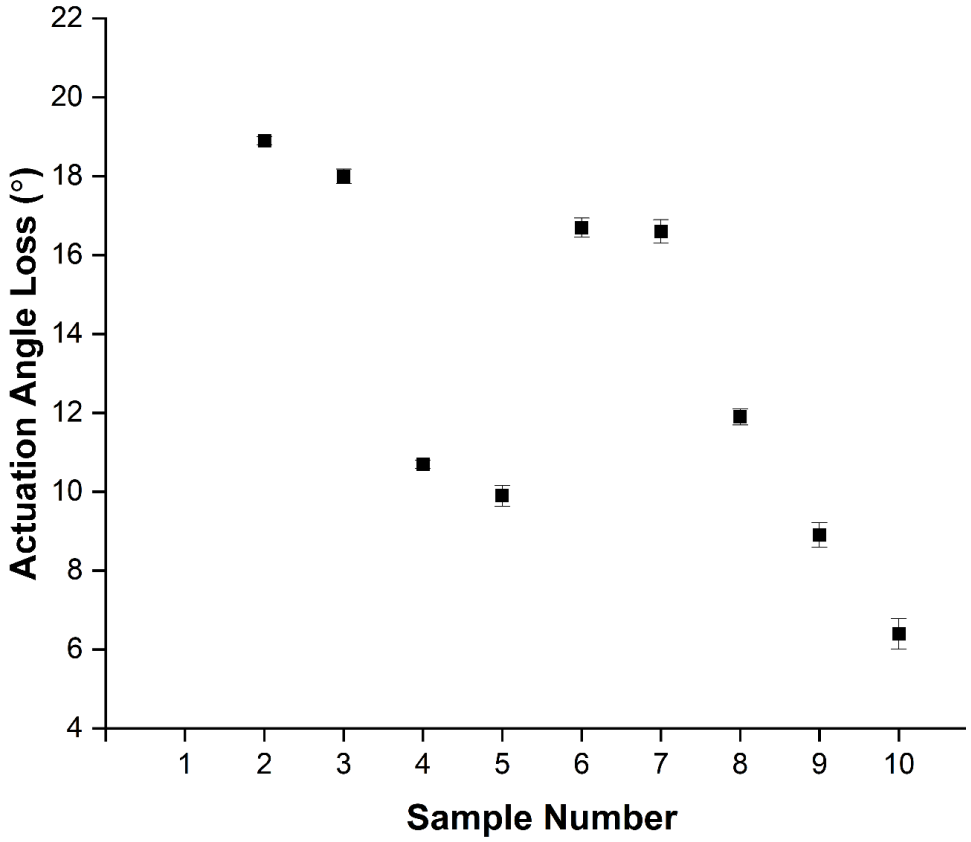

Figure 3-8: Loss of actuation angle from desired shape (°) for the heat-treated samples.

Samples heat treated at 450 °C show a different relationship between angle and heat treatment time. The lowest angle occurred in the sample heated for 30 min (sample 5), achieving an angle of 10.10°. The angle increased drastically to 16.92° at 60 min (sample 6) and showed only a slight decrease to 16.74° for 120 min (sample 7).

For samples heat treated at 500 °C, a decrease in angle with increasing heat treatment time was observed. The sample treated for 30 min (sample 8) achieved an angle of 12.07°. The samples treated at 60 min (sample 9) and 120 min (sample 10) both produced the lowest actuation angular loss compared to any of the other samples at 9.22° and 6.75°, respectively, as shown in **Figure 3-8**.

3.3.6 Recovery strain of heat-treated nitinol wires

The recorded recovery strains (unitless) of the heat-treated nitinol wires, after bending the wires and then recovering once they were heated above the A_f temperature, are shown in **Figure 3-9**. For the samples heat treated at 400 °C, an increasing extent of recovery in the strain values was observed with an increasing heat treatment time. A similar trend was observed for the samples heat treated at 500 °C with maximum recovery strain achieved for the sample heat treated at 500 °C for the longest duration of 120 min.

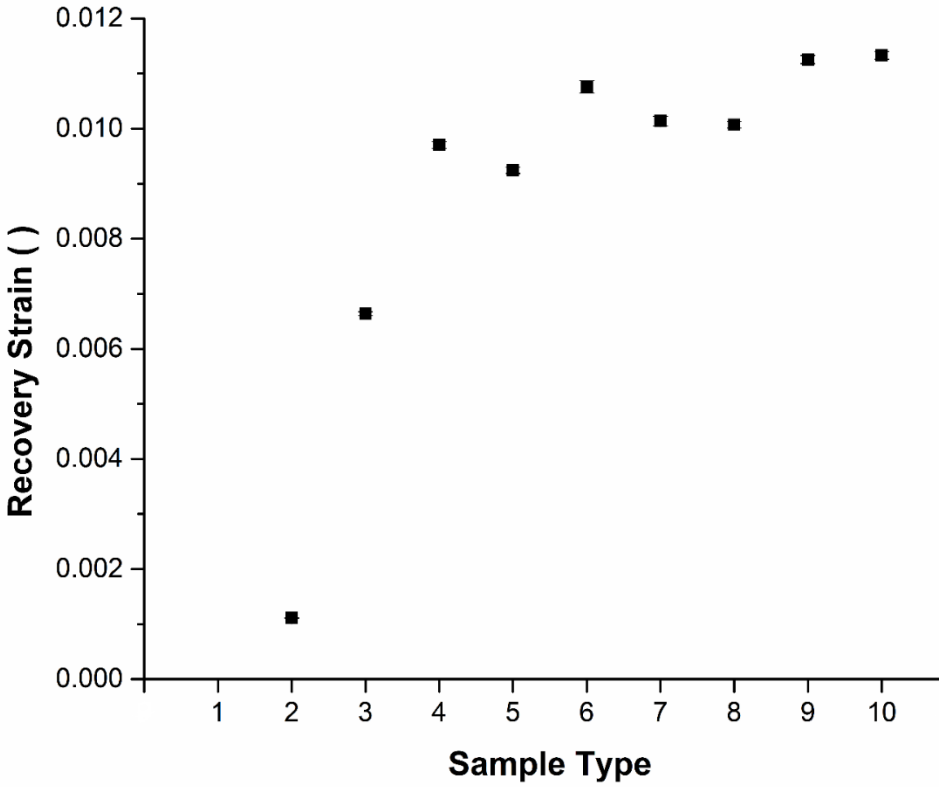

Figure 3-9: Recovery strain values for the heat-treated samples, n = 3.

For the samples heat treated at 450°C, the lowest time of 30 mins showed the lowest recovery in the strain values; Increasing the time of 60 minutes heat treatment showed an increase in the recovery strain value, whereas a further increase in the heat treatment time to 120 minutes resulted in a drop in the recovery strain value.

3.4 Discussion

Main aims of this study were to determine how the nitinol wire heat treatment process parameters relate to the resulting shape recovery response and mechanical properties. In this work, wire samples were heat treated in a box furnace at three different temperatures of 400 °C, 450 °C, and 500 °C with varying times of 30, 60, and 120 min for each

temperature. The samples were heat treated in atmospheric conditions and air cooled outside the furnace. As shown in **Figure 3-9**, the recovery strain response of the heat-treated samples increased as the heat treatment temperature increased. A maximum recovery strain value was observed for the wires heat treated at 500 °C for 120 min. This result correlates well with the measured loss of actuation angle that was found to be the lowest for the wires heat treated in this condition, see **Figure 3-8**. There was an increase in the change in the radius of curvature of the wire as the heat treatment temperature of the wire was increased. Wires with the highest recoverable strain provide the maximum shape recovery capability. The chemical composition of nitinol significantly influences the performance of the shape memory alloy, demanding close monitoring of the sample's composition. As mentioned earlier, the chemical composition of the samples used in this study was found to be Ni55 wt.% and Ti45 wt.%. A more Ti-rich nitinol alloy exhibits better shape memory property and higher phase transformation temperature [171,172]. The density of the phases present in the produced parts can be directly correlated to the hardness values measured. In previous work from Rondelli et al. [162], Ni_4Ti_3 precipitates have been identified in heat-treated NiTi samples with more precipitates occurring at higher aging temperatures and with longer heat treatment periods. The lower hardness values for the samples heat treated at 450 °C and 500 °C is likely caused by the increased presence of the Ni_4Ti_3 precipitates in the wire samples, thereby lowering the hardness values compared to samples heat treated at 400 °C [115,170]. As indicated previously in the study conducted by Khalil-allafi et al. [150], at the ageing temperature range of 400 to 600 °C, heterogenous distribution of the Ni_4Ti_3 precipitates has been observed. It has also been reported that the grain size increases with increasing ageing temperature that leads to lowering of the hardness values. In the work of Adharapurapu et al. [170], the samples that were heat treated at 400 °C for 5 h exhibited the best hardness values. From this previous study, the sample heat treated at 500 °C for 5 h also displayed a lower hardness value, however, for sample heat treated at this temperature for longer periods of 10 h or more, the hardness increased. This finding directly correlates with our results. The trend of decreasing hardness values with increasing temperatures and times also is expected to be attributed to the formation of an increased Ti-rich matrix due to the formation and growth of Ni_4Ti_3 and Ni_3Ti_2 precipitates. A clear indication of the changes in the A_f temperature has been observed because of the heat treatment process, see **Figure 3-6**. From the graph, it is apparent that there is a decrease in A_f temperature with increasing heat treatment temperature. The heat treatment time,

however, has a relatively small effect on the transformation temperatures, indicating that the main driver for the reduction in A_f is the heat treatment temperature rather than time. The samples heat treated at same temperature of 400 °C but for varying times, however, show a general increase in A_f temperature with heat treatment time that has also been reported in the literature due to an increase in Ni_4Ti_3 precipitation [173,174]. Furthermore, a noticeable increase in the sharpness of the transformation peaks was observed with extended time and temperature. This trend was accompanied by a decrease in A_f and a heightened precision in the transformation peaks, as both temperature and time increased [78,151]. This phenomenon can be attributed to the relaxation of residual stress and the correction of microstructural defects that hinder crystal mobility during heating. The alteration in the A_f temperature caused by the heat treatment process is advantageous, as it offers the potential for adjusting the phase change temperature according to specific application requirements. In this work, a straightforward and quick method of calculating the actuation of a wire at the actuation angle was developed. The results show that the actuation improved with both heat treatment temperature and time. The largest shape recovery was achieved with the sample heated at the highest temperature for the longest time (500 °C for 120 min), while the lowest shape recovery was recorded at the lowest temperature and shortest time (400 °C for 30 min). The growth of the metastable finer Ti-rich precipitates with the increase in the heat treatment temperature to 500 °C resulted in more martensitic phases that increased the shape memory response [119,150]. This study explores the impact of heat treatment parameters on the performance of nitinol wires, specifically focusing on actuation characteristics. While the primary focus is on understanding the material behaviour, the results of this research can have direct applicability in industries where nitinol-based actuators are used. By optimizing the heat treatment parameters, the study shows how to enhance the actuator performance, which is valuable for the development of robotic, aerospace, and medical actuator devices. This work, therefore, adds a new scientific knowledge base to inform future practical product designs. The study utilizes a novel approach involving image analysis to measure recovery strain during wire actuation. This methodological innovation can be used by the scientific community as a new practical and robust technique for assessing shape memory alloy behaviour.

3.5 Conclusion

Wire samples of nitinol manufactured using traditional wire-drawing techniques were examined to determine the effect of heat treatment time and temperature on the density, hardness, material composition, surface morphology, transformation temperature, angular displacement, and strain recovery. The conclusions drawn from the obtained results are as follows:

- The hardness results show a general decrease with heat treatment time and temperature.
- There is a decrease in the density between the as-received samples and the heat-treated samples, except for sample 3. Sample 3 was treated at 400 °C for 60 min with an increase in density from 6.45 g/cm^3 (as received) to 6.85 g/cm^3. The results show that the heat treatment time and temperature can be used to control the density within the range of 5.85 to 6.85 g/cm^3.
- From the EDX and SEM results, the as-received wire has a uniform distribution of Ni and Ti with a surface oxide layer due to titanium's highly oxidizing nature.
- The DSC curves show that increasing heat treatment time and temperature decreases the A_f temperature and increases the sharpness of the phase transition curves. This indicates that higher temperatures (500 °C) for longer times (120 min) result in an increased reduction in residual stress and crystal defect.
- NiTi heat treated at 400 °C for up to 60 min and 450 °C for 60 to 120 min fails to result in a high level of shape memory response. Heat treating NiTi at 500 °C for 60 (8.9°) and 120 min (6.4°) results in an increasing shape memory effect with the greatest shape recovery observed in the sample treated for 120 min.
- The strain recovery increases with increasing heat treatment time and temperature. The maximum strain recovery occurred in the sample heated at 500 °C for 120 min.

In terms of limitations, the size of the samples was too small to allow XRD testing. Sheet samples could potentially be used to allow for XRD analysis due to its larger surface area. Future studies should prioritize in-depth investigations aimed at achieving the maximum shape memory effect tailored specifically to the desired application. Future work could also examine the heat treatment of the wire samples at higher temperatures (e.g., 550 °C or 600 °C) and for longer periods of time (e.g., 150 and 180 min). More rapid cooling of the samples such as the use of water quenching of the wires after the heat treatment process should also be further examined.

Chapter 4: Influence of laser powder bed fusion and ageing heat treatment parameters on the phase structure and physical behavior of Ni-rich nitinol parts

Publication Status: Published

Agarwal, N., Bourke D., Obeidi, M. A., & Brabazon, D. (2024). Influence of laser powder bed fusion and ageing heat treatment parameters on the phase structure and physical behavior of Ni-rich nitinol parts, *Journal of Materials Research and Technology*, *30*, 4527-4541. https://doi.org/10.1016/j.jmrt.2024.04.198

4 Abstract

This paper examines the effect of ageing temperatures (400, 500, & 600 °C) and times (30, 60, & 90 mins) on Ni-rich NiTi samples produced via the Laser Powder Bed Fusion (L-PBF) technique. Variations in the process parameters of the L-PBF which were examined included laser power at 150W and 180W, and the scanning strategy at 500 mm/s and 1000mm/s. Ageing heat treatment enabled setting the functional properties of phase change temperatures, stress-strain response, and phase change enthalpies. Samples aged at 400°C were found to have much higher austenitic finish temperature (40 to 60 °C) whereas those aged at 600°C had near-zero or sub-zero A_f temperatures. This was due to the lower nickel concentration resulting from the higher heat treatment temperature. Samples heat-treated at 500°C exhibited A_f temperature which was near to the room temperature and showed co-existence of both austenitic and martensitic phases. It was also found that the crystallite size increased from 6 to 22 nm for an ageing temperature of 400 °C, to between 38 to 48 nm for an ageing temperature of 600 °C. The highest microhardness value of 380HV was recorded from the lower heat treatment temperature and the lowest microhardness of 270HV was recorded for samples heat-treated at 600 °C. This decrease in the microhardness values is attributed to the increased crystallite size of the aged samples at higher temperatures. This work identifies for the first time the novel ability to control NiTi phase change temperature and mechanical properties using ageing heat treatments which is critical for the materials application for personalised stents. Higher heat treatment temperatures were found to lead to larger crystallite sizes.

Keywords: NiTi, ageing heat treatment, L-PBF, phase transformation temperature, microhardness, crystallite size

4.1 Introduction

A binary alloy, nitinol (NiTi) has recently seen advances due to its excellent properties of high biocompatibility, high corrosion resistance, damping capacity, high fatigue resistance, superelasticity and shape memory [19,156,167,175,176]. Nitinol is essentially made up of near-equiatomic nickel and titanium. Nitinol finds its applications due to its excellent and varied properties in the automobile, aerospace, biomedical, energy and robotics industries [42,109,115,177–179]. Laser powder bed fusion (L-PBF) has made the processing of nitinol possible as other conventional techniques have proven difficult to achieve high precision and accuracy of the fabricated parts [19,37,140]. Although L-

PBF possesses several benefits, it also has its limitations such as high residual stresses and generation of several phases during rapid solidification [101,180]. The thermal cycle of melting and solidification of the L-PBF process generates inhomogeneous microstructures which are vastly influenced by the process parameters such as laser power, hatch spacing, spot size of the laser and layer thickness [84,181–185].

Ageing has been proven as a post-processing technique widely utilised to alter the phase transformation temperatures and improve the mechanical properties of the Ni-rich NiTi parts [86,186]. To achieve the desired shape with maximum strength for the fabricated parts, heat treatment is performed to adjust the Ni/Ti ratio in the NiTi matrix, thereby, altering the phase transformation temperatures [152,187,188]. Consequently, heat treatment can generate a stable single austenitic phase depending on the heat treatment parameters and the cooling technique [170,189–191]. Several researchers have reported multi-stage heat treatment consisting of an initial solution heat treatment followed by an ageing heat treatment. One such researcher, Khalil-Allafi et. al. [192] has reported solution heat treatment of 50.7 at.% Ni–49.3 at.% Ti at 800 °C with ageing at 400 °C and 450 °C for times of 1hr and 10 hrs followed by water quenching. It was noted that heterogeneous Ni_4Ti_3 precipitates were formed with a corresponding lowering of the phase transformation temperatures, as the ageing temperature and times were increased. Mohamad et. al. [193] performed ageing of 51 at.% Ni–49 at.% Ti wires and found that the DSC response exhibited two peaks in the cooling cycle when aged at 500 °C for 30 mins. On the other hand, Kustov et. al. [194] aged 50.8 at.% Ni – 49.2 at.% Ti alloy at 996 °C for 2 hrs and reported suppression of B2 › B19’ transformation without forming the R phase. It was also found that small nm-size precipitates were formed during ageing. In other work using the same composition, L-PBF samples were aged at 350 °C and 450 °C after solution treatment to achieve high recoverability [76]. Higher phase transformation temperatures were observed in the ageing of the samples, and superelasticity was found to be much higher, for samples aged at 350 °C compared to 450 °C. Fan et. al. [195] also conducted the ageing of Ni-rich NiTi and also reported an increase in the transformation temperatures with increasing ageing temperatures up to 500°C after solution treatment. In previous work from the authors, the effect of ageing heat treatment times (30-120mins) and temperatures (400°C to 500°C) on NiTi wires which are conventionally cold drawn were examined [74]. A decrease in the austenitic finish temperature was found, dropping from 42.8°C to 24.4°C, with an increase in the

ageing temperature from 400°C to 500°C. It was further reported that a negative relation was established between the microhardness and the heat treatment parameters. This was attributed to the formation of Ni_4Ti_3 precipitates.

As discussed above, several researchers have reported in the past exhibiting the effects and importance of heat treatment to achieve the desired properties of the fabricated NiTi parts with better strength and mechanical properties [71,196–199]. Different heat treatment regimes have also been tested and reported by researchers in the past [102,147,150,152,162,200]. These past studies largely focus on a solution heat treatment followed by an ageing heat treatment. The utilization of a single-step ageing heat treatment offers significant advantages in terms of reducing both time and production costs. However, despite these benefits, there has been a lack of comprehensive studies focusing on single-step ageing heat treatments. This paper addresses the existing literature gap by investigating the effects of single-step ageing heat treatment, utilizing specified temperatures (400, 500, & 600 °C) and durations (30, 60, & 90 mins), on Ni-rich NiTi cuboid samples produced via L-PBF.

The study delves into the impact of these heat treatment parameters on critical material properties such as phase transformation temperatures, microhardness, phase volume fractions, and crystallite sizes. It highlights the often-overlooked influence of crystallite size on the thermomechanical properties of aged samples, in addition to transformation temperatures, which are typically considered the most crucial property in determining part behavior. Significantly, this research explores, for the first time, the feasibility of employing a single-step ageing heat treatment with a higher Ni concentration (52.39 at. % Ni – 47.61 at. % Ti) alloy, which has not been previously investigated. By doing so, the paper enhances our understanding of how ageing heat treatment affects crystallite size and phase transformation temperatures, crucial factors in achieving desired properties for applications of Ni rich NiTi such as stents. Hence, this study provides a foundation for tailoring the material properties of Ni-rich NiTi alloys by opening avenues for optimizing their performance for various engineering applications. This advancement contributes to the broader field of materials science and engineering, facilitating the development of more efficient and effective manufacturing processes and products with Ni-rich NiTi alloys.

4.2 Materials and methods

4.2.1 Powder material

For the fabrication of the nitinol parts via laser powder bed fusion (L-PBF) technique, gas-atomised Ni-rich nitinol (NiTi) powder was utilised which was supplied by Fort Wayne Metals Inc., Castlebar, Ireland. **Table 4-1** shows the summarised elemental composition of the powder verified using the Energy Dispersive X-ray spectroscopy (EDX) analysis, INCA, Oxford Instruments EDX. EDX analysis of the printed parts was also performed and reported. There were 21 EDX measurements taken, each over an area map covering 10 by 10 micrometres for each sample. The average and standard deviation of these measurements were calculated and reported. The morphology of the as-received powder was analysed using a Zeiss EVO LS-15 Scanning Electron Microscope.

Table 4-1: Elemental composition and particle size distribution of the NiTi powder used as feedstock.

Elemental Composition		**Particle Size Distribution (µm)**		
Ni	Ti	D_{10}	D_{50}	D_{90}
52.39	47.61	12.3	27.4	47.6

The supplied powder was spherical as shown in **Figure 4-1**. This morphology is important to accomplish better fluidity of the powder to overcome the challenges faced during the processing of the parts using LBPF [201]. Some satellite particles were also visible which were the partially melted particles due to the gas atomisation process. The particle size distribution (PSD) of the NiTi powder was conducted using a Malvern Mastersizer 3000 equipped with an Aero S dispersion unit. Particle Size Distribution (PSD) of D10 to D90 for the NiTi powder was found to be in the range of 12.3 to 47.6 µm. PSD is important to facilitate the LPBF process to help produce denser parts.

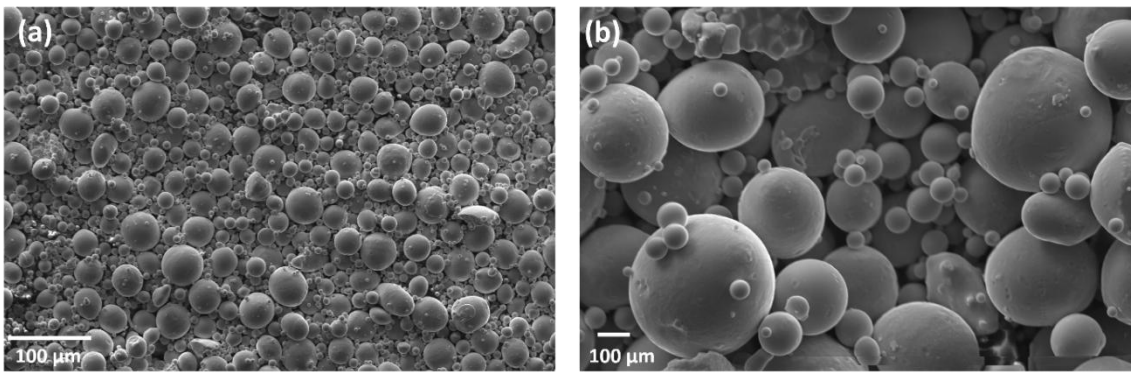

Figure 4-1: Surface morphology (SEM) images of the gas-atomised NiTi powder.

4.2.2 Fabrication of the NiTi parts

NiTi cuboids with the dimensions of 5 x 5 x 6 mm were fabricated using the AconityMINI GmbH 3D metal printer from Aachen, Germany. The metal printer is equipped with a 200 W fibre laser and a wavelength of 1068 nm from IPG Photonics, Germany. Argon gas with a purity of 99.9996% was employed to maintain an inert and oxygen-free environment inside the printer chamber during the build process. A supply factor of 2.5 times was used for the powder to ensure enough powder was deposited for each layer. A scanning strategy with a rotation of 90° between layers was used during the fabricating of the parts. The hatching strategy was kept for all samples as an alternative raster scan for consistency of processing. Process parameters used for the fabrication of the NiTi parts along with their corresponding volume energy densities (VED) in J/mm^3 are tabulated **Table 4-2**. The volumetric energy densities were calculated using equation (1) considering the Laser Power (P), scanning speed (S) and hatch spacing (H) along with the layer thickness (t) which was maintained at 60 µm.

$$\mathrm{VED} = \frac{\mathrm{P\ (W)}}{\mathrm{S}\left(\frac{\mathrm{mm}}{\mathrm{sec}}\right).\ \mathrm{t\ (mm)}\ .\ \mathrm{H\ (mm)}} \qquad (1)$$

Table 4-2: Processing parameters used to produce the NiTi parts with a constant laser spot size and hatch spacing of 60 µm and 80 µm respectively.

Sample Set Number	Laser Power (W)	Scanning Speed (mm/s)	VED_H (J/mm^3)
S1	150	1000	31.25
S2	150	500	62.5
S3	180	1000	37.5
S4	180	500	75

4.2.3 Ageing heat treatment

Heat treatment of the NiTi parts was conducted in a box furnace under atmospheric conditions. The samples were placed in an alumina boat crucible (15 mm in length, 8 mm wide and 5 mm high) before being placed in the furnace. To understand the effect of the ageing heat treatment on the transformation temperatures, crystallographic variations, and mechanical properties, the NiTi samples were heated to temperatures of 400, 500 and 600 °C and times of 30, 60 and 90 minutes, as listed in **Table 4-3**. The parts are

labelled as sample set numbers followed by heating temperature and times as listed in **Table 4-3**. After heat treatment time, the sample was extracted from the furnace and left to cool on the bench within its alumina crucible.

Table 4-3: Ageing temperatures and times used for the L-PBF-produced samples.

Sample ID	Ageing Temperature (°C)	Ageing Time (mins)
400_30	**400**	**30**
400_60	400	60
400_90	400	90
500_30	500	30
500_60	**500**	**60**
500_90	500	90
600_30	600	30
600_60	600	60
600_90	**600**	**90**

4.2.4 Phase transformation studies

Phase transformation studies were carried out using a TA Instruments® Discovery DSC2500. The measurements for the differential scanning calorimeter (DSC) generate a reliable and repeatable curve to help determine the critical phase transformation temperatures of the test sample. Samples of about 20 mg were placed in aluminium pans with lids for the DSC testing. All the as-fabricated and heat-treated samples were subjected to a heating and cooling cycle between the temperatures of -100 °C and 150 °C at a ramp-up rate of 10 °C/min. Two section of 20 mg were taken from each sample, and each was measured using DSC to check for measurement repeatability.

4.2.5 Crystallographic studies with microstructural characterization

A Cu Kα source of wavelength 1.5406Å equipped on a Bruker D8 X-ray diffractometer was utilised to conduct the crystallographic studies. To determine the crystallinity of the NiTi parts under examination, the 2theta angle ranged between 10 and 100 degrees. A locked coupled setting with a step increment of 0.01° and 8s/step was used for the scans.

The microstructural examination was performed on the XY plane of the fabricated samples using a Keyence-VHX2000E optical microscope. Before conducting the microstructural analysis, the samples were cold mounted to help avoid the heating of the samples which may occur using a hot press resin mounting procedure. SiC emery papers of varying grit sizes starting from 80 up to 4000 grit were used with a rotation speed of 250 rpm for 5-10 mins at each step. Finer diamond polishing of the sample surface was

conducted using diamond suspensions of 9, 6, 3 and 1 micron. An etchant with a composition of 41 mL distilled water + 5 mL HNO3 + 4 mL HF (Kroll's solution) was applied for 30-60 secs to reveal the microstructures as well as the substructures of the samples. The elemental composition of the samples was reported using the EDS analysis with map area measurements.

4.2.6 Microhardness measurements

The polished surface of the samples was used for both as-fabricated and heat-treated samples with a dimension of 5 x 5 mm using Leitz MiniLoad 2® equipment for measuring the Vickers microhardness. All the samples were exposed with a force of 981 mN onto the surface of the samples with a holding time of 20 seconds. Five different point measurements were made on the XY plane of the samples and average results and variability were calculated as standard deviation. Tests were carried out under standard laboratory conditions.

4.3 Result and Discussion

4.3.1 Effect of ageing parameters on the phase transformation temperatures

Phase transformation temperatures were measured for the as-fabricated and aged NiTi samples using the DSC. The monoclinic B19' crystal structure, martensite phase, and the body-centred cubic (BCC) B2 crystal structure, austenite phase, are the two primary phases of nitinol [128,173,202]. An additional unstable R* phase (rhombohedral crystal structure) is often present along with either the austenitic or martensitic phase for nickel-rich nitinol [40]. Post-processing methods such as heat treatment of the additively manufactured parts also result in the introduction of such unstable R* phases [203]. The measurements from the DSC exhibited the presence of an unstable R* phase for the samples processed with a scanning speed of 500 mm/s irrespective of the laser power as shown in **Figure 4-2**. This exhibited that the phase transformation took place as a 2-step process of transformations by B2 › R* › B19'. The samples processed with a higher scanning speed of 1000 mm/s resulted in a single stable phase transformation by B2 › B19'. These phase transformations are reversible. All of the as-fabricated samples resulted in an austenitic finish temperature lower than that of the room temperature, see **Figure 4-2**. As per the ASTM F2004 – 17, the intersecting tangent method can be used to determine the phase transformation temperatures [204]. For this to provide accurate results, the slope of the phase change peaks should be sharp (i.e. there should be a high

rate of energy change wrt temperature). The peaks of the as-fabricated samples are broad and have low intensity in comparison to the aged samples. During the heating cycle, an endothermic reaction occurs which is primarily an indication of the heat absorbed. The enthalpy is calculated as the area under the peak (measured in Joules/grams). Similarly, the cooling cycle exhibits an exothermic reaction indicating the heat released during the reaction. In the case of the as-fabricated samples, the austenite and martensite phase change temperatures could be measured with a high level of accuracy; however, the peaks were not sufficiently sharp to determine with high accuracy the critical temperatures for the R* phase transformation.

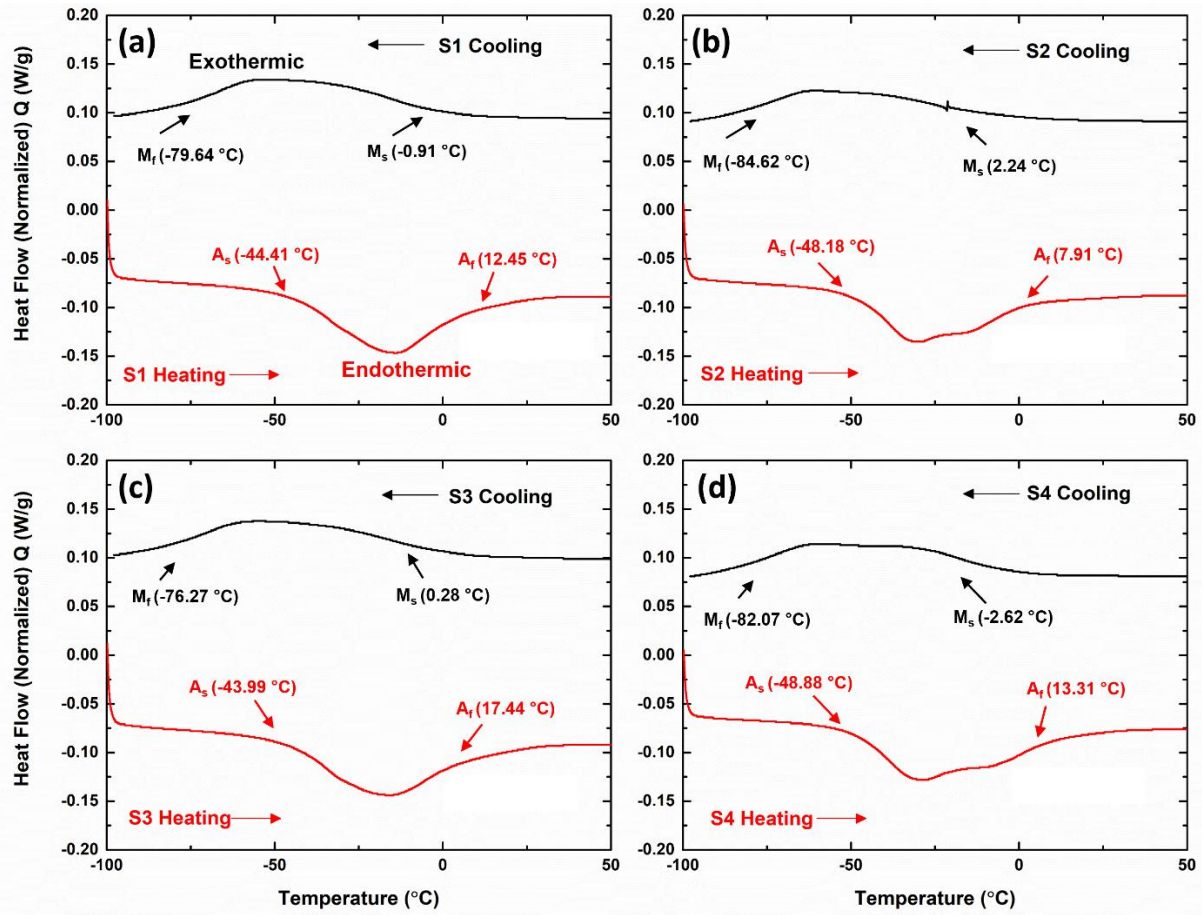

Figure 4-2: DSC curves of as-fabricated NiTi parts with their respective austenitic finish Af temperatures for (a) S1, (b) S2, (c) S3 and (d) S4.

Heating and cooling cycles resulting from the DSC measurements for selected heat-treated samples are presented in **Figure 4-3**. As observed the peak heights of the heat-treated samples are higher and sharper as compared to the peaks of the respective as-fabricated samples. However, the peak height of the sample heat-treated at 500°C for 60

minutes is more pronounced than that of the other heat-treated samples exhibiting greater homogeneity in the microstructures, lower defects as well as reduced residual stresses.

Additively manufactured (AM) NiTi samples which were heat treated at 400°C for 30 minutes showed an unstable R* phase in the heating cycle with the stable austenitic phase as shown in **Figure 4-3**. The presence of austenitic R* phase is induced by the post-processing using the heat treatment technique attributed to the residual stresses [148]. Increasing the heat treatment temperature and time to 500°C and 60 minutes respectively, resulted in the induced R* phase to shift from the heating cycle to the cooling cycle. As reported previously by Khan et. al. [205], heat treatment induces the R* phase making the Ni-rich nitinol parts superelastic. Further increase in temperature and time to 600°C and 90 minutes, led to no formation of the unstable R* phase, therefore exhibiting a direct phase transformation between the two primary phases.

From **Figure 4-3** and **Figure 4-4**, it can be seen that there is a shift, for all samples irrespective of printing parameters, of both the austenitic as well as the martensitic phases to lower temperatures as the heat treatment temperatures and times are increased. This is also indicated by the enthalpy change as indicated in Appendix **Table A.1** along with the transition temperatures.

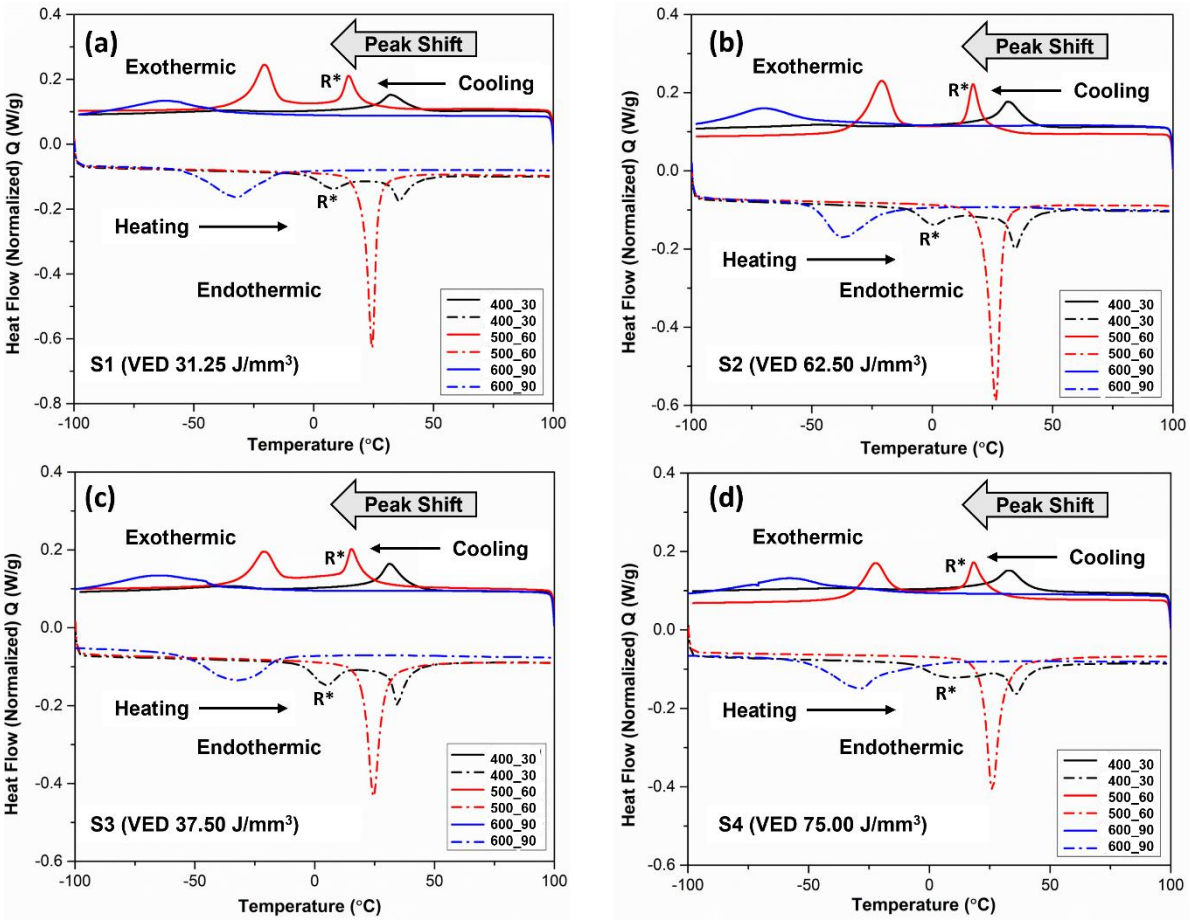

Figure 4-3: DSC curves with varying temperatures and times of selected heat-treated samples (a) S1, (b) S2, (c) S3 and (d) S4.

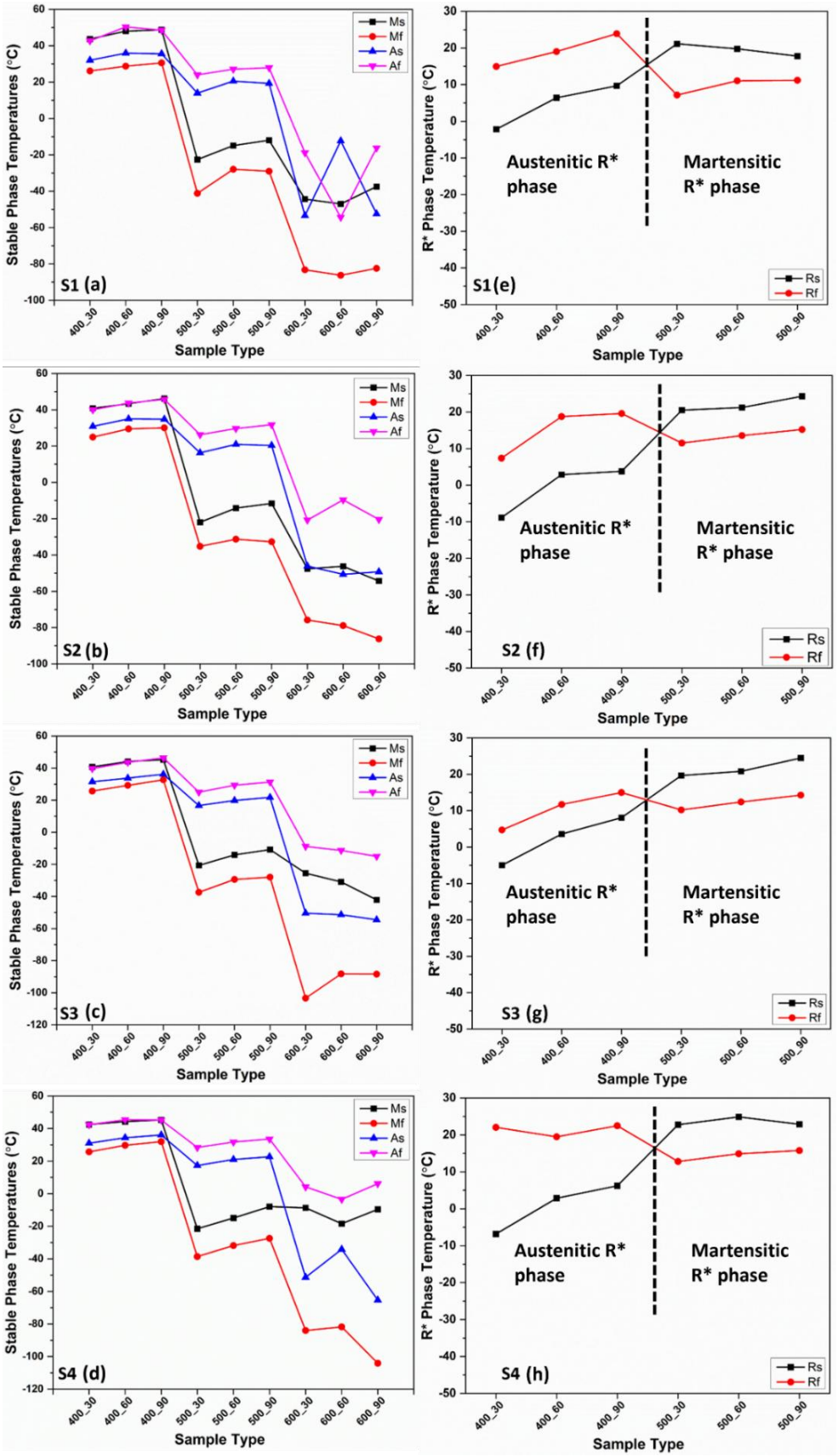

Figure 4-4: Variation in critical phase transformation temperatures due to the variation in the heat treatment parameters for S1, S2, S3, and S4 for the (a-d) martensitic and austenitic start and finish temperatures and for the (e-h) resulting R* phase.

4.3.1.1 Effect of heat treatment on the induction of unstable phase in the heating cycle of phase transformation

As observed in **Figure 4-3**, the reverse transformation occurs from B19' to B2 during heating along with the induction of the R* phase. This is indicated by the presence of two peaks on the curves for the heating cycle. At the ageing temperature of 400°C for 30 mins, the transformation interval is observed to be larger than that of the respective as-fabricated samples. As seen from **Figure 4-4**(e-h), the unstable R* phase start temperature (R_s) increases as the ageing time is increased from 30 to 60 to 90 minutes respectively. For the sample sets of S1, S2, S3 and S4, the R_s temperature ranges between -10°C to 10°C with an increasing trend observed for all the samples. This observation suggests that there is distortion of the austenitic B2 phase leading to the formation of the unstable phase before the completion of the transformation to the martensitic phase. With the increase of the ageing time keeping the temperature constant at 400°C, the distortion in the austenitic phase occurs at a higher temperature as confirmed by the trend shown in the **Figure 4-4**(e-h).

4.3.1.2 Effect of heat treatment on the induction of unstable phase in the cooling cycle of phase transformation

At the constant temperature of 500°C with varying times of 30, 60 and 90 minutes, the phase transformation occurs in the cooling cycle with the transformation occurring by B2 › R* › B19', as shown in **Figure 4-3**. A second peak is observed in the cooling cycle indicating the presence of an unstable phase during this transformation. The peaks resulting from ageing at 500 °C are narrower as well as higher than that of the samples aged at 400°C, suggesting that the samples aged at 500°C have a higher extent of microstructural homogeneity during the transformation. As seen from **Figure 4-4**(e-h), the samples aged at 500 °C exhibit higher Rs temperatures than of the samples aged at 400°C; and lower Rf temperatures. This shows that the transformation interval is larger for the samples heat-treated at 500°C, irrespective of the ageing time, compared to their counterparts which are aged at 400°C. The Rs of all samples range from 12°C to 25°C.

4.3.1.3 Effect of heat treatment on the critical phase transformation temperatures

The critical phase transformation temperatures for the DSC curves are shown in **Figure 4-3**. With the help of these temperatures, the necessary phase transformation can be

evaluated. As observed, the austenite start (As) and austenite finish (Af) temperatures range between -65.31°C to 36.05°C and -54.37°C and 50.32°C respectively. This broad range in the reverse transformation from B19' to B2 can be achieved by ageing the samples at the evaluated specific temperatures and times opening the venue for several applications. On the forward transformation, the transformation temperatures play a vital role in determining the shape memory effect of the produced parts. In this study, Ms ranges from -54.34°C to 48.75°C and Mf ranges from -104.13°C to 32.72°C covering a broad range of temperatures.

From **Figure 4-4**(a-d), it can be deduced that the Af for the samples aged at the temperature of 400°C with varying times of 30, 60 and 90 minutes are much higher than the room temperature and ranges from 39.71°C to 50.32°C which indicates that the martensitic phase is dominant. Af is observed to increase with increasing ageing time keeping the temperature constant at 400°C. At this temperature of 400°C, an unstable R* phase is also observed in the heating cycle in a reverse transformation from B19' › R* › B2 as depicted in **Figure 4-4**(e-h). With a further increase in the ageing temperatures to 500°C, there is a shift of the induced R* to the cooling cycle, from the heating cycle, along with the stable martensitic phase forward transformation of B2 › R* › B19'. This increase in the ageing temperature lowers the austenitic finish temperatures to slightly higher than the room temperature in the range of 24°C to 31.78°C. Increasing the ageing temperature further to 600°C leads to no formation of the unstable R* phase, therefore exhibiting a direct transformation between the two primary phases. Also, further reduction in austenitic finish temperature is observed to even with sub-zero temperatures for the samples ranging from -54.37°C to 6.17°C. This decrease in the austenitic finish temperature for the samples aged at 600°C is a result of the release of the residual stresses and formation of nickel rich precipitates [77]. It is worth highlighting that these trends are commonly seen for all the samples irrespective of their printing process parameters.

4.3.2 Effect of ageing temperatures on the resultant crystallographic phase characteristics

Figure 4-5 exhibits the identified spectral peaks as observed with the help of the XRD scans. As shown, the distinct peaks observed were austenitic NiTi (B2 phase) and martensitic NiTi (B19' phase). The L-PBF process leads to the generation as well as the co-existence of these two phases for a wide range of temperatures [62]. Several other researchers have also reported the presence of the B2 austenitic NiTi phase as a result of

the processing of nitinol via L-PBF [71,206]. The presence of these two phases was also examined by Rietveld refinement analysis of the XRD scans. The Crystallographic Open Database was utilised to confirm the crystal structures shown: B2 austenitic phase of NiTi (96-110-0133) and B19' martensitic phase of NiTi (96-210-6109). As indicated by the phase diagram of NiTi, there is a possibility of the co-existence of the B2 phase with Ni-rich precipitates such as Ni_4Ti_3 for a Ni-rich NiTi composition as reported by Khalil-Allafi et. al. [150]. The phases which are formed during the processing of NiTi are greatly controlled by the elemental composition of the NiTi powder used for the processing of the samples. During the L-PBF processing of the Ni-rich NiTi powder, preferential nickel evaporation has been observed due to a lower melting point of nickel compared to that of titanium [93]. Post-processing of the samples with ageing temperatures leads to distortion of the localised NiTi matrix leading to change in the crystal structure of the matrix. This observation has been made for the samples heat treated at 400°C where the B2 cubic crystal structure is distorted to a trigonal hexagonal crystal structure (COD: 96-901-4316) with a unit cell of a= 7.3410 Å c= 5.2700 Å in comparison to a= 3.0150 Å (B2 parent phase). No Ti-rich intermetallic phases were observed in the XRD scans.

Further increasing of the ageing temperature to 500°C, leads to a complete transformation of the B2 parent phase to the B19' martensitic phase which was also indicated by the DSC response in this study. However, the phase volume fractions of the B2 austenitic phase and B19' martensitic phase are not reliable as the austenitic finish temperature (A_f) is close to the room temperature. As reported earlier by Santoro et. al. [207], the co-existence of austenite and martensite phases of NiTi at room temperature with variations in transitional temperature ranges resulted from retained residual stress. These results are in agreement with those of other investigations which also showed variations in critical phase transformation temperatures and phase transformations resulting from various heat treatment temperatures and times [176,208]. Further increasing the ageing temperature leads to a one-step phase transformation from the B2 parent phase to the B19' martensitic phase. This was confirmed by the XRD scans conducted in the study as well which exhibited that the aged samples were fully austenitic with the presence of only the B2 austenitic phase.

The strong affinity of titanium to oxidise results in the formation of a passivation layer of TiO_2 on the sample surface. The presence of this phase was not indicated by the XRD scans which may be due to the typical thin layer nature of this oxide on the sample

surface. It has been commonly reported in several studies that the ageing of Ni-rich NiTi alloy induces the formation of Ni_4Ti_3 precipitates [209–211]. In the NiTi matrix, it has been reported that the Ni_4Ti_3 precipitates are present in the $\{111\}_{B2}$ plane of the NiTi system which is formed due to either heat treatment or thermomechanical exposure [148,212]. Eight variants of the Ni_4Ti_3 precipitates are formed as each of the four $\{111\}_{B2}$ planes of the parent phases is linked to two variants. Notably, this crystallographic relation and the heat treatment parameters control the crystallite size and orientation of the Ni_4Ti_3 precipitates. A study from Oncel et. al. [117] showed that the crystallite size increases when the heat treatment temperature is above 500°C, which initiates the re-dissolving process in the austenitic NiTi matrix. Although the DSC response curves in this study show the presence of the R* phase when the samples are aged at temperatures of 400°C and 500°C, no distinct peaks were observed in the XRD spectra. This made the possibility of the phase volume fraction and identification of the Ni_4Ti_3 precipitates quite challenging. Due to the overlapping 2θ of the Ni_4Ti_3 precipitates with that of the B2 parent phase, these precipitates are not considered in this study. The influence of these precipitates would require in-depth investigation which is beyond the current scope of this study. The formation of these precipitates is controlled by the internal strain field resulting from the heat treatment. As the temperature and time for the heat treatment is increased, the Ni composition in the NiTi matrix decreases [100,211]. As shown in **Figure 4-4**, an increase in the R_s has been observed indicating that an increase in the heat treatment temperatures and times critically affects the formation and growth of the Ni_4Ti_3 precipitates. Several researchers have reported that an unusual two-stage R-phase transformation takes place for Ni-rich NiTi aged at lower temperatures, below 250°C [187,213] [129]. In this case of lower temperature heat treatment, the precipitates are susceptible to being formed at the grain boundaries and finer precipitates generated lead to the two-stage R-phase transformation. However, in the current study, only one-stage R-phase transformation was observed for the samples aged at 400°C and 500°C.

4.3.2.1 Effect of ageing parameters on the crystallite size of the resultant phases

Upon further examination of the XRD spectra, the crystallite size was calculated from the Full Width Half Maxima (FWHM) of the resultant phases. As shown in **Figure 4-5**(e-h), upon heat treatment of the fabricated samples at a temperature of 400°C, it was found that the crystallite size ranged from 6 to 22 nm which was lower than the crystallite size

of the samples which were aged at higher temperatures of 500°C and 600°C. The crystallite size increased with the ageing temperature of 500°C to range between 6.5 to 28 nm. This increased the lattice parameter which has been discussed in the previous section. The DSC response curves for the heat-treated samples at 500 °C exhibited transformation to B19'; however, the complete transformation did not occur resulting in the martensitic R* phase, as shown in **Figure 4-3**. As the ageing temperature was further increased to 600 °C, the crystallite size further increased to a range of 38.40 to 47.58 nm. As seen in the DSC curves in this study (**Figure 4-3**), the samples heat treated at 600 °C were fully austenitic which have a flat plate microstructural form, rather than being needle or dendritic in nature. All the samples, irrespective of the printing process parameters, showed increasing crystallite size with higher ageing temperatures and times.

$$\tau = \frac{K.\lambda}{\beta.\cos\theta} \qquad (2)$$

where K is a "shape factor" between 0-1 that depends on the shape of the crystallite (usual values are about 0.9), λ is the X-ray wavelength (0.154 nm), β is the FWHM for the 2θ peak, and θ is the position of the peak. Scherrer's equation is an indication of the average crystallite size of the samples under consideration and was used to quantitatively calculate the crystallite size. It relates the width of the peaks of the XRD spectra directly with the crystallite size. The results from the Scherrer's equation represents the thickness that is perpendicular to the crystal plane being measured. The width of the XRD peaks is determined by the micro-level changes of the sample such as the crystallite sizes and the lattice distortion [214,215]. In this work, XRD measurements were carried out using a Bruker system which has a large goniometer radius. Even without a monochromator, the instrumental contribution to peak broadening in such systems is typically minimal—especially when analysing nanocrystalline materials. As calculated with the help of Scherrer's equation, the crystallite sizes of the samples were well below 100 nm, the instrumental broadening becomes negligible, Therefore, no correction was applied in the calculations for the crystallite sizes.

▲ NiTi (B2 austenite)
★ NiTi (B19' martensite)

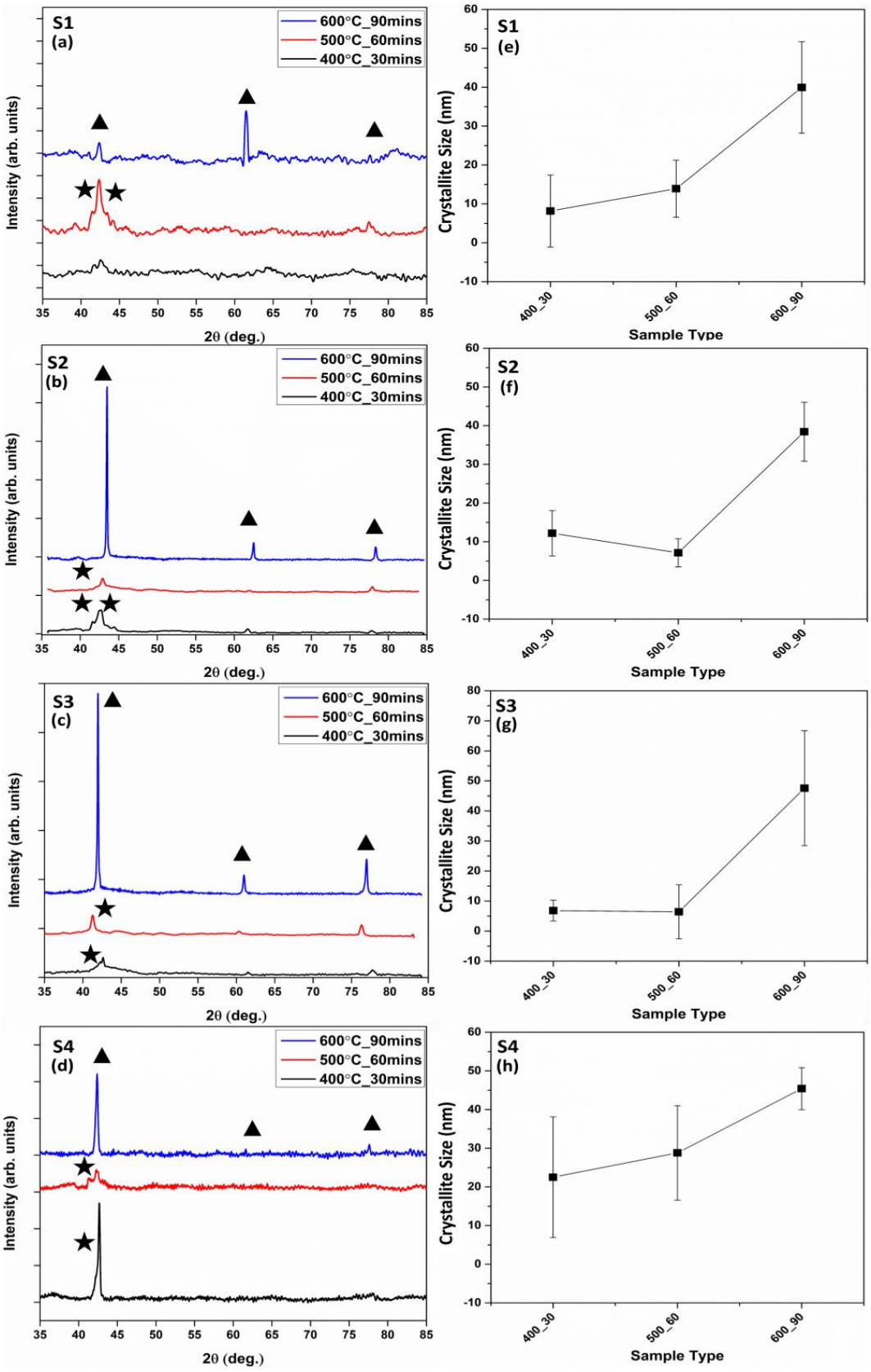

Figure 4-5: Comparison of the aged NiTi samples for S1, S2, S3, and S4 of the resulting (a-d) XRD spectra at room temperature and (e-h) crystallite size, n = 3.

4.3.2.2 Effect of ageing parameters on the phase volume fractions of the resultant phases

Phase volume fractions were calculated from the XRD spectra using Rietveld refinement along with the Full Prof suite of the Match software (see Appendix **Table A. 2**). B2 austenitic phase and B19' martensitic phase volume fractions are shown in **Figure 4-6**. The determination of the phase volume fractions was a challenging task due to the overlapping nature of the different phases of NiTi. However, at the ageing temperature of 400°C, higher volume fractions of the B19' phase were found. As demonstrated in **Figure 4-6**, B19' phase volume fractions were observed to be in the range of 53.1 to 87.7% for S1, S2, S3, and S4. This trend showed that the samples aged at this temperature of 400°C were in the transformation stage which was not completed and had a presence of unstable phase. This was also confirmed by the DSC response curve in this study. At the higher ageing temperature of 600°C, complete transformation had occurred which resulted in fully austenitic phase structure at room temperature. This was also confirmed by the XRD spectra which confirmed that the B2 phase volume fraction was 100% for all the sample sets.

However, the samples aged at 500°C were difficult to analyse at room temperature. The DSC response curves exhibited that the samples S2 (500°C for 60mins) and S3 (500°C for 60mins) had very close austenitic finish temperatures (A_f) of 29.69 °C and 29.33 °C, respectively which was slightly higher than the room temperature. The analysis of XRD scans displayed that the phase volume fractions for these samples were higher in B19's phase volume fraction of 88.3 and 98.1% for S2 and S3 respectively compared to S1 and S4. Whereas the samples S1 (500°C for 60mins) and S4 (500°C for 60mins) had higher austenitic B2 phase volume fractions of 88.8 and 92.1% respectively.

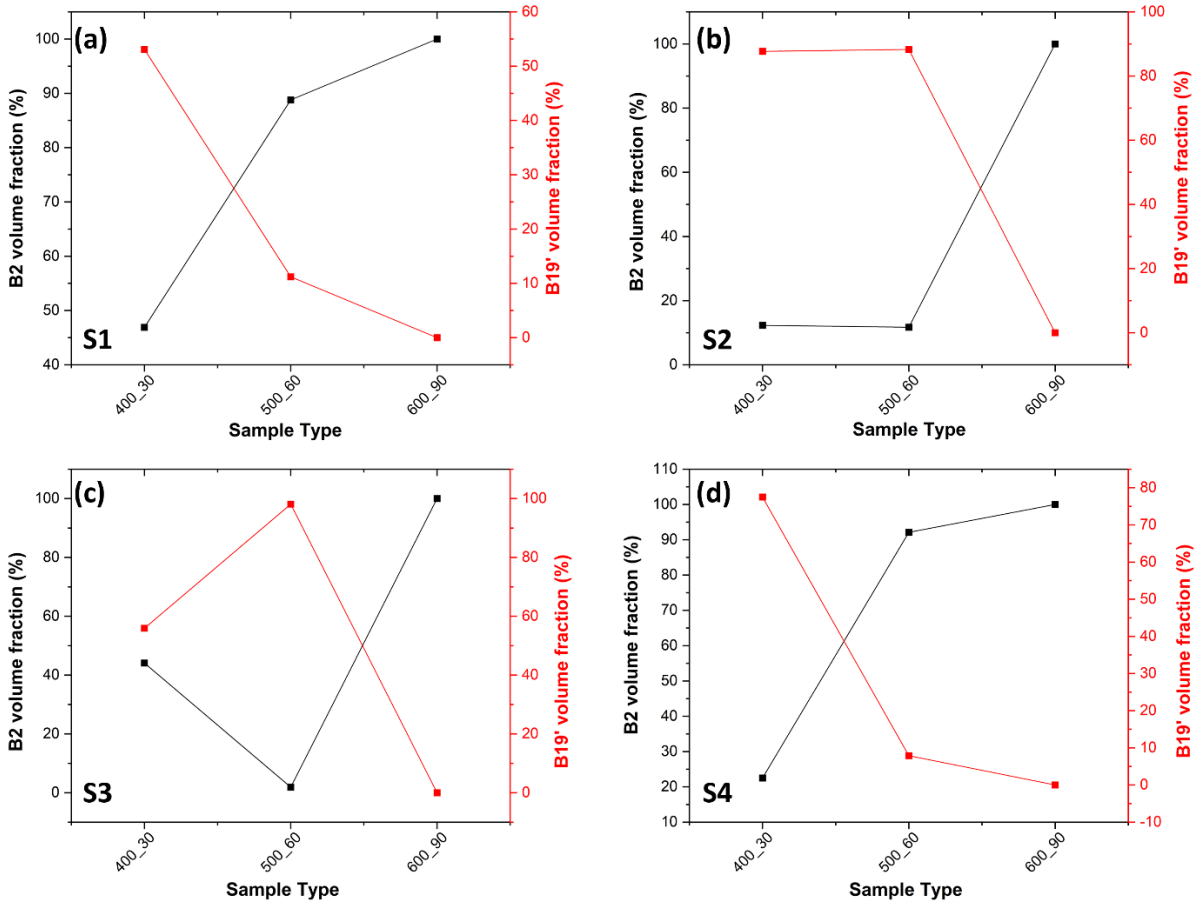

Figure 4-6: Phase volume fractions for the aged NiTi samples belonging to sample sets (a) S1, (b) S2, (c) S3 and (d) S4.

4.3.3 Effect of ageing temperatures on the microhardness

Vickers microhardness tests were conducted at five random locations on each sample to determine the effect of heat treatment on the hardness behaviour of the NiTi samples as shown in **Figure 4-7**. As observed, the hardness values increased for the heat-treated samples from that of the as-fabricated samples. As seen **Figure 4-7**, all the as-fabricated samples (S1, S2, S3, S4) exhibited hardness values in the range between 250 and 300 HV whereas the heat-treated samples had higher hardness values. The hardness values for the heat-treated samples ranged between 300 and 450 HV.

The L-PBF process produces higher hardness levels compared to conventional slower cooling rate processes due to the L-PBF process involving rapid solidification of the melt pool leading to finer crystallites. As observed in **Figure 4-4**, samples aged at 400°C are martensitic B19' phase dominant. For NiTi, the martensite phase is known to be harder than the austenite phase [216,217]. The lower heat treatment temperatures and times were shown to result in smaller crystallite size, see section 3.2.1. Finer crystallites increase

the hardness of NiTi samples [170]. As the ageing time was increased from 30 to 60 and then to 90 minutes, the hardness values decreased due to the phases shift towards more a austenitic phase structure and larger crystallite sizes. This is also verified by the decreasing austenitic finish temperatures (**Figure 4-4**(a-d)) and the recorded shift in the martensitic start temperatures. Further increasing the temperature to 500°C lowered the microhardness values due to the co-existence of the austenitic and martensitic phases. The average crystallite size was calculated and reported above although the values are not reliable due to the challenging nature of the present phases. Increasing the ageing temperature to 600°C, a one-step transformation occurs to a fully austenitic B2 phase with increased crystallite size which in turn lowers the hardness values.

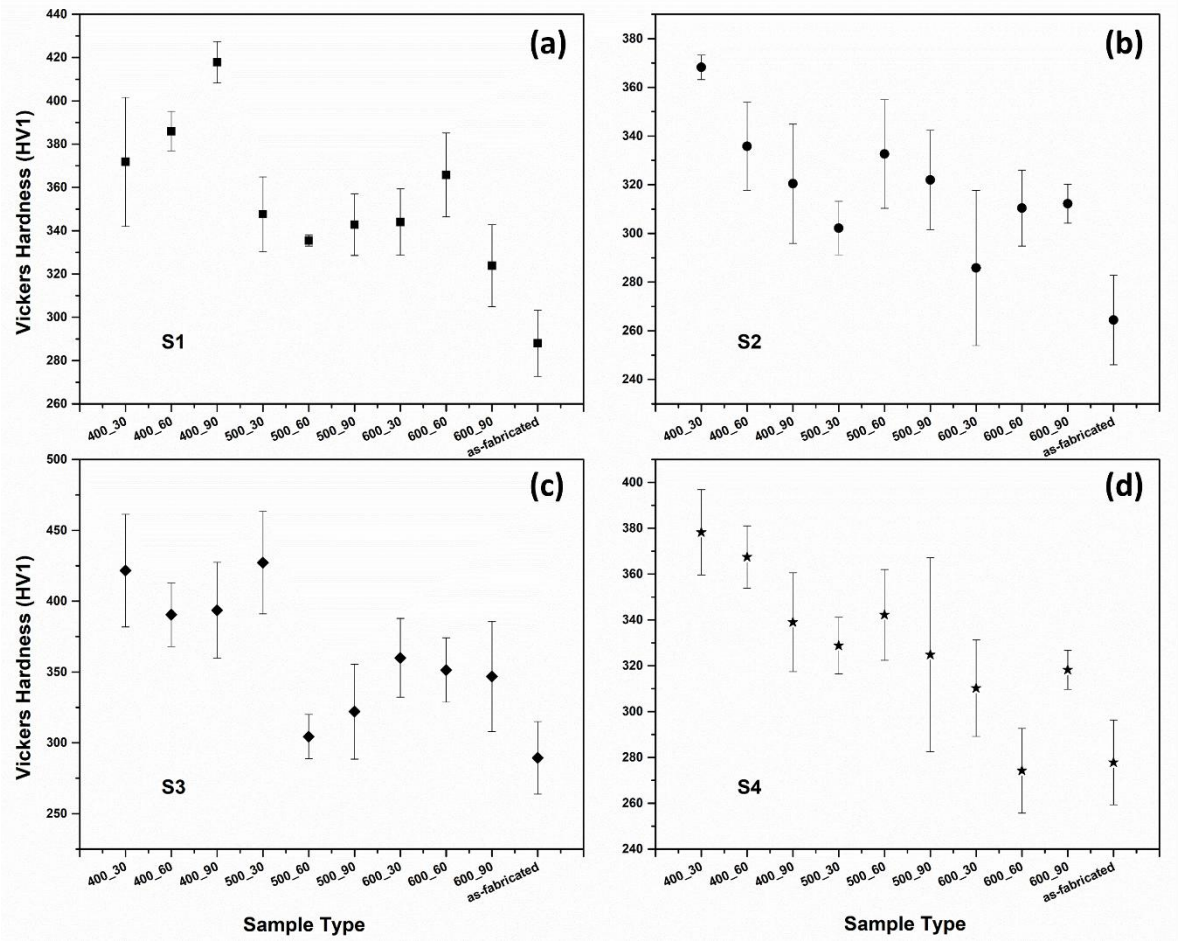

Figure 4-7: Vickers microhardness values of all the as-fabricated and heat-treated NiTi samples (a) S1, (b) S2, (c) S3 and (d) S4, n = 5.

4.3.4 Effect of ageing temperatures on the resulting microstructures

Figure 4-8 shows the optical micrographs of aged NiTi samples at different temperatures of 400°C, 500°C and 600°C, and holding times of 30mins, 60mins and 90 mins. These

optical micrographs are from sample S4 which was processed using a laser power of 180W with a scanning speed of 500 mm/s. The optical micrographs of the as-fabricated samples with detailed characterisation have previously been published by the authors [93]. The samples fabricated at the higher laser power of 180W exhibited bimodal microstructures with a combination of coarse as well as fine crystallites. However, samples processed with laser power of 150W showed unimodal structures with coarser B2 phase domination. This occurred due to the Oswald ripening effect [85]. Due to the nature of re-melting and rapid solidification of the molten metal in the L-PBF process, the crystallites formed upon solidification are observed to be relatively fine compared to conventional processing methods.

Due to the complex nature of the L-PBF process with layer-by-layer deposition, observation of the phases optically is quite challenging. However, this was achieved with the help of a systematic metallographic preparation method detailed in section 2.5, including etching with Kroll's solution. The metallographic images for S4 are shown in **Figure 4-8**. For the sample aged at 400°C, see **Figure 4-8** (a), two distinct phases were observed with larger plate-like crystallites of B2 austenitic phase and finer martensitic B19' phase laths. The distribution of these phases is distinct and corresponds to the types of coarse and fine crystallites found within the as-fabricated S4 sample which exhibits bimodal crystallite structures with finer crystallites within the coarser crystallites of the B2 phase. This shows the effect of this ageing temperature on the elementary processes of the martensitic transformation [218]. SEM micrographs (**Figure 4-8**(d)) also exhibit coarser columnar dendritic crystallites upon closer examination of the microstructures. At a higher temperature of 600°C (**Figure 4-8** (c)), a fully austenitic B2 phase was achieved as depicted by the results from the DSC response curves (**Figure 4-3**(d)) and XRD scans (**Figure 4-5**(d)). This was also observed in the optical micrographs showing a larger plate-like B2 austenitic phase with coarser crystallites as the transformation gets fully completed from B19' › B2 in a single step. Planar equiaxed crystallites are the typical form of the B2 austenitic phase which is also confirmed by the SEM micrograph as depicted by **Figure 4-8** (f).

However, for the samples aged at 500°C, the co-existence of both the B2 austenitic phase and B19' martensitic phase was achieved as shown by the XRD scans. These samples have austenitic finish temperature near room temperature which makes the identification and separation of the two phases very challenging. The optical micrographs have shown

the co-existence of both phases as shown in **Figure 4-8** (b). Also, it depicts that the average crystallite sizes are dependent on the grain boundaries and the layer-by-layer fabrication of the NiTi part. SEM micrographs also shows the presence of finer dendritic structures which also contributes to higher hardness than the as-fabricated samples.

It has been previously reported that the restructuring of the phases occurs at temperatures of above 200°C which could be seen in the NiTi phase diagram [148]. However, this restructuring is also influenced by the final composition, residual stresses, as well as the cooling rate which is related to the applied volumetric energy density [219,220]. Crystallite size calculations with optical microscopy were not possible and have been calculated based on the FWHM obtained through the XRD scans, see section 3.2.1.

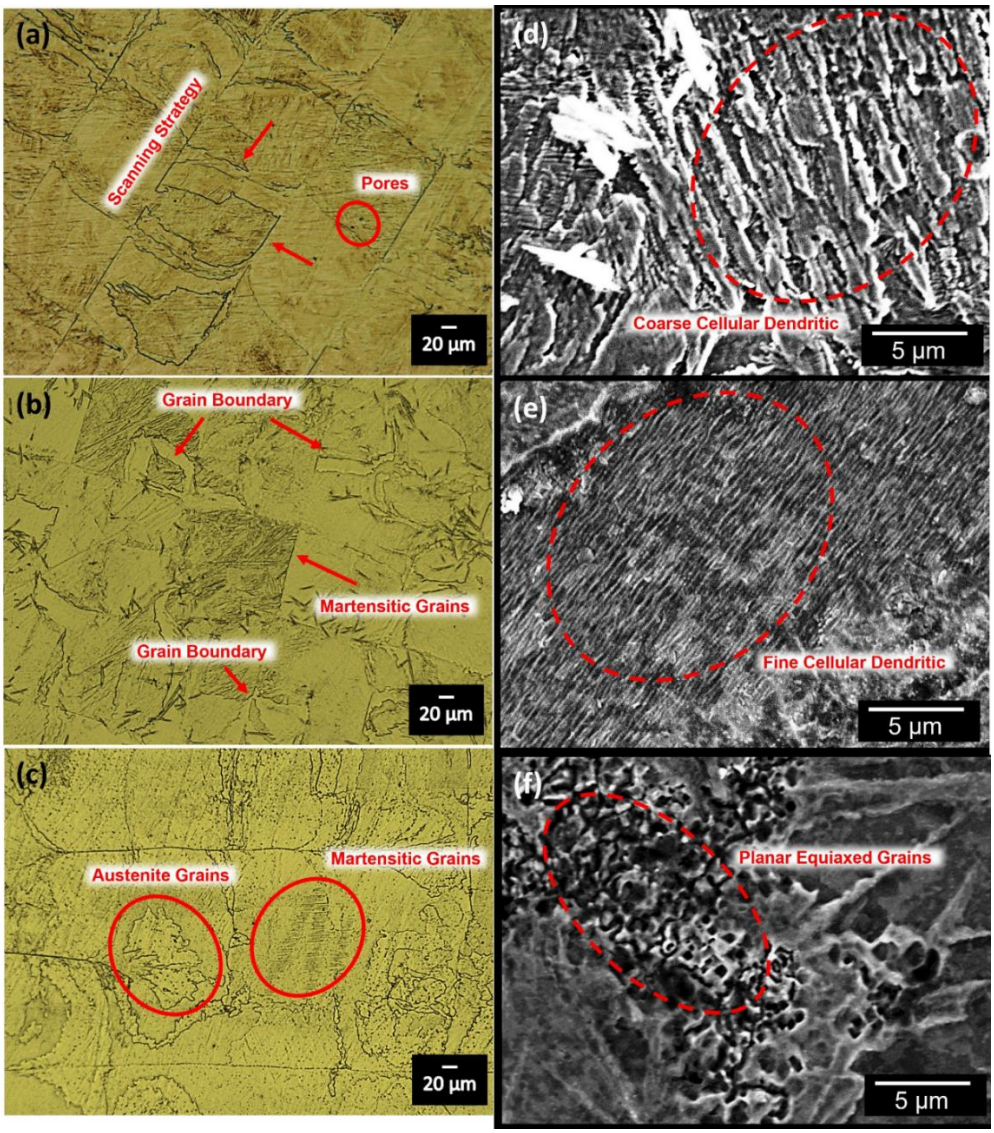

Figure 4-8: Optical micrographs of samples aged at (a) 400°C for 30 mins, (b) 500°C for 60 mins and (c) 600°C for 90 mins and SEM micrographs of samples aged at (d) 400°C for 30 mins, (e) 500°C for 60 mins and (f) 600°C for 90 mins.

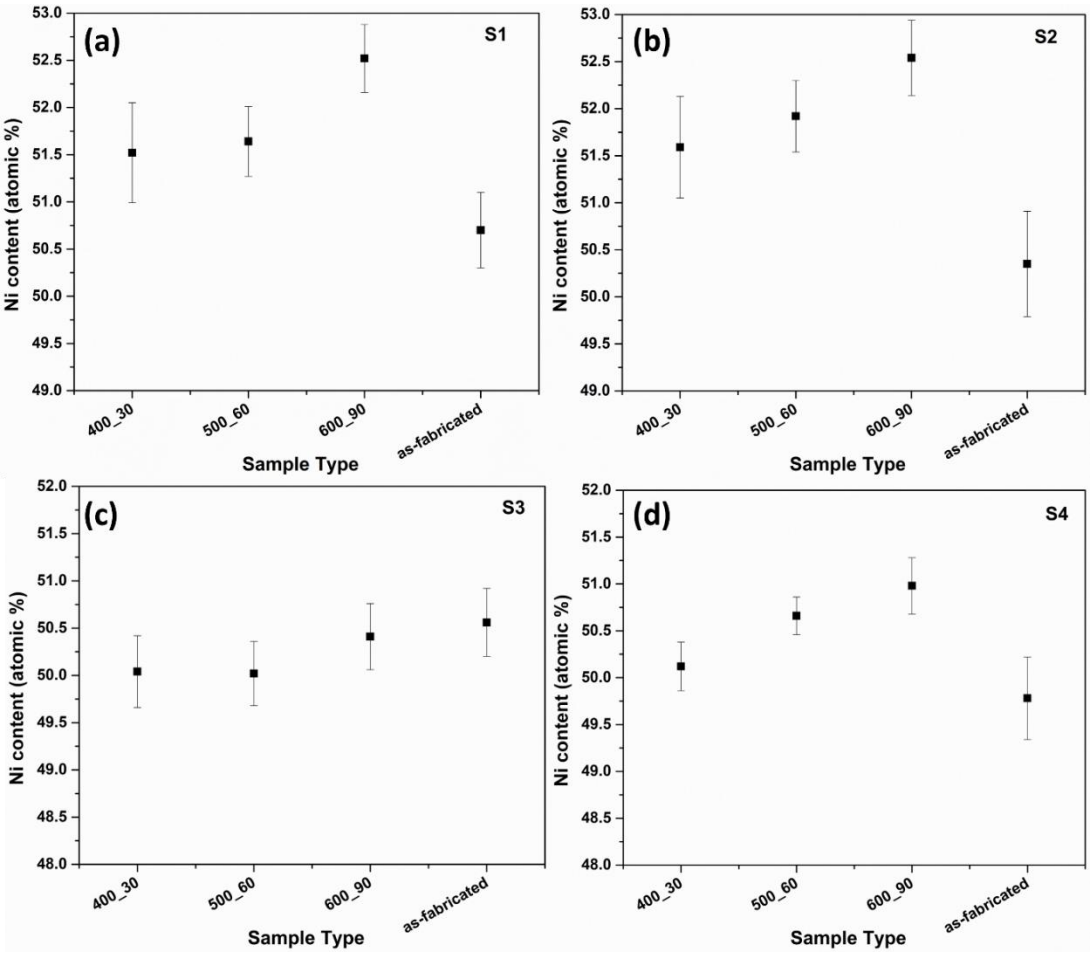

Figure 4-9: Elemental composition of as-fabricated and aged samples for sample sets (a) S1, (b) S2, (c) S3 and (d) S4, n = 3.

The heat treatment process affects the restructuring of the phases. This occurs for heat treatments above 200°C and is highly dependent on the elemental composition of the produced samples [169]. As presented in **Figure 4-9**, the composition of all aged samples was found to have increasing nickel content with increasing heat treatment temperatures and times. The samples aged at the temperature of 400°C for 30 mins showed lower nickel content than the samples aged at higher temperatures of 500°C and 600°C. This trend of increasing nickel content with increasing ageing parameters indicates that the heat treatments have led to an increased amount of austenitic phase in the NiTi matrix. This is shown from the optical micrographs and the XRD data. As expected, the increase in the nickel content favours the formation of austenitic phase.

4.4 Conclusion

The present research examines how a single-step heat treatment during ageing affects Ni-rich NiTi cuboids produced through L-PBF. Different ageing conditions were employed,

including varying temperatures (400°C, 500°C, & 600 °C) and durations (30 mins, 60 mins, & 90 mins). These settings were then correlated with phase transformation temperatures, phase characteristics (such as crystallite sizes and phase volume fractions), and microhardness. Comprehensive characterization and analysis were carried out following the ageing process, leading to the following conclusions:

a. Each of the samples fabricated using L-PBF displayed an austenitic finish temperature (A_f) lower than room temperature, indicating superelastic behavior at room temperature.
b. Samples subjected to ageing at 400°C resulted in an austenitic finish temperature surpassing the room temperature. With longer ageing durations, greater phase volume fractions of the martensitic phase were generated. Conversely, samples aged at 500°C showed austenitic finish temperatures near room temperature, accompanied by the presence of both martensitic and austenitic phases at room temperature.
c. A significant reduction in the austenitic finish temperature (A_f) was noted in the samples subjected to ageing at 600°C, accompanied by the presence of a fully austenitic phase, as verified by XRD scans.
d. Samples aged at 400°C exhibited smaller crystallite sizes ranging from 6 to 22 nm, with the martensitic phase predominating. Conversely, samples aged at 600°C displayed larger crystallite sizes ranging from 38.40 to 47.58 nm, characterized by fully austenitic phases.
e. The microhardness of the aged samples decreased as the ageing temperatures and durations increased, dropping from 380HV to 270HV for sample set S4. This trend was similarly observed in the other samples produced with three different sets of L-PBF parameters (S1, S2, and S3).

This study reveals that the heat treatment process offers a valuable means to adjust transformation temperatures and attain specific mechanical properties suitable for various applications. For the first time, this research provides a thorough examination of how manipulating both L-PBF and ageing process parameters for Ni-rich NiTi components can determine crystallite size, transformation temperatures, and resultant phases. From these results, L-PBF can be seen to be promising method for fabricating NiTi parts, particularly in demanding sectors such as aerospace, energy, and medical industry, facilitating intricate designs such as stents.

Chapter 5: Study of the effects of laser power and scanning speed on the microstructural morphologies and physical properties of L-PBF produced $Ni_{52.39}Ti_{47.61}$

Publication Status: Published

Agarwal, N., Monu, M. C., Selvam, K. T., Obeidi, M. A., & Brabazon, D. (2023). Study of the effects of laser power and scanning speed on the microstructural morphologies and physical properties of L-PBF produced Ni52. 39Ti47. 61. *Journal of Materials Research and Technology*, *27*, 8334-8343. https://doi.org/10.1016/j.jmrt.2023.11.146

5 Abstract

This study examined the effect of variations in the laser power and scan speed for 52.39at.%Ni-47.61at.%Ti samples produced via laser powder bed fusion (L-PBF). The laser power was varied between 150W and 180 W, the scanning speeds were varied between 500mm/s and 1000mm/s, and other process parameters were kept constant. The resulting microstructures and physical properties of the produced samples were evaluated. In particular, the phase type and phase transformation characteristics, composition, Vickers microhardness, and microstructures were examined. It was observed that variation in the mean microhardness and relative density were not significant at a constant scan speed of 1000 mm/s, regardless of the laser power value. Samples processed at a laser power of 180W (with all other parameters kept constant) exhibited a bimodal micro- and nano structures. It was found that the samples with bimodal microstructure had a higher lattice strain, extent of B2 phase, and higher phase transformation temperatures.

Keywords: Nitinol, 3D printing, phase transformation temperature, mechanical properties, microstructural analysis.

5.1 Introduction

Nitinol (NiTi), a shape memory alloy of titanium and nickel, is becoming a popular material of choice for the medical (stents, guidewires, etc.), robotics, aerospace, and automobile industries requiring precise deformation and recovery repeatedly [221]. Nitinol's versatility of its functional properties such as biocompatibility [177,222–224] and thermomechanical properties [122,225] has led its adoption in various cutting edge technologies and innovation. These unique properties are facilitated by the reversible phase transformation between austenite and martensite. Nitinol has the unique properties of superelasticity and shape memory effect. The superelastic behaviour of the nitinol component is highly influenced by the elemental composition [76,226,227], manufacturing techniques and post processing methods such as heat treatment [228,229]. The alloy elemental composition and stress conditions greatly affects the phase transformation temperature [40,41] and thus, the phase characteristics. The phase change in the Ni-Ti system does not occur at a certain temperature but over a range of temperatures as shown in the NiTi phase diagram [42]. Laser powder bed fusion (L-PBF) has been explored as a manufacturing technique for NiTi components with complex geometries and high dimensional accuracy [37,140]. The layer-by-layer deposition

facilitates the rapid melting and solidification process and repeated thermal cycling of the alloy. Thus, components fabricated by this technique may differ in their microstructural properties along with phase characteristics and thermomechanical properties [19,76,227].

Phase transformation behaviour is greatly influenced by the starting composition of the nickel as well as the final composition of the produced part after fabrication. There is a noticeable difference in the composition due to the nickel evaporation resulting from the processing via L-PBF. Increase in the phase transformation temperatures have been reported by several researchers for the samples processed with higher volumetric energy densities resulting in higher nickel evaporation [63,220,230]. A broader width of the transformation peak indicates the presence of precipitates. Studies have also shown that with same energy density, obtained with different combinations of laser power, scanning speed and hatch spacing being applied, can lead to different transformation behaviours [96,184]. The phase transformation is also highly dependent on the level of stress applied to the NiTi material. Residual stresses before the cold work as well as the precipitation of excess nickel in solution can generate stresses that can significantly affect the transformation [43,231].

Control of the laser power and scanning speed parameters of the L-PBF technique can in turn control the grain morphology [10,232] as well as temperature and size of the molten pool which is highly dependent on the input energy density. The repeated thermal cycles and high cooling rates of L-PBF creates heterogeneous and complex microstructures [233,234]. Several studies have reported that the microstructures, determined by the laser processing parameters, greatly influence the phase transformation behaviour [235–239]. Due to the temperature gradient and the solidification rates controlled by the laser processing parameters, the most observed structures are cellular dendritic, columnar dendritic and equiaxed. According to the Hall -Petch relation [240], grain type and size in metals and alloys determine the mechanical properties of the component such as toughness, strength and hardness. The layer wise deposition technique of L-PBF leads to anisotropic microstructures and sub-structures with grain formation in the built direction determined by the melting and solidification process [241–244]. NiTi components fabricated using L-PBF often exhibits complex microstructures which are completely inhomogeneous [245] with columnar grains along the built direction and micro-lamelle as reported by Nigito et. al. [246]. Hamilton et. al. [247] has also reported that the grains

exhibit columnar structures covering several layers corresponding to the maximum thermal gradient in the build direction. Previous studies have determined the complex nature of the microstructures formed resulting from the processing parameters. The present study presents the formation of unimodal and bimodal grains formed due to variations in the laser power and scanning speed within the L-PBF process for Ni-rich nitinol. The new understanding presented within this paper for how these structures form helps to fill this knowledge gap, allowing specific microstructures with resulting specific properties to be achieved.

5.2 Materials and Methods

Gas-atomised Ni-rich NiTi (52.39 at.% Ni) powder supplied by Fort Wayne Metals Ireland was utilised in this study. An Aconity MINI GmbH L-PBF printer equipped with a 200 W fibre laser at a wavelength of 1068 nm was used to fabricate the four sets of test samples with the dimensions of 5×5×6 mm. By varying the laser power and scan speed, four different processing parameters as summarised in **Table 5-1**, with distinct volumetric energy densities based on constant hatch spacing of 80 µm were adopted for fabricating the test samples. The layer thickness and laser spot size were also kept constant at 60 µm. The 0 ° - 90 ° bi-directional scanning pattern was adopted, as a compromise between desired mechanical properties and thermally residual stress [248]. Research-grade argon gas of 99.9996% purity was used as the inert gas environment.

Table 5-1: Processing parameters used to produce the cuboidal samples.

Sample ID	Laser Power (W)	Scanning Speed (mm/s)	Hatch Spacing (µm)	VED_H (J/mm^3)
S1	150	1000	80	31.25
S2	150	500	80	62.5
S3	180	1000	80	37.5
S4	180	500	80	75

The process parameters were selected on the criteria of attaining near-full density. The density of the fabricated samples was then confirmed/measured by Archimedes, using ethanol as the test fluid according to the standard ASTM B962-13 [249]. The measurements were repeated three times for each sample. To determine the critical phase transformation temperatures of the samples, Differential Scanning Calorimetric (DSC) analysis was performed using a TA Instruments® Discovery DSC2500 and the

transformation temperatures were calculated with the help of the tangent method according to the standard ASTM F2004 – 17 [204]. The tests were conducted in the temperature range of -100 °C and 150 °C at a ramp rate of 10 °C/min. TZero aluminium pan with TZero lids and a sample mass of around 20 mg were used to carry out the tests. A Bruker D8 X-ray Diffractometer was employed to carry out the crystallographic studies in the 2θ scan range between 10 °C and 100 °C. A Cu Kα source of a wavelength of 1.5406Å, and a step size of 0.01° at 8s/step were used for the XRD scans. Samples were cold mounted in epoxy resin, ground using silicon carbide papers from 80 to 4000 grit, and polished using diamond suspensions of 9, 6, 3 and 1 micron and an Alphacloth M. The polished samples were etched using an etchant comprised of 41 mL distilled water + 5 mL HNO_3 + 4 mL HF for 3-6 secs. A JEOL JSM-IT 100 InTouchScope scanning electron microscope (SEM) was utilised for micron- and sub-micron microstructural analysis at an accelerating voltage of 10 kV and a working distance of 9 mm. A Keyence-VHX2000E optical microscope was employed for the macrostructural analysis. Vickers microhardness testing was conducted using the Leitz MiniLoad 2® equipment, applying a test force of 981 mN and holding it for 20 seconds. For each sample, we performed five measurements at random locations across the sample surface. We maintained a minimum distance between indent locations equivalent to five times the diagonal distance of the indentation. Pyramidal indents were made on the polished surface for the measurement of the Vickers microhardness in accordance with the ASTM E92-17 standard [250].

5.3 Results and Discussion

5.3.1 Density analysis and Vickers microhardness results

The relative density and Vickers microhardness of the NiTi samples are comparatively shown in **Figure 5-1**. Achieving theoretical densities in L-PBF components is prohibitive because of inherent microstructural defects such as porosities from keyholing phenomena, pores due to gas entrapment, or micro-cracks due to residual stresses. Notwithstanding, Samples S1, S3, and S4 had relative densities > 99.5% while S2 had a slightly lower relative density at 97.9%. Importantly however, **Figure 5-1** shows that at constant laser power (P) of either 150 W or 180 W, reducing the scanning speed (S) from 1000 mm/s (S1 and S3) to 500 mm/s (S2 and S4) consistently led to a reduction in relative density. The same trend was observed in the hardness values which ranged from 250 to

300 HV0.1, with Sample S2 having the lowest hardness. Decreasing the scan speed to 500 mm/s at constant laser power increases the scan time per unit length, resulting in higher volumetric energy as calculated and shown in **Table 5-1**. This increase in volume energy fractionally increases the thermal energy during melt pool solidification, which in turn should lead to relative grain coarsening compared to the average grain size at 1000 mm/s. According to the classic Hall-Petch relation, a coarsening of grain size should lead to a decrease in hardness [251].

Although hardness and density are two different physical properties of a material and are not inherently linked to each other, some materials with high densities, such as metals, tend to have relatively high hardness values. This is particularly true for L-PBF processed NiTi alloys in the as-built condition as shown in **Figure 5-1** and in agreement with observations by Monu et al., [252]. This is because; (a) the rapid cooling rates of the L-PBF process [180,253,254] lead to fast melt pool solidification which results in finer recrystallised grains compared to grain sizes of conventionally manufactured components, (b) at a constant hatch spacing (H) value across a sample group, the H parameter significantly influences the intra-metallurgical bonding between the adjacent melt pool solidification substructures [255], and (c) the constant layer thickness (L) parameter influences the inter-metallurgical bonding between the built layers [182,256]. Thus, the close packing of atoms in a dense L-PBF processed NiTi leads to stronger interatomic or intermolecular forces, resulting in increased hardness in the as-built state/condition. An observation worth mentioning is that increasing the P from 150W to 180W (sample S1 and S3) but at a constant S of 1000 mm/s, did not affect the mean hardness and relative density values. Conversely, significant changes in mean hardness and relative density values of samples S2 and S4 are observed when P is changed but at a constant S of 500 mm/s. The measured microhardness range of the L-PBF processed nitinol samples in this study was 265 HV to 290 HV. Other researchers have found microhardness values below that of this range from other manufacturing process, also for Ni-rich compositions. As reported by Bhardwaj et. al [257]., the microhardness of austenitic NiTi (Ni-rich nitinol) processed by constrained groove pressing (CGP) is about 118 HV if water quenched and reaches a maximum of 206 HV after two CGP passes. This variation in hardness can be explained by the fact that microhardness is influenced by the combined effect of defects, grain size, and volume phase fraction at temperature of measurement (usually room temperature) as reported by Gao et. al. [79]. Further on,

it has been observed that the grain sizes, the different grain morphologies (i.e., unimodal, bimodal, or multi-modal sub-grain structures) and global grain size, affects hardness according to the classic Hall-Petch relation [251]. While conventional manufacturing methodologies like casting often generate unimodal sub-grain structures, the parametric nature of the PBF-LB manufacturing technique permits for microstructural tailoring by changing one or more process parameters as demonstrated in this current study. These microstructural features, phase characteristics, and further corroborating details on the density and microhardness will be elucidated in subsequent sections of the study.

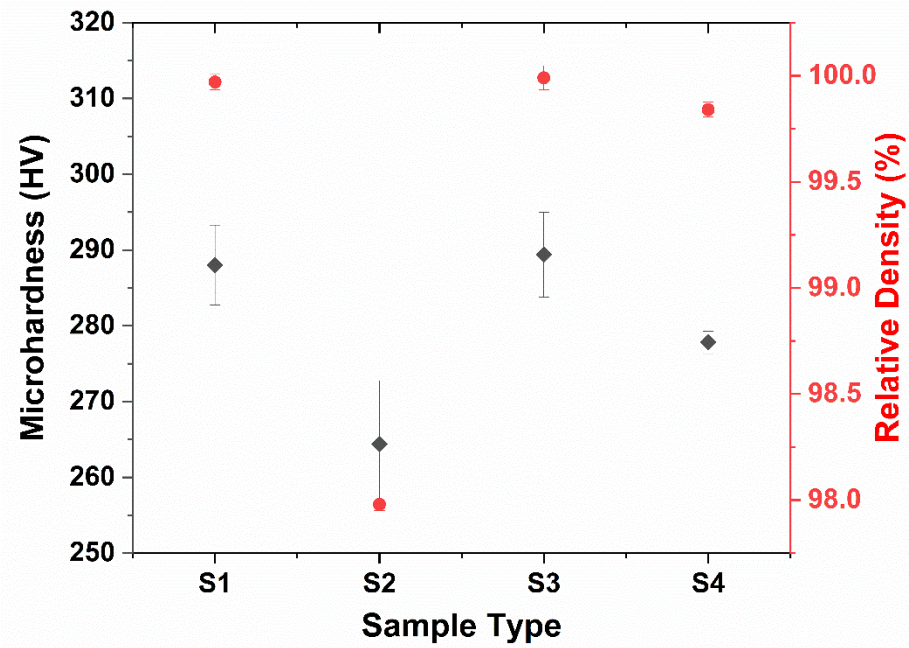

Figure 5-1: Density and Vickers microhardness of additively manufactured samples.

5.3.2 Effect of process parameters on resulting melt pool macro-structures

The L-PBF process involves the remelting and solidification process due to the layer-by-layer deposition of the material which governs the grain formation and growth. It significantly influences the melt pool solidification dynamics and the resulting metallographic features (i.e., macro-and micro-structures) [258]. Typical macro-features observable with the naked eye or low magnification optical microscopy include track solidification patterns, pores (porosity), lack of fusion defects, surface hillocks due to balling phenomena [259], and features of extreme residual stresses such as delamination, warpage, and outright build failures [9]. For the L-PBF processed Ni-rich samples in this study, the macro-features are characterised by a few pores and chessboard (checkerboard or grid) patterned macrostructure as shown in **Figure 5-2**. The observed checkerboard

substructures are characteristic of the laser-powder interaction paths due to the bi-directional scanning patterns when the angular rotation of laser scan vectors between successful layers is 90° [260]. Meanwhile, porosity inhibits the attainment of full theoretical density (refer to **Figure 5-1**). Well established in the literature, pores form due to the collapse or inability of the molten melt pool to fill a topologically depressed cavity of the melt pool as the laser beam moves away [66]. This topologically depressed cavity is created in the melt pool just beneath the laser beam due to recoil pressure effects [66]. The depth of the depressed cavity increases as the energy density increases, and thus, the tendency of pore (void) formation in the propagation path of the laser beam is increased. In corroboration with discussions in **Section 5.3.1**, the density of the samples fabricated at higher energy density [(S2 at P = 150W and S4 at P = 180W) at constant slow S of 500 mm/s] were lower than S1 and S3 fabricated at the lower energy density. In agreement with the observations by Guo et al. [261], they reported a decrease in porosity and pore count in L-PBF processed NiTi alloys if S increases from 500 mm/s to 1000 mm/s.

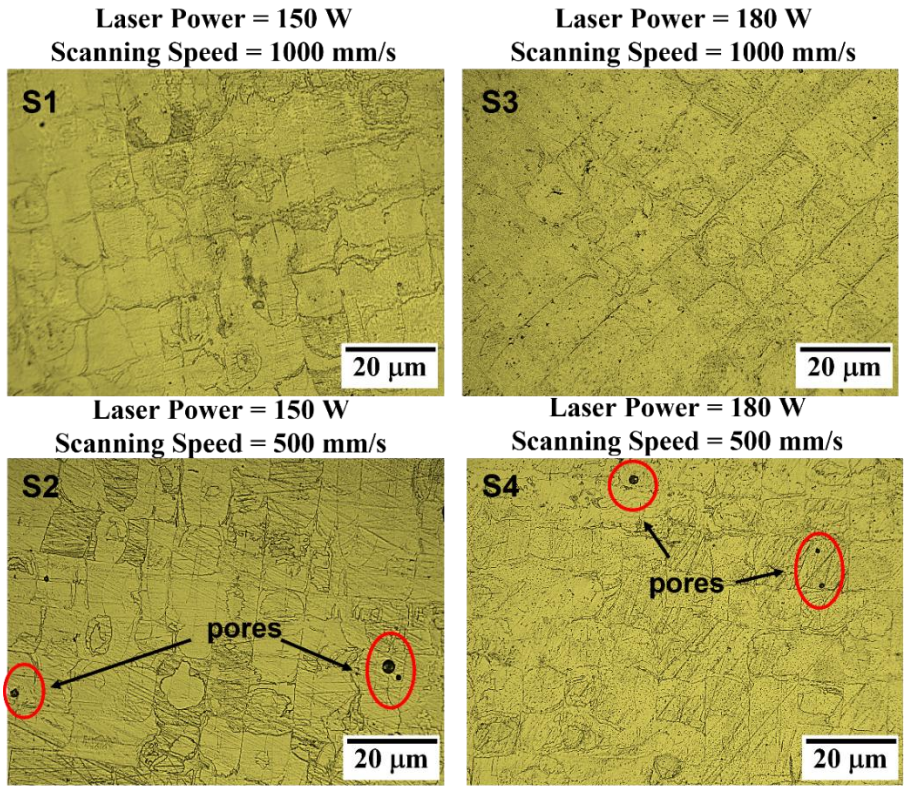

Figure 5-2: Representative micrographs showing the effects of laser power (P = 150 and 180 W) and scanning speed of (500 mm/s and 1000 mm/s) on the checkerboard macro-features of the L-PBF processed Ni-rich NiTi samples.

5.3.3 Effect of processing parameters on unimodal and bimodal grain

Higher magnification of the microstructure reveals distinct microstructural features as shown in **Figure 5-3**. Specifically, at constant power, P of 150 W, decreasing the S from 1000 mm/s to 500mm/s (**Figure 5-3**a and c respectively) resulted in unimodal (i.e., relatively uniform, or one-sized) B2 austenite grains. Comparatively, the grain sizes for sample S1 fabricated at S = 1000 mm/s (**Figure 5-3**a) are significantly smaller, but very coarse for sample S2 fabricated with the same P but at S = 500 mm/s (**Figure 5-3**c). Conversely, bimodal grain structures (i.e., distinctly coexisting coarse and fine grains) are observed at a higher constant P of 180 W for both scanning speeds (**Figure 5-3**b and d). Like the observation in **Figure 5-3**c, the bimodal grain sizes are relatively larger in sample S4 fabricated at S = 500 mm/s. The advantage of bimodal-grained components is that it improves strength-ductility synergy, and structural efficiency in NiTi components [262,263].

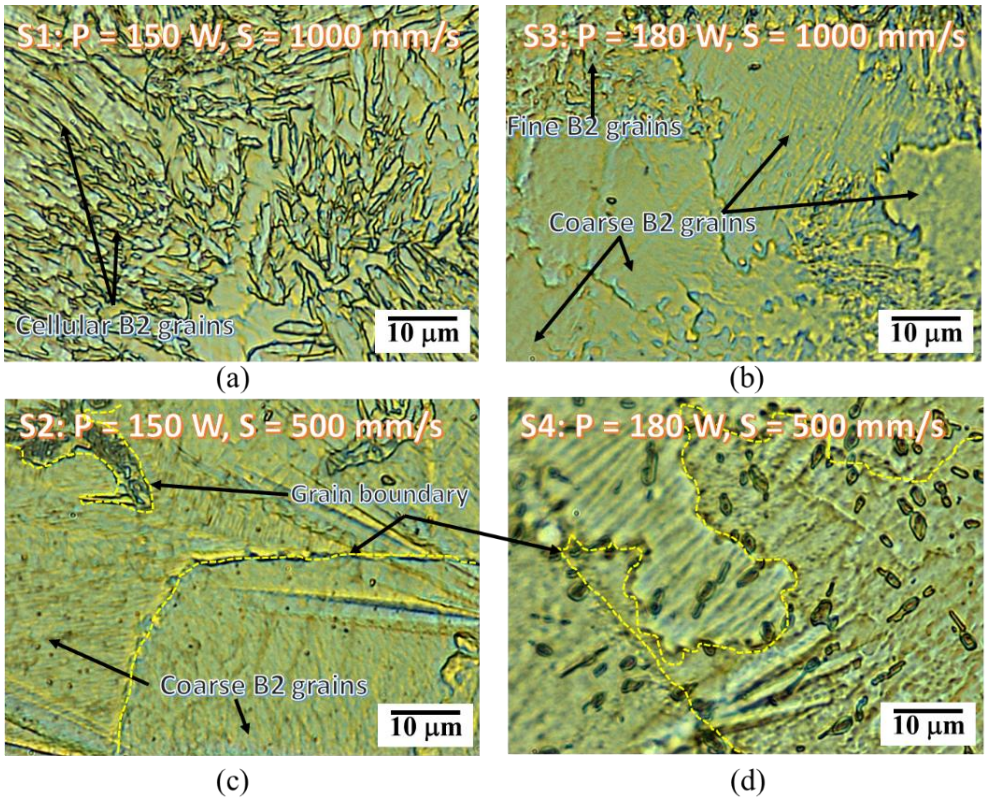

Figure 5-3: Representative micrographs depicting the characteristic grain structures due to effect of different laser powers; (a) fine unimodal cellular austenite (B2) grains for P = 150 W, and (b) bimodal B2 grains for P =180 W at constant scanning speed of 1000 mm/s, (c) very coarse unimodal B2 grains for P = 150 W, and (b) bi-modal B2 grains for P =180 W at constant scanning speed of 500 mm/s.

5.3.4 Mechanism of unimodal and bimodal grain effects due to scanning speed and laser power

Fundamentally, the increase in grain size at S = 500 mm/s (S2 and S4 shown in **Figure 5-3**c and d) is due to the influence of the increased scan time per unit length (i.e., laser beam resident time) on the directional melt pool solidification dynamics experienced during L-PBF processing [71], and the cellular and primary dendritic arm spacing, λ_1. The Hunt model given in Eq. 7 provides the relationship between λ_1 and solidification parameters (growth rate, V and temperature gradient, G).

$$\lambda_1 = 2.83 \left[\frac{m\,(k-1)D\Gamma C_0}{V}\right]^{0.25} G^{-0.5} \tag{7}$$

where m is the liquidus slope, k is the solute partition coefficient, C_0 is the solute concentration, and D is the liquid solute diffusivity. Γ represents the Gibbs–Thomson coefficient for determining the structural melting of a solid particle of diameter x in its own liquid, and expressed as [264]:

$$\Gamma = \Delta T_m(x) = T_{mB}\frac{3\sigma_{sl}}{H_f \rho_s r} \tag{8}$$

where T_m is the melting point of the crystal size (x), T_{mB} represents the bulk melting temperature (1310 °C for NiTi), σ_{sl} is the solid-liquid interface energy (per unit area), H_f is the bulk enthalpy of fusion per gram of material (NiTi in this study), ρ_s is the density of solid (6.45 g/cm^3 for NiTi), and r is the radius of the crystal. From Eq. 7 and 8, most of the parameters are either constants or have the same material-dependent variable since all samples in this study were fabricated from the same powder bed of Ni-rich NiTi. Thus, Eq. (7) can be simplified as [265]:

$$\lambda_1 = A(G\nu)^{-n} \tag{9}$$

Where ν represents the cooling rate, which ranges from $10^2 – 10^7$ K/sec for a typical laser scan speed of 1 m/s during a L-PBF process [180,253,254]. A and n are material-related constants, for which n > 0. Meanwhile, the relationship between cooling rate (ν) and laser scan speed S in the L-PBF process (synonymous to weld travel speed, V_d) is expressed as [266]:

$$\nu = S\cos\alpha \equiv V_d\cos\alpha \tag{10}$$

where α represents the angle between the laser scan direction (or travel direction in conventional welding) and the normal to the melt pool boundary. Substituting Eq. 10 into Eq. 9 gives:

$$\lambda_1 = A(GScos\alpha)^{-n} \tag{11}$$

From eq. (11) It can be deduced that primary cellular or dendrite spacing, λ_1 decreases with increasing scan speed S. This explains the observed unimodal fine B2 grains at S = 1000 mm/s (S1), the coarse unimodal B2 grain structures at S = 500 mm/s (S2), and partially explains the presence of coarse grains in bimodal microstructures presented in **Figure 5-3**.

At higher laser power, P = 180 W (**Figure 5-3**b and d), bimodal microstructures can be observed for both scanning speeds. The bimodal grain size distribution is explained by a superposition of Ostwald Ripening (OR) effects resulting in relatively large grains, and the inherent and concurrent formation of relatively small grains during L-PBF processing compared to casting or welding processes [267]. For an ideal hatch spacing, H to laser spot size, f ratio during the L-PBF processing, OR occurs via the dissolution of melt pool matter at regions of the inherently fine grains due to the rapid cooling rates and recrystallization effects associated with the L-PBF process (unimodal fine grains), and the re-precipitation at regions with a large radius of grain curvature as illustrated in **Figure 5-4.** It is mathematically expressed as:

$$S_r = S_\infty \exp\left(\frac{2\gamma V_m}{RT_r}\right) \tag{12}$$

where V_m is the molar volume of the solute, γ is the interfacial tension, R is the gas constant (8.31 $JK^{-1}mol^{-1}$), S_∞ is the solubility of the solute in the continuous phase for a crystal with infinite curvature (i.e., a planar interface), and S_r is the solubility of the solute when contained in a spherical nucleus (grain) of radius r. In polycrystals, the solubility of dispersed grain nuclei is influenced by the concentration gradient between small and large grain nuclei. As such, larger grains grow at the expense of the smaller ones. At steady state conditions, the rate of grain growth due to OR (Ω_3) is given by the Lifshitz and Slyozov theory [268] Eq. 13.

$$\Omega_\alpha = \frac{dr^\alpha}{dt} = \frac{8\gamma V_m S_\infty D}{9RT_r} \tag{13}$$

where for diffusion-controlled ripening across a continuous phase, $\alpha = 3$ (note that $\alpha = 2$ for permeation-controlled ripening), D represents the diffusion coefficient of atoms at the solid-liquid interface through the continuous phase, and all other terms represent same parameters as in Eq. 6. The study by Thampy et al., [181] demonstrates that in L-PBF processing, increase in laser power (all other parameters constant), linearly decreases meltpool cooling rates (i.e., rate of undercooling). Therefore, the increase in laser power from 150 W to 180 W in this study could have resulted in a low rate of undercooling. This results in a low-temperature gradient (dt = G in Eq.(10)), an increase in time available for atomic diffusion (D), which then favours the coalescence and growth of grains (dr^{α}). Thus, the rate of grain growth due to OR increases competitively with the inherently fine grains due to the L-PBF process compared to casting or welding processes. Bormann, et al., [267] also observed bimodal microstructures in L-PBF processed NiTi by increasing laser power.

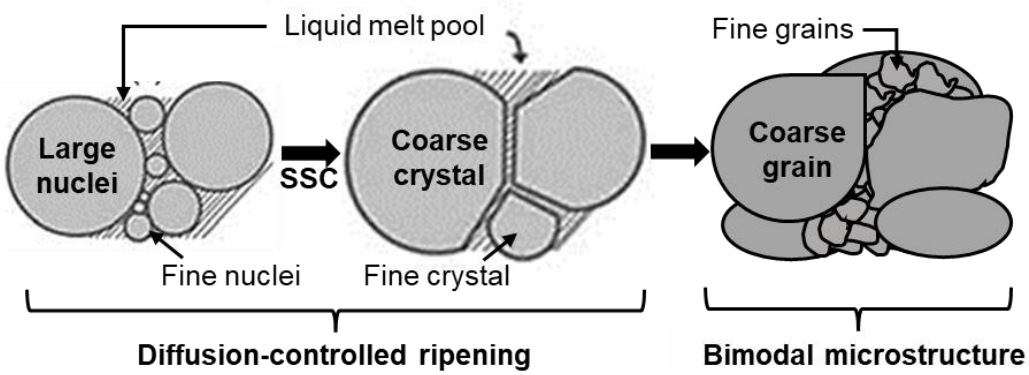

Figure 5-4: Formation of bimodal grain distribution due to Ostwald-ripening mechanisms for grain shape accommodation, neck growth and solution re-precipitation; with steady-state conditions (SSC), adapted from Huo et al. [269].

5.3.5 Unimodal and bimodal sub-grain morphologies

As already established in Sections 4.4.3 and 4.4.4, the observed unimodal and bimodal grain morphologies are highly dependent on the input power and the scanning speed of the laser. Upon closer examination of **Figure 5-3**, in-grain orientation gradients are visible. This suggests the formation of, and the existence of repetitive sub-grain structures in the grains (i.e., substructures). Further examination by SEM was conducted of these sub-grains for which representative micrographs are shown in **Figure 5-5**. At constant P

of 150 W, **Figure 5-5** a reveals that the sub-grains are predominantly coarse columnar dendritic at S = 1000 mm/s, but fine cellular at S = 500 mm/s (**Figure 5-5**c). Meanwhile, the bimodal microstructures at constant P of 180 W at S = 1000 mm/s consisted of fine cellular substructures in the coarse B2 grains and a combination of equiaxed and cellular substructures in the fine B2 grains (**Figure 5-5**b). At constant P = 180 W at S = 500 mm/s, the coarse B2 grains consisted of coarse planar substructures, and equiaxed substructures in the fine B2 grains as shown in **Figure 5-5**d.

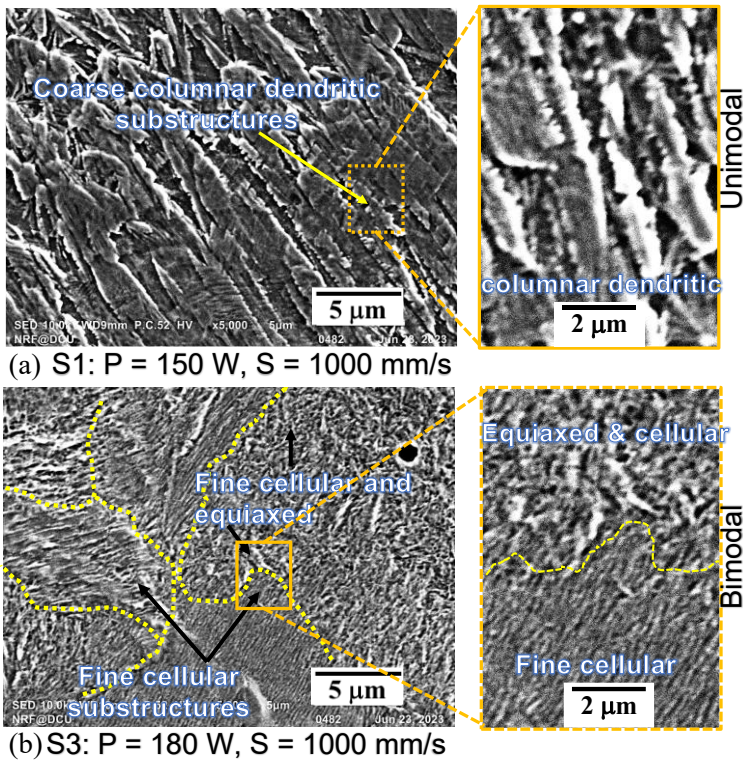

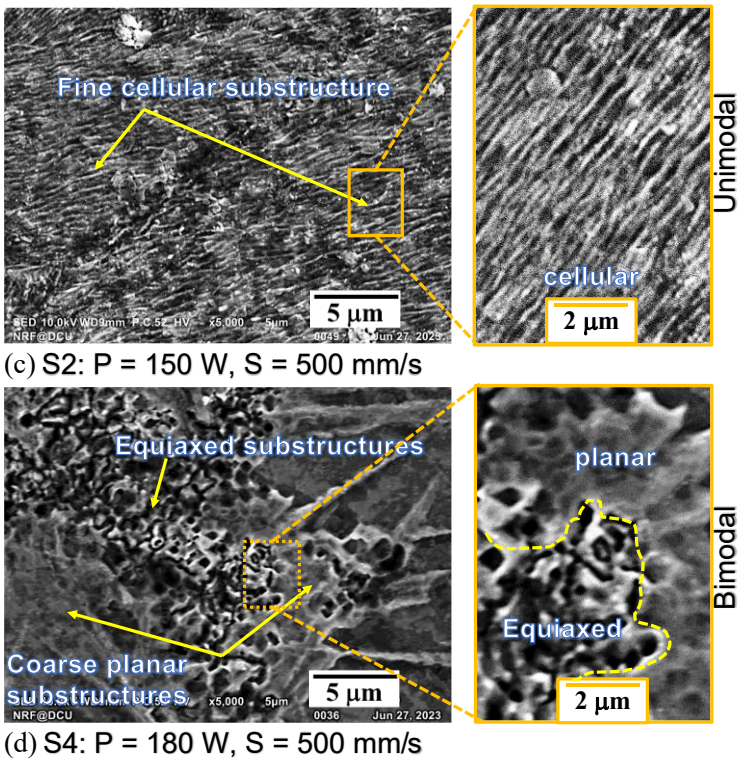

Figure 5-5: Representative brightfield SEM micrographs showing the effect of laser power (P) and scanning speed (S) on subgrain morphologies; (a and c) substructures in unimodal B2 microstructures (P =150 W and S = 1000, and 500 mm/s), and (b and d) substructures of the bimodal microstructures at P =180 W and S = 1000 mm/s, and 500 mm/s.

The presence of unimodal and bimodal substructures, as shown in **Figure 5-5**, within the same samples exhibiting both unimodal and bimodal grain morphologies suggests that similar mechanisms govern solidification and grain formation. Complementing the analytical justifications outlined in **Section 5.3.5,** the respective subgrain types observed in **Figure 5-5** can be attributed to the interplay between thermal gradients (G) and interface velocity or solidification growth rate (R). This relationship is commonly represented as the solidification map or G-versus-R map, as illustrated in **Figure 5-6** [270].

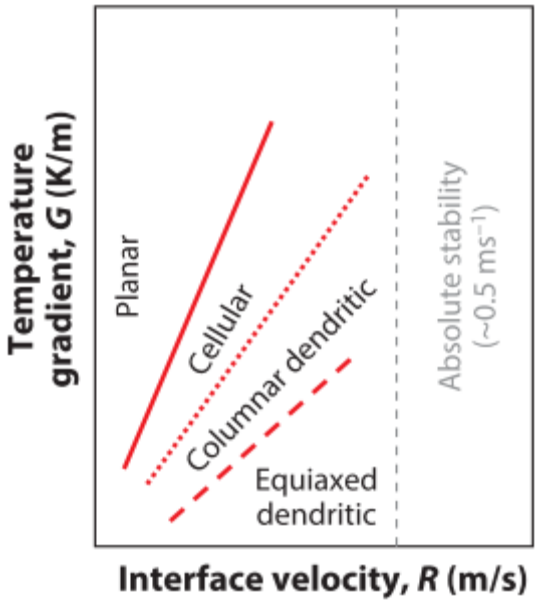

Figure 5-6: Schematic illustration of substructure formations (solidification modes) based on solidification map [68].

It's important to note that determining the precise G and R conditions necessitates either analytical or numerical methods, which rely on the mean melt pool temperature field (i.e., temperature data integrated over the meltpool depth) resulting from the laser process conditions, P and S [81]. However, delving into these intricacies falls beyond the purview of the current study. Nevertheless, our future endeavours include leveraging the in-situ melt pool temperature monitoring capabilities of the L-PBF process via infrared pyrometers. This will enable us to compile and analyse the melt pool temperature field data, subsequently correlating it with G-R conditions—a promising avenue for further research.

5.3.6 Effect of laser power and scanning speed on phase characteristics

The consequence of the observed and discussed grain and subgrain morphologies in **Sections 5.3.3** to **5.3.5** is that it influences the phase characteristics and lattice (micro) strains. The X-ray diffraction (XRD) spectra of the as-printed NiTi samples are presented in **Figure 5-7**a-b. The peak reflections were indexed using the B2 NiTi (96-110-0133) crystal structure obtained from the Crystallography Open Database (COD) [271,272]. In all samples, the B2 cubic planes of (101), (200), and (211), corresponding to 2θ angles of approximately 42.36°, 61.46°, and 77.48°, respectively, were observed. This indicates that the dominant crystal structure after the L-PBF processing is the B2 cubic phase (NiTi austenite).

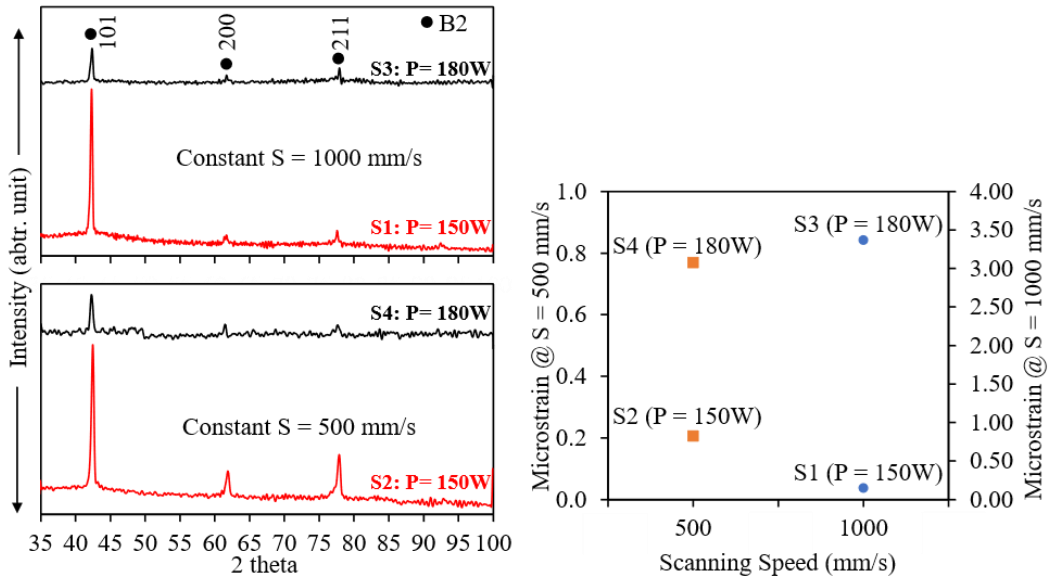

Figure 5-7: Effect of 150 W and 180W laser power, P on the diffraction patterns of NiTi samples fabricated at scanning speeds, S of (a) 1000 mm/s, and (b) 500 mm/s; and (c) the calculated microstrains (με) developed in the samples.

Comparing the peak intensities in **Figure 5-7**a-b, it can be observed that increasing the laser power from 150 W to 180 W resulted in a significant reduction in the intensity of all the B2 peaks. This trend is evident for scanning speeds (S) of both 1000 mm/s (**Figure 5-7**a) and 500 mm/s (**Figure 5-7**b). The decrease in the relative peak intensities (height) at higher laser power (180 W for S3, and S4) indicates the presence of larger micro (lattice) strains, which often result in higher residual stresses within the microstructure [252,273].

From **Table 5-1** previously presented, it can be observed that for the same hatch spacing (H) and scanning speed (S), the relative energy input per volume of powder deposited in the powder bed during the L-PBF process increases as the laser power increases [274]. As demonstrated in the study by Monu, et al., [252] this increase in volumetric energy density leads to a decrease in B2 peaks due to higher internal residual stresses in the as-built parts. While direct measurement of residual stress is beyond the scope of this study, the microstrains were instead calculated from the XRD spectra to investigate the significant decrease in the XRD peak heights at higher laser power. For this, Rietveld refinement analysis was performed to determine the Full Width at Half Maximum (FWHM) for the (101), (200), and (211) B2 cubic planes. The microstrains were calculated using the relationship: $\varepsilon_{(\mu)} = \frac{\beta}{4 \tan \theta}$ [275]. **Figure 5-7**c illustrates that the

calculated microstrains are highest for samples fabricated at a higher laser power of 180 W (i.e., S3= 3.3708 and S4 = 0.7684). Thus, supporting the role of higher lattice strains (and the ensuing residual stresses) in stunting the B2 phase reflections. In this work, instrumental broadening was negligible as the Bruker system used for the measurement has a large goniometer radius resulting in the instrumental contribution to peak broadening be minimal.

Per Khorsand, et al., [276], various factors, including microstructural sub-structures, residual stresses, process-induced lattice strains, dislocations, and variations in elemental composition, exert an influence on the phase characteristics. Specifically, when considering the microstructural aspects, samples S3 and S4, characterized by bimodal microstructures, displayed distinctive features such as reduced XRD peak intensities and larger lattice strains. Prior research has consistently reported that lattice strain, as determined from X-ray broadening, tends to increase as grain size decreases, and the maximum lattice strain rises with the reduction in minimum grain size [277]. While this principle generally holds for samples with predominantly unimodal microstructures, it does not apply in the same way to samples S3 and S4 in this study, with pronounced bimodal microstructures prevalent. This deviation can be attributed to the complex strain fields arising from the prevalent dual-sized grains within the microstructures.

5.3.7 Effect on phase transformation temperatures

The determination of phase transformation temperatures was carried out through DSC analysis, and the response curves for both the samples and the feedstock powder are presented in **Figure 5-8**. Each DSC response curve represents a distinct phase transition, delineating its respective starting and ending temperatures. Comparatively, **Figure 5-8**a reveals that the peaks of the DSC response curve for the feedstock powder are positioned further to the right. This positioning signifies higher critical transformation temperatures when compared to the L-PBF processed samples. The critical transformation temperatures, including Martensite start (Ms), Martensite finish (Mf), Austenite start (As), and Austenite finish (Af), are highest for the powder, as summarized in **Table 5-2**.

Although the DSC curves for samples S1 and S3, both fabricated at S = 1000 mm/s, display minimal differences at different laser powers of P = 150W and 180W (as depicted in Figure 8b), a notable contrast emerges when examining the DSC curves for samples S2 and S4. These samples, produced at S = 500 mm/s for both P = 150W and 180W,

exhibit a distinct pattern consisting of a primary peak and a smaller hump (i.e., two endothermic peaks) during the heating phase. These double endothermic peaks typically indicate the presence of the R-phase, suggesting a two-step reverse transformation from B19' $\rightarrow$ R $\rightarrow$ B2 on heating [200,278]. It's worth highlighting that the humps are relatively small, rendering it challenging to establish a baseline for extracting meaningful R-phase critical temperatures as per the intersecting tangent method outlined in ASTM F2004 – 17 [204].

Nonetheless, the implications of these humps are significant. They lead to lower A_f temperatures for the Samples S2 (7.19 °C) and Sample S4 (13.31 °C) in comparison to those of samples S1 and S3, as summarized in **Table 5-2**. In summary, irrespective of the processing parameters adopted and the resulting microstructural states, it's noteworthy that all the as-printed samples in this study exhibit A_f temperatures below room temperature. This observation suggests that the L-PBF process and the parameters explored herein can be effectively employed to fabricate near-fully dense Nitinol for superelastic applications, such as in the production of stents.

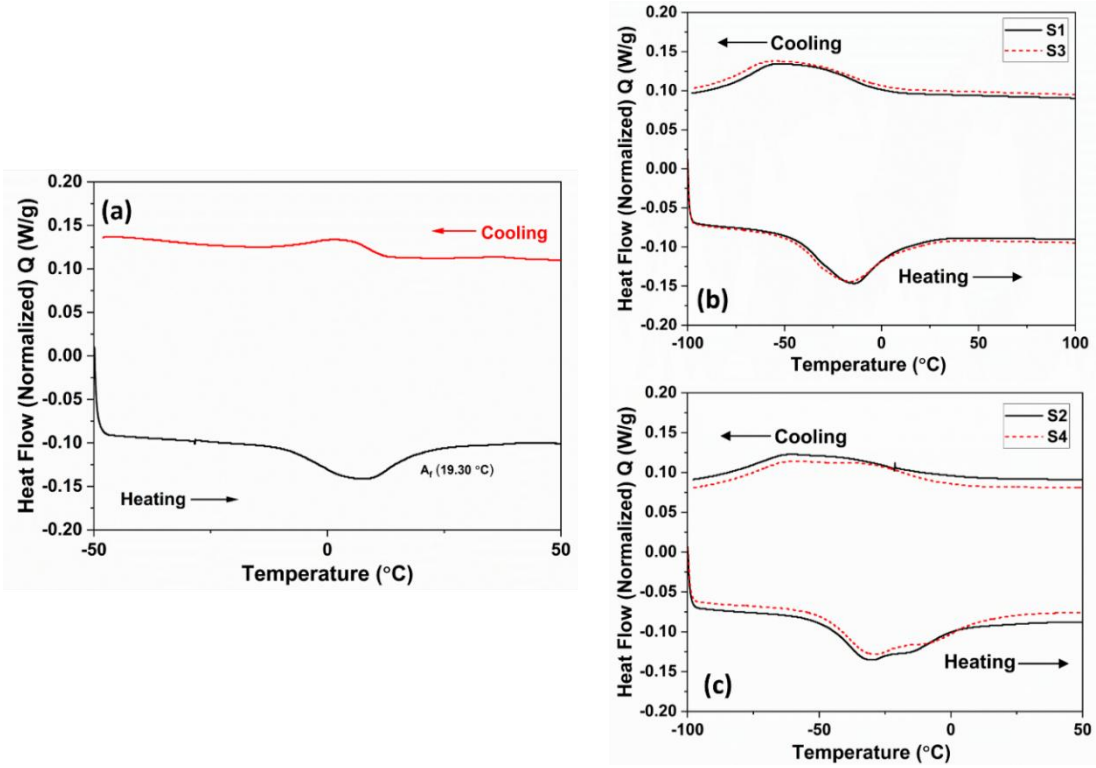

Figure 5-8: DSC phase transformation response curve of (a) pre-alloyed NiTi powder, (b) fabricated samples at a laser power of 150W, and (c) laser power of 180W, with the same scan speeds of 500 mm/s and 1000 mm/s respectively.

Table 5-2: Critical phase transformation temperatures from DSC.

Sample ID	Martensite Start M_s (°C)	Martensite Finish M_f (°C)	Austenite Start A_s (°C)	Austenite Finish A_f (°C)	M_s - M_f (°C)	A_f - A_s (°C)
S1	-0.91	-79.64	-44.41	12.45	78.73	56.86
S2	2.24	-84.62	-48.18	7.19	86.86	55.37
S3	0.28	-76.27	-43.99	17.44	76.55	61.43
S4	-2.62	-82.07	-48.88	13.31	79.45	62.19
Powder	12.62	-5.85	-8.70	19.30	18.47	28.00

As evident from **Figure 5-8**, the fabricated samples exhibit broader peaks in both cooling and heating cycles when compared to the virgin powder. This broadening of the peaks signifies the transformation temperature interval or width (TTI), which is quantitatively determined by the difference between the relevant start and finish transformation temperatures. As summarised in **Table 5-2**, the broad TTI in the as-built samples indicates that the phase transformation or transition takes place over a wider temperature range, compared to the virgin powder feedstock which has a TTI of 18.47°C and 28.00°C. This phenomenon could be attributed to the observed microstructural inhomogeneities and changes in chemical composition in the fabricated samples, in contrast to the gas-atomised virgin powder.

On the subject of chemical composition, Li et al. [279] and Sadrnezhaad [139], reported that the phase transformation temperatures and intervals were highly dependent on the composition of Ni in the NiTi matrix. This is depicted in **Figure 5-9**, which shows the variation in atomic percentages of nickel, determined from EDX. The nickel content decreases with lower scanning speeds of 500 mm/s (observed in Samples S2 and S4) for both laser power settings. Similarly, the nickel content decreases with an increase in laser power for the same scan speeds. This suggests that that higher laser power and extended resident time of the laser beam pass at slower scanning speeds, result in increased nickel evaporation from the NiTi matrix as supported by other studies [40,64,280]. In a broader context, this nickel evaporation correlates with an increase in volumetric energy input, calculated based on hatch spacing and denoted as VED_H. Specifically, an increase in

VED_H. results in increased nickel evaporation (decreased Ni content) as shown in **Figure 5-9**.

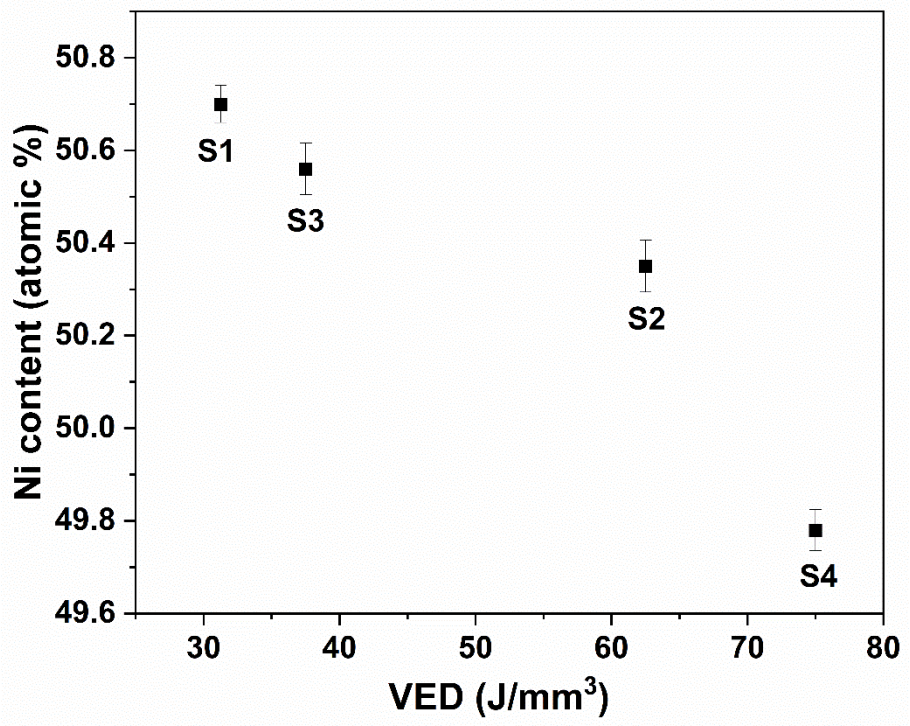

Figure 5-9: Relationship between the sample nickel content and volumetric energy density.

5.4 Conclusion

The purpose of this work was to examine the effects of laser power (P = 150 W and 180 W) and scanning speed (S = 500 mm/s and 1000 mm/s) on the physical characteristics and microstructural morphologies of Ni-rich nitinol components that were produced using L-PBF. Investigations were conducted on phase characteristics, composition, density, Vickers microhardness, and microstructure. The following conclusion is drawn from the data and findings:

a. Sample density ranged from 97.9% to 99.5%, while microhardness ranged from 250 to 300 HV0.1. However, at a constant S of 1000 mm/s, P of either 150W or 180W did not affect the mean hardness and relative density values. Conversely, a P of either 150 W or 180 W and a constant S of 500 mm/s, lower mean hardness and relative densities were recorded.
b. Scanning electron microscopy revealed that grain sizes were relatively larger in samples processed at S of 500 mm/s, regardless of the P. This is attributed to

increased scan time per unit length (i.e., laser beam resident time) at S = 500 mm/s, according to the scanning speed - primary cellular or dendrite spacing, λ_1 defined by $A(GS\cos\alpha)^{-n}$.

c. All samples processed at P =180 W exhibited bimodal grains and subgrain microstructures due to the superposition of Ostwald Ripening (OR) effects resulting in relatively large grains, and the recrystallised fine grains inherent of the L-PBF process at higher P. These bimodal-grained samples displayed also exhibited stunted B2 austenite peak intensities and larger lattice strains. These samples also exhibited dual endothermic transformation peaks on heating (transformation from martensitic to austenitic phase), higher A_f temperatures of 17.44 °C and 13.31 °C, and larger transformation temperature intervals of 61.43°C and 62.19 at S = 1000 mm/s and 500 mm/s respectively.
d. On the other hand, all samples processed at P = 150W exhibited unimodal grains and sub-grain microstructures, with higher B2 austenite peak intensities, relatively smaller lattice strains, and single endo-and exo-thermic transformation peaks.
e. The observed nickel evaporation increased with increased equivalent volumetric energy density. At the higher scanning speed of 1000 mm/s, the nickel content decreased from 50.7at.% to 50.56at.% with the increased power of 150W to 180W. The nickel content decreased from 50.35at.% to 49.78at.% when the scanning speed was decreased to 500 mm/s.

This work has clarified further the impact of just varying the laser power and scan speeds on the microstructure and physical characteristics of L-PBF treated samples, but it has also shown that these L-PBF process parameters are appropriate to produce stents. This is because all the resulting Af values were below room temperature, indicating that this parameter set is adequate for producing austenitic NiTi materials, such as stents, regardless of the degree of nickel evaporation arising from the process parameters.

Chapter 6: Influence of processing parameters on the corrosion resistance of additively manufactured nitinol parts for biomedical applications

Publication Status: Published

Agarwal, N., Gallagher, K. A., Carton, J. G., Brabazon, D., & Obeidi, M. A. (2024). Influence of processing parameters on the corrosion resistance of additively manufactured nitinol parts for biomedical applications. *Results in Materials*, 100536. https://doi.org/10.1016/j.rinma.2024.100536

6 Abstract

The usefulness of additively manufactured (AM) nitinol and Ti6Al4V parts for the aerospace, automotive, machine and tooling, and biomedical industries depends on how well they withstand corrosion. AM is a manufacturing process that makes it possible to create intricate geometries at a reasonable price. Although significant progress has been made in decreasing metal corrosion, not much research has been done on optimizing input processing parameters to lower corrosion rates. Unique phase structures and preferential evaporation of alloying components might arise because of the melting and quick re-solidification that take place during additive manufacturing. This study looks at how processing parameter changes impact the metal parts made by laser-powder bed fusion (L-PBF) in terms of their ability to resist corrosion in a bodily environment. Electrochemical testing was used to conduct the research at a body temperature of 37°C in both Hanks and Ringers solutions. The findings suggest that an increase in laser power during AM improves the passivation layer of the metal. Furthermore, compared to nitinol, Ti6AL4V exhibits a greater corrosion resistance. When a smaller hatch distance and lower laser beam strength were used, the nitinol sample's susceptibility to corrosion was reduced. This study demonstrates how the corrosion resistance of metal parts made by additive manufacturing can be increased by adjusting the laser powder bed fusion processing parameters in a bodily environment.

Keywords: Corrosion resistance, Passivation layer, EIS, Cyclic Polarization, Processing Parameters

6.1 Introduction

Nitinol, a shape memory bimetallic alloy, is suitable for diverse fields of implantation from cardiovascular to orthopaedics due to its mechanical compatibility with living tissues [42,109,281]. The superior performance exhibited by nitinol makes it a suitable material candidate in energy [282], transportation [283,284], aerospace [179], and automobile industries [285]. The higher content of nickel is constantly challenged for biocompatibility due to its toxicity and allergic effects [13,122]. Titanium oxide is formed as a protective layer on the surface. Optimal thickness and chemically homogeneous surfaces protect nitinol against corrosion and Ni-ion release. Testing to ensure low rates of corrosion and metal ion release is necessary for implantable medical devices to be reliable over the long term. The device's structural integrity may be compromised by corrosion, and the emission of metal ions has been linked to negative

immunological reactions. The most used implant material is Ti-6Al-4V exhibiting good corrosion resistance, toughness, high strength, and low density. Although it has good mechanical properties, Ti-6Al-4V has a higher elastic modulus and higher stiffness than that of human bone which could potentially lead to implant failure [286,287]. Studies have also revealed that the emission of aluminum and vanadium ions from the alloy, Ti-6Al-4V, may cause diseases such as peripheral neuropathy, osteomalacia, and Alzheimer's disease [288,289]. The corrosion resistance of nitinol falls in between that of Ti-6Al-4V and SS316. So, the effectiveness regarding biocompatibility and corrosion resistance can be significantly improved in nitinol implants by the formation of a thin protective layer of titanium oxide coating.

Additive manufacturing (AM) can produce complex geometric shapes that can allow cells to easily dissipate into the part allowing for complete cell function [290]. The AM process allows the possibility of producing parts at a lower cost with shorter production time and minimal waste [55,291]. One limitation to AM includes the size of the print, though while medical parts will not be significantly large prints, their microstructures can become weaker. Poor surface quality may be exhibited after the part is printed and laser, chemical, electrochemical, or mechanical polishing may be required. The phases and microstructures that are formed during the AM process govern the corrosion behavior of the part depending on the grain distribution, grain size, and even the orientation of the phases. Nickel evaporation is a common result of the AM process due to the laser energy input. However, using a higher concentration of nickel in nitinol would be useful to compensate for the nickel loss to produce the part of the desired chemical composition required for the medical device.

Few studies have been performed on orthodontic nitinol wire under different strain conditions to understand the effect of stress-induced martensite on corrosion resistance. Rondelli et al. [292] investigated the effect of corrosion under different strains (0 - 6 %) in saline and 0.9 % NaCl solution. They concluded that the pitting potential and general corrosion resistance of the material remained unaltered. A different study by Pun et al. [293] with orthodontic wires at different temperatures closer to austenite start, austenite finish, martensite start, and finish temperatures in artificial saliva supports similar findings. They concluded that the corrosion rate at room temperature for austenite and martensite phases remains comparable. However, corrosion at 45° C resulted in increased corrosion of the martensite phase. Chakraborty et al.[294] investigated the effect of laser processing (2 -11 J/mm^2) on nitinol (austenite phase) and reported the corrosion

behavior. They concluded that processing at lower energy density resulted in pure martensite and correspondingly low corrosion resistance. While processing at medium energy density it resulted in the formation of martensite phase with rich titanium and nano-sized intermetallic phases increasing the overall corrosion resistance of the material. This supports that post-processing could fine tune the surface property with preferred modulus value and corrosion resistance. In a recent study conducted by Nagaraja et al. [295], pitting corrosion tests were conducted in phosphate buffer solution on three different microstructural purity NiTi samples produced by standard VAR (vacuum arc re-melting), H.P. VAR and VAR/EBR. No significant difference was observed in pitting corrosion between the samples however, electropolishing was found to improve the corrosion resistance. In a study conducted by Carroll et al. [296], it was reported that the corrosion performance was better for the samples tested in Ringers solution than other bodily fluids such as 0.9% NaCl solution. Guo et al. [97] reported that the addition of rare-earth CeO2 to NiTi improved the corrosion performance by forming NiCe precipitates when tested in 3.5% wt. NaCl solution. Limited studies have been conducted to evaluate the corrosion resistance of NiTi especially in bodily fluids and temperatures.

Several studies have shown that additively manufactured Ti-6Al-4V parts have good corrosion resistance properties. As reported by Wu et. al. [297], the formation of the coarser grains during the AM process of Ti-6Al-4V leads to better corrosion behavior in the build direction when tested in NaCl. Similar studies were conducted by Chiu et. al. [298] and Chen et. al. [299] investigating the corrosion behavior of Ti-6Al-4V AM parts in the build direction using NaCl as the electrolyte.

The electrochemical behavior and corrosion performance of both NiTi and Ti-6Al-4V AM components in Hanks and Ringer's solution at 37°C body temperature is evaluated for the first time in this study. For the first time, a comparison of the two distinct materials (NiTi and Ti-6Al-4V) demonstrating the corrosion behavior of the AM parts has been published. The study's selected parts were produced with varying printing processing settings. These factors affect the final element composition of the prints, and in-vitro tests were used to determine the best combination of these factors using both Electrochemical Impedance Spectrometry (EIS) and Cyclic Polarization (CP) [298,300].

6.2 Materials and Methods

Nitinol and Ti-6Al-4V test samples were processed using the 3D metal printer, Aconity MINI GmbH from Aachen, Germany into the dimensions of 15 × 15 × 2 mm. A 200 W fibre laser with a wavelength of 1068 nm acquired from IPG Photonics in Germany was used in the printer. During the fabrication of the test samples, an inert gas atmosphere with 99.9996% pure research-grade argon gas was used. Nitinol samples were processed with a powder composition of 52.39 at.% nickel and 47.61 at.% titanium pre-alloyed by Fort Wayne Metals Inc., Castlebar, Ireland. The layer thickness of the samples was maintained at 60µm for both NiTi and Ti-6Al-4V. The printing process was carried out by varying three factors on two levels. These factors are scanning speed (mm/sec), the hatch distance (µm), and the laser beam power (W) as listed in **Table 6-1**. Only one set of printing processing parameters was used during the production of the Ti-6Al-4V samples since this process was already optimized in a previous study [24]. The corrosion testing parameters are listed in **Table 6-2**.

Table 6-1: Additive manufacturing processing parameter of NiTi and Ti-6Al-4V samples.

Samples	Scanning Speed (mm/sec)	Hatch Distance (µm)	Laser Power (W)
NiTi 1	750	70	120
NiTi 2	1500	70	120
NiTi 3	1500	90	120
NiTi 4	750	90	120
NiTi 5	750	70	150
NiTi 6	1500	70	150
NiTi 7	1500	90	150
NiTi 8	750	90	150
Ti-6Al-4V	1000	95	160

Table 6-2: Material property data for NiTi and Ti-6Al-4V used for corrosion testing.

Material	Property	Value
NiTi	Equivalent Weight	26.87
NiTi	Density	6.45 g/cm^3
Ti-6Al-4V	Equivalent Weight	12
Ti-6Al-4V	Density	4.43 g/cm^3

The samples followed mechanical polishing using P240 and P600 grit paper to eliminate surface roughness and prevent any ease of crack initiation. The samples were then

cleaned using deionized water and dried to remove any excess material that could affect the outcome of the results. Nail varnish was utilized to control the surface area for the electrochemical experiments resulting in a sample exposure area of 1.5 ± 0.1 cm^2 for electrochemical testing.

6.2.1 Corrosion Testing

Corrosion testing was conducted with the help of the Gamry instrument. Firstly, an Open Circuit Potential (OCP) test, refers to the resting potential of the material at which there is no current. This was followed by the potentiostatic EIS and the use of small amplitude and alternating current to examine a cell's impedance properties, its effective resistance, and passivation behavior. Another OCP test was completed before the final test, then cyclic polarisation was carried out. Cyclic polarisation follows both anodic and cathodic polarisation to measure the pitting tendencies of the metal samples. Sample test surfaces were isolated for the test by covering the remaining areas in nail polish. As the reference electrode, a saturated Ag/AgCl electrode (SCE), and for the counter electrode, graphite was used. Both electrodes and the sample were immersed in an electrolyte. Hanks and Ringer's solutions, identified in **Table 6-3**, were chosen to analyze the sample's biocompatibility, due to their comparability to that of the human body fluids. Corrosion tests were performed at 37±2°C like normal body temperature [301,302].

The initial OCP was monitored for one hour until stability was reached. The EIS setup followed the initial frequency of 100,000Hz to a final frequency of 0.1Hz. The cyclic polarisation was conducted between -0.3V to 0.3V using a scanning rate of 0.166 mV/s. A low scanning rate was chosen to increase the accuracy of results. All four stages of the test were completed in 8 hours. Corrosion testing followed all ASTM F2129 procedures. All samples were tested in Hanks and Ringer's electrolyte repeated 3 times for each. After each corrosion test, samples were re-polished.

Table 6-3: Composition of Hank's and Ringer's solution.

Contents	Hanks Solution	Ringers Solution
NaCl	8g	7.2g
KCl	0.4g	0.37g
CaCl2	0.14g	0.17g
MgSO4 · 7H2O	0.1g	
MgCl2·6H2O	0.1g	
Na2HPO4	0.06g	
KH 2 PO 4	0.06g	

D-Glucose	1g	
NaHCO3	0.35g	

The corrosion rate can be calculated using the following equation.

$$CR = K.\frac{i_{corr}}{\rho}.EW \qquad (14)$$

where K is constant, i_{corr} is the corrosion current density, ρ refers to the density of the sample and EW is the equivalent weight of the sample.

6.2.2 Optical Analysis

To examine the surfaces of the samples, Keyence VHX2000E optical microscope was used. Selected samples were examined before electrochemical testing and post-testing for the corrosion morphology. This method is useful for the characterization of corrosion pits or surface defects. Zeiss scanning electron microscope (SEM) equipped with Oxford energy dispersive X-ray spectroscopy (EDX) was used to carry out chemical compositions of the pits, defects, and surface morphology.

6.3 Results and Discussion

6.3.1 Electrochemical tests

6.3.1.1 EIS Nyquist tests

Nyquist plots are created in order to have a better understanding of the mechanics underlying the samples' passive film formation and corrosion resistance. For analysis, the inhomogeneities of the sample's surface structure, as seen in **Figure 6-1**, were explained by the constant phase element, or CPE.

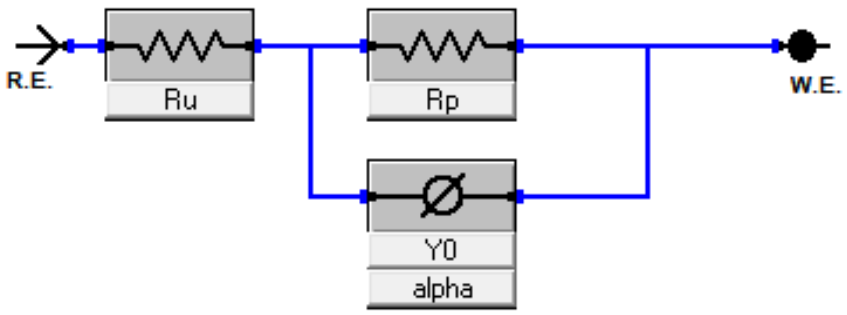

Figure 6-1: Schematic representation of the equivalent circuit used for the interpretation of EIS spectra.

The EIS data achieved after open circuit potential for Hanks and Ringers are displayed in Nyquist plots **Figure 6-2**(a) and (b). The calculations of polar resistance were completed by fitting curves on the Nyquist plots. The polarisation resistance, a measure of corrosion resistance along with the other fitting parameters of the impedance data are depicted in **Table 6-4**, directly derived from the graphs. The general depiction of Nyquist plots is represented as a semi-circle arc, it is observed in the experimental results the arc is unfinished. A larger arc radius of a Nyquist plot's curves denotes improved corrosion resistance. According to the Nyquist plots NiTi5 and Ti-6Al-4V have the highest real impedance, indicating a higher corrosion resistance in both Ringers and Hanks. There is a lower impedance for the Ti-6Al-4V sample in Hank's solution than in the Ringer, likely a cause of the high oxidation layer that forms on the Ti-6Al-4V surface in which the Hanks could not break through to initiate corrosion, also validated by Kuromoto et. al. [303].

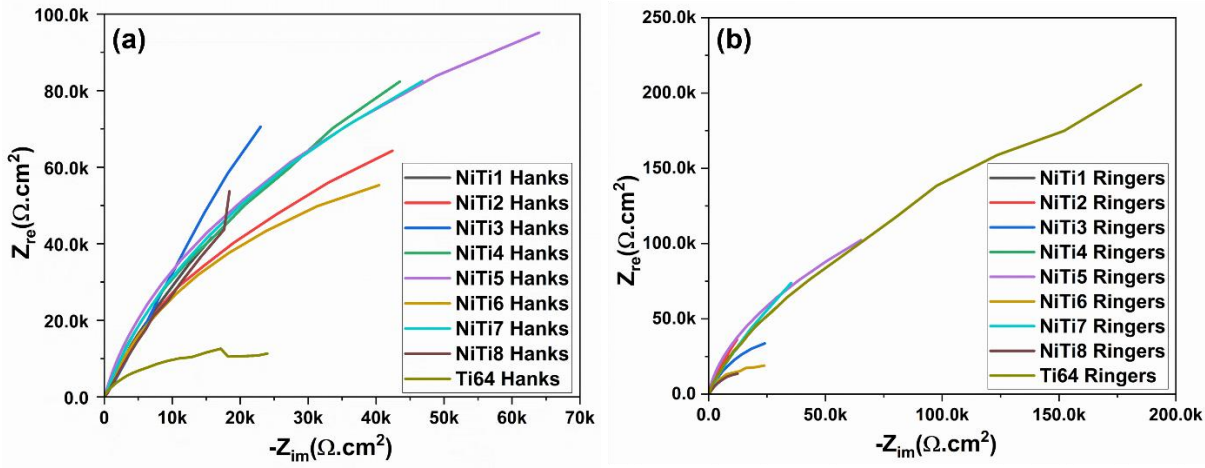

Figure 6-2: (a) Nyquist plots from the EIS measurement in Hank's solution and (b) Nyquist plots from the EIS measurement in Ringer's solution.

Table 6-4: Fitted parameters of the impedance data in both Hanks and Ringers solutions.

Sample	**Hanks Solution**				**Ringers Solution**			
	Ru (Ω.cm^2)	Rp (KΩ.cm^2)	Y_0 (μΩ^{-1}.cm^{-2})	η	Ru (Ω.cm^2)	Rp (KΩ.cm^2)	Y_0 (μΩ^{-1}.cm^{-2})	η
NiTi 1	23.7	427.5	232.5	0.84	22.32	628.2	224.5	0.86
NiTi 2	18.64	731.8	125.9	0.78	31.22	634.5	202.1	0.85
NiTi 3	19.62	392.7	124.1	0.77	18.86	313.6	228.8	0.78

NiTi 4	33.34	276.5	111.7	0.81	28.93	510.4	120.5	0.83
NiTi 5	27.5	489.6	744.2	0.86	25.34	293.0	8.83.7	0.90
NiTi 6	20.65	253.8	134.6	0.01	23.10	544.0	255.0	0.83
NiTi 7	28.85	725.7	710.3	0.82	33.58	495.9	115.7	0.81
NiTi 8	25.14	497.7	110.0	0.84	22.22	156.2	277.6	0.75
Ti-6Al-4V	6.221	265.2	113.5	0.86	38.58	416.2	275.6	0.85

To understand the degradation behavior and the mechanisms involved in the corrosion, the different stages were evaluated using the values in **Table 6-4**. When the samples are first exposed to electrolytes, a corrosion process begins. The electrolyte ions dissolve and penetrate the sample when the electrolyte meets the full surface of the sample. In the second stage, the sample's surface accumulates corrosion products, which causes a passivation coating to form (TiO_2). Prolonged submersion in the electrolyte restricts the electrolyte's penetration, greatly lowering the corrosion reaction. The passivation layer thickens because of this. The TiO_2 passivation layer is partially dissolved in the electrolyte and eliminated in the final stage. The sample is kept from coming into direct touch with the corrosive electrolyte (Hanks and Ringer's solution) by the passivation layer that is left on its surface. Localized corrosion may nevertheless occur on the sites of additively created NiTi and Ti-6Al-4V samples, depending on the printing conditions that result in pores and flaws on the sample surface.

6.3.1.2 EIS Bode tests

The bode plots, **Figure 6-3**(a-h), are observed in the frequency range 150,000 Ohm to 10 Ohm with phase angles between -90° to 5°. At high frequencies of log|Z| the phase angles are represented at low phase angle values in the range of 0-10°. In areas of low frequency, the phase angle approaches values of up to -90° suggesting there is a formation of a passive layer on the surface of all the samples. This finding is corroborated by the use and measurement of Tafel curves. The graph, **Figure 6-3**(f and h) depicts the bode phase angle of samples Ti-6Al-4V, NiTi7, and NiTi5 reach close to -90°. This supports the Nyquist results indicating a more stable passive film, with higher impedances at the final frequencies. King et. al. [304] discussed the formation of a preferred dense metal by increasing both the scanning speeds and the laser power, this can be validated by the EIS data, a laser power of 150W is optimum for an improved passive layer. Feng et al [305]

evaluate a small hatch spacing contributing to a large overlap scale between molten pools that can effectively be a cause of severe element burning loss as accounted for in samples NiTi1 and NiTi2.

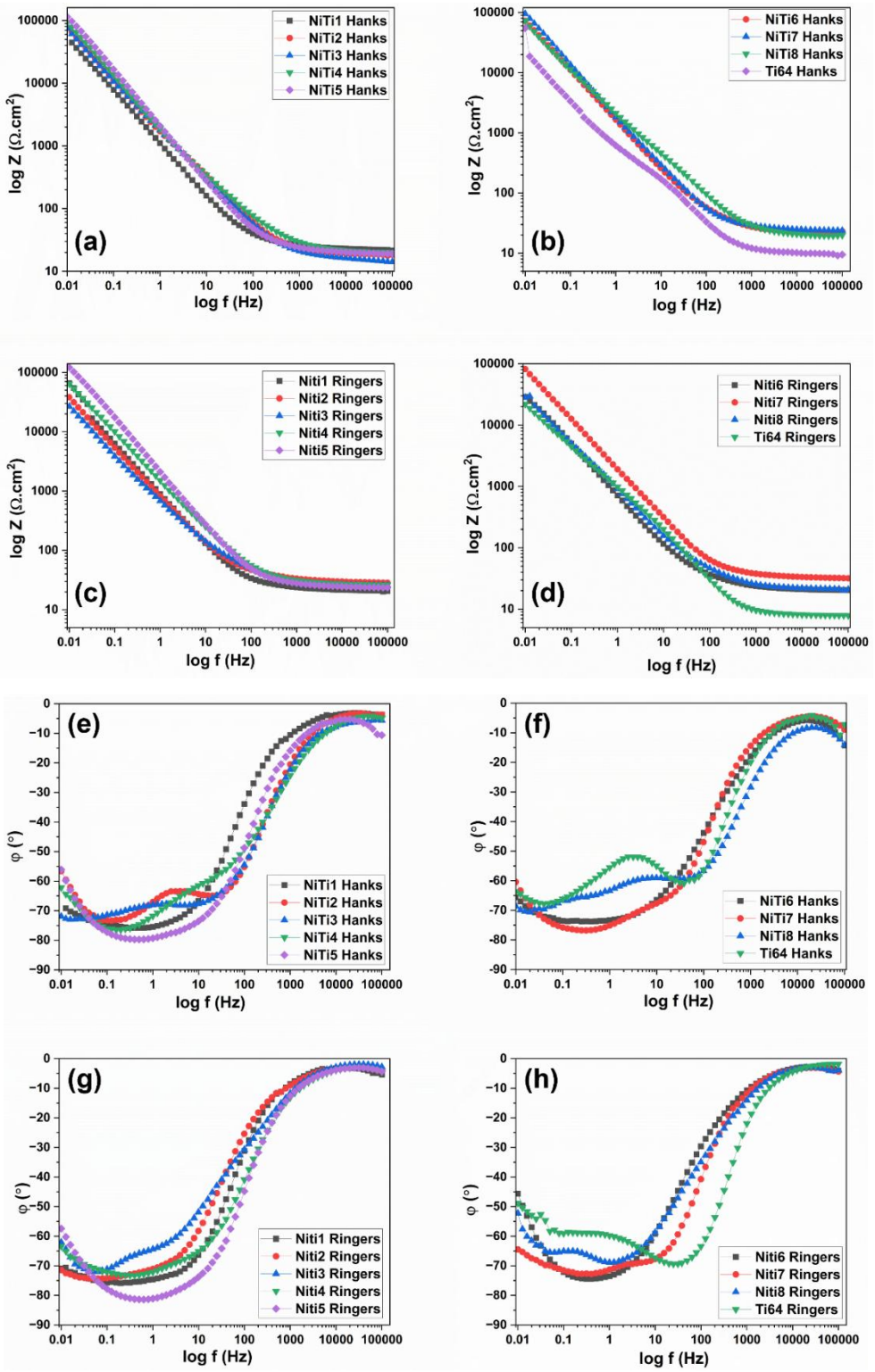

Figure 6-3: Electrochemical impedance measurements showing the bode plots concerning the Log|Z| (a-d) and the phase angle (e-h) of the experimental samples.

6.3.2 Cyclic Polarisation

Cyclic polarisation results of the samples show typical characteristics of metal passivation. The results of E_{corr} and i_{corr} are measured using the Tafel extrapolation method. Samples with higher printing parameters suggest a more stable oxide layer with lower corrosion rates. NiTi5 and NiTi7 have relatively low E_{corr} values as seen in **Figure 6-4** which is unvarying from the EIS results. The lower the corrosion current density, i_{corr}, the stronger the passivation layer. It is noted that NiTi5 allows a higher current to flow through so that the corrosion rate is maintained. Liu et al [306], denotes any i_{corr} value less than 0.1 µAcm2 indicates successful passive film protection. Liu conducted a study on NiTi samples with the respective parameters: hatch distance (120-140µm), laser power (250W), and scanning velocities (1250, 800, 500mm/s). The i_{corr} values obtained in **Table 6-5** and **Table 6-6**, reported significantly improved corrosion current densities than Liu et al observed. The results of this study suggest improved processing parameters for the corrosion behavior of NiTi. The samples with higher corrosion rates were comparable in terms of their lower laser power and hatch distance, reducing the dislocation density of the sample. Relatively consistent Ti-6Al-4V E_{corr} and i_{corr} values were observed in the study by Chen et al [307] of the metal in static and dynamic Hank's solutions. The acceptable rate of corrosion for metallic implants is ideally around 2.5×10^{-4} mm/yr, or 0.01mpy [308]. The results of this study suggest favorable results for corrosion rates in **Table 6-5** and **Table 6-6**. NiTi1 and NiTi2 depict a higher corrosion rate compared to Ti-6Al-4V results. A contradiction to the corrosion rates identified by Ti-6Al-4V, **Table 6-5** and **Table 6-6**, is displayed in **Figure 6-5**. The cyclic polarization curves of the Ti-6Al-4V samples in both Ringers and Hanks demonstrate that there is an absence of localized corrosion, and the passivation of the metal is conducted. The visual appearance of the cyclic polarization curves shows thick lines in some cases: NiTi1 (Ringers), NiTi4 (Hanks), NiTi6 (Hanks), and NiTi8 (Hanks). This is an indication of entrapped gas pores opening, Basu et. al. [70] found that using processing parameters with higher energy densities can reduce this effect.

Table 6-5: Polarisation curve parameters in Hank's solution.

Hanks	E_{corr} (mV)	i_{corr} (nA)	b_a ($Vdec^{-1}$)	b_c ($Vdec^{-1}$)	Corrosion Rate (mpy)
NiTi 1	-223.7	32.31	0.0855	0.0515	0.01216
NiTi 2	-156.88	29.67	0.0561	0.0718	0.0106
NiTi 3	-147.7	14.36	0.103	0.0517	0.00436
NiTi 4	-162.5	20.89	0.0743	0.08559	0.00747
NiTi 5	-131.35	61.69	0.170	0.162	0.01495
NiTi 6	-185.5	12.10	0.0527	0.0410	0.00509
NiTi 7	-133.36	20.48	0.0645	0.05832	0.00732
NiTi 8	-151.06	40.99	0.0732	0.05461	0.00369
Ti-6Al-4V	-28.76	70.21	0.1050	0.07759	0.02482

Table 6-6: Polarisation curve parameters in Ringer's solution.

Ringer	E_{corr} (mV)	i_{corr} (nA)	b_a ($Vdec^{-1}$)	b_c ($Vdec^{-1}$)	Corrosion Rate (mpy)
NiTi 1	-187.04	27.82	0.125	0.07221	0.0110
NiTi 2	-96.205	55.97	0.236	0.081865	0.020025
NiTi 3	-145.9	17.17	0.0213	0.00881	0.00613
NiTi 4	-97.98	102.9	0.358	0.208	0.05889
NiTi 5	-117.0	39.64	0.0796	0.0679	0.01418
NiTi 6	-225.2	13.722	0.4607	0.08707	0.142
NiTi 7	-124.3	9.317	0.0304	0.03442	0.00333
NiTi 8	-172.5	23.33	0.0732	0.05461	0.003697
Ti-6Al-4V	-116.72	47.24	0.0470	0.36625	0.016005

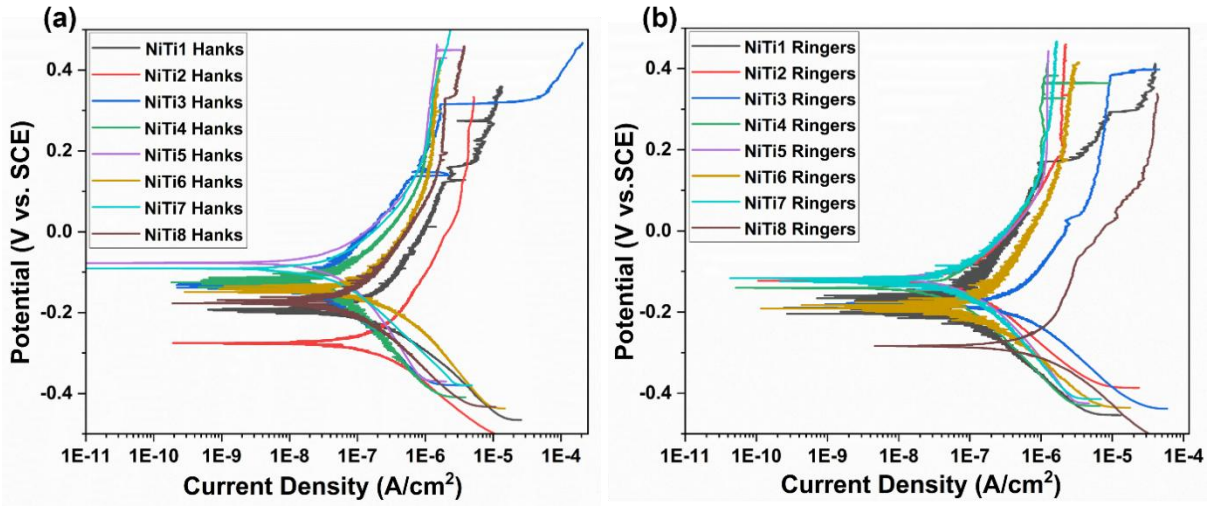

Figure 6-4: Cyclic polarisation curves of NiTi in (a) Hanks and (b) Ringers solution, n = 3.

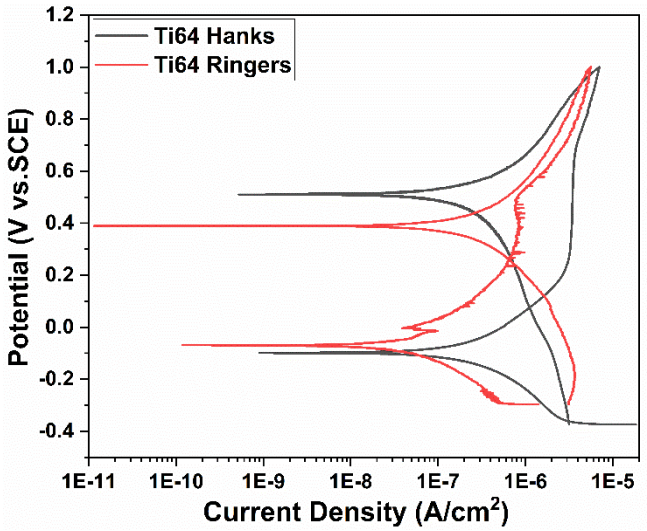

Figure 6-5: Cyclic polarisation curves of Ti-6Al-4V in Ringers and Hanks solutions, n = 3.

In order to examine the impact of process parameters on the corrosion rate (CR), a measurable outcome, a statistical data analysis model was adjusted. The standard error was calculated using the scanning speed and hatch distance as input values. It was observed that 135 W with a volumetric energy density of 25 J/mm^3, was the ideal input laser beam power level for minimizing the CR. **Figure 6-6** illustrates the significant reduction in CR that occurred when the power level was increased or decreased. The CR is primarily controlled by laser power levels, which may be explained by the over melting and lack of fusion that occur at those levels, respectively, where a large amount of porosity arises in addition to the production of unstable phases and electrolytic cells that accelerate the rate of corrosion. The outstanding mechanical qualities, high density, and stable chemical composition of NiTi components made by L-PBF with comparable processing parameter levels have already been reported in similar accomplishments [70,308].

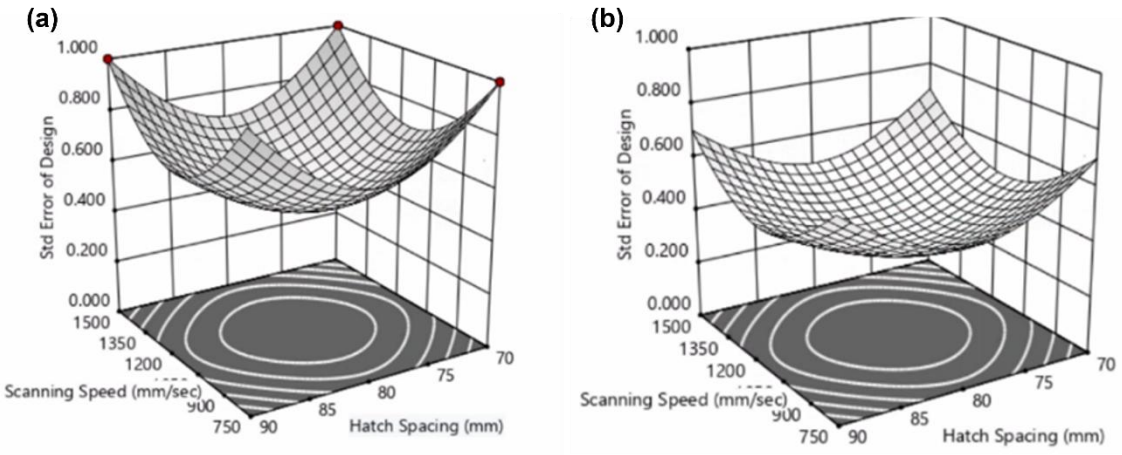

Figure 6-6: Standard error analysis at a laser power level of (a) 120W and (b) 135W.

By using the Response Surface Methodology (RSM) and the process parameters listed in **Table *6-1***, it was possible to compare the corrosion rates of laser powers of approximately 120W and 150W. Furthermore, **Figure 6-7**'s results indicate which processing parameters might be applied to reach a desired level of corrosive behaviour. RSM was finished with the aid of Hank's solution.

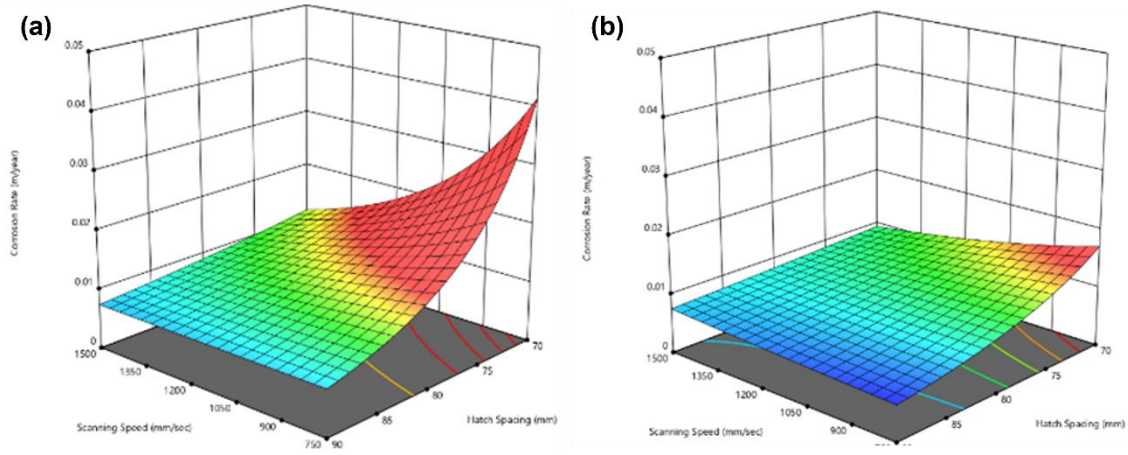

Figure 6-7: Response Surface Maps (RSM) using (a) 120W and (b) 150W.

6.3.3 Optical and Compositional Analysis

Optical analysis was conducted on all samples post-electrochemical testing. Results concluded little to no pitting was formed due to the corrosion of samples, but defects were identified due to the porosity of the prints manufactured. NiTi6 sample exhibited the poorest corrosion resistance with NiTi7 showing the highest corrosion resistance as shown in **Figure 6-8**. NiTi6 sample displayed a few corrosion spots on the surface but there was no significant difference was found in the chemical composition of these spots

in comparison to the sample with the highest corrosion resistance, NiTi7. No defects were evident in the Ti-6Al-4V samples and in the remaining NiTi samples defects were less significant using optimized processing parameters.

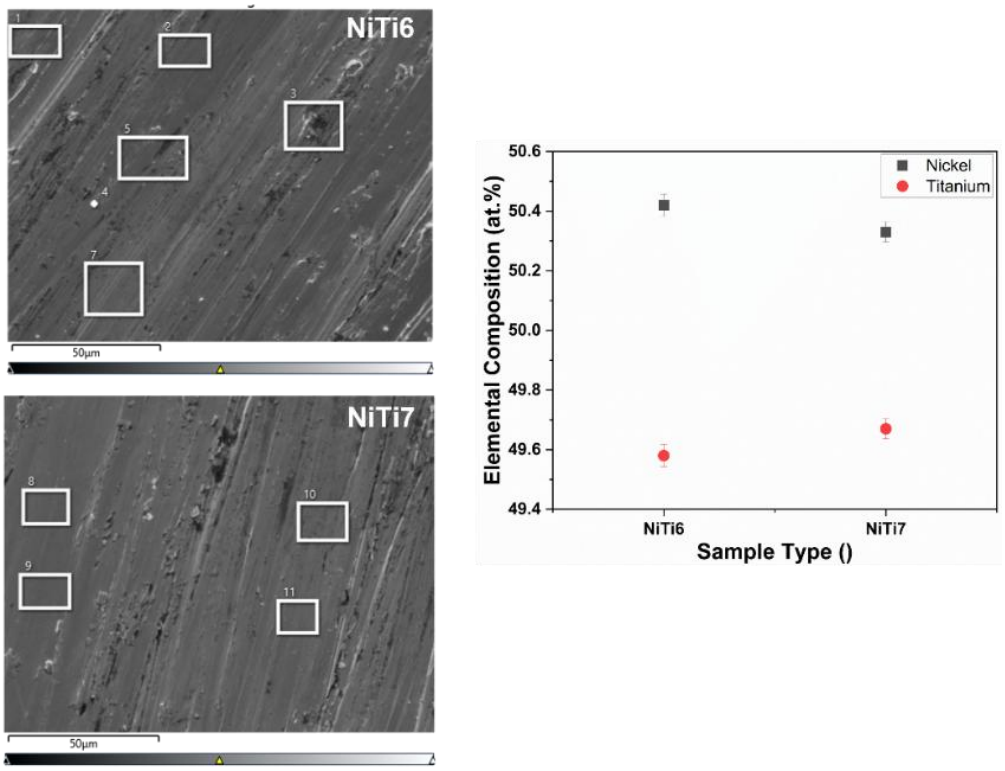

Figure 6-8: SEM micrographs of (a) NiTi6, (b) NiTi7, and (c) EDX elemental composition of NiTi6 and NiTi7 post-Hanks electrochemical testing.

6.4 Conclusion

This work used a 2^3 design of experiments with compositional and electrochemical an alysis as output measures to investigate the corrosion properties with respect to processi ng parameters of L-PBF manufactured nitinol and Ti-6Al-4V samples. The following are the primary conclusions:

1. It was established from the EIS results that NiTi exhibited good corrosion resistance, which is higher when the laser power and scanning speed were increased. NiTi5, NiTi7, and Ti-6Al-4V have increased stability in their passive film. When laser power is increased with a low hatch distance, it helps in increasing the passivation layer.
2. Cyclic polarisation of the samples indicated favourable corrosion characteristics for both Hanks and Ringers solution. The L-PBF NiTi and Ti-6Al-4V samples tested have the corresponding corrosion resistance from high to low:

(NiTi1, NiTi2, NiTi5, and Ti-6Al-4V) < (NiTi6, NiTi7) with nitinol samples NiTi3, NiTi4, NiTi8 ranging in-between.

3. The corrosion resistance was found to be higher in samples with low laser power of 120W and a smaller hatch distance (70 μm), NiTi1, and NiTi2 than the samples processed with a higher hatch distance of 90 μm. A similar trend was observed when the laser power was increased to 150W. Optical analysis and cyclic polarisation also indicated gas pore defects in the AM-processed parts and the data collected stipulated an increase in corrosion as the defects were exposed during electrochemical testing.
4. The investigation shows the optimum laser power for processing to optimize corrosion resistance was identified as 135W by performing statistical analysis with 1125 mm/s scanning speed and 0.08 mm hatch distance as the input parameters.

Chapter 7: Control of surface finish and mechanical properties of nitinol stents fabricated via laser powder bed fusion

Publication Status: Published

Agarwal, N., Bahramyan, M., Healy, P., Obeidi, M. A., & Brabazon, D. (2025). Control of surface finish and mechanical properties of nitinol stents fabricated via laser powder bed fusion, *Journal of Materials Research and Technology, 37, 1808-1821, https://doi.org/10.1016/j.jmrt.2025.06.128*

7 Abstract

This study provides a comprehensive analysis of how laser powder bed fusion (L-PBF) processing parameters influence the functional properties of nitinol stents, leveraging a Box-Behnken design of experiments. The novelty of this work lies in its systematic investigation of the key attributes, including relative density, surface morphology (pre- and post-electropolishing), dimensional accuracy, composition, phase transformation behaviour, and mechanical performance, offering new insights into process-property relationships for L-PBF fabricated nitinol stents. An important observation is that L-PBF-produced stent strut diameters (148–201µm) exceed the CAD defined strut diameter of 100 µm, highlighting the challenges and effect of melt pool width on achieving required levels of dimensional accuracy. Electropolishing proved highly effective, reducing surface roughness by up to 87%, from an initial range of 11.8–22.8 µm to a minimum of 1.8 µm. Relative density varied from 85.2% to 99.5%, while in-situ thermal measurements revealed mean layer temperatures between 750 and 1150°C. Differential scanning calorimetry (DSC) analysis indicated varying austenitic finish temperatures of 23–29°C and martensitic start temperatures of 7.5–10.5°C, resulting from a 1–2% nickel loss during processing. By achieving high-precision fabrication with excellent surface quality and tailored functional properties, this research establishes L-PBF as a promising technique for manufacturing complex nitinol stents. This study demonstrates that precise control of L-PBF parameters is critical for optimizing porosity, phase transformation characteristics, and mechanical performance. Furthermore, for the first time, thermal gradient graphs for intricate structures such as stents have been captured and analysed using infrared (IR) pyrometry. This novel approach provides valuable insights into the thermal behaviour during L-PBF processing, offering a deeper understanding of heat distribution and its influence on the final properties of nitinol stents.

Keywords: Nitinol stents, thermal gradient, recoverability, L-PBF, electropolishing

7.1 Introduction

Arterial blockages formed due to the accumulation of plaque and fat deposits commonly related to peripheral arterial disease and coronary artery disease are usually treated with the help of vascular stents [309]. Stents are usually complex tubular structures designed to function as an arterial wall holding open the narrowed / blocked blood vessels to enable blood flow [310]. As highlighted by CSIRO, Australia [311], the optimum selection of the stents must be made, including the production of bespoke stents, to suit the complex

anatomical geometry of the damaged vessel and also fit the patient's personal specific blood vessel geometry [312].

Conventional methods of producing stents by laser cutting have been popular due their widespread use. However, this method lacks the ability of customization according to the needs of the individual patient. Standard designs of stents often do not comply optimally with the biomechanical needs of a specific patient's vessels [313]. Stents which are customised according to the patients specifics would be helpful to avoid long-term complications such as thrombosis, restenosis as well as improper fit of the stents in the patient's body, more likely leading to no need of further surgeries [314]. Fatigue strength properties of these stents are of utmost importance as the deployed stents undergo continuous cyclic loading-unloading cycles, under external biomechanical forces from the blood vessels [315]. Traditional manufacturing techniques include several steps relying on machining, laser cutting, drilling and surface modifications. Apart from requiring many processes, other challenges possessed by this subtractive process are material wastage, longer production times, and high production costs [316]. Additional post processing such as electropolishing, mechanical polishing, thermal treatments, chemical etching and coatings to modify the surface of the fabricated part to enhance mechanical and surface properties and corrosion resistance, add to the complexity and expense of production [317,318]. Additive manufacturing (AM) can be used to address these limitations and help in the production of patient-specific stents with tailored properties.

Laser powder bed fusion (L-PBF) additive manufacturing vastly contributes to the manufacturing ability of bespoke stents due to its higher design freedom and flexibility while providing reduced material wastage when compared to the other traditional manufacturing techniques. Significant enhancement in the fabrication of complex geometries has proven to be beneficial over the laser micro-machining route for the production of stents [319]. Good microstructural feature and macroscopic dimensional control of the stents can be provided from the L-PBF process [93,320]. However, several manufacturing challenges of the L-PBF technique include the high surface roughness, porosity, defect formation, compositional changes due to nickel evaporation as well as inheriting residual stresses [7,321,322]. Due to the rapid solidification, high cooling rates of 10^5 – 10^7 K/s and the re-melting of the underlying layers during processing often,

entrained residual stresses often occur [53,323]. As discussed by Yan et. al. [108], such changes during the fabrication process along with compositional changes affect the mechanical properties and biocompatibility of the fabricated stents [324]. It is observed that parts produced with non-optimised processing parameters can exhibit poor mechanical properties. Due to the inheritance of residual stresses and inhomogeneities in the microstructural features in the fabricated parts, the functional properties can vary [325]. This necessitates the development of optimised process strategies including laser processing parameters and post-processing techniques to improve the structural integrity and performance of the AM-fabricated parts [326].

In case of stents, surface roughness plays an important role in controlling the mechanical performance, biocompatibility and corrosion resistance. Several disadvantages of high surface roughness include a reduction in fatigue life, increased susceptibility to corrosion, and poor mechanical integrity which could lead to failures [327]. Higher surface roughness increases the problems as it increases thrombogenicity which negatively affects the device performance of the vascular stents [328]. This excessive surface roughness is a result of the partially melted particles adhered on to the surface and the stair-step effect due to the layer-by-layer fabrication process [329].

Some of the exceptional properties such as biocompatibility, shape memory effect and superelasticity of nitinol, a nickel and titanium alloy, makes it a suitable material for the fabrication of stents [14,42,121,330]. Nitinol has proven to have excellent corrosion resistance, great strength and flexibility making it desirable to be utilized to form complex and intricate structures such as stents to fit the human cardio vasculature [123,331]. Nitinol is also used in other biomedical implants such as orthodontics. To eliminate the design restriction constraint of the conventional techniques of manufacturing stents, AM has gained popularity within implant research and development for the fabrication of nitinol stents. L-PBF has also paved way for producing parts with tailored functional properties required for the stents. The superelastic property of the fabricated stents is highly dependent on the phase transformation temperatures which is impacted by even small variations in the Ni concentration [109]. Therefore, it is essential to have precise control over the nitinol feedstock and processing conditions of the stent being produced to have the intended functional properties.

This work evaluates the possibility of using L-PBF to fabricate microscale stent struts with diameters as small as 100 µm— which is the lower limit of L-PBF resolution. While high-resolution techniques such as localized electrochemical deposition (LED) can produce fine features [332–334], they face challenges in scalability, material compatibility, and mechanical robustness for free-standing biomedical structures with intricate geometries such as stents. In contrast, L-PBF is a mature, industry-relevant additive manufacturing process well-suited for producing three dimensional complex geometries in biocompatible alloys like NiTi and CoCr. By examining the challenges associated with fabricating such fine features, including geometric fidelity and surface quality, this work evaluates L-PBF for the production of miniaturized biomedical device applications such as stents.

In this study, we address the critical challenge of surface roughness of the fabricated nitinol stents through the post processing method of electropolishing. For the first time, this study also looks into the mean temperature per layer with the help of the IR data and represents the overall thermal data of the fabricated stents. The work evaluates and reports the influence of the laser processing parameters with the mechanical and physical properties of the produced parts in terms of relative density, dimensional accuracy, surface morphology, phase transformation temperatures and stress strain curves. By improving the surface quality of the L-PBF manufactured nitinol stents, this study aims to enhance the functional properties by optimizing the print as well as electropolishing strategies. This research study presents a significant step-forward in nitinol stent production with optimized geometries, enhanced biocompatibility and long-term durability. These advancements could also prove the basis for other applications such as orthopaedic implants and hard-tissue engineering scaffolds highly impacting the biomedical industry and thus accelerating the adoption of AM in the healthcare sector.

7.2 Materials and Methods

7.2.1 Materials

Gas atomized pre-alloyed Ni-rich nitinol (NiTi) powder was obtained from Fort Wayne Metals, Castlebar, Ireland. The Ni and Ti content and particle size were measured and are shown in **Table 7-1**. The elemental composition of the NiTi powders was measured using an Oxford Energy Dispersive X-ray Spectrometer (EDX) equipped with a Zeiss Scanning Electron Microscope (SEM). A Malvern Particle Size analyser was used to

measure the particle size distribution of the as-received NiTi powder. A spherical morphology of the powder was observed, see **Figure 7-1** with an average size of the particles of 28.8 µm. The spherical nature of the powder with the presence of only a few satellites suggested it would have good flowability which is advantageous for achieving a good powder distribution on the machine bed. This powder characteristic would enable the formation of a thin film of uniform thickness on the powder bed.

Table 7-1: Elemental composition and particle size distribution of the NiTi powder.

NiTi powder	Elemental Composition		Particle Size Distribution		
	Ni (at.%)	Ti (at.%)	D_{10}	D_{50}	D_{90}
As-received	52.3	47.7	13.5	28.8	48.4

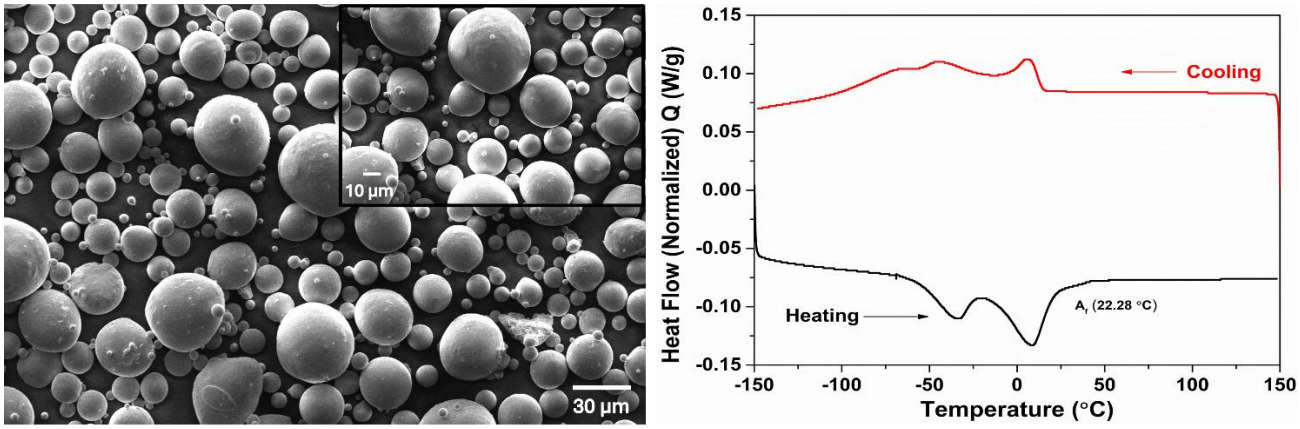

Figure 7-1: (a) SEM micrograph of the NiTi powder used for the fabrication of the stent samples and (b) corresponding DSC curve.

7.2.2 Fabrication of nitinol stents via L-PBF

A commercially used stent design was fabricated using an Aconity3DMINI metal printer manufactured by Aconity3D, Aachen, Germany, which was equipped with a 200W Yb-fibre laser. The laser was supplied by IPG Photonics and has an operating wavelength of 1068 nm. A commercial stent design was printed with the longitudinal axis printed in the vertical build direction. The length of the stents were 50 mm, in the build direction, and they had a diameter of 12 mm and were printed in the vertical direction as shown in **Figure 7-2**. The designed stent strut diameter is of 100 µm according to the CAD model. A high-purity research-grade argon gas was used during the manufacturing of stents while maintaining the oxygen level < 20 ppm during the entire process. A layer thickness

and laser spot size of 60 µm were kept constant. A supply factor of 2 times the layer thickness was utilized to ensure full coverage of the powder bed without any missing locations. A 67° scanning rotation angle was used between the subsequent layers during the processing of the stents. The variation in the laser processing parameters were arranged according to a Box-Behnken design of experiments, see **Table 7-2**.

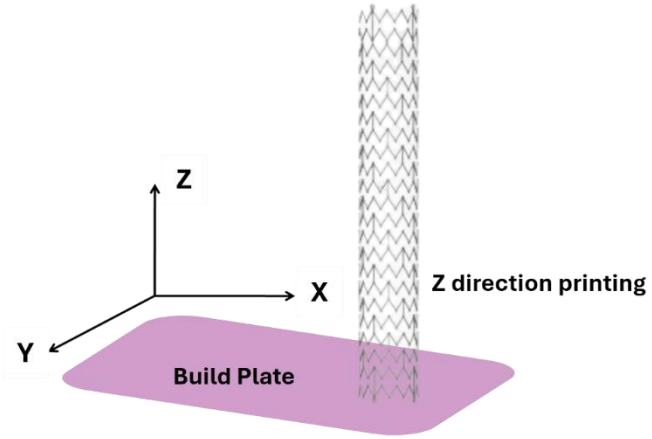

Figure 7-2: Schematic showing the nitinol stent built in the Z direction on the build plate.

Table 7-2: Processing parameters according to a Box-Behnken design used for fabricating the NiTi stents along with their corresponding volumetric energy density (VED).

Sample ID	Laser Processing Parameters			VED (J/mm^3)
	Laser Power (W)	Scanning Speed (mm/s)	Hatch Space (µm)	
S1	120	750	45	59.26
S2	120	500	60	66.67
S3	180	500	60	100.00
S4	150	1000	45	55.56
S5	150	750	60	55.56
S6	150	750	60	55.56
S7	150	750	60	55.56
S8	150	750	60	55.56
S9	180	1000	60	50.00
S10	150	750	60	55.56
S11	180	750	75	53.33
S12	150	500	45	111.11
S13	120	750	75	35.56
S14	120	1000	60	33.33
S15	150	500	75	66.67
S16	180	750	45	88.89
S17	150	1000	75	33.33

7.2.3 Microstructural characterization

The morphology of the stents was examined using a German-made Zeiss Scanning Electron Microscope (SEM), coupled with an Oxford Inca Energy-Dispersive X-ray Spectroscopy (EDX) system from Oxford Instruments, UK. A Keyence-VHX2000E by Keyence, UK, optical analysis system was utilized for the macrostructural analysis on resin mounted and mechanically polished samples. Porosity levels within the structures were assessed through both optical microscopy. The samples with highest and lowest density were mounted in cold resin and polished using SiC papers (80-4000 grit size). Final polishing was done using diamond suspension solutions (9 μm down to 1 μm). Analysis of these images were done with the help of ImageJ processing software. With the help of the analyze particles processing on the images and dividing the pore area by the sample area, the porosity percentage of each image was calculated.

7.2.4 Relative Density

The Archimedes density measurement technique was employed to determine the relative density of the stent samples using a Sartorius Entris II Essential BCE124I-1S analytical balance with an accuracy and repeatability of ±0.1 mg manufactured by Sartorius, Germany. Ethanol was used as the liquid medium and three measurements were recorded from each sample, according to the ASTM B962 standard [249].

7.2.5 Phase transformation temperatures using DSC

The phase transformation temperature of the original metal powder and all the stent samples were investigated using the Differential Scanning Calorimetry (DSC) test, performed with the TA Discovery DSC2500 instrument supplied by TA Instruments, New Castle, United States. This test produces highly consistent curves, with tangents employed to identify the start (M_s, A_s), finish (M_f, A_f), and peak (M_{Peak}, A_{Peak}) temperatures of martensite and austenite phases in the analysed samples. The test involves thermal cycling of the specimen, heating and cooling it between -100°C and 150°C, at a rate of 10°C/min. Phase formation temperatures were determined from the measured heat flows. Specimens weighing between 10 mg and 20 mg were utilized for this investigation.

Figure 7-1(b) presents a DSC thermogram of the as-received NiTi powder, capturing its phase transformation behaviour. The normalized heat flow is plotted as a function of temperature for both the heating (black curve) and cooling (red curve) cycles. During

heating, a clear endothermic peak is observed, corresponding to A_f temperature of 22.28 °C. The cooling curve shows the exothermic transformation back to martensite.

7.2.6 Surface roughness

The surface roughness profile was assessed using non-contact, Bruker Contour GT 3D profilometer by Bruker, Germany, for all the stent samples. Equipped with VISION 64 software, the instrument facilitated data analysis, visualization of surface profiles, and evaluation of surface roughness descriptors. For each sample in the Design of Experiments (DoE), a minimum of three surface roughness profiles was obtained parallel to the stent axis. The average surface roughness was then computed from these profiles, along with the corresponding 95% confidence intervals (CI). In this study, Sa and Sz were measured and discussed. Sa represents the mean of the absolute values of surface deviations above and below the mean plane within the sampling area, and, Sz represents the average height difference between the five highest peaks and the five lowest valleys. Due to the complex geometry of the stent, particularly the struts that are not perfectly aligned with the stent axis, the profiles appear as distinct segments each corresponding to a local portion of a strut. The intrinsic curvature is notable, with a typical radius of curvature in the order of ~100 µm, reflecting the underlying strut geometry. The high-frequency roughness features are superimposed on this curvature and are characteristic of the LPBF process as shown schematically in **Figure 7-3**.

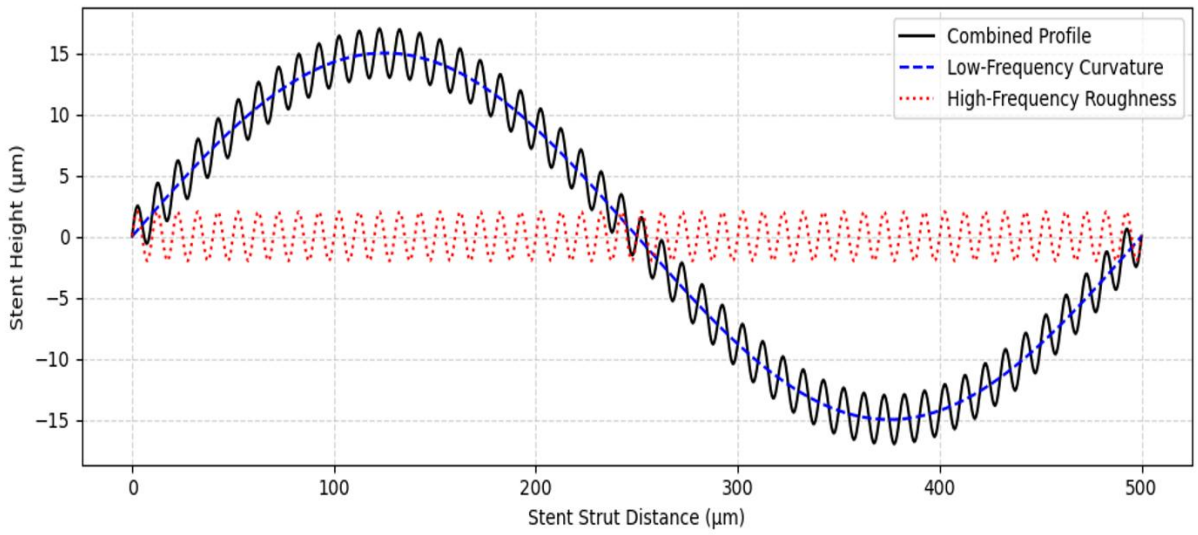

Figure 7-3: Representative schematic of a surface profile of an LPBF-fabricated stent strut, measured along the stent axis.

7.2.7 Electropolishing

The electropolishing process, recognized as an effective post-cleaning technique, was employed to enhance surface finish and decrease the thickness of the stent surface by the removing of residual melted particles. The stents underwent etching for a duration of 60s with a voltage of 10V in a commercial A3 electrolyte solution from LectroPol-5 from Struers, Denmark. Subsequently, they were rinsed in distilled water for five minutes followed by a rinse with ethanol to complete the surface cleaning process. Although the this work does not focus on a systematic study of the influence of the electropolishing parameters, the electropolishing regime was selected based on the combination of prior experimental experience of nitinol, manufacturer guidelines and the published literature.

7.2.8 IR data analysis

The Aconity metal 3D printer features two pyrometers supplied by KLEIBER Infrared GMBH, Germany, capturing infrared (IR) data of the melt pool to monitor its temperature. These pyrometers were used to meausre the light emitted within the 1500–1700 nm range from the laser-affected area and output the data in millivolt (mV) units. This data is recorded at 100kHz along with the corresponding x, y coordinates on the build plate. Python was employed to process the pyrometer data to create 3D tomographic point clouds. Statistical analyses were then conducted on these point clouds, both layer by layer and for the entire sample. Subsequently, Plotly was utilized to generate plots and figures, facilitating efficient data visualization through tomograms.

In typical scenarios, a substantial amount of data is collected from the pyrometer after each build. For instance, in this study, the IR-data file yielded nearly 1.98 million data points per build layer. Each data point includes the (x, y) coordinates on the build plate along with the corresponding temperature measurement in millivolts (mV).

7.2.9 Compression testing

A Cell Scale Tester tensile-compression testing machine from CellScale, Waterloo, United States, was utilized to conduct this test under laboratory conditions at 20°C. TestXpert software was employed to operate and control the machine, programmed to conduct compression tests at a rate of 1 mm/min in the direction of sample part build until sample failure. In this manner, the sample stress-strain data was recorded and correlation plots were generated.

7.3 Results and Discussion

7.3.1 Dimensional Accuracy

Figure 7-4 shows SEM images of a printed stent struts. Dimensions of the struts printed were compared to the original stent CAD file. An important observation to be made is that despite the extremely small strut sizes, the processing parameters enabled the fabrication of the entire stent for all 17 samples without failures. It has been already known that samples manufactured via L-PBF have a higher surface roughness which is a result of the melting of the underlying layer while a layer is being deposited on top of it. This melting usually promotes the epitaxial solidification. Heat accumulation in the melt pool and the surrounding material is a common result of the repeated laser scanning and shorter cooling periods, during the L-PBF process. Therefore, the interaction time between the molten metal and the surrounding particles is higher due to localized thermal buildup leading to lower viscosity. This results in more of loose powder particles or partially melted particles getting adhered to surface, leading to increased surface roughness [335,336]. Furthermore, the scanning strategy, laser power and VED together effect the powder spattering and the satellite particle formation on the surface during processing [304,337]. As depicted in **Figure 7-4**(a), individual layers can be observed while the average measured layer thickness is much higher than the process set layer thickness of 60 µm provided for the stent fabrication. This is due to the re-melting of the underlying layer that occurs during the process thus forming a larger melt pool.

On the other hand, the strut size was observed to have a much higher dimension than the dimension provided in the CAD file. The observed strut diameters ranged between a low of 148 µm to a high of 201 µm. The strut diameter provided in the CAD file was of 100 µm. This difference in the strut size can be attributed to the fact that the melt pool is larger in the x and y directions that the set CAD file dimension, as well as being larger in the depth direction as noted above. A laser spot size of 60 µm was utilized for the fabrication of the stents and as is often the case, the melt pool in this work was found to be larger than the spot size. The combination of a larger melt pool along with the adherence of the powder particles on the surface led to an increase in the dimension of the final stent part, above that of the CAD file, see **Figure 7-4**(b).

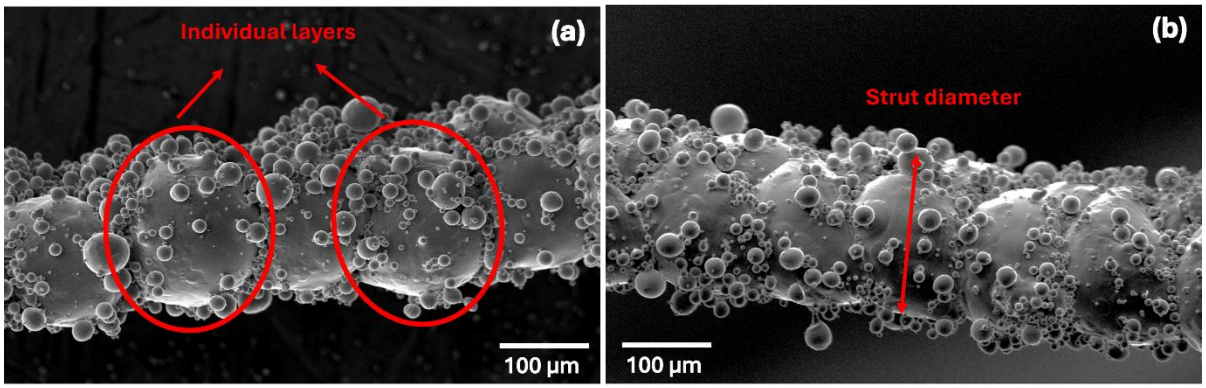

Figure 7-4: SEM micrograph of a stent sample (a) exhibiting the individual layers of the L-PBF processing and (b) showing the strut diameter.

The resulting strut diameter is highly dependent on the laser processing parameters and the powder feedstock as well. It has been well established in literature that any changes in the Ni content of the NiTi composition of the powder would lead to changes in the transformation temperatures and the resulting superelastic behaviour, as shown by Walker et. al. [338]. To mitigate nickel evaporation during the L-PBF process, Jamshidi et. al. [339] added 2% elemental nickel powder to the pre-alloyed equiatomic NiTi powder feedstock to fabricate stents. In contrast, the Ni-rich 52.39at.%Ni-47.61at.%Ti pre-alloyed powder feedstock was used in this study which one might expect would give a more homogeneous composition in the resulting prints.

7.3.2 Surface Morphology

The surface morphology of stents depicting the highest relative density and the lowest relative density produced via L-PBF are shown in **Figure 7-5**. Sample S4 showed the highest density and S16 exhibited the lowest, see **Table 7-3**. As shown in the figure, several unmolten powder particles are attached to the surface of the stent parts. The presence of partially melted and resolidified powder particles can be seen across the surface of all the produced stents. However, the surface morphology change is observed as the adjoining layers show triangular-shaped overlaps of each subsequent layer for sample S4, see **Figure 7-5**(a). The spacing between the layers is minimal owing to a higher relative density of 99.49%. On the other hand, sample S16 exhibited a spherical-shaped melt pools which overlapped with each layer yet left a discernible space of spandrel geometry between the layers. This resulted in a lower density of the stent as represented by **Figure 7-5**(b). It is thought that this lower density was due to the solvent not fully filling these many small spaces between adjacent melt pools, thereby giving a larger volume for the measure weight.

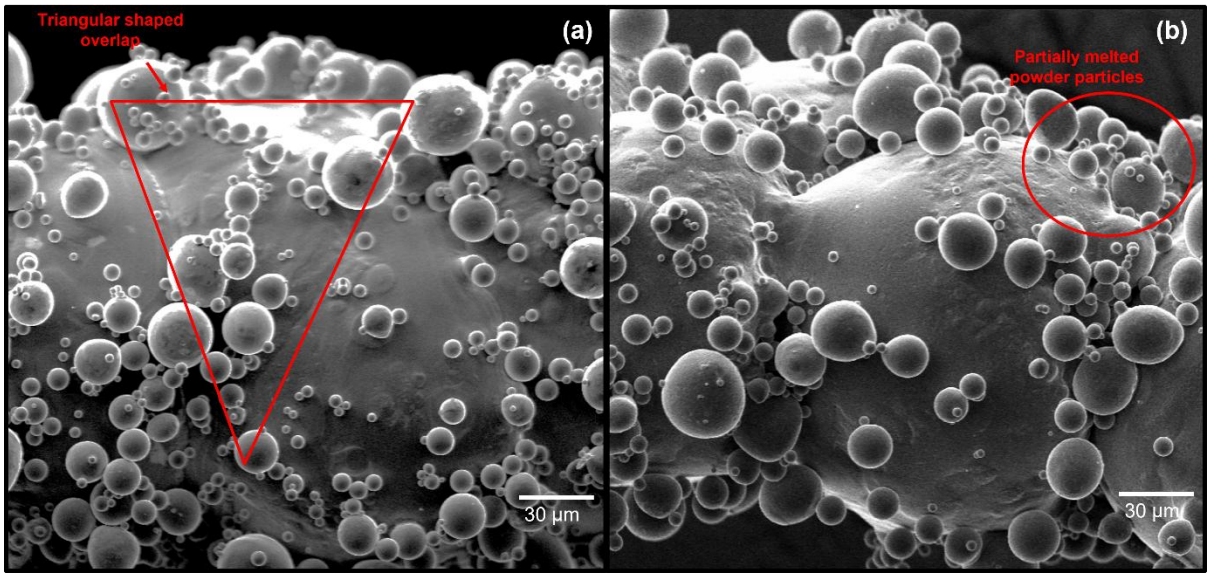

Figure 7-5: (a) SEM micrograph of sample S4 with a VED of 55.56 J/mm^3 and highest relative density and (b) SEM micrograph of sample S16 with a VED of 88.89 J/mm^3 and lowest relative density.

Regarding processing parameters, both samples were processed with the same hatch spacing of 45 µm and a layer thickness of 60 µm, but the laser power and the scanning speed were varied. As depicted by **Figure 7-6**(a), owing to the lower laser power and higher scanning speed relative to sample S16, the surface morphology of sample S4 exhibits partially molten particles on the surface that have emerged from the melt pool due to the faster solidification process and faster cooling time. The attached partially melted and resolidified powder particles on the surface led to an increase in the stent's surface roughness. On the other hand, the surface of sample S16 shows geometric spaces of spandrel geometry which are formed due to the higher laser power and lower scanning speed used for processing this sample. A surface tension gradient would be expected as a result of the higher VED which would cause a higher Marangoni effect resulting in a higher concentrations of adhered powder particles [340]. Such an increased number of adhered particles on the surface would be expected to lead to an increase in the surface roughness. From **Table 7-4**, it can be seen that the measured Sa value for S4 produced with lower VED was 15.4 µm, compared to 17.8 µm for S16 which was produced with the higher VED.

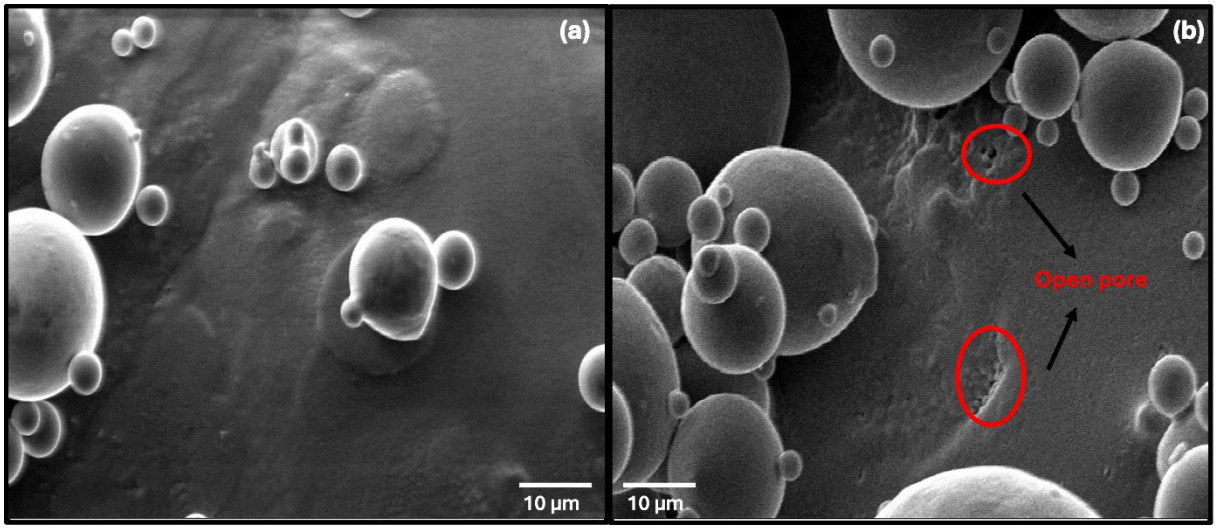

Figure 7-6: (a) Magnified SEM micrograph of sample S4 with a VED of 55.56 J/mm^3 and (b) magnified SEM micrograph of sample S16 with a VED of 88.89 J/mm^3.

7.3.3 Relative Density

The relative densities of the fabricated stents are shown in **Table 7-3.** The results indicated that S4 exhibited the highest relative density of 99.49% with the lowest relative density for S16 at 85.19%. It was further observed that the hatch spacing for these samples was 45 µm, and the resulting VED was 55.56 and 88.89 J/mm^3 respectively due to the different laser powers and scan speeds used for the fabrication of the samples.

Samples 8 and 11 also exhibited high relative densities of 99.40% and 99.11% respectively with slight variation in the VED from 55.56 to 53.33 J/mm^3. Different relative densities were obtained for the samples resulting in the same VED of 55.56 J/mm^3 due to the different process parameters.

An interesting observation to be made was the maximum difference in the relative densities ranged up to a maximum of 14% for the varying process parameters used. Although two or more samples could have the same resulting VED, however, the input processing parameters would be different. This often results in different relative densities due to the varying geometry, solidification, and overlapping of the melt pool. In this study, samples S13 and S17 have a VED of 33.33 J/mm^3 but they have different relative densities although they have the same hatch spacing of 75 µm. It should be thus noted that caution should be used when discussing VED's correlation to density or defects of parts produced using L-PBF [341].

Table 7-3: Relative density of the fabricated stents.

Sample Name	Laser Power (W)	Scanning Speed (mm/s)	Hatch Space (μm)	VED (J/mm^3)	Relative Density (%)
S1	120	750	45	59.26	85.41 ± 0.31
S2	120	500	60	66.67	98.95 ± 0.02
S3	180	500	60	100.00	88.90 ± 0.24
S4	150	1000	45	55.56	99.49 ± 0.01
S5	150	750	60	55.56	96.64 ± 0.07
S6	150	750	60	55.56	95.21 ± 0.10
S7	150	750	60	55.56	90.99 ± 0.19
S8	150	750	60	55.56	99.40 ± 0.01
S9	180	1000	60	50.00	88.07 ± 0.25
S10	150	750	60	55.56	91.80 ± 0.17
S11	180	750	75	53.33	99.11 ± 0.01
S12	150	500	45	111.11	98.53 ± 0.03
S13	120	750	75	35.56	97.44 ± 0.05
S14	120	1000	60	33.33	86.89 ± 0.28
S15	150	500	75	66.67	96.98 ± 0.06
S16	180	750	45	88.89	85.19 ± 0.32
S17	150	1000	75	33.33	85.62± 0.31

7.3.4 Surface Roughness

Table 7-4 presents the average surface roughness Sa along with the maximum height Sz and the reduction in average surface roughness Sa of the fabricated stents before and after electropolishing. As tabulated, the average surface roughness ranged between 11.81 and 22.81 μm and the maximum height Sz ranged between 104.87 to 178.83 μm for the stents before electropolishing. Response Surface Maps (RSM) are helpful to illustrate the influence of laser power, scanning speed and hatch spacing on the surface roughness before production of the stent parts. The ANOVA results showed low p-values (<0.05) proving that these factors were statistically significant and have a strong impact on the surface roughness of the as-fabricated of the stents. A strong positive correlation has been observed between the hatch spacing and surface roughness indicating that the surface roughness increases when the hatch spacing increases from 45 to 75 μm. It has been observed from **Figure 7-7**.

Figure 7-7 that the higher laser powers with lower scanning speed minimizes the surface roughness irrespective of variations in the hatch spacing. Conversely, at higher hatch spacing and scanning speeds with lower laser power led to an increase in the surface roughness. At lower hatch spacings, the distribution of the points relative to the

predicated surface indicates a reasonable fit of the model with high R^2 values which is close to 1.

Table 7-4: Surface roughness of the stents before and after electropolishing.

Sample No.	Sa (µm) before polishing	Sa (µm) after polishing	Sz (µm) before polishing	Sz (µm) after polishing	Sa Roughness reduction (%)	Sz Roughness reduction (%)
S1	16.7 ± 0.8	7.1 ± 0.3	130.2 ± 6.7	86.9 ± 3.1	57.3	33.2
S2	22.6 ± 1.2	3.1 ± 0.4	178.8 ± 5.5	49.6 ± 7.8	85.9	72.2
S3	18.7 ± 2.2	4.9 ± 2.6	146.3 ± 3.4	77.5 ± 9.1	73.4	47.0
S4	15.4 ± 0.6	5.6 ± 0.6	142.8 ± 3.4	65.5 ± 2.3	63.5	54.0
S5	22.8 ± 1.0	3.4 ± 0.6	140.9 ± 9.7	39.9 ± 4.9	85.0	71.6
S6	13.9 ± 2.5	3.2 ± 0.3	128.3 ± 5.6	32.3 ± 4.3	76.5	74.7
S7	17.1 ± 0.8	3.6 ± 0.1	110.0 ± 6.9	45.9 ± 4.9	78.7	58.2
S8	22.7 ± 3.0	5.0 ± 0.3	147.3 ± 8.6	58.8 ± 6.5	78.0	60.0
S9	13.3 ± 0.9	1.8 ± 0.2	120.1 ± 7.7	19.7 ± 1.2	86.1	83.5
S10	16.6 ± 3.6	2.1 ± 0.1	120.2 ± 4.9	12.4 ± 0.6	87.2	89.6
S11	18.8 ± 1.5	4.6 ± 0.6	129.0 ± 4.8	26.3 ± 0.9	75.7	79.6
S12	12.2 ± 0.6	3.5 ± 0.7	104.8 ± 9.2	40.7 ± 3.4	71.1	61.1
S13	21.9 ± 0.1	3.6 ± 0.5	152.2 ± 2.3	17.9 ± 2.8	83.5	88.2
S14	17.8 ± 0.8	5.8 ± 0.5	129.8 ± 3.5	47.5 ± 0.7	67.4	63.3
S15	19.1 ± 0.3	3.1 ± 0.2	129.6 ± 9.8	33.3 ± 9.1	83.9	74.2
S16	17.8 ± 0.7	3.1 ± 1.0	118.7 ± 0.2	22.3 ± 3.6	82.3	81.1
S17	11.8 ± 0.1	3.2 ± 0.3	125.0 ± 6.6	26.8 ± 1.3	72.5	78.4

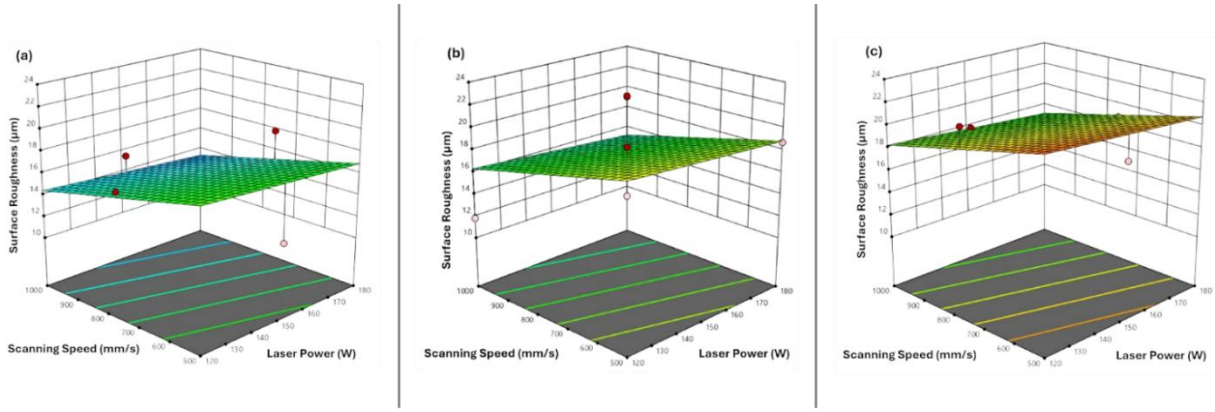

Figure 7-7:RSM graphs of the surface roughness (µm) before electropolishing versus the different input processing parameters: Hatch spacing (a) 45 µm, (b) 60 µm and (c) 75 µm.

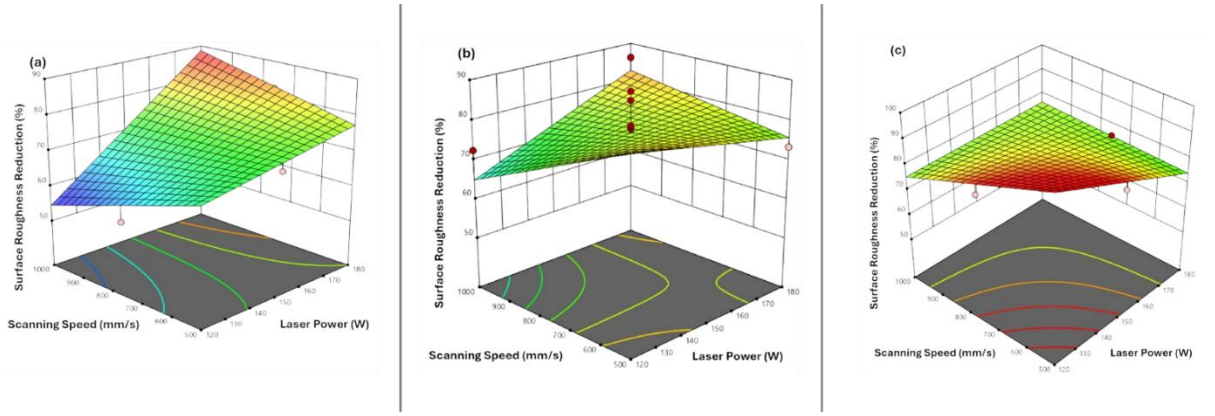

Figure 7-8: RSM graphs of the surface roughness reduction (%) after electropolishing versus the different input processing parameters: Hatch spacing (a) 45 µm, (b) 60 µm and (c) 75 µm.

As observed after electropolishing, there was a significant reduction in the average roughness of up to 87.25% for sample S10 where the average roughness Sa decreased from 16.64 to 2.12 µm. Samples S14 and S17 with the same VED of 33.33 J/mm^3 exhibited a similar roughness reduction of around 70%. On the other hand, the samples S4, S5, S6, S7, S8 and S10 had a VED of 55.56 J/mm^3 and the average roughness reduction ranged from 63.52 to 87.25%. In agreement with the study conducted by Li et. al. [107], as the electropolishing time is increased, the unmelted particles along with the rippling structures on the surface were removed. After electropolishing, the surface becomes much smoother and shows a undulating profile along its length as seen in **Figure 7-9**. Although the VED for these samples are same, the variation in the processing parameters resulted in the difference in the roughness reduction with the different hatch spacings (45, 60 and 75 µm) impacting significantly. In comparison to 60 and 75 µm

hatch spacing, a lower hatch spacing of 45 µm leads to a higher and more consistent surface roughness reduction as depicted by **Figure 7-8**. A lower hatch spacing of 45 µm enhanced the energy distribution and track overlap resulting in a reduction of the surface roughness with other input parameters of high laser power and lower scanning speeds. This also resulted in a low p-value ($p<0.05$) suggesting a statistically significance of the input parameters.

Figure 7-9 displays a straight edge and the strut joint of a stent sample after electropolishing. As shown, the surface roughness has reduced significantly to achieve better surface finish for the stents. As the surface roughness of stents should be between 1 to 5 µm to enhance the biocompatibility [342], electropolishing technique has reduced the average roughness of sample S9 to 1.83 µm. In a study conducted by Safdel et. al. [87], the surface roughness of as-fabricated different stent designs varied between 9.07 to 6.64 µm with strut diameters ranging from 435 to 132 µm. They also found that electropolishing could be used to improve the surface roughness. In the current study, a commercial electrolyte was used to remove unmelted particles on the surface, to smoothen the surface morphology and achieve a roughness, Sa of 1.83 µm compared to 13.3 µm starting value.

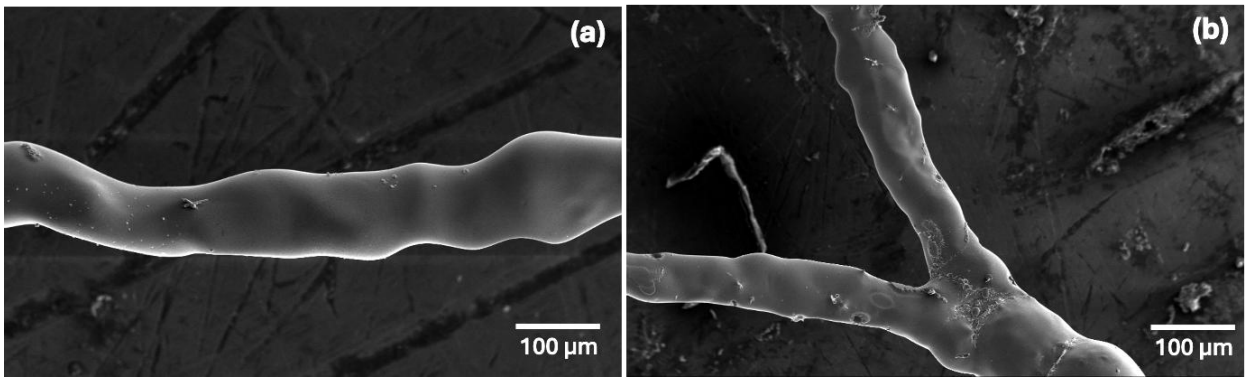

Figure 7-9: SEM graphs of stent samples after electropolishing showing (a) a single strut and (b) a strut joint.

7.3.5 Defect Formation

Figure 7-10 exhibits the optical micrographs showing the pores on the samples S4 and S16 which has showed the highest and lowest relative densities. Also, **Table 7-5** presents the average porosity (%) of these samples which has been calculated using ImageJ for analysis.

As shown by the **Figure 7-10**(a) & (b), sample S4 has a lower average number of pores as calculated using ImageJ. Lower average porosity indicates that the sample has less defects resulting in a higher density. As verified in Section 3.3, the relative density of S4 is the highest amongst all the processed samples. Also, fewer defects help in improving the overall quality of the produced part and its integrity. On the other hand, sample S16 (as shown in **Figure 7-10**(c) & (d)) has higher average porosity resulting in decreased quality and performance of the stent sample. This also indicates poor mechanical strength and resistance to failure. Although this ImageJ analysis can be an indicator of the localized porosity in the stent samples, however, the overall porosity could have significant variations. Further characterization techniques should be utilized to understand the overall distribution of porosity such as X-ray micro CT.

Table 7-5: Average porosity (%) of the samples with highest and lowest relative densities.

Sample Name	Average Porosity (%)
S4	0.55
S16	1.24

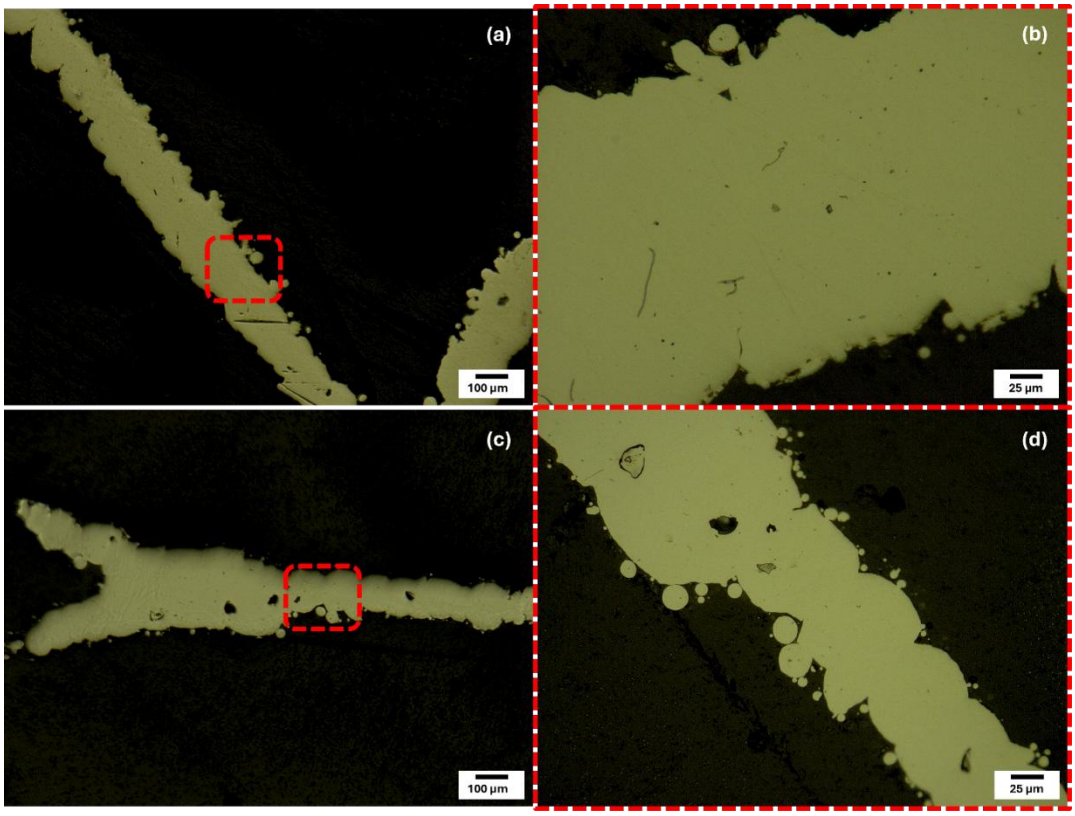

Figure 7-10: Optical micrographs exhibiting defects of sample: (a) S4, (b) magnified image of S4, (c) S16 and (d) magnified image of S16.

7.3.6 Phase Transformation Temperatures

The austenitic finish (Af) and martensitic start (Ms) temperatures, which are the most critical temperatures representing the phase transformation behaviour of the L-PBF produced stents processed using different VED's has been represented in **Figure 7-11**. As shown in **Figure 7-11**(a), the austenitic finish temperatures of all the samples lies in the range of 23 to 29°C. For a stent to exhibit superelasticity, the austenitic finish temperature should be below its intended use temperature, which is the human body temperature of 37°C in the case of stents [14,338,343]. Since, the processed stent samples have Af temperature below this temperature, they exhibit superelasticity behaviour as discussed by Agarwal et. al. [74]. The extent of their superelastic property varies and is highly dependent on the final composition of the produced sample [139,279]. Another important temperature which determines the functionality of the produced part is the martensitic start temperature (Ms). The relationship between Ms and the Ni content of the final product is well defined [98]. As discussed by Frenzel et. al. [94], the Ms temperature decreases with increase in Ni content which is influenced by the VED with which the part has been processed. As shown by Error! Reference source not found.(b), t

he Ms temperatures recorded in this work ranged from 7.5°C to 10.5°C. However, the typical trend of increasing Af and Ms with increasing VED was not evident. This could be due to the range of process parameters examined here not being wide enough in terms of laser power, scanning speed and hatch spacing, which in turn lead to relatively little difference in resulting Ms phase transformation temperatures. Additionally, this lack of phase change temperature variability or trend is likely a result of superimposed microstructural differences, including grain size, precipitate distribution, and local composition variations—all of which are known to influence transformation behaviour in shape memory alloys.

According to the study by Yan et. al. [108], laser process parameters which causes minimal changes to M_s temperature of the fabricated part when compared to that of the NiTi powder feedstock are the most suitable for the fabrication of the stents. In this study, the M_s temperature of the powder feedstock was found to be 14.35 °C which was also found to be close to the range of M_s of the fabricated stents. Therefore, it suggests that these laser process parameters are suitable for the fabrication of biomedical devices such as stents.

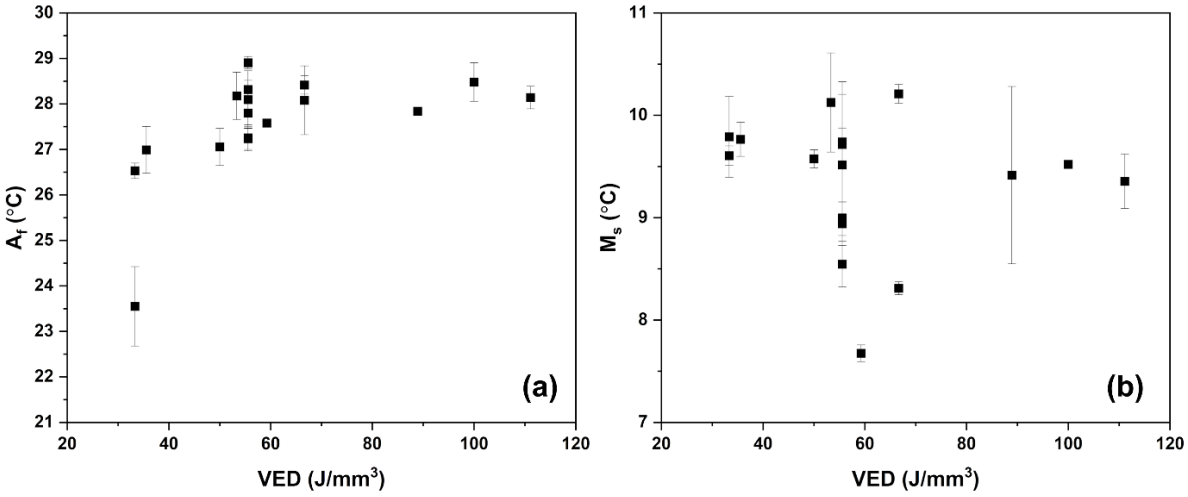

Figure 7-11: Phase transformation temperatures of L-PBF produced stents (a) Austenitic finish temperatures (A_f) and (b) Martensitic start temperatures (M_s).

Ni content of the samples was determined using EDX as shown in **Figure 7-12**. As discussed by Agarwal et. al. [321], Ni loss increases with an increase in the input energy density. A similar trend was observed in this study. With the varying process parameters resulting in variation of VED, Ni loss was observed of up to 2 at. %. Similar extent of Ni loss has been reported by several other researchers [72,189,344]. This Ni evaporation

from the NiTi matrix which takes place during the processing of the samples is a result of the high input energy resulting from the combination of the set laser power, scanning speed and hatch spacing.

Although Jamshidi et. al. [339] compensated the Ni loss due to the L-PBF process, the phase transformation temperatures were much higher ranging from 37 to 80 °C. In this study, all the as-fabricated stents had exhibited superelastic behaviour with A_f ranging between 23 to 29 °C showing that the pre-alloyed feedstock NiTi and the L-PBF process settings are essential control parameters. In agreement with the study conducted by Jamshidi et. al. [339] and Shen et. al. [82], the combination of Ni content and the phase transformation behaviour determines the functional properties of the stents including its superelastic behaviour and mechanical properties.

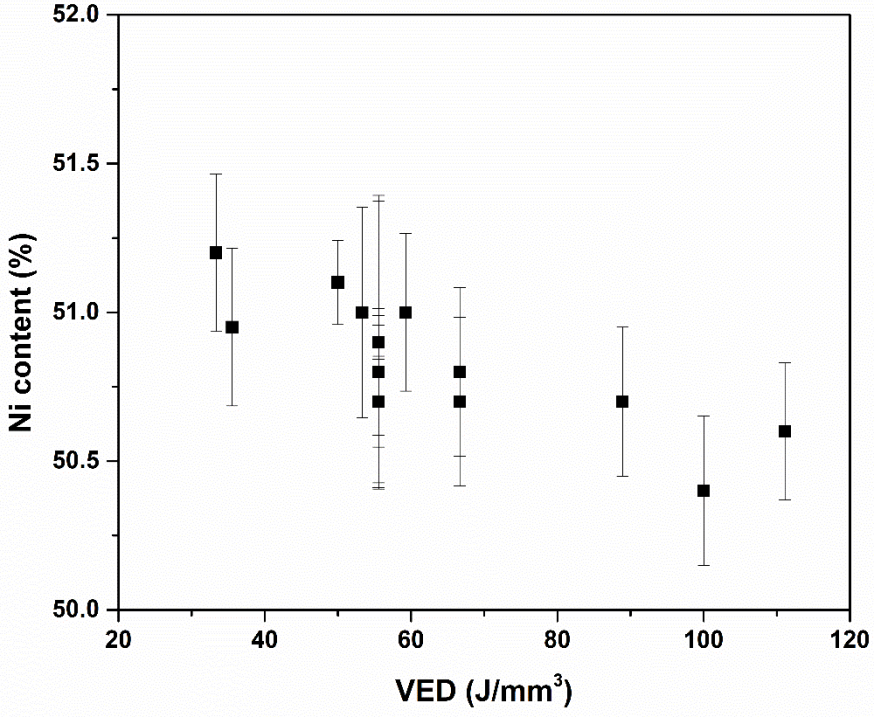

Figure 7-12: Ni content of the stent samples with their respective VED.

7.3.7 Thermal Gradient during processing

The study of thermal characteristics is helpful to understand the relation between the relative density, dimensional accuracy, surface morphology, nickel loss, surface roughness and the mechanical performance of the fabricated stents. The variation in the colour intensity from purple to yellow exhibit the temperature changes as captured by the in-situ infra-red (IR) sensors during the processing as depicted in **Figure 7-13**. The thermal characteristics of the fabricated stent samples with the highest and the lowest

relative densities, namely, S4 and S16 has been shown in **Figure 7-13** (a & d) respectively. As depicted by **Figure 7-14** samples S4 and S16 have a similar range of the normalized temperature per layer although there is a difference in their VED's as 55.56 and 88.89 J/mm3 respectively. As the VED increases, the nickel evaporation also increases as shown in **Figure 7-12** as nickel has a lower boiling point than titanium. The variations in the temperature per layer is of high importance to impact the mechanical performance, defect formation, microstructures, as well as phase transformation temperatures along with the nickel loss during the L-PBF processing [339]. These variations in higher thermal gradients leads to higher thermal cycling resulting in re-melting of the subsequent layers. Due to the lack of reliable emissivity data for the NiTi surface during LPBF, converting infrared sensor output (mV) to absolute temperature (°C) is prone to significant error. To address this, the thermal data has been presented as normalized temperature, calculated using equation (1):

$$\mathrm{Tnorm} = \frac{\mathrm{V} - \mathrm{Vmin}}{\mathrm{Vmax} - \mathrm{Vmin}} \qquad (1)$$

The pyrometer used measures in-line with the laser optical path. The recorded data is therefore recorded at the same time and location of the laser interaction with the surface. This approach ensures consistent thermal comparison while avoiding inaccuracies from uncertain emissivity. Normalized mapping has been used in prior work to highlight relative heat input and spatial gradients within metal AM produced parts [71,345–347].

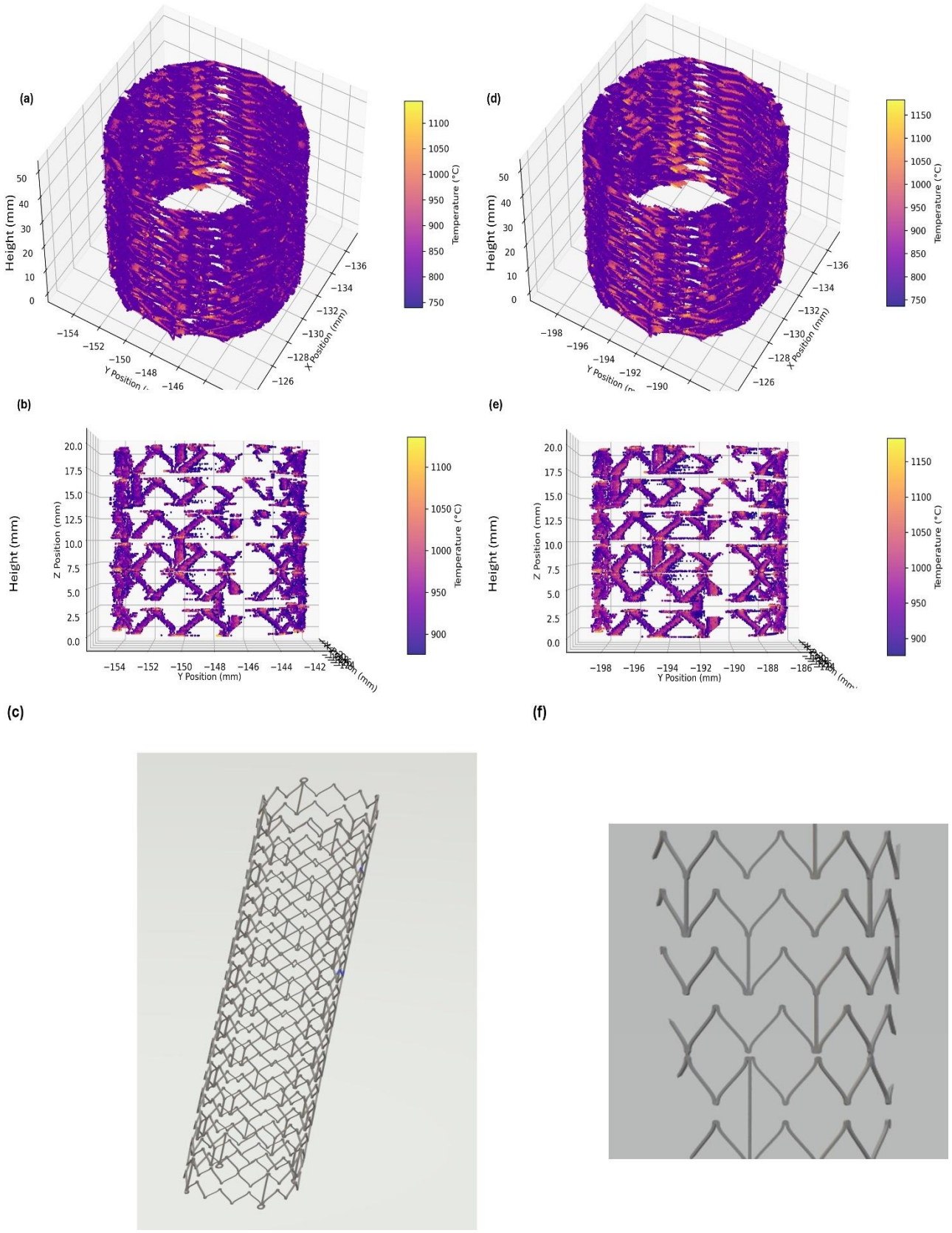

Figure 7-13: Thermal distribution of the stent samples (a) Isometric view S4 (b) Side view S4, (c) CAD file, (d) Isometric view S16, (e) side view S16 and (f) CAD file of side face.

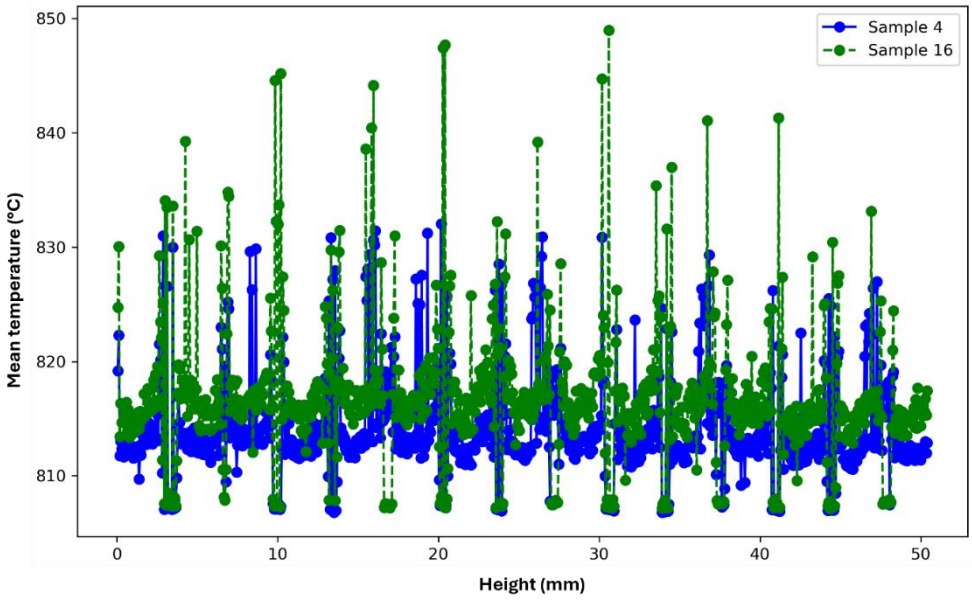

Figure 7-14: Mean temperature per layer of selected samples.

7.3.8 Stress-Strain Analysis

The load-displacement response has been presented in **Figure 7-15**(a) for the samples with highest relative density S4 and one with the lowest relative density S16 in comparison with a commercially available nitinol stent. **Figure 7-15** displays the normalized displacement plotted against the load as this was a load-controlled experiment. As observed both the samples processed via L-PBF exhibits total recoverability. It is also evident that the slope of the curve is very steep which is attributed by the release of the internal stresses. Another important factor determining the load-displacement performance is the strut size of the stents. This has been exhibited in a study conducted by Xiong et. al. [73] where higher strut diameter of 500 µm showed poor deformation capacity in comparison to thinner strut diameters of 100 µm. It has been noted that thinner struts of lesser than 200 µm as depicted in this study, deliver better flexibility, thereby increasing the recoverability of the stent structure.

As shown by **Figure 7-15** (b), an aged L-PBF produced stent sample has been compared to a commercial nitinol stent. The heat treatment of the stent sample was performed in a tube furnace in argon atmosphere at 450 °C for 1.5 hours. The stent sample was cooled down to room temperature in the tube furnace itself. The aged stent sample could withstand a higher force than the commercial stent which proves that ageing heat

treatment is a promising post-processing technique to improve the mechanical performance of the L-PBF fabricated nitinol sample.

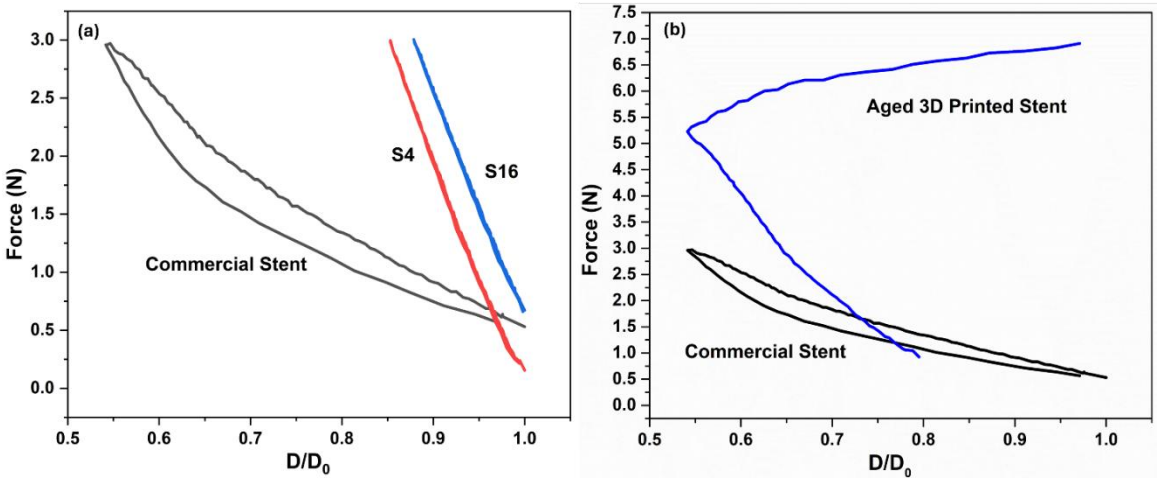

Figure 7-15: Load-displacement graph for (a) L-PBF produced stents vs commercial nitinol stents and (b) Aged L-PBF produced stents vs commercial nitinol stents, n = 3.

7.4 Conclusion

In this study, the L-PBF processing parameters according to the Box-Behnken design of the nitinol stents has been related to the relative density, defect formation, surface roughness before and after electropolishing, surface morphology, dimensional accuracy, composition, phase transformation temperatures and mechanical performance. The thermal gradient per layer of the stents were gathered during processing and analysed. The main findings and results are summarized as follows:

a. The L-PBF process led to a strut diameter ranging from 148 to 201 µm which was higher than that provided in the CAD file of 100 µm.

b. The average surface roughness Sa of the as-fabricated nitinol stent samples ranged from 11.81 to 22.81 µm. A reduction of up to 87.25% was observed for the sample S10 with a final surface roughness of 2.21 µm after electropolishing.

c. Sample S4 had highest relative density (99.49%) with S16 showing the lowest density (85.19%). Samples S8 and S11 had high relative densities of 99.40 and 99.11% respectively.

d. Sample S4 exhibited an average porosity of 0.55% and S16 showed the lowest average porosity of 1.24%. ImageJ analysis provides a good indication of the localised porosity of the samples. However, further analysis is needed for the overall porosity measurement.

e. The DSC curves exhibited the austenitic finish temperatures in the range of 23 to 29 °C owing to superelastic nature of the as-fabricated stents. A nickel loss of up to 2% was observed which produced M_s values of the stent samples between 7.5 to 10.5 °C.

f. Electropolishing was found to be an effective method to attain the surface finish needed by removing the unmelted particles after L-PBF processing and reduce the high surface roughness of the stent surface.

To better understand the phase characteristics, XRD of the samples larger than the stents must be assessed. SEM-EBSD characterization should be considered to fully understand the complexity of the microstructures formed which further controls the functionality of the stents. However, this study reveals that L-PBF is a suitable manufacturing technique to produce complex and intricate stents structures with the processing parameters helpful to produce them with an austenitic finish temperature below the room temperature. A further confirmation through this study was made that electropolishing is a good post-processing technique to achieve the desired surface finish of the stent structures. To optimize the dimensional accuracy, porosity levels, phase characteristics and mechanical performance along with the surface finish of the stents, it is essential to carefully control the processing parameters of the L-PBF technique and the electropolishing process. Further optimization of the electropolishing parameters such as voltage, time and flow rate could further reduce the surface roughness of the stent samples. Another electrolyte with a combination of methanol with perchloric acid could also be utilised to enhance the surface finish of the stent samples.

Chapter 8

8 Conclusion and future work

8.1 Research summary

An alloy of nickel and titanium, nitinol has found its place at the forefront of innovative solutions for biomedical applications, specifically as a material of choice for stents. The unique properties of nitinol add to the functionality for the stents over traditional materials such as stainless steel or cobalt-chromium alloys. Its ability to undergo high deformation and recovery to its original shape make it applicable to the dynamic conditions of biomedical implant applications. Still, its machinability is challenging via conventional manufacturing techniques. Additionally, the complex phase transformation behaviour and high work hardening rates restrict design capabilities and manufacturing precision. These constraints act as a barrier to produce bespoke, detailed and high-performing biomedical devices.

This doctoral thesis presents a detailed investigation in the potential of Laser Powder Bed Fusion (L-PBF) to combat these challenges and utilize the full capability of nitinol in biomedical applications. Explicitly, this work examines the effects of the L-PBF process parameters and the post-processing parameters of ageing heat treatments and electropolishing on the functional properties of Ni-rich nitinol for the use as stents. The thesis addresses the gap of knowledge and provides a new complex understanding of the links between additive manufacturing, post-processing strategies and the resulting performance for nitinol for application as printed stents.

Chapter 3 investigates the influence of heat treatment time and temperature on the physical, mechanical, and functional properties of nitinol wire samples manufactured through traditional wire-drawing techniques. It was determined that post-processing such as ageing heat treatment was successful in changing the transformation temperatures, and hardness values and increasing the recovery strain of Ni-rich nitinol wires. This preliminary examination confirmed the effect of heat treatment on the wires to achieve targeted functional properties for the intended applications. It was shown from this work that increasing heat treatment temperatures and times increased the samples' hardness and improved the nitinol wires' recovery strain with wires treated at 500°C for 120 mins

showing the highest recovery. While most heat-treated samples showed a decrease in density compared to the as-received wire (6.45 g/cm³), one exception—sample 3, treated at 400 °C for 60 minutes—exhibited an increased density of 6.85 g/cm³. This shows that both time and temperature can be tailored to modulate density within a controlled range of 5.85 to 6.85 g/cm³. Thermal analysis showed that higher heat treatment temperatures reduced the austenite finish (Af) temperature and sharpened the phase transition curves, pointing to decreased internal stresses and enhanced lattice mobility. These findings highlight the importance of carefully optimizing heat treatment protocols to tailor nitinol's performance characteristics for biomedical and actuation-based applications, particularly where high strain recovery and precise transformation behaviour are required. Since post-processing on traditionally manufactured nitinol wires to achieve altered functional properties was found to be successful, further investigations were conducted on samples produced via L-PBF.

Chapter 4 investigates the effects of single-step ageing heat treatment on Ni-rich NiTi cuboid samples fabricated via L-PBF, with a focus on how varying ageing temperatures (400°C, 500°C, and 600°C) and durations (30, 60, and 90 minutes) influence the material properties. All L-PBF-fabricated samples initially exhibited Af temperatures below room temperature, indicating expected superelasticity. Ageing at 400°C caused the Af to rise above room temperature, and longer ageing durations promoted higher martensitic phase fractions. At 500°C, the Af remained closer to room temperature, with both martensitic and austenitic phases present, suggesting a transitional phase state. Samples aged at 600°C exhibited significantly lower Af values and were composed entirely of the austenitic phase, as confirmed by XRD. These high-temperature-aged samples also demonstrated the largest crystallite sizes, ranging from 38.4 to 47.58 nm, whereas samples aged at 400°C retained smaller crystallite sizes between 6 and 22 nm. As temperature and time increased, a consistent decrease in microhardness was observed across all sample groups, with values dropping from 380 HV in as-fabricated samples to as low as 270 HV in highly aged conditions (particularly in sample S4). This softening is attributed to the reduction in internal stresses and changes in phase constitution, particularly the dominance of the more ductile austenitic phase at higher ageing temperatures. The same softening behavior was observed in other L-PBF sample sets (S1, S2, and S3), indicating the broad applicability of these trends regardless of initial print settings. In conclusion, the study highlights the critical impact of ageing parameters

on tailoring the phase stability, crystallinity, and hardness of NiTi components. Through precise control of ageing temperature and time, the performance characteristics of L-PBF-produced NiTi alloys can be optimized for specific applications, especially in fields requiring finely tuned superelastic and shape memory effects and mechanical performance, such as biomedical implants and actuators.

From Chapter 5, it was shown how variations in laser power (150 W and 180 W) and scanning speed (500 mm/s and 1000 mm/s) influence the physical properties and microstructural characteristics of Ni-rich nitinol components fabricated via L-PBF. The sample densities ranged between 97.9% and 99.5%, while microhardness values were measured within the range of 250 to 300 HV0.1. At a constant scanning speed of 1000 mm/s, variations in power had minimal effect on both hardness and density. However, at a slower scanning speed of 500 mm/s, lower hardness and density values were observed, regardless of power. Microstructural analysis revealed that samples processed at 500 mm/s displayed larger grain sizes due to the prolonged laser exposure, allowing more time for grain growth—a behavior explained by the scanning speed's effect on dendritic spacing. Additionally, samples processed with 180 W laser power exhibited a bimodal grain structure resulting from the dual effects of Ostwald Ripening and L-PBF-induced recrystallization. These samples also had higher lattice strain, weakened B2 austenite peak intensities, and dual-phase transformation peaks during DSC analysis, along with higher austenite finish temperatures (Af) and wider transformation intervals. In contrast, samples produced at 150 W laser power exhibited unimodal grain and subgrain structures with stronger B2 peak intensities, lower lattice strains, and single, well-defined transformation peaks. The thermal response was more stable in these lower-power samples, suggesting improved structural homogeneity. Moreover, nickel evaporation was found to correlate with higher energy input, particularly at lower scanning speeds. Overall, the study underscores the critical role of energy input—regulated in this case by both power and speed—in tailoring the microstructural and functional performance of L-PBF-processed nitinol components.

Chapter 6 explores the influence of L-PBF processing parameters on the corrosion behaviour of NiTi and Ti-6Al-4V alloys through a 2^3 design of experiments, using compositional and electrochemical analyses as key evaluative methods. The corrosion resistance of the fabricated samples was primarily assessed using EIS and cyclic polarisation in both Hanks and Ringer's solutions. Results from EIS confirmed that both

NiTi and Ti-6Al-4V exhibited good corrosion resistance, which improved with higher laser power and scanning speed. Samples such as NiTi5, NiTi7, and Ti-6Al-4V demonstrated greater stability in their passive oxide films. Interestingly, a lower hatch distance increased elemental loss, yet combining a low hatch distance with higher laser power proved effective in enhancing the passivation layer and therefore corrosion resistance. Microscopic evaluation and polarisation testing further revealed that the presence of gas pore defects, typical in additively manufactured components, negatively impacted corrosion resistance as these defects became exposed during testing. It was found that such imperfections could serve as initiation sites for corrosion. Through statistical analysis, the optimal processing parameters for achieving improved corrosion resistance in NiTi samples were determined to be a laser power of 135W, a scanning speed of 1125 mm/s, and a hatch distance of 0.08 mm. Overall, this study provides critical insights into how L-PBF process parameters directly affect corrosion resistance, and it underscores the importance of carefully balancing laser power, scanning speed, and hatch distance to tailor surface passivation and structural integrity for biomedical and engineering applications.

Chapter 7 explores the additive manufacturing of Ni-rich nitinol vascular stents using L-PBF, aiming to optimize process parameters for improved mechanical performance, surface quality, and biocompatibility. Nitinol's superelastic and shape memory properties make it ideal for biomedical applications, but traditional manufacturing techniques are limited in producing complex, patient-specific designs. Through a Box-Behnken Design of Experiments, the effects of L-PBF parameters on relative density, surface roughness, porosity, microstructure, and phase transformation behaviour were systematically investigated. Dimensional analysis revealed that fabricated struts exceeded the CAD design dimensions, while surface roughness ranged from 11.81 to 22.81 μm. Electropolishing significantly improved surface finish, reducing roughness by up to 87.25%. Relative densities reached up to 99.49% in optimal samples, and in-situ thermal monitoring showed build-layer temperatures between 750–1150 °C, influencing microstructural development. DSC confirmed the preservation of superelastic behaviour, with austenitic finish temperatures between 23–29 °C and martensitic start temperatures from 7.5–10.5 °C. The study demonstrates that combining L-PBF with targeted post-processing—particularly electropolishing—enables the fabrication of functionally viable nitinol stents with enhanced performance and biocompatibility. These findings lay the

groundwork for future advancements in patient-specific medical devices using additive manufacturing technologies.

8.2 Future scope of work

The key findings of this study has laid a strong foundation in understanding the influence of optimized L-PBF parameters and post-processing techniques for Ni-rich nitinol in biomedical stent applications. Although several findings of this doctoral thesis has contributed in addressing the knowledge gaps for fabrication of Ni-rich nitinol stents via L-PBF, there are various numerous avenues for further investigations. Several promising directions for future work are suggested as below:

- In depth microstructural characterization can be conducted using advanced analytical techniques such as transmission electron microscopy (TEM), electron back scattered diffraction (EBSD) and atom probe tomography (APT) to better understand the nanoscale precipitates, grain orientation and crystallographic texture. These fine-scale features could offer deeper understanding to correlate the microstructures with the functional and mechanical properties of the fabricated nitinol parts.
- Further investigations should be conducted to combine multi-stage post-processing protocol incorporating hot isostatic pressing (HIP) for defect reduction, surface passivation for better corrosion resistance and surface finishing techniques to further improve surface quality. Investigating the synergies between these techniques could lead to further enhancements in device performance and longevity.
- Comprehensive mechanical testing comprising of fatigue tests under cyclic loading, tensile testing and radial compression tests should be conducted in simulated body fluids at elevated temperatures of 37 °C to better mimic the operational environment of the stents.
- In vivo tests for long-term biological performance should be conducted to understand the inflammatory response, cell proliferation and implantation to establish the safety and efficacy of L-PBF manufactured nitinol stents.
- Further analysis should be made to understand how the recyclability of the nitinol powder affects the properties of the produced parts. Powder degradation

mechanisms and their impact on the parts should be employed to quantify the environmental benefits and trade-offs using life cycle assessments (LCA) and energy audits.

- Compliance with medical device regulations should also be looked into by developing a robust quality assurance protocol, documentation standards and repeatability tests to align with the implantable medical device industry.

Continuous advancements in this sector will be pivotal to develop next-generation stents which are durable and customisable to the individual needs of the patient. The combination of L-PBF with advanced post-processing will enhance the stents performance leading to a redefinition the paradigm of personalized medical implants.

References

[1] Swain R. Stents Market - By Product (Vascular Stents, Non-vascular Stents), By Material (Metal, Polymer), By Type, (Self-expandable Stents, Balloon-expandable Stents), By End-use (Hospitals, Ambulatory Surgical Centers) & Forecast, 2022-2028 2022:300. https://www.gminsights.com/industry-analysis/stent-market.

[2] Mani G, Feldman MD, Patel D, Agrawal CM. Coronary stents: A materials perspective. Biomaterials 2007;28:1689–710. https://doi.org/10.1016/j.biomaterials.2006.11.042.

[3] Dutau H, Musani AI, Plojoux J, Laroumagne S, Astoul P. The use of self-expandable metallic stents in the airways in the adult population. Expert Rev Respir Med 2014;8:179–90. https://doi.org/10.1586/17476348.2014.880055.

[4] Ar N, Ae O, Be N. Case Report Choanoplasty in a 10 Day Old Child : A Case Report 2020:2–4.

[5] Agnusdei L, Del Prete A. Additive manufacturing for sustainability: A systematic literature review. Sustain Futur 2022;4:100098. https://doi.org/10.1016/j.sftr.2022.100098.

[6] Javaid M, Haleem A, Singh RP, Suman R, Rab S. Role of additive manufacturing applications towards environmental sustainability. Adv Ind Eng Polym Res 2021;4:312–22. https://doi.org/10.1016/j.aiepr.2021.07.005.

[7] Ford S, Despeisse M. Additive manufacturing and sustainability: an exploratory study of the advantages and challenges. J Clean Prod 2016;137:1573–87. https://doi.org/10.1016/j.jclepro.2016.04.150.

[8] Yang S, Tang Y, Zhao YF. A new part consolidation method to embrace the design freedom of additive manufacturing. J Manuf Process 2015;20:444–9. https://doi.org/10.1016/j.jmapro.2015.06.024.

[9] Mercelis P, Kruth J. Residual stresses in selective laser sintering and selective laser melting. Rapid Prototyp J 2006;12:254–65. https://doi.org/10.1108/13552540610707013.

[10] DebRoy T, Wei HL, Zuback JS, Mukherjee T, Elmer JW, Milewski JO, et al.

Additive manufacturing of metallic components – Process, structure and properties. Prog Mater Sci 2018;92:112–224. https://doi.org/10.1016/j.pmatsci.2017.10.001.

[11] Kumar P, Huang S. Effect of Pre-strain, Temperature, and Time on the Recovery Behavior of Nitinol. Shape Mem Superelasticity 2023;9:5–10. https://doi.org/10.1007/s40830-023-00413-5.

[12] Wadood A. Brief overview on nitinol as biomaterial. Adv Mater Sci Eng 2016;2016. https://doi.org/10.1155/2016/4173138.

[13] Ryhänen J. Biocompatibility of Nitinol. Minim Invasive Ther Allied Technol 2000;9:99–105. https://doi.org/10.3109/13645700009063056.

[14] Sachdeva RCL, Miyazaki S, Dughaish ZH. Nitinol as a Biomedical Material. Ref Modul Mater Sci Mater Eng 2016:1–13. https://doi.org/10.1016/b978-0-12-803581-8.02246-3.

[15] Chaudhari R, Vora JJ, Parikh DM. A Review on Applications of Nitinol Shape Memory Alloy. vol. Part F1363. 2021. https://doi.org/10.1007/978-981-33-4176-0_10.

[16] Tarniţă D, Tarniţă DN, Bîzdoacă N, Mîndrilă I, Vasilescu M. Properties and medical applications of shape memory alloys. Rom J Morphol Embryol 2008;50:15–21.

[17] Bhardwaj A, Gupta AK, Padisala SK, Poluri K. Characterization of mechanical and microstructural properties of constrained groove pressed nitinol shape memory alloy for biomedical applications. Mater Sci Eng C 2019;102:730–42. https://doi.org/10.1016/j.msec.2019.04.070.

[18] Duerig TW, Wholey M. A comparison of balloon- and self-expanding stents. Minim Invasive Ther Allied Technol 2002;11:173–8. https://doi.org/10.1080/136457002760273386.

[19] Elahinia MH, Hashemi M, Tabesh M, Bhaduri SB. Manufacturing and processing of NiTi implants: A review. Prog Mater Sci 2012;57:911–46. https://doi.org/10.1016/j.pmatsci.2011.11.001.

[20] Shukla U, Garg K. Journey of smart material from composite to shape memory

alloy (SMA), characterization and their applications-A review. Smart Mater Med 2023;4:227–42. https://doi.org/10.1016/j.smaim.2022.10.002.

[21] Tarniţă D, Tarniţă DN, Hacman L, Copiluş C, Berceanu C. In vitro experiment of the modular orthopedic plate based on nitinol, used for human radius bone fractures. Rom J Morphol Embryol 2010;51:315–20.

[22] Ikeda T. 11 - The use of shape memory alloys (SMAs) in aerospace engineering. In: Yamauchi K, Ohkata I, Tsuchiya K, Miyazaki S, editors. Shape Mem. Superelastic Alloy., Woodhead Publishing; 2011, p. 125–40. https://doi.org/https://doi.org/10.1533/9780857092625.2.125.

[23] York PA, Wood RJ. Nitinol living hinges for millimeter-sized robots and medical devices. Proc - IEEE Int Conf Robot Autom 2019;2019-May:889–93. https://doi.org/10.1109/ICRA.2019.8794091.

[24] Shopinde. Blossom Collection/ Shape memory Jewellery n.d. https://shopinde.com/product/7745.

[25] Biffi CA, Fiocchi J, Tuissi A. Relevant aspects of laser cutting of NiTi shape memory alloys. J Mater Res Technol 2022;19:472–506. https://doi.org/10.1016/j.jmrt.2022.03.146.

[26] Fu CH, Liu JF, Guo A. Statistical characteristics of surface integrity by fiber laser cutting of Nitinol vascular stents. Appl Surf Sci 2015;353:291–9. https://doi.org/10.1016/j.apsusc.2015.06.105.

[27] Bernini M, Hellmuth R, O'Sullivan M, Dunlop C, McKenna CG, Lucchetti A, et al. Shape-Setting of Self-Expanding Nickel–Titanium Laser-Cut and Wire-Braided Stents to Introduce a Helical Ridge. Cardiovasc Eng Technol 2024;15:317–32. https://doi.org/10.1007/s13239-024-00717-2.

[28] Wen B, Shen L, Kang X. Laser Welding of Micro-Wire Stent Electrode as a Minimally Invasive Endovascular Neural Interface. Micromachines 2025;16. https://doi.org/10.3390/mi16010021.

[29] GEE. The Ulimate Guide to Nitinol Stent Manufacturing 2024. https://www.geenitinol.com/blog/ultimate-guide-nitinol-stent-manufacturing.

[30] NED. Medical Stents: Behind the Manufacturing Process 2021.

https://www.newequipment.com/learning-center/article/21154754/laser-processing-systems-for-medical-stent-manufacturing.

[31] Peters B, Ewert P, Berger F. The role of stents in the treatment of congenital heart disease: Current status and future perspectives. Ann Pediatr Cardiol 2009;2:3–23. https://doi.org/10.4103/0974-2069.52802.

[32] Zahedmanesh H, Lally C. Determination of the influence of stent strut thickness using the finite element method: Implications for vascular injury and in-stent restenosis. Med Biol Eng Comput 2009;47:385–93. https://doi.org/10.1007/s11517-009-0432-5.

[33] Palmaz JC. Intravascular stents: Tissue-stent interactions and design considerations. Am J Roentgenol 1993;160:613–8. https://doi.org/10.2214/ajr.160.3.8430566.

[34] Duerig TW, Tolomeo DE, Wholey M. An overview of superelastic stent design. Minim Invasive Ther Allied Technol 2000;9:235–46. https://doi.org/10.1080/13645700009169654.

[35] Stoeckel D, Pelton A, Duerig T. Self-expanding Nitinol stents: Material and design considerations. Eur Radiol 2004;14:292–301. https://doi.org/10.1007/s00330-003-2022-5.

[36] Zhang X, M. Q. Magnetic Shape Memory Alloys. Springer Singapore; 2022.

[37] Liu Y, Van Humbeeck J, Stalmans R, Delaey L. Some aspects of the properties of NiTi shape memory alloy. J Alloys Compd 1997;247:115–21. https://doi.org/10.1016/S0925-8388(96)02572-8.

[38] Yang L, Chen X, Zhang L, Li L, Kang S, Wang C, et al. Additive Manufacturing in Vascular Stent Fabrication. MATEC Web Conf 2019;253:03003. https://doi.org/10.1051/matecconf/201925303003.

[39] Liu X, Wang Y, Yang D, Qi M. The effect of ageing treatment on shape-setting and superelasticity of a nitinol stent. Mater Charact 2008;59:402–6. https://doi.org/10.1016/j.matchar.2007.02.007.

[40] Chekotu J, Groarke R, O'Toole K, Brabazon D. Advances in Selective Laser Melting of Nitinol Shape Memory Alloy Part Production. Materials (Basel)

2019;12:809. https://doi.org/10.3390/ma12050809.

[41] Hamilton RF, Bimber BA, Palmer TA. Correlating microstructure and superelasticity of directed energy deposition additive manufactured Ni-rich NiTi alloys. J Alloys Compd 2018;739:712–22. https://doi.org/10.1016/j.jallcom.2017.12.270.

[42] Duerig T. The metallurgy of Nitinol as it pertains to medical devices. Titan. Med. Dent. Appl., Elsevier; 2018, p. 555–70. https://doi.org/10.1016/B978-0-12-812456-7.00025-1.

[43] Goldstein D, Kabacoff L, Tydings J. Stress Effects on Nitinol Phase Transformations. JOM 1987;39:19–26. https://doi.org/10.1007/BF03258874.

[44] Adharapurapu RR. Phase transformations in nickel-rich nickel-titanium alloys : influence of strain-rate, temperature, thermomechanical treatment and nickel composition on the shape memory and superelastic characteristics. UC San Diego, 2007.

[45] Saedi S. Shape Memory Behavior of Dense and Porous NiTi Alloys Fabricated by Selective Laser Melting 2017:192.

[46] Ntina MI, Sophianopoulos DS. A new rate-dependent constitutive model of superelastic shape memory alloys and its simple application in a special truss moment frame simulation. Adv Civ Eng 2018;2018. https://doi.org/10.1155/2018/1634702.

[47] Dadbakhsh S, Speirs M, Van Humbeeck J, Kruth JP. Laser additive manufacturing of bulk and porous shape-memory NiTi alloys: From processes to potential biomedical applications. MRS Bull 2016;41:765–74. https://doi.org/10.1557/mrs.2016.209.

[48] Patel SK, Swain B, Roshan R, Sahu NK, Behera A. A brief review of shape memory effects and fabrication processes of NiTi shape memory alloys. Mater Today Proc 2020;33:5552–6. https://doi.org/10.1016/j.matpr.2020.03.539.

[49] Wei B, Liu Z, Nong B, Cao B, Lv X, Ren Y, et al. Microstructure, cracking behavior and mechanical properties of René 104 superalloy fabricated by selective laser melting. J Alloys Compd 2021;867.

https://doi.org/10.1016/j.jallcom.2020.158377.

[50] Seifi M, Salem A, Beuth J, Harrysson O, Lewandowski JJ. Overview of Materials Qualification Needs for Metal Additive Manufacturing. Jom 2016;68:747–64. https://doi.org/10.1007/s11837-015-1810-0.

[51] Farber E, Zhu JN, Popovich A, Popovich V. A review of NiTi shape memory alloy as a smart material produced by additive manufacturing. Mater Today Proc 2019;30:761–7. https://doi.org/10.1016/j.matpr.2020.01.563.

[52] Biffi CA, Fiocchi J, Valenza F, Bassani P, Tuissi A. Selective Laser Melting of NiTi Shape Memory Alloy: Processability, Microstructure, and Superelasticity. Shape Mem Superelasticity 2020;6:342–53. https://doi.org/10.1007/s40830-020-00298-8.

[53] Bartlett JL, Li X. An overview of residual stresses in metal powder bed fusion. Addit Manuf 2019;27:131–49. https://doi.org/10.1016/j.addma.2019.02.020.

[54] Daiy H, Najafi Y, Ragheb ZD, Abedi HR. A review study on thermal stability of powder-based additively manufactured alloys. J Alloys Compd 2023;965:171384. https://doi.org/10.1016/j.jallcom.2023.171384.

[55] Herzog D, Seyda V, Wycisk E, Emmelmann C. Additive manufacturing of metals. Acta Mater 2016;117:371–92. https://doi.org/10.1016/j.actamat.2016.07.019.

[56] Song X, Feih S, Zhai W, Sun CN, Li F, Maiti R, et al. Advances in additive manufacturing process simulation: Residual stresses and distortion predictions in complex metallic components. Mater Des 2020;193:108779. https://doi.org/10.1016/j.matdes.2020.108779.

[57] Boccato S, Torchio R, Kantor I, Morard G, Anzellini S, Giampaoli R, et al. The Melting Curve of Nickel Up to 100 GPa Explored by XAS. J Geophys Res Solid Earth 2017;122:9921–30. https://doi.org/10.1002/2017JB014807.

[58] Fischer P, Locher M, Romano V, Weber HP, Kolossov S, Glardon R. Temperature measurements during selective laser sintering of titanium powder. Int J Mach Tools Manuf 2004;44:1293–6. https://doi.org/10.1016/j.ijmachtools.2004.04.019.

[59] Dong W, Liang X, Chen Q, Hinnebusch S, Zhou Z, To AC. A new procedure for implementing the modified inherent strain method with improved accuracy in predicting both residual stress and deformation for laser powder bed fusion. Addit Manuf 2021;47:102345. https://doi.org/10.1016/j.addma.2021.102345.

[60] Jiménez A, Bidare P, Hassanin H, Tarlochan F, Dimov S, Essa K. Powder-based laser hybrid additive manufacturing of metals: a review. Int J Adv Manuf Technol 2021;114:63–96. https://doi.org/10.1007/s00170-021-06855-4.

[61] Bozkurt Y, Karayel E. 3D printing technology; methods, biomedical applications, future opportunities and trends. J Mater Res Technol 2021;14:1430–50. https://doi.org/10.1016/j.jmrt.2021.07.050.

[62] Cascadan D, Roberto Grandini C. Structure, Microstructure, and Some Selected Mechanical Properties of Ti-Ni Alloys. Recent Adv Metall Eng Electrodepos 2020. https://doi.org/10.5772/intechopen.86717.

[63] Halani PR, Kaya I, Shin YC, Karaca HE. Materials Science & Engineering A Phase transformation characteristics and mechanical characterization of nitinol synthesized by laser direct deposition. Mater Sci Eng A 2013;559:836–43. https://doi.org/10.1016/j.msea.2012.09.031.

[64] Halani PR, Shin YC. In Situ Synthesis and Characterization of Shape Memory Alloy Nitinol by Laser Direct Deposition. Metall Mater Trans A 2012;43:650–7. https://doi.org/10.1007/s11661-011-0890-x.

[65] Sadrnezhaad SK, Hosseini SA. Fabrication of porous NiTi-shape memory alloy objects by partially hydrided titanium powder for biomedical applications. Mater Des 2009;30:4483–7. https://doi.org/10.1016/j.matdes.2009.05.034.

[66] Aggarwal A, Kumar A. Particle scale modelling of porosity formation during selective laser melting process using a coupled DEM - CFD approach. IOP Conf Ser Mater Sci Eng 2019;529. https://doi.org/10.1088/1757-899X/529/1/012001.

[67] Hosseini SA, Karimidoost M, Emamian M, Mehrjoo M, Alishahi M. Electrochemical dealloying of porous NiTi alloy: Porosity evolution, corrosion resistance, and biocompatibility behavior. Intermetallics 2023;152:107756. https://doi.org/10.1016/j.intermet.2022.107756.

[68] Gu D, Ma C, Dai D, Yang J, Lin K, Zhang H, et al. Additively manufacturing-enabled hierarchical NiTi-based shape memory alloys with high strength and toughness. Virtual Phys Prototyp 2021;16:S19–38. https://doi.org/10.1080/17452759.2021.1892389.

[69] Kai WY, Chang KC, Wu HF, Chen SW, Yeh AC. Formation mechanism of Ni2Ti4Ox in NITI shape memory alloy. Materialia 2019;5:100194. https://doi.org/10.1016/j.mtla.2018.100194.

[70] Basu D, Wu Z, Meyer JLL, Larson E, Kuo R, Rollett A. Entrapped Gas and Process Parameter-Induced Porosity Formation in Additively Manufactured 17-4 PH Stainless Steel. J Mater Eng Perform 2021;30:5195–202. https://doi.org/10.1007/s11665-021-05695-3.

[71] Obeidi MA, Monu M, Hughes C, Bourke D, Dogu MN, Francis J, et al. Laser beam powder bed fusion of nitinol shape memory alloy (SMA). J Mater Res Technol 2021;14:2554–70. https://doi.org/10.1016/j.jmrt.2021.07.126.

[72] Ye D, Li SF, Misra RDK, Zheng R, Yang YF. Ni-loss compensation and thermomechanical property recovery of 3D printed NiTi alloys by pre-coating Ni on NiTi powder. Addit Manuf 2021;47. https://doi.org/10.1016/j.addma.2021.102344.

[73] Xiong Z, Li H, Yang H, Yang Y, Liu Y, Cui L, et al. Micro laser powder bed fusion of NiTi alloys with superior mechanical property and shape recovery function. Addit Manuf 2022;57:102960. https://doi.org/10.1016/j.addma.2022.102960.

[74] Agarwal N, Ryan Murphy J, Hashemi TS, Mossop T, O'Neill D, Power J, et al. Effect of Heat Treatment Time and Temperature on the Microstructure and Shape Memory Properties of Nitinol Wires. Materials (Basel) 2023;16. https://doi.org/10.3390/ma16196480.

[75] Resnina N, Palani IA, Belyaev S, Singh S, Liulchak P, Karaseva U, et al. Influence of heat treatment on the structure and martensitic transformation in NiTi alloy produced by wire arc additive manufacturing. Materialia 2021;20:101238. https://doi.org/10.1016/j.mtla.2021.101238.

[76] Saedi S, Turabi AS, Andani MT, Haberland C, Karaca H, Elahinia M. The influence of heat treatment on the thermomechanical response of Ni-rich NiTi alloys manufactured by selective laser melting. J Alloys Compd 2016;677:204–10. https://doi.org/10.1016/j.jallcom.2016.03.161.

[77] Yan X, Van Humbeeck J. Effect of Annealing on Strain-Temperature Response under Constant Tensile Stress in Cold-Worked NiTi Thin Wire. Smart Mater Res 2011;2011:1–6. https://doi.org/10.1155/2011/160927.

[78] Marattukalam JJ, Balla VK, Das M, Bontha S, Kalpathy SK. Effect of heat treatment on microstructure, corrosion, and shape memory characteristics of laser deposited NiTi alloy. J Alloys Compd 2018;744:337–46. https://doi.org/10.1016/j.jallcom.2018.01.174.

[79] Gao S, Bodunde OP, Qin M, Liao WH, Guo P. Microstructure and phase transformation of nickel-titanium shape memory alloy fabricated by directed energy deposition with in-situ heat treatment. J Alloys Compd 2022;898:1–22. https://doi.org/10.1016/j.jallcom.2021.162896.

[80] Karlík M, Haušild P, Adámek J, Drahokoupil J, Novák P, Perrière L. Microstructure of Ni–48 at.%Ti alloy prepared from powder and by conventional metallurgy. Acta Phys Pol A 2018;134:765–8. https://doi.org/10.12693/APhysPolA.134.765.

[81] Kurz BW. Solidification Microstructure - Processing Maps : Solidification Microstructure- Processing Maps : Theory and Application ** 2014;2648:443–52.

[82] Shen FL, Li HQ, Guo H, Guo NN, Fang XY. Effect of energy density on the superelastic property of Ni-rich NiTi alloy fabricated by laser powder bed fusion. Mater Sci Eng A 2022;854. https://doi.org/10.1016/j.msea.2022.143874.

[83] Shi G, Li L, Yu Z, Sha P, Cao Q, Xu Z, et al. Effect of crystallographic anisotropy on phase transformation and tribological properties of Ni-rich NiTi shape memory alloy fabricated by LPBF. Opt Laser Technol 2023;157:108731. https://doi.org/10.1016/j.optlastec.2022.108731.

[84] Guo W, Feng B, Yang Y, Ren Y, Liu Y, Yang H, et al. Effect of laser scanning

speed on the microstructure, phase transformation and mechanical property of NiTi alloys fabricated by LPBF. Mater Des 2022;215. https://doi.org/10.1016/j.matdes.2022.110460.

[85] Bormann T, Müller B, Schinhammer M, Kessler A, Thalmann P, De Wild M. Microstructure of selective laser melted nickel-titanium. Mater Charact 2014;94:189–202. https://doi.org/10.1016/j.matchar.2014.05.017.

[86] Adharapurapu RR. Phase transformations in nickel-rich nickel-titanium alloys : influence of strain-rate, temperature, thermomechanical treatment and nickel composition on the shape memory and superelastic characteristics. UC San Diego Electron Theses Diss 2008;3.

[87] Safdel A, Torbati-Sarraf H, Elbestawi MA. Laser powder bed fusion of differently designed NiTi stent structures having enhanced recoverability and superelasticity. J Alloys Compd 2023;954:170196. https://doi.org/10.1016/j.jallcom.2023.170196.

[88] Chen W, Yang Q, Huang S, Huang S, Kruzic JJ, Li X. Laser power modulated microstructure evolution, phase transformation and mechanical properties in NiTi fabricated by laser powder bed fusion. J Alloys Compd 2021;861:157959. https://doi.org/10.1016/j.jallcom.2020.157959.

[89] Chmielewska A, Wysocki BA, Gadalińska E, MacDonald E, Adamczyk-Cieślak B, Dean D, et al. Laser powder bed fusion (LPBF) of NiTi alloy using elemental powders: the influence of remelting on printability and microstructure. Rapid Prototyp J 2022;28:1845–68. https://doi.org/10.1108/RPJ-08-2021-0216.

[90] Wang Z, Yang Z, Liu F, Zhang W. Influence of the scanning angle on the grain growth and mechanical properties of Ni10Cr6W1Fe9Ti1 HEA fabricated using the LPBF–AM method. Mater Sci Eng A 2023;864:144596. https://doi.org/10.1016/j.msea.2023.144596.

[91] Ehsan Saghaian S, Nematollahi M, Toker G, Hinojos A, Shayesteh Moghaddam N, Saedi S, et al. Effect of hatch spacing and laser power on microstructure, texture, and thermomechanical properties of laser powder bed fusion (L-PBF) additively manufactured NiTi. Opt Laser Technol 2022;149:107680. https://doi.org/10.1016/j.optlastec.2021.107680.

[92] Yoon SH, Yeo DJ. Phase transformations of nitinol shape memory alloy by varying with annealing heat treatment conditions. Smart Mater III 2004;5648:208. https://doi.org/10.1117/12.582381.

[93] Agarwal N, Monu MCC, Tamil Selvam K, Obeidi MA, Brabazon D. Study of the effects of laser power and scanning speed on the microstructural morphologies and physical properties of L-PBF produced Ni52.39Ti47.61. J Mater Res Technol 2023. https://doi.org/https://doi.org/10.1016/j.jmrt.2023.11.146.

[94] Frenzel J, George EP, Dlouhy A, Somsen C, Wagner MFX, Eggeler G. Influence of Ni on martensitic phase transformations in NiTi shape memory alloys. Acta Mater 2010;58:3444–3458. https://doi.org/DOI.

[95] Patel SK, Swain B, Roshan R, Sahu NK, Behera A. A brief review of shape memory effects and fabrication processes of NiTi shape memory alloys. Mater Today Proc 2020;33:5552–6. https://doi.org/10.1016/j.matpr.2020.03.539.

[96] Speirs M, Wang X, Van Baelen S, Ahadi A, Dadbakhsh S, Kruth J-P, et al. On the Transformation Behavior of NiTi Shape-Memory Alloy Produced by SLM. Shape Mem Superelasticity 2016;2:310–6. https://doi.org/10.1007/s40830-016-0083-y.

[97] Guo Y, Xu Z, Liu Y, Liu M, Sha P, Li L, et al. Achieving illustrious friction and corrosion resistance on a laser powder bed fusion nitinol rare earth alloy. Mater Today Adv 2023;17:100350. https://doi.org/10.1016/j.mtadv.2023.100350.

[98] Wen S, Liu Y, Zhou Y, Zhao A, Yan C, Shi Y. Effect of Ni content on the transformation behavior and mechanical property of NiTi shape memory alloys fabricated by laser powder bed fusion. Opt Laser Technol 2021;134:106653. https://doi.org/10.1016/j.optlastec.2020.106653.

[99] Guo Y, Klink A, Fu C, Snyder J. Machinability and surface integrity of Nitinol shape memory alloy. CIRP Ann - Manuf Technol 2013;62:83–6. https://doi.org/10.1016/j.cirp.2013.03.004.

[100] Gall K, Tyber J, Wilkesanders G, Robertson SW, Ritchie RO, Maier HJ. Effect of microstructure on the fatigue of hot-rolled and cold-drawn NiTi shape

memory alloys. Mater Sci Eng A 2008;486:389–403. https://doi.org/10.1016/j.msea.2007.11.033.

[101] Laleh M, Sadeghi E, Revilla RI, Chao Q, Haghdadi N, Hughes AE, et al. Heat treatment for metal additive manufacturing. Prog Mater Sci 2023;133:101051. https://doi.org/10.1016/j.pmatsci.2022.101051.

[102] Liu X, Wang Y, Yang D, Qi M. The effect of ageing treatment on shape-setting and superelasticity of a nitinol stent. Mater Charact 2008;59:402–6. https://doi.org/10.1016/j.matchar.2007.02.007.

[103] Pelton AR, Russell SM, Dicello J. The Physical Metallurgy of Nitinol for Medical Applications. JOM Phys Metall 2003;33.

[104] Duerig TW. The use of superelasticity in modern medicine. MRS Bull 2002;27:101–4. https://doi.org/10.1557/mrs2002.44.

[105] Pelton AR, Russell SM, DiCello J. The physical metallurgy of nitinol for medical applications. JOM 2003;55:33–7. https://doi.org/10.1007/s11837-003-0243-3.

[106] Shabalovskaya S, Anderegg J, Van Humbeeck J. Critical overview of Nitinol surfaces and their modifications for medical applications. Acta Biomater 2008;4:447–67. https://doi.org/10.1016/j.actbio.2008.01.013.

[107] Li X, Hao S, Du B, Feng B, Li H, Qiu P, et al. High-Performance Self-Expanding NiTi Stents Manufactured by Laser Powder Bed Fusion. Met Mater Int 2023;29:1510–21. https://doi.org/10.1007/s12540-022-01317-2.

[108] Yan L, Soh SL, Wang N, Ma Q, Lu WF, Dheen ST, et al. Evaluation and characterization of nitinol stents produced by selective laser melting with various process parameters. Prog Addit Manuf 2022;7:1141–53. https://doi.org/10.1007/s40964-022-00289-4.

[109] Pelton AR, Stöckel D, Duerig TW. Medical Uses of Nitinol. Mater Sci Forum 2000;327–328:63–70. https://doi.org/10.4028/www.scientific.net/MSF.327-328.63.

[110] Obeidi MA. Metal additive manufacturing by laser-powder bed fusion:Guidelines for process optimisation. Results Eng 2022;15:100473.

https://doi.org/10.1016/j.rineng.2022.100473.

[111] Ibrahim P, Garrard R, Penchev P, Man K, Cox SC, Dimov S, et al. Hybrid manufacturing and performance evaluation of β Ti-alloy stents. Mater Des 2024;247:113420. https://doi.org/10.1016/j.matdes.2024.113420.

[112] ISO. Standards n.d. https://www.iso.org/standards.html.

[113] ASTM. Annual Book of ASTM Standards n.d. https://www.astm.org/standards-and-solutions/bos.

[114] Trivedi M, Jee J, Silva S, Blomgren C, Pontinha VM, Dixon DL, et al. Additive manufacturing of pharmaceuticals for precision medicine applications: A review of the promises and perils in implementation. Addit Manuf 2018;23:319–28. https://doi.org/10.1016/j.addma.2018.07.004.

[115] Stockel D. Nitinol-A material with unusual properties. Endovasc Updat 11 1998:1–8.

[116] Chaghazardi Z, Wüthrich R. Review—Electropolishing of Additive Manufactured Metal Parts. J Electrochem Soc 2022;169:043510. https://doi.org/10.1149/1945-7111/ac6450.

[117] Oncel L, Acma ME. Effect of Heat Treatment Temperature and Heat Treatment Time on Properties and use of NiTi Shape Memory Implant Material. IARJSET 2017;4:64–9. https://doi.org/10.17148/iarjset.2017.4115.

[118] Akin E. Effect of Aging Heat Treatments on Ni52Ti48 Shape Memory Alloy. Dissertation 2010.

[119] Michutta J, Carroll MC, Yawny A, Somsen C, Neuking K, Eggeler G. Martensitic phase transformation in Ni-rich NiTi single crystals with one family of Ni4Ti3 precipitates. Mater Sci Eng A 2004;378:152–6. https://doi.org/10.1016/j.msea.2003.11.061.

[120] M. Karimzadeh M. R. Aboutalebi MTSSMA, Morakabati M. Adjustment of Aging Temperature for Reaching Superelasticity in Highly Ni-Rich Ti-51.5Ni NiTi Shape Memory Alloy. Mater Manuf Process 2016;31:1014–21. https://doi.org/10.1080/10426914.2015.1048468.

[121] Shamimi A, Amin-Ahmadi B, Stebner A, Duerig T. The Effect of Low Temperature Aging and the Evolution of R-Phase in Ni-Rich NiTi. Shape Mem Superelasticity 2018;4:417–27. https://doi.org/10.1007/s40830-018-0193-9.

[122] Shabalovskaya SA, Anderegg J, Laab F, Thiel PA, Rondelli G. Surface conditions of nitinol wires, tubing, and as-cast alloys. The effect of chemical etching, aging in boiling water, and heat treatment. J Biomed Mater Res Part B Appl Biomater 2003;65:193–203.

[123] Pelton AR. Nitinol fatigue: A review of microstructures and mechanisms. J Mater Eng Perform 2011;20:613–7. https://doi.org/10.1007/s11665-011-9864-9.

[124] Zapata Martínez R, Bose-Bandyopadhyay S, Burl A, Contreras-Almengor Ó, Aguilar Vega C, Saleeby K, et al. Comparative analysis of machining and electropolishing for surface quality improvement of shape memory nitinol samples additively manufactured by laser powder bed fusion. Addit Manuf Lett 2025;12. https://doi.org/10.1016/j.addlet.2024.100261.

[125] Reedlunn B, Daly S, Shaw J. Superelastic shape memory alloy cables: Part i - Isothermal tension experiments. Int J Solids Struct 2013;50:3009–26. https://doi.org/10.1016/j.ijsolstr.2013.03.013.

[126] Strand P. Standard Specification for iTeh Standards Document Preview iTeh Standards 1860;i:4–5.

[127] Semba H, Okabe N, Yamaji T, Okita K, Yamauchi K. Axial Compressive Behavior of Single-Stage Bellows of TiNi Shape Memory Alloy for Seismic Applications. Mater Sci Forum 2005;475–479:2055–8. https://doi.org/10.4028/www.scientific.net/msf.475-479.2055.

[128] Duerig TW, Pelton AR, Bhattacharya K. The Measurement and Interpretation of Transformation Temperatures in Nitinol. Shape Mem Superelasticity 2017;3:485–98. https://doi.org/10.1007/s40830-017-0133-0.

[129] Liu Y, Chen X, McCormick PG. Effect of low temperature ageing on the transformation behaviour of near-equiatomic NiTi. J Mater Sci 1997;32:5979–84. https://doi.org/10.1023/A:1018615127911.

[130] Rahim M, Frenzel J, Frotscher M, Pfetzing-Micklich J, Steegmüller R,

Wohlschlögel M, et al. Impurity levels and fatigue lives of pseudoelastic NiTi shape memory alloys. Acta Mater 2013;61:3667–86. https://doi.org/10.1016/j.actamat.2013.02.054.

[131] Maleckis K, Deegan P, Poulson W, Sievers C, Desyatova A, MacTaggart J, et al. Comparison of femoropopliteal artery stents under axial and radial compression, axial tension, bending, and torsion deformations. J Mech Behav Biomed Mater 2017;75:160–8. https://doi.org/10.1016/j.jmbbm.2017.07.017.

[132] Grenadier E, Shofti R, Beyar M, Lichtig H, Mordechowitz D, Globerman O, et al. Self-expandable and highly flexible nitinol stent: Immediate and long-term results in dogs. Am Heart J 1994;128:870–8. https://doi.org/10.1016/0002-8703(94)90582-7.

[133] ASTM Int. Standard Specification for Wrought Nickel-Titanium Shape Memory Alloys for Medical Devices and Surgical Implants. Annu B ASTM Stand 2012:1–6. https://doi.org/10.1520/F2063.

[134] ASTM. Standard Specification for Wrought 35Cobalt-35Nickel-20Chromium-10Molybdenum Alloy for Surgical Implant Applications (UNS R30035) n.d. https://store.astm.org/f0562-22.html.

[135] ASTM. Standard Specification for Wrought 18Chromium-14Nickel-2.5Molybdenum Stainless Steel Bar and Wire for Surgical Implants (UNS S31673) n.d. https://store.astm.org/f0138-19.html.

[136] Hughes SW. Archimedes revisited: A faster, better, cheaper method of accurately measuring the volume of small objects. Phys Educ 2005;40:468–74. https://doi.org/10.1088/0031-9120/40/5/008.

[137] ASTM B962: Standard test methods for density of compacted or sintered powder metallurgy (PM) products using Archimedes' Principle. 2017. https://doi.org/doi.org/10.1520/B0962-17.

[138] Sartorius. Manual of Weighing Applications, Part 1, Density. Mark Weigh Technol 1999:62.

[139] Sadrnezhaad K, Mashhadi F, Sharghi R. Heat treatment of Ni-Ti alloy for improvement of shape memory effect. Mater Manuf Process 1997;12:107–15.

https://doi.org/10.1080/10426919708935124.

[140] Elahinia MH. Shape memory alloy actuators: design, fabrication, and experimental evaluation. 1st ed. John Wiley \& Sons; 2016.

[141] Mao C, Dong J, Li H, Ou J. Seismic performance of RC shear wall structure with novel shape memory alloy dampers in coupling beams. In: Tomizuka M, Yun C-B, Lynch JP, editors., 2012, p. 83454G. https://doi.org/10.1117/12.917304.

[142] Fu CH, Sealy MP, Guo YB, Wei XT. Austenite-martensite phase transformation of biomedical Nitinol by ball burnishing. J Mater Process Technol 2014;214:3122–30. https://doi.org/10.1016/j.jmatprotec.2014.07.019.

[143] Vojtěch D. INFLUENCE OF HEAT TREATMENT OF SHAPE MEMORY NiTi ALLOY ON ITS MECHANICAL PROPERTIES n.d.

[144] Metals FW. Shape Setting n.d.

[145] Benafan O, Brown J, Calkins FT, Kumar P, Stebner AP, Turner TL, et al. Shape memory alloy actuator design: CASMART collaborative best practices and case studies. Int J Mech Mater Des 2014;10:1–42. https://doi.org/10.1007/s10999-013-9227-9.

[146] Drexel M, Selvaduray G, Pelton A. The effects of cold work and heat treatment on the properties of Nitinol wire. Med. Device Mater. IV Proc. Mater. Process. Med. Devices Conf. 2007, 2008, p. 114–9. https://doi.org/10.1361/cp2007mpmd114.

[147] Kök M, Dałdelen F, Aydołdu A, Aydołdu Y. The change of transformation temperature on NiTi shape memory alloy by pressure and thermal ageing. J. Phys. Conf. Ser., vol. 667, Institute of Physics Publishing; 2016. https://doi.org/10.1088/1742-6596/667/1/012011.

[148] Otsuka K, Ren X. Physical metallurgy of Ti-Ni-based shape memory alloys. Prog Mater Sci 2005;50:511–678. https://doi.org/10.1016/j.pmatsci.2004.10.001.

[149] Holec D, Bojda O, Dlouhý A. Ni4Ti3 precipitate structures in Ni-rich NiTi shape memory alloys. Mater Sci Eng A 2008;481–482:462–5. https://doi.org/10.1016/j.msea.2006.11.182.

[150] Khalil-Allafi J, Dlouhy A, Eggeler G. Ni4Ti3-precipitation during aging of NiTi shape memory alloys and its influence on martensitic phase transformations. Acta Mater 2002;50:4255–74. https://doi.org/10.1016/S1359-6454(02)00257-4.

[151] Sadiq H, Wong MB, Al-Mahaidi R, Zhao XL. The effects of heat treatment on the recovery stresses of shape memory alloys. Smart Mater Struct 2010;19. https://doi.org/10.1088/0964-1726/19/3/035021.

[152] Ma X, Zhou Y, Chen X, Lu G, Ji J, Zhao S. Effect of Temperature on Phase Transformation of NiTi-based Shape Memory Alloy. J Phys Conf Ser 2021;2109:012001. https://doi.org/10.1088/1742-6596/2109/1/012001.

[153] Golberg D, Xu Y, Murakami Y, Otsuka K, Ueki T, Horikawa H. High-temperature shape memory effect in Ti50Pd50 - xNix (x = 10, 15, 20) alloys. Mater Lett 1995;22:241–8. https://doi.org/10.1016/0167-577X(94)00256-8.

[154] Lahoz R, Puértolas JA. Training and two-way shape memory in NiTi alloys: Influence on thermal parameters. J Alloys Compd 2004;381:130–6. https://doi.org/10.1016/j.jallcom.2004.03.080.

[155] Luo HY, Abel EW. A comparison of methods for the training of NiTi two-way shape memory alloy. Smart Mater Struct 2007;16:2543–9. https://doi.org/10.1088/0964-1726/16/6/058.

[156] Speicher M, Hodgson DE, Desroches R, Leon RT. Shape memory alloy tension/compression device for seismic retrofit of buildings. J Mater Eng Perform 2009;18:746–53. https://doi.org/10.1007/s11665-009-9433-7.

[157] Aryan H, Ghassemieh M. A superelastic protective technique for mitigating the effects of vertical and horizontal seismic excitations on highway bridges. J Intell Mater Syst Struct 2017;28:1533–52. https://doi.org/10.1177/1045389X16672593.

[158] Shaw JA, Grummon DS, Foltz J. Superelastic NiTi honeycombs: Fabrication and experiments. Smart Mater Struct 2007;16. https://doi.org/10.1088/0964-1726/16/1/S17.

[159] Taha OY. Experimental study on two way shape memory effect training procedure for NiTiNOL shape memory alloy Transient Natural convection of

High Prandtl Number Fluids View project CFD and Experimental of Sand Screen Erosion View project 2018.

[160] Mechanical errors. Precis Manuf 2008:121–66. https://doi.org/10.1007/978-0-387-68208-2_4.

[161] NaberTherm. NaberTherm Laboratory furnaces brochure 2021.

[162] Rondelli G, Vicentini B. Localized corrosion behaviour in simulated human body fluids of commercial Ni-Ti orthodontic wires. Biomaterials 1999;20:785–92.

[163] labratories E. Density Determination of Solids and Liquids 2021.

[164] Elmer P. Guide to selection of differential scanning calorimetry (dsc) sample pans 2021.

[165] Commons W. User A1 2021.

[166] Rueden CT, Schindelin J, Hiner MC, DeZonia BE, Walter AE, Arena ET, et al. ImageJ2: ImageJ for the next generation of scientific image data. BMC Bioinformatics 2017;18. https://doi.org/10.1186/s12859-017-1934-z.

[167] Buehler WJ, Wang FE. A summary of recent research on the nitinol alloys and their potential application in ocean engineering. Ocean Eng 1968;1:105–20. https://doi.org/https://doi.org/10.1016/0029-8018(68)90019-X.

[168] Xu L, Wang R. The Effect of Annealing and Cold-drawing on the Super-elasticity of the Ni-Ti Shape Memory Alloy Wire. Mod Appl Sci 2010;4.

[169] Lee J, Shin YC. Effects of Composition and Post Heat Treatment on Shape Memory Characteristics and Mechanical Properties for Laser Direct Deposited Nitinol. Lasers Manuf Mater Process 2019;6:41–58. https://doi.org/10.1007/s40516-019-0079-5.

[170] Adharapurapu RR, Jiang F, Vecchio KS. Aging effects on hardness and dynamic compressive behavior of Ti-55Ni (at.%) alloy. Mater Sci Eng A 2010;527:1665–76. https://doi.org/10.1016/j.msea.2009.10.069.

[171] Haberland C, Elahinia M, Walker JM, Meier H, Frenzel J. On the development of high quality NiTi shape memory and pseudoelastic parts by additive

manufacturing. Smart Mater Struct 2014;23. https://doi.org/10.1088/0964-1726/23/10/104002.

[172] Haberland C, Meier H, Frenzel J. SMASIS2012-8040 ON THE PROPERTIES OF NI-RICH NITI SHAPE MEMORY PARTS PRODUCED BY SELECTIVE LASER MELTING 2012.

[173] Gallardo Fuentes, J.M.;Gumpel P. Phase Change Behavior of Nitinol Shape Memory Alloys. Adv Eng Mater 2002;4:437–52. https://doi.org/10.1002/1527-2648(20020717)4:7.

[174] SPINI TS, VALARELLI FP, CANÇADO RH, FREITAS KMS de, VILLARINHO DJ. Transition temperature range of thermally activated nickel-titanium archwires. J Appl Oral Sci 2014;22:109–17. https://doi.org/10.1590/1678-775720130133.

[175] Barik L, Samal S, Behera A, Rajak DK, Pruncu CI. On the replacement of steel by NITINOL as coupling agent in automobile shaft. ISSS J Micro Smart Syst 2021;10:87–102. https://doi.org/10.1007/s41683-021-00075-4.

[176] Ferreira. Systematic Review NiTi Wires 2012;17:71–82.

[177] Es-Souni M, Es-Souni M, Fischer-Brandies H. Assessing the biocompatibility of NiTi shape memory alloys used for medical applications. Anal Bioanal Chem 2005;381:557–67. https://doi.org/10.1007/s00216-004-2888-3.

[178] Costanza G, Tata ME. Developments , and New Applications : Materials (Basel) 2020;13:1–16.

[179] Hartl DJ, Lagoudas DC. Aerospace applications of shape memory alloys. Proc Inst Mech Eng Part G J Aerosp Eng 2007;221:535–52. https://doi.org/10.1243/09544100JAERO211.

[180] Thijs L, Montero Sistiaga ML, Wauthle R, Xie Q, Kruth JP, Van Humbeeck J. Strong morphological and crystallographic texture and resulting yield strength anisotropy in selective laser melted tantalum. Acta Mater 2013;61:4657–68. https://doi.org/10.1016/j.actamat.2013.04.036.

[181] Thampy V, Fong AY, Calta NP, Wang J, Martin AA, Depond PJ, et al. Subsurface Cooling Rates and Microstructural Response during Laser Based

Metal Additive Manufacturing. Sci Rep 2020;10:1–9. https://doi.org/10.1038/s41598-020-58598-z.

[182] Thijs L, Verhaeghe F, Craeghs T, Humbeeck J Van, Kruth J-P. A study of the microstructural evolution during selective laser melting of Ti–6Al–4V. Acta Mater 2010;58:3303–12. https://doi.org/10.1016/j.actamat.2010.02.004.

[183] Chen Z, Lu Y, Luo F, Zhang S, Wei P, Yao S, et al. Effect of Laser Scanning Speed on the Microstructure and Mechanical Properties of Laser-Powder-Bed-Fused K418 Nickel-Based Alloy. Materials (Basel) 2022;15. https://doi.org/10.3390/ma15093045.

[184] Wang X, Speirs M, Kustov S, Vrancken B, Li X, Kruth J-P, et al. Selective laser melting produced layer structured NiTi shape memory alloys with high damping properties and Elinvar effect. Scr Mater 2018;146:246–50. https://doi.org/10.1016/j.scriptamat.2017.11.047.

[185] Xue L, Atli KC, Zhang C, Hite N, Srivastava A, Leff AC, et al. Laser Powder Bed Fusion of Defect-Free NiTi Shape Memory Alloy Parts with Superior Tensile Superelasticity. Acta Mater 2022;229:117781. https://doi.org/10.1016/j.actamat.2022.117781.

[186] Wei S, Kumar P, Lau KB, Wuu D, Liew LL, Wei F, et al. Effect of heat treatment on the microstructure and mechanical properties of 2.4 GPa grade maraging steel fabricated by laser powder bed fusion. Addit Manuf 2022;59:103190. https://doi.org/10.1016/j.addma.2022.103190.

[187] Xue D, Zhou Y, Ren X. The effect of aging on the B2-R transformation behaviors in Ti-51at%Ni alloy. Intermetallics 2011;19:1752–8. https://doi.org/10.1016/j.intermet.2011.07.014.

[188] Bansiddhi A, Sargeant TD, Stupp SI, Dunand DC. Porous NiTi for bone implants: A review. Acta Biomater 2008;4:773–82. https://doi.org/10.1016/j.actbio.2008.02.009.

[189] Adharapurapu RR, Vecchio KS. Superelasticity in a new bioImplant material: Ni-rich 55NiTi alloy. Exp Mech 2007;47:365–71. https://doi.org/10.1007/s11340-006-9004-x.

[190] Stanford MK. Hardness and microstructure of binary and ternary nitinol compounds. Nasa/Tm—2016-218946 2016:46.

[191] Chad Hornbuckle B, Yu XX, Noebe RD, Martens R, Weaver ML, Thompson GB. Hardening behavior and phase decomposition in very Ni-rich Nitinol alloys. Mater Sci Eng A 2015;639:336–44. https://doi.org/10.1016/j.msea.2015.04.079.

[192] Khalil-Allafi J, Eggeler G, Dlouhy A, Schmahl WW, Somsen C. On the influence of heterogeneous precipitation on martensitic transformations in a Ni-rich NiTi shape memory alloy. Mater Sci Eng A 2004;378:148–51. https://doi.org/10.1016/j.msea.2003.10.335.

[193] Mohamad H, Mahmud AS, Nashrudin MN, Razali MF. Effect of ageing temperatures on pseudoelasticity of Ni-rich NiTi shape memory alloy. AIP Conf Proc 2018;1958. https://doi.org/10.1063/1.5034539.

[194] Kustov S, Mas B, Salas D, Cesari E, Raufov S, Nikolaev V, et al. On the effect of room temperature ageing of Ni-rich Ni-Ti alloys. Scr Mater 2015;103:10–3. https://doi.org/10.1016/j.scriptamat.2015.02.025.

[195] Fan QC, Zhang YH, Wang YY, Sun MY, Meng YT, Huang SK, et al. Influences of transformation behavior and precipitates on the deformation behavior of Ni-rich NiTi alloys. Mater Sci Eng A 2017;700:269–80. https://doi.org/10.1016/j.msea.2017.05.107.

[196] Obeidi MA, Mussatto A, Dogu MN, Sreenilayam SP, McCarthy E, Ahad IU, et al. Laser surface polishing of Ti-6Al-4V parts manufactured by laser powder bed fusion. Surf Coatings Technol 2022;434:128179. https://doi.org/10.1016/j.surfcoat.2022.128179.

[197] Obeidi MA, Conway A, Mussatto A, Dogu MN, Sreenilayam SP, Ayub H, et al. Effects of powder compression and laser re-melting on the microstructure and mechanical properties of additively manufactured parts in laser-powder bed fusion. Results Mater 2022;13:100264. https://doi.org/10.1016/j.rinma.2022.100264.

[198] Monu MCC, Kumar S. S, Brabazon D. Heat treatment of NiTi alloys: Influence of volumetric energy density on ageing parameters and the resulting physical

properties. J Mater Res Technol 2023;26:9532–55. https://doi.org/10.1016/j.jmrt.2023.09.251.

[199] Mussatto A, Groarke R, O'Neill A, Obeidi MA, Delaure Y, Brabazon D. Influences of powder morphology and spreading parameters on the powder bed topography uniformity in powder bed fusion metal additive manufacturing. Addit Manuf 2021;38:101807. https://doi.org/10.1016/j.addma.2020.101807.

[200] Wang Z, Everaerts J, Salvati E, Korsunsky AM. Evolution of thermal and mechanical properties of Nitinol wire as a function of ageing treatment conditions. J Alloys Compd 2020;819:153024. https://doi.org/10.1016/j.jallcom.2019.153024.

[201] Hadibeik S, Spieckermann F, Nosko M, Khodabakhshi F, Heydarzadeh Sohi M, Eckert J. High-Entropy Alloy-Induced Metallic Glass Transformation: Challenges Posed by in situ Alloying via Additive Manufacturing. Adv Eng Mater 2023;25. https://doi.org/10.1002/adem.202200764.

[202] CROSS WB, KARIOTIS AH, STIMLER FJ. Nitinol Characrerization Study. NASA Contract Reports 1969.

[203] Uchil J, Mohanchandra KP, Mahesh KK, Ganesh Kumara K. Thermal and electrical characterization of R-phase dependence on heat-treat temperature in Nitinol. Phys B Condens Matter 1998;253:83–9. https://doi.org/10.1016/S0921-4526(98)00378-0.

[204] ASTM F2004-17. Standard Test Method For Transformation Temperature Of Nickel-Titanium Alloys By Thermal Analysis. ASTM International, West Conshohocken, PA,: 2017. https://doi.org/10.1520/F2004-17.

[205] Khan LA, McCarthy E, Muilwijk C, Ahad IU, Brabazon D. Analysis of nitinol actuator response under controlled conductive heating regimes. Results Eng 2023;18. https://doi.org/10.1016/j.rineng.2023.101047.

[206] Ekoi EJ, Degli-Alessandrini G, Zeeshan Mughal M, Vijayaraghavan RK, Obeidi MA, Groarke R, et al. Investigation of the microstructure and phase evolution across multi-material Ni50.83Ti49.17-AISI 316L alloy interface fabricated using laser powder bed fusion (L-PBF). Mater Des 2022;221:110947.

https://doi.org/10.1016/j.matdes.2022.110947.

[207] Santoro M, Beshers DN. Nickel-titanium alloys: Stress-related temperature transitional range. Am J Orthod Dentofac Orthop 2000;118:685–92. https://doi.org/10.1067/mod.2000.98113.

[208] Florian G, Gabor AR, Nicolae CA, Rotaru A, Stănică N, Bîzdoacă NG, et al. Thermomechanical, calorimetric and magnetic properties of a Ni–Ti shape-memory alloy wire. J Therm Anal Calorim 2020;140:527–44. https://doi.org/10.1007/s10973-019-08869-3.

[209] Saburi T, Nenno S, Fukuda T. Crystal structure and morphology of the metastable X phase in shape memory Ti-Ni alloys. J Less Common Met 1986;125:157–66. https://doi.org/https://doi.org/10.1016/0022-5088(86)90090-1.

[210] Nishida M, Wayman CM, Honma T. Precipitation processes in near-equiatomic TiNi shape memory alloys. Metall Trans A 1986;17:1505–15. https://doi.org/10.1007/BF02650086.

[211] Tadaki T, Nakata Y, Shimizu K, Otsuka K. CRYSTAL STRUCTURE, COMPOSITION AND MORPHOLOGY OF A PRECIPITATE IN AN AGED Ti-51 AT. %Ni SHAPE MEMORY ALLOY. Trans Japan Inst Met 1986;27:731–40. https://doi.org/10.2320/matertrans1960.27.731.

[212] Ageing. Ann Acad Med Singapore 1987;16:1–162.

[213] Kim JI, Liu Y, Miyazaki S. Ageing-induced two-stage R-phase transformation in Ti - 50.9at.%Ni. Acta Mater 2004;52:487–99. https://doi.org/10.1016/j.actamat.2003.09.032.

[214] Nasiri S, Rabiei M, Palevicius A, Janusas G, Vilkauskas A, Nutalapati V, et al. Modified Scherrer equation to calculate crystal size by XRD with high accuracy, examples Fe2O3, TiO2 and V2O5. Nano Trends 2023;3:100015. https://doi.org/10.1016/j.nwnano.2023.100015.

[215] Burton AW, Ong K, Rea T, Chan IY. On the estimation of average crystallite size of zeolites from the Scherrer equation: A critical evaluation of its application to zeolites with one-dimensional pore systems. Microporous Mesoporous Mater 2009;117:75–90.

https://doi.org/10.1016/j.micromeso.2008.06.010.

[216] Qin Q, Peng H, Fan Q, Zhang L, Wen Y. Effect of second phase precipitation on martensitic transformation and hardness in highly Ni-rich NiTi alloys. J Alloys Compd 2018;739:873–81. https://doi.org/10.1016/j.jallcom.2017.12.128.

[217] Arciniegas M, Casals J, Manero JM, Peña J, Gil FJ. Study of hardness and wear behaviour of NiTi shape memory alloys. J Alloys Compd 2008;460:213–9. https://doi.org/10.1016/j.jallcom.2007.05.069.

[218] Simsek GM, Yapici GG. Influence of heat treatment parameters on the functional behavior and corrosion performance of a shape memory wire actuator. Mater Sci Forum 2020;986 MSF:55–60. https://doi.org/10.4028/www.scientific.net/msf.986.55.

[219] Burow J, Frenzel J, Somsen C, Prokofiev E, Valiev R, Eggeler G. Grain Nucleation and Growth in Deformed NiTi Shape Memory Alloys: An In Situ TEM Study. Shape Mem Superelasticity 2017;3:347–60. https://doi.org/10.1007/s40830-017-0119-y.

[220] Khanlari K, Shi Q, Li K, Hu K, Cao P, Liu X. Intermetallics Effects of printing volumetric energy densities and post-processing treatments on the microstructural properties , phase transformation temperatures and hardness of near-equiatomic NiTinol parts fabricated by a laser powder bed fusion techn 2021;131. https://doi.org/10.1016/j.intermet.2021.107088.

[221] Zhang X, M. Q. No Title. Magn. Shape Mem. Alloy., Springer Singapore; 2022.

[222] Zheng YF, Zhang BB, Wang BL, Wang YB, Li L, Yang QB, et al. Introduction of antibacterial function into biomedical TiNi shape memory alloy by the addition of element Ag. Acta Biomater 2011;7:2758–2767. https://doi.org/10.1016/j.actbio.2011.02.010.

[223] Plant SD, Grant DM, Leach L. Behaviour of human endothelial cells on surface modified NiTi alloy. Biomaterials 2005;26:5359–5367. https://doi.org/10.1016/j.biomaterials.2005.01.067.

[224] Constant C, Nichols S, Wagnac É, Petit Y, Desrochers A, Braïlovski V. Biocompatibility and mechanical stability of Nitinol as biomaterial for intra-

articular prosthetic devices. Materialia 2020;9:100567. https://doi.org/10.1016/j.mtla.2019.100567.

[225] Maffia S, Finazzi V, Berti F, Migliavacca F, Petrini L, Previtali B, et al. Selective laser melting of NiTi stents with open-cell and variable diameter. Smart Mater Struct 2021;30:105010.

[226] Elahinia M, Shayesteh Moghaddam N, Taheri Andani M, Amerinatanzi A, Bimber BA, Hamilton RF. Fabrication of NiTi through additive manufacturing: A review. Prog Mater Sci 2016;83:630–63. https://doi.org/10.1016/j.pmatsci.2016.08.001.

[227] Wang X, Kustov S, Van Humbeeck J. A Short Review on the Microstructure, Transformation Behavior and Functional Properties of NiTi Shape Memory Alloys Fabricated by Selective Laser Melting. Materials (Basel) 2018;11:1683. https://doi.org/10.3390/ma11091683.

[228] Conde FF, Escobar JD, Oliveira JP, Béreš M, Jardini AL, Bose WW, et al. Effect of thermal cycling and aging stages on the microstructure and bending strength of a selective laser melted 300-grade maraging steel. Mater Sci Eng A 2019;758:192–201. https://doi.org/10.1016/j.msea.2019.03.129.

[229] Conde FF, Escobar JD, Oliveira JP, Jardini AL, Bose Filho WW, Avila JA. Austenite reversion kinetics and stability during tempering of an additively manufactured maraging 300 steel. Addit Manuf 2019;29. https://doi.org/10.1016/j.addma.2019.100804.

[230] Walker J. AN INVESTIGATION OF EFFECTIVE PROCESS PARAMETERS ON PHASE TRANSFORMATION TEMPERATURE OF NITINOL MANUFACTURED BY work piece quality and inhibit the precise machining 2014:1–5.

[231] Daly S, Ravichandran G, Bhattacharya K. Stress-induced martensitic phase transformation in thin sheets of Nitinol 2007;55:3593–600. https://doi.org/10.1016/j.actamat.2007.02.011.

[232] Verhaeghe F, Craeghs T, Heulens J, Pandelaers L. A pragmatic model for selective laser melting with evaporation. Acta Mater 2009;57:6006–12.

https://doi.org/10.1016/j.actamat.2009.08.027.

[233] Ma M, Wang Z, Wang D, Zeng X. Control of shape and performance for direct laser fabrication of precision large-scale metal parts with 316L Stainless Steel. Opt Laser Technol 2013;45:209–16. https://doi.org/10.1016/j.optlastec.2012.07.002.

[234] Song RB, Xiang JY, Hou DP. Characteristics of mechanical properties and microstructure for 316L austenitic stainless steel. J Iron Steel Res Int 2011;18:53–9. https://doi.org/10.1016/S1006-706X(11)60117-9.

[235] Frenzel J, George EP, Dlouhy A, Somsen C, Wagner MF-X, Eggeler G. Influence of Ni on martensitic phase transformations in NiTi shape memory alloys. Acta Mater 2010;58:3444–58. https://doi.org/10.1016/j.actamat.2010.02.019.

[236] Frenzel J, Wieczorek A, Opahle I, Maaß B, Drautz R, Eggeler G. On the effect of alloy composition on martensite start temperatures and latent heats in Ni–Ti-based shape memory alloys. Acta Mater 2015;90:213–31. https://doi.org/10.1016/j.actamat.2015.02.029.

[237] Zhang J, Somsen C, Simon T, Ding X, Hou S, Ren S, et al. Leaf-like dislocation substructures and the decrease of martensitic start temperatures: a new explanation for functional fatigue during thermally induced martensitic transformations in coarse-grained Ni-rich Ti–Ni shape memory alloys. Acta Mater 2012;60:1999–2006. https://doi.org/10.1016/j.actamat.2011.12.014.

[238] Simon T, Kröger A, Somsen C, Dlouhy A, Eggeler G. On the multiplication of dislocations during martensitic transformations in NiTi shape memory alloys. Acta Mater 2010;58:1850–60. https://doi.org/10.1016/j.actamat.2009.11.028.

[239] Frenzel J, Zhang Z, Somsen C, Neuking K, Eggeler G. Influence of carbon on martensitic phase transformations in NiTi shape memory alloys. Acta Mater 2007;55:1331–41. https://doi.org/10.1016/j.actamat.2006.10.006.

[240] Whang SH. No Title n.d.

[241] Weaver JS. NIST Advanced Manufacturing Series 100-44 Understanding Anisotropic Tensile Properties of Laser Powder Bed Fusion Additive Metals : A

Detailed Review of Select Examples NIST Advanced Manufacturing Series 100-44 Understanding Anisotropic Tensile Properties n.d.

[242] Yu C, Lin R, Lik T, Luzin V, Lundgren J, Moverare J. Materials Science & Engineering A Anisotropic behaviours of LPBF Hastelloy X under slow strain rate tensile testing at elevated temperature 2022;844.

[243] Li P, Kim Y, Bobel AC, Jr LGH, Sachdev AK, Kumar S, et al. Acta Materialia Microstructural origin of the anisotropic flow stress of laser powder b e d fuse d AlSi10Mg 2021;220. https://doi.org/10.1016/j.actamat.2021.117346.

[244] Kunz J, Herzog S, Kaletsch A, Broeckmann C, K ML. Materials Science & Engineering A Microstructure analysis of novel LPBF-processed duplex stainless steels correlated to their mechanical and corrosion properties 2021;801. https://doi.org/10.1016/j.msea.2020.140432.

[245] Fu J, Hu Z, Song X, Zhai W, Long Y, Li H, et al. Micro selective laser melting of NiTi shape memory alloy : Defects , microstructures and thermal / mechanical properties. Opt Laser Technol 2020;131:106374. https://doi.org/10.1016/j.optlastec.2020.106374.

[246] Nigito E, Diemer F, Husson S, Ou SF, Tsai MH. Microstructure of NiTi superelastic alloy manufactured by selective laser melting 2022;324:7–9. https://doi.org/10.1016/j.matlet.2022.132665.

[247] Hamilton RF, Bimber BA, Taheri M, Elahinia M. Multi-scale shape memory e ff ect recovery in NiTi alloys additive manufactured by selective laser melting and laser directed energy deposition. J Mater Process Tech 2017;250:55–64. https://doi.org/10.1016/j.jmatprotec.2017.06.027.

[248] Monu MCC, Afkham Y, Chekotu JC, Ekoi EJ, Gu H, Teng C, et al. Bi-directional Scan Pattern Effects on Residual Stresses and Distortion in As-built Nitinol Parts: A Trend Analysis Simulation Study. Integr Mater Manuf Innov 2023;12:52–69. https://doi.org/10.1007/s40192-023-00292-9.

[249] ASTM B962: Standard test methods for density of compacted or sintered powder metallurgy (PM) products using Archimedes' Principle. 2017. https://doi.org/10.1520/B0962-17.

[250] E92-17 A. Standard test methods for Vickers hardness and Knoop hardness of metallic materials. West Conshohocken ASTM Int 2017.

[251] Rafi HK, Pal D, Patil N, Starr TL, Stucker BE. Microstructure and Mechanical Behavior of 17-4 Precipitation Hardenable Steel Processed by Selective Laser Melting. J Mater Eng Perform 2014;23:4421–8. https://doi.org/10.1007/s11665-014-1226-y.

[252] Monu MCC, Ekoi EJ, Hughes C, Kumar S. S, Brabazon D. Resultant physical properties of as-built nitinol processed at specific volumetric energy densities and correlation with in-situ melt pool temperatures. J Mater Res Technol 2022;21:2757–77. https://doi.org/10.1016/j.jmrt.2022.10.073.

[253] Vrancken B, Cain V, Knutsen R, Van Humbeeck J. Residual stress via the contour method in compact tension specimens produced via selective laser melting. Scr Mater 2014;87:29–32. https://doi.org/10.1016/j.scriptamat.2014.05.016.

[254] Laleh M, Sadeghi E, Revilla RI, Chao Q, Haghdadi N, Hughes AE, et al. Heat treatment for metal additive manufacturing. Prog Mater Sci 2023;133:101051. https://doi.org/10.1016/j.pmatsci.2022.101051.

[255] Kim J, Ji S, Yun Y-S, Yeo J-S. A Review: Melt Pool Analysis for Selective Laser Melting with Continuous Wave and Pulse Width Modulated Lasers. Appl Sci Converg Technol 2018;27:113–9. https://doi.org/10.5757/asct.2018.27.6.113.

[256] Moghaddam NS, Saedi S, Amerinatanzi A, Hinojos A, Ramazani A, Kundin J, et al. Achieving superelasticity in additively manufactured NiTi in compression without post-process heat treatment. Sci Rep 2019;9:1–11. https://doi.org/10.1038/s41598-018-36641-4.

[257] Bhardwaj A, Gupta AK, Padisala SK, Poluri K. Characterization of mechanical and microstructural properties of constrained groove pressed nitinol shape memory alloy for biomedical applications. Mater Sci Eng C 2019;102:730–42. https://doi.org/10.1016/j.msec.2019.04.070.

[258] Kruth J-P, Dadbakhsh S, Vrancken B, Kempen K, Vleugels J, Van Humbeeck J. Additive manufacturing of metals via selective laser melting process aspects and

material developments 2016.

[259] Tolochko NK, Mozzharov SE, Yadroitsev IA, Laoui T, Froyen L, Titov VI, et al. Balling processes during selective laser treatment of powders. Rapid Prototyp J 2004;10:78–87. https://doi.org/10.1108/13552540410526953.

[260] Sun S, Brandt M, Easton M. Powder bed fusion processes: an overview. Laser Addit. Manuf. - Mater. Des. Technol. Appl., 2017, p. 62.

[261] Guo W, Feng B, Yang Y, Ren Y, Liu Y, Yang H, et al. Effect of laser scanning speed on the microstructure, phase transformation and mechanical property of NiTi alloys fabricated by LPBF. Mater Des 2022;215:110460. https://doi.org/10.1016/j.matdes.2022.110460.

[262] Wang Z, Chen J, Kocich R, Tardif S, Dolbnya IP, Kunčická L, et al. Grain Structure Engineering of NiTi Shape Memory Alloys by Intensive Plastic Deformation. ACS Appl Mater Interfaces 2022;14:31396–410. https://doi.org/10.1021/acsami.2c05939.

[263] Mikula J, Quek SS, Joshi SP, Wu DT, Ahluwalia R. The role of bimodal grain size distribution in nanocrystalline shape memory alloys. Smart Mater Struct 2018;27. https://doi.org/10.1088/1361-665X/aada30.

[264] Jackson CL, McKenna GB. The melting behavior of organic materials confined in porous solids. J Chem Phys 1990;93:9002–11. https://doi.org/10.1063/1.459240.

[265] Zhong C, Chen J, Linnenbrink S, Gasser A, Sui S, Poprawe R. A comparative study of Inconel 718 formed by High Deposition Rate Laser Metal Deposition with GA powder and PREP powder. Mater Des 2016;107:386–92. https://doi.org/10.1016/j.matdes.2016.06.037.

[266] Kou S. Welding Metallurgy. Wiley; 2002. https://doi.org/10.1002/0471434027.

[267] Bormann T, Müller B, Schinhammer M, Kessler A, Thalmann P, De Wild M. Microstructure of selective laser melted nickel-titanium. Mater Charact 2014;94:189–202. https://doi.org/10.1016/j.matchar.2014.05.017.

[268] Laurençot P. The Lifshitz--Slyozov equation with encounters. Math Model Methods Appl Sci 2001;11:731–48.

[269] Huo SH, Qian M, Schaffer GB, Crossin E. Aluminium powder metallurgy. Woodhead Publishing Limited; 2010. https://doi.org/10.1533/9780857090256.3.655.

[270] Collins PC, Brice DA, Samimi P, Ghamarian I, Fraser HL. Microstructural Control of Additively Manufactured Metallic Materials. Annu Rev Mater Res 2016;46:63–91. https://doi.org/10.1146/annurev-matsci-070115-031816.

[271] Gražulis S, Merkys A, Vaitkus A. Crystallography Open Database (COD). Handb. Mater. Model., Cham: Springer International Publishing; 2020, p. 1863–81. https://doi.org/10.1007/978-3-319-44677-6_66.

[272] Gražulis S, Merkys A, Vaitkus A. Crystallography Open Database (COD) - Information card for entry 1100132. Crystallogr Open Database 2023.

[273] Lozano DE, Totten GE, Bedolla-Gil Y, Guerrero-Mata M, Carpio M, Martinez-Cazares GM. X-ray Determination of compressive residual stresses in spring steel generated by high-speed water quenching. Materials (Basel) 2019;12. https://doi.org/10.3390/ma12071154.

[274] Buhairi MA, Foudzi FM, Jamhari FI, Sulong AB, Radzuan NAM, Muhamad N, et al. Review on volumetric energy density: influence on morphology and mechanical properties of Ti6Al4V manufactured via laser powder bed fusion. Prog Addit Manuf 2022 2022:1–19. https://doi.org/10.1007/S40964-022-00328-0.

[275] Dolabella S, Borzì A, Dommann A, Neels A. Lattice Strain and Defects Analysis in Nanostructured Semiconductor Materials and Devices by High-Resolution X-Ray Diffraction: Theoretical and Practical Aspects. Small Methods 2022;6. https://doi.org/10.1002/smtd.202100932.

[276] Khorsand Zak A, Abd. Majid WH, Abrishami ME, Yousefi R. X-ray analysis of ZnO nanoparticles by Williamson–Hall and size–strain plot methods. Solid State Sci 2011;13:251–6. https://doi.org/10.1016/j.solidstatesciences.2010.11.024.

[277] Mohamed FA. Correlation between the minimum grain size obtainable by ball milling and lattice strain. Mater Sci Eng A 2019;752:15–7. https://doi.org/10.1016/j.msea.2019.02.049.

[278] Duerig TW, Bhattacharya K. The Influence of the R-Phase on the Superelastic Behavior of NiTi. Shape Mem Superelasticity 2015;1:153–61. https://doi.org/10.1007/s40830-015-0013-4.

[279] Li B-Y, Rong L-J, Li Y-Y, Gjunter VE. An investigation of the synthesis of Ti-50 At. pct Ni alloys through combustion synthesis and conventional powder sintering. Metall Mater Trans A 2000;31:1867–71. https://doi.org/10.1007/s11661-006-0242-4.

[280] Shaw JA, Churchill CB, Iadicola MA. Tips and tricks for characterizing shape memory alloy wire: Part 1-differential scanning calorimetry and basic phenomena. Exp Tech 2008;32:55–62. https://doi.org/10.1111/j.1747-1567.2008.00410.x.

[281] Pelton AR, Russell SM, Dicello J. The Physical Metallurgy of Nitinol for Medical Applications. JOM Phys Metall 2003;33.

[282] Ibrahim G, Haggag S, Lde DO, Dgl DQG, Ri H, Qjlqhhlqj M. Thermal (ngine 8 sing Nitinol : ire 2019:1353–8.

[283] Lakshmi Supriya. Possible Applications of Shape Memory Alloys. AZoM 2018.

[284] Perry MD. Applications of shape memory alloys in the transportation industry. SAE Tech Pap 1987;96:522–6. https://doi.org/10.4271/871578.

[285] Barik L, Samal S, Behera A, Rajak DK, Pruncu CI. On the replacement of steel by NITINOL as coupling agent in automobile shaft. ISSS J Micro Smart Syst 2021;10:87–102. https://doi.org/10.1007/s41683-021-00075-4.

[286] Parthasarathy J, Starly B, Raman S, Christensen A. Mechanical evaluation of porous titanium (Ti6Al4V) structures with electron beam melting (EBM). J Mech Behav Biomed Mater 2010;3:249–59. https://doi.org/10.1016/j.jmbbm.2009.10.006.

[287] Niinomi M, Nakai M. Titanium-based biomaterials for preventing stress shielding between implant devices and bone. Int J Biomater 2011;2011. https://doi.org/10.1155/2011/836587.

[288] Deng T, Zhong X, Zhong M, Lai Y, Zhu Z, Zhang L, et al. Effect of scandium on microstructure and corrosion resistance of Ti64 alloy in NaCl solution. Mater

Charact 2023;197:112671. https://doi.org/10.1016/j.matchar.2023.112671.

[289] Mahmud A, Wu Z, Zhang J, Liu Y, Yang H. Surface oxidation of NiTi and its effects on thermal and mechanical properties. Intermetallics 2018;103:52–62. https://doi.org/10.1016/j.intermet.2018.09.013.

[290] Balasubramanian Gayathri YK, Kumar RL, Ramalingam VV, Priyadharshini GS, Kumar KS, Prabhu TR. Additive Manufacturing of Ti-6Al-4V alloy for Biomedical Applications. J Bio- Tribo-Corrosion 2022;8:98. https://doi.org/10.1007/s40735-022-00700-1.

[291] He J, Jiang B, Xu J, Zhang J, Yu X, Liu B, et al. Effect of texture symmetry on mechanical performance and corrosion resistance of magnesium alloy sheet. J Alloys Compd 2017;723:213–24. https://doi.org/10.1016/j.jallcom.2017.06.269.

[292] Rondelli G, Vicentini B. Evaluation by electrochemical tests of the passive film stability of equiatomic Ni-Ti alloy also in presence of stress-induced martensite. J Biomed Mater Res 2000;51:47–54. https://doi.org/10.1002/(SICI)1097-4636(200007)51:1<47::AID-JBM7>3.0.CO;2-P.

[293] Pun DK, Berzins DW. Corrosion behavior of shape memory, superelastic, and nonsuperelastic nickel-titanium-based orthodontic wires at various temperatures. Dent Mater 2008;24:221–7. https://doi.org/10.1016/j.dental.2007.05.003.

[294] Chakraborty R, Datta S, Raza MS, Saha P. A comparative study of surface characterization and corrosion performance properties of laser surface modified biomedical grade nitinol. Appl Surf Sci 2019;469:753–63. https://doi.org/10.1016/j.apsusc.2018.11.045.

[295] Nagaraja S, Sena G, Stafford P, Braeuner C, Hempel P, Pelton AR, et al. Effects of Nitinol Microstructural Purity on Localized and Uniform Corrosion Susceptibility. Shape Mem Superelasticity 2022;8:118–28. https://doi.org/10.1007/s40830-022-00366-1.

[296] Carroll WM, Kelly MJ. Corrosion behavior of nitinol wires in body fluid environments. J Biomed Mater Res - Part A 2003;67:1123–30. https://doi.org/10.1002/jbm.a.10099.

[297] Wu B, Pan Z, Li S, Cuiuri D, Ding D, Li H. The anisotropic corrosion behaviour

of wire arc additive manufactured Ti-6Al-4V alloy in 3.5% NaCl solution. Corros Sci 2018;137:176–83. https://doi.org/10.1016/j.corsci.2018.03.047.

[298] Chiu TM, Mahmoudi M, Dai W, Elwany A, Liang H, Castaneda H. Corrosion assessment of Ti-6Al-4V fabricated using laser powder-bed fusion additive manufacturing. Electrochim Acta 2018;279:143–51. https://doi.org/10.1016/j.electacta.2018.04.189.

[299] Chen LY, Huang JC, Lin CH, Pan CT, Chen SY, Yang TL, et al. Anisotropic response of Ti-6Al-4V alloy fabricated by 3D printing selective laser melting. Mater Sci Eng A 2017;682:389–95. https://doi.org/10.1016/j.msea.2016.11.061.

[300] Wu B, Pan Z, Li S, Cuiuri D, Ding D, Li H. The anisotropic corrosion behaviour of wire arc additive manufactured Ti-6Al-4V alloy in 3.5% NaCl solution. Corros Sci 2018;137:176–83. https://doi.org/10.1016/j.corsci.2018.03.047.

[301] Pohrelyuk IM, Tkachuk O V., Proskurnyak R V. Corrosion Behaviour of Ti-6Al-4V Alloy with Nitride Coatings in Simulated Body Fluids at <math id="M1"> <mrow> <msup> <mrow> <mn mathvariant="bold">36</mn> </mrow> <mo mathvariant="bold">∘</mo> </msup> <mtext>C</mtext> </mrow> </math> and <math id="M2"> <. ISRN Corros 2013;2013:1–7. https://doi.org/10.1155/2013/241830.

[302] Wong MH, Cheng FT, Man HC. Comparison of corrosion resistance and apatite-forming ability of NiTi treated by different low-temperature methods. J Alloys Compd 2008;466:L5–10. https://doi.org/10.1016/j.jallcom.2007.11.077.

[303] Kuromoto NK, Simão RA, Soares GA. Titanium oxide films produced on commercially pure titanium by anodic oxidation with different voltages. Mater Charact 2007;58:114–21. https://doi.org/10.1016/j.matchar.2006.03.020.

[304] King WE, Barth HD, Castillo VM, Gallegos GF, Gibbs JW, Hahn DE, et al. Observation of keyhole-mode laser melting in laser powder-bed fusion additive manufacturing. J Mater Process Technol 2014;214:2915–25. https://doi.org/10.1016/j.jmatprotec.2014.06.005.

[305] Feng B, Wang C, Zhang Q, Ren Y, Cui L, Yang Q, et al. Effect of laser hatch spacing on the pore defects, phase transformation and properties of selective

laser melting fabricated NiTi shape memory alloys. Mater Sci Eng A 2022;840:142965. https://doi.org/10.1016/j.msea.2022.142965.

[306] Liu M, Zhu J-N, Popovich VA, Borisov E, Mol JMC, Gonzalez-Garcia Y. Passive film formation and corrosion resistance of laser-powder bed fusion fabricated NiTi shape memory alloys. J Mater Res Technol 2023;23:2991–3006. https://doi.org/10.1016/j.jmrt.2023.01.204.

[307] Chen L-Y, Zhang H-Y, Zheng C, Yang H-Y, Qin P, Zhao C, et al. Corrosion behavior and characteristics of passive films of laser powder bed fusion produced Ti–6Al–4V in dynamic Hank's solution. Mater Des 2021;208:109907. https://doi.org/10.1016/j.matdes.2021.109907.

[308] Singh D, Singh R, Boparai KS, Farina I, Feo L, Verma AK. In-vitro studies of SS 316 L biomedical implants prepared by FDM, vapor smoothing and investment casting. Compos Part B Eng 2018;132:107–14. https://doi.org/10.1016/j.compositesb.2017.08.019.

[309] Tang GL, Morasch MD. Role of Stents, Drug-Eluting Stents, and Stent-Grafts in Treatment of Infrainguinal Arterial Disease. Semin Vasc Surg 2007;20:37–41. https://doi.org/10.1053/j.semvascsurg.2007.02.004.

[310] rogers-edelman-1995-endovascular-stent-design-dictates-experimental-restenosis-and-thrombosis n.d.

[311] Australia, CSIRO. World's first 3D printed nitinol stent 2021. https://www.csiro.au/en/research/production/materials/3d-printed-nitinol-stent?utm_source=chatgpt.com.

[312] Kapoor A, Jepson N, Bressloff NW, Loh PH, Ray T, Beier S. The road to the ideal stent: A review of stent design optimisation methods, findings, and opportunities. Mater Des 2024;237:1–36. https://doi.org/10.1016/j.matdes.2023.112556.

[313] Chiastra C, Migliori S, Burzotta F, Dubini G, Migliavacca F. Patient-specific modeling of stented coronary arteries reconstructed fromoptical coherence tomography: Towards a widespread clinical use of fluid dynamics analyses. J Cardiovasc Transl Res 2017;11:156–72. https://doi.org/10.1007/s12265-017-

9777-6.

[314] Garcia-Garcia HM, Costa MA, Serruys PW. Imaging of coronary atherosclerosis: Intravascular ultrasound. Eur Heart J 2010;31:2456–69. https://doi.org/10.1093/eurheartj/ehq280.

[315] Oliver AA, Sikora-Jasinska M, Demir AG, Guillory RJ. Recent advances and directions in the development of bioresorbable metallic cardiovascular stents: Insights from recent human and in vivo studies. Acta Biomater 2021;127:1–23. https://doi.org/10.1016/j.actbio.2021.03.058.

[316] Salmi M. Additive manufacturing processes in medical applications. Materials (Basel) 2021;14:1–16. https://doi.org/10.3390/ma14010191.

[317] Fu J, Su Y, Qin YX, Zheng Y, Wang Y, Zhu D. Evolution of metallic cardiovascular stent materials: A comparative study among stainless steel, magnesium and zinc. Biomaterials 2020;230:119641. https://doi.org/10.1016/j.biomaterials.2019.119641.

[318] Davoodi E, Montazerian H, Mirhakimi AS, Zhianmanesh M, Ibhadode O, Shahabad SI, et al. Additively manufactured metallic biomaterials. vol. 15. KeAi Communications Co., Ltd; 2022. https://doi.org/10.1016/j.bioactmat.2021.12.027.

[319] Van Humbeeck J. Additive Manufacturing of Shape Memory Alloys. Shape Mem Superelasticity 2018;4:309–12. https://doi.org/10.1007/s40830-018-0174-z.

[320] Gong G, Ye J, Chi Y, Zhao Z, Wang Z, Xia G, et al. Research status of laser additive manufacturing for metal: a review. J Mater Res Technol 2021;15:855–84. https://doi.org/10.1016/j.jmrt.2021.08.050.

[321] Agarwal N, Bourke D, Obeidi MA, Brabazon D. Influence of laser powder bed fusion and ageing heat treatment parameters on the phase structure and physical behavior of Ni-rich nitinol parts. J Mater Res Technol 2024;30:4527–41. https://doi.org/10.1016/j.jmrt.2024.04.198.

[322] Agarwal N, Obeidi MA, Brabazon D, Asal K, Faraoni A, Pola A. Effect of Solution Heat Treatment of Nitinol (Ni55%-Ti45%) Manufactured via L-PBF.

SMST 2024 Ext Abstr from Int Conf Shape Mem Superelastic Technol 2024;84840:3–4. https://doi.org/10.31399/asm.cp.smst2024p0003.

[323] Parry LA, Ashcroft IA, Wildman RD. Geometrical effects on residual stress in selective laser melting. Addit Manuf 2019;25:166–75. https://doi.org/10.1016/j.addma.2018.09.026.

[324] Sing SL, Yeong WY, Wiria FE, Tay BY, Zhao Z, Zhao L, et al. Direct selective laser sintering and melting of ceramics: A review. Rapid Prototyp J 2017;23:611–23. https://doi.org/10.1108/RPJ-11-2015-0178.

[325] Sign H, Graepel T. Mechanical Properties and Microstructural Evolution of Additively Manufactured Nickel Alloys Under Industrial Heat Treatment 2024. https://doi.org/10.13140/RG.2.2.23856.37129.

[326] Shishkovsky I, Yadroitsev I, Smurov I. Direct Selective Laser Melting of Nitinol Powder. Phys Procedia 2012;39:447–54. https://doi.org/10.1016/j.phpro.2012.10.060.

[327] Wu X, Kanz P, Mahmoud H, Millar J, Shabani P, Torres JM. Characterization of the microstructure and surface roughness effects on fatigue life using the tanaka–mura–wu model. Appl Sci 2021;11. https://doi.org/10.3390/app11219955.

[328] Gegenschatz-Schmid K, Buzzi S, Grossmann J, Roschitzki B, Urbanet R, Heuberger R, et al. Reduced thrombogenicity of surface-treated Nitinol implants steered by altered protein adsorption. Acta Biomater 2022;137:331–45. https://doi.org/10.1016/j.actbio.2021.10.022.

[329] Kruth JP, Levy G, Klocke F, Childs THC. Consolidation phenomena in laser and powder-bed based layered manufacturing. CIRP Ann - Manuf Technol 2007;56:730–59. https://doi.org/10.1016/j.cirp.2007.10.004.

[330] Morgan NB. Medical shape memory alloy applications - The market and its products. Mater Sci Eng A 2004;378:16–23. https://doi.org/10.1016/j.msea.2003.10.326.

[331] Agarwal N, Perumal G, Obeidi MA, Brabazon D. Investigating the effect of the addition of WC into NiTi for stent application. Mater Res Proc 2024;41:249–56. https://doi.org/10.21741/9781644903131-28.

[332] Jain M, Sharma A, Schürch P, Ventura NM Della, Koelmans WW, Maeder X, et al. Strengthening of 3D printed Cu micropillar in Cu-Ni core-shell structure. Mater Des 2023;227:111717. https://doi.org/10.1016/j.matdes.2023.111717.

[333] Xu J, Ren W, Lian Z, Yu P, Yu H. A review: development of the maskless localized electrochemical deposition technology. Int J Adv Manuf Technol 2020;110:1731–57. https://doi.org/10.1007/s00170-020-05799-5.

[334] Schürch P, Osenberg D, Testa P, Bürki G, Schwiedrzik J, Michler J, et al. Direct 3D microprinting of highly conductive gold structures via localized electrodeposition. Mater Des 2023;227:111780. https://doi.org/10.1016/j.matdes.2023.111780.

[335] Wang W, Liang SY. Prediction of molten pool height, contact angle, and balling occurrence in laser powder bed fusion. Int J Adv Manuf Technol 2022;119:6193–202. https://doi.org/10.1007/s00170-021-08633-8.

[336] Yang T, Liu T, Liao W, Wei H, Zhang C, Chen X, et al. Effect of processing parameters on overhanging surface roughness during laser powder bed fusion of AlSi10Mg. J Manuf Process 2021;61:440–53. https://doi.org/10.1016/j.jmapro.2020.11.030.

[337] Yasa E, Deckers J, Kruth JP. The investigation of the influence of laser re-melting on density, surface quality and microstructure of selective laser melting parts. Rapid Prototyp J 2011;17:312–27. https://doi.org/10.1108/13552541111156450.

[338] Walker J, Andani MT, Haberland C, Elahinia M. Additive Manufacturing of Nitinol Shape Memory Alloys to Overcome Challenges in Conventional Nitinol Fabrication 2014. https://doi.org/10.1115/IMECE2014-40432.

[339] Jamshidi P, Panwisawas C, Langi E, Cox SC, Feng J, Zhao L, et al. Development, characterisation, and modelling of processability of nitinol stents using laser powder bed fusion. J Alloys Compd 2022;909:164681. https://doi.org/10.1016/j.jallcom.2022.164681.

[340] Pal S, Lojen G, Hudak R, Rajtukova V, Brajlih T, Kokol V, et al. As-fabricated surface morphologies of Ti-6Al-4V samples fabricated by different laser

processing parameters in selective laser melting. Addit Manuf 2020;33:101147. https://doi.org/10.1016/j.addma.2020.101147.

[341] Agarwal N, Gallagher KA, Keaveny S, Carton JG, Brabazon D, Obeidi MA. Influence of processing parameters on the corrosion resistance of additively manufactured nitinol parts for biomedical applications. Results Mater 2024;21:100536. https://doi.org/10.1016/j.rinma.2024.100536.

[342] Wang Y, Wei X, Li Z, Sun X, Liu H, Jing X, et al. Experimental Investigation on the Effects of Different Electrolytic Polishing Solutions on Nitinol Cardiovascular Stents. J Mater Eng Perform 2021;30:4318–27. https://doi.org/10.1007/s11665-021-05736-x.

[343] Jamshidi P, Panwisawas C, Langi E, Cox SC, Feng J, Zhao L, et al. Development, characterisation, and modelling of processability of nitinol stents using laser powder bed fusion. J Alloys Compd 2022;909:164681. https://doi.org/10.1016/j.jallcom.2022.164681.

[344] Ren Q, Chen C, Lu Z, Wang X, Lu H, Yin S, et al. Effect of a constant laser energy density on the evolution of microstructure and mechanical properties of NiTi shape memory alloy fabricated by laser powder bed fusion. Opt Laser Technol 2022;152:108182. https://doi.org/10.1016/j.optlastec.2022.108182.

[345] Everton SK, Hirsch M, Stavroulakis PI, Leach RK, Clare AT. Review of in-situ process monitoring and in-situ metrology for metal additive manufacturing. Mater Des 2016;95:431–45. https://doi.org/10.1016/j.matdes.2016.01.099.

[346] Obeidi MA. Achieving high quality nitinol parts with minimised input thermal energy by optimised pulse wave laser powder bed fusion process. Results Mater 2022;14:100279. https://doi.org/10.1016/j.rinma.2022.100279.

[347] Smoqi Z, Gaikwad A, Bevans B, Kobir MH, Craig J, Abul-Haj A, et al. Monitoring and prediction of porosity in laser powder bed fusion using physics-informed meltpool signatures and machine learning. J Mater Process Technol 2022;304:117550. https://doi.org/10.1016/j.jmatprotec.2022.117550.

[348] Tuissi A, Carr S, Butler J, Gandhi AA, O'Donoghue L, McNamara K, et al. Radiopaque Shape Memory Alloys: NiTi–Er with Stable Superelasticity. Shape

Mem Superelasticity 2016;2:196–203. https://doi.org/10.1007/s40830-016-0066-z.

[349] Park C, Kim S, Kim HE, Jang TS. Mechanically stable tantalum coating on a nano-roughened NiTi stent for enhanced radiopacity and biocompatibility. Surf Coatings Technol 2016;305:139–45. https://doi.org/10.1016/j.surfcoat.2016.08.014.

[350] States U, Ordnance N, Oak W. Ezf ~~~ E ~ 1965.

[351] Mussatto A, Groarke R, Vijayaraghavan RK, Obeidi MA, MacLoughlin R, McNally PJ, et al. Laser-powder bed fusion in-process dispersion of reinforcing ceramic nanoparticles onto powder beds via colloid nebulisation. Mater Chem Phys 2022;287:126245. https://doi.org/10.1016/j.matchemphys.2022.126245.

[352] Yang Z, Fan J, Liu Y, Nie J, Yang Z, Kang Y. Effect of the particle size and matrix strength on strengthening and damage process of the particle reinforced metal matrix composites. Materials (Basel) 2021;14:1–12. https://doi.org/10.3390/ma14030675.

Appendix for Chapter 4

Table A.1: Critical phase transformation temperatures with the enthalpy change.

Sample ID	M_s (°C)	M_f (°C)	H_M (J/g)	A_s (°C)	A_f (°C)	H_A (J/g)	R_s (°C)	R_f (°C)	H_R (J/g)
S1-400_30	43.66	26.14	4.51	32.01	42.69	2.43	-2.17	14.97	1.52
S1-400_60	48.03	28.75	3.94	35.94	50.32	1.23	6.43	19.02	0.56
S1-400_90	48.75	30.56	4.48	35.59	48.5	2.06	9.68	23.91	1.60
S1-500_30	-22.59	-41.17	5.02	13.95	24	15.57	21.16	7.17	2.96
S1-500_60	-14.93	-27.93	7.83	20.52	27.07	18.33	19.78	11.05	4.07
S1-500_90	-11.99	-29.01	8.36	19.25	27.87	19.60	17.79	11.18	3.948
S1-600_30	-44.33	-83.21	4.29	-53.42	-18.85	10.35	-	-	-
S1-600_60	-46.99	-86.25	5.62	-12.31	-54.37	12.18	-	-	-
S1-600_90	-37.45	-82.42	9.59	-52.47	-16.2	14.12	-	-	-
S1-as-fabricated	-0.91	-79.64	5.61	-44.41	12.45		-	-	-
S2-400_30	40.84	24.96	5.11	30.86	40.01	3.45	-8.88	7.38	1.07
S2-400_60	43.35	29.51	5.46	35	43.69	3.40	2.88	18.76	2.13
S2-400_90	46.2	30.07	4.96	34.81	45.75	2.91	3.79	19.59	2.73
S2-500_30	-21.93	-35.23	7.89	16.31	26.32	19.94	20.51	11.51	3.94
S2-500_60	-14.17	-31.3	8.75	20.96	29.69	20.01	21.24	13.56	3.68
S2-500_90	-11.59	-32.68	6.83	2034	31.78	18.45	24.31	15.22	4.08
S2-600_30	-47.59	-75.82	9.89	-46.1	-20.78	15.27	-	-	-
S2-600_60	-46.25	-78.91	6.83	-50.66	-9.64	12.09	-	-	-
S2-600_90	-54.34	-86.23	7.26	-49.26	-20.41	12.09	-	-	-
S2-as-fabricated	2.24	-84.62	6.01	-48.18	7.19		-	-	-
S3-400_30	40.72	25.68	4.86	31.47	39.71	3.54	-4.98	12.6	1.62
S3-400_60	44.14	29.22	6.36	33.75	43.57	2.13	3.61	20.85	1.65
S3-400_90	45.22	32.72	4.84	36.16	46.37	2.34	8.09	23.30	3.43
S3-500_30	-20.62	-37.41	7.15	16.65	24.99	18.034	19.68	10.22	3.65
S3-500_60	-14.08	-29.37	4.78	19.81	29.33	17.032	20.84	12.41	3.01
S3-500_90	-10.78	-27.95	6.44	21.76	31.30	16.63	24.49	14.28	3.7245
S3-600_30	-25.5	-103.4	9.02	-50.38	-8.78	14.398	-	-	-
S3-600_60	-30.89	-88.22	11.81	-51.35	-11.27	14.095	-	-	-
S3-600_90	-42.10	-88.38	10.81	-54.52	-15.02	13.60	-	-	-
S3-as-fabricated	0.28	-76.27	8.95	-43.99	17.44	12.935	-	-	-
S4-400_30	42.46	25.66	5.08	30.98	42.37	2.14	-6.81	22.05	1.71

S4-400_60	44.27	29.71	5.72	34.33	45.42	3.59	2.85	19.50	1.62
S4-400_90	45.27	31.97	5.22	36.05	45.19	3.32	6.23	22.48	3.81
S4-500_30	-21.54	-38.62	5.94	17.28	28.37	18.49	22.77	12.80	4.06
S4-500_60	-14.91	-31.83	5.53	21.00	31.74	17.44	24.89	14.91	4.11
S4-500_90	-7.94	-27.43	5.68	22.66	33.55	17.05	22.88	15.77	3.72
S4-600_30	-8.71	-84.02	9.17	-51.36	4.21	11.40	-	-	-
S4-600_60	-18.41	-81.81	11.86	-34.17	-3.45	13.20	-	-	-
S4-600_90	-9.62	-104.13	12.28	-65.31	6.17	13.40	-	-	-
S4-as-fabricated	-2.62	-82.07	7.30	-48.88	13.31	10.682	-	-	-

Table A. 2: Rietveld Refinement information of the heat treated samples.

Sample ID	**Bragg R-factor**	**Reduced Chi^2**	**Austenite Phase Volume Fraction (%)**	**Martensite Phase Volume Fraction (%)**
S1-400_30	15.2	0.4	46.9	53.1
S1-500_60	20.6	0.7	88.8	11.2
S1-600_90	16.1	1.9	100	-
S2-400_30	4.3	6.0	12.3	87.7
S2-500_60	1.2	1.7	11.7	88.3
S2-600_90	1.8	2.1	100	-
S3-400_30	3.4	5.3	44.1	55.9
S3-500_60	1.4	1.9	1.9	98.1
S3-600_90	2.7	4.4	100	-
S4-400_30	5.7	0.7	22.5	77.5
S4-500_60	2.8	0.9	92.1	7.9
S4-600_90	0.1	1.5	100	-

Appendix A: Conference paper 1

Investigating the effect of the addition of WC into NiTi for stent application

Neha Agarwal[1,2, a, *], Gopinath Perumal[1, b], Muhannad Ahmed Obeidi[1,2, c], Dermot Brabazon[1,2, d]

[1]School of Mechanical and Manufacturing Engineering, Dublin City University, Dublin 9, Ireland
[2] I-Form Advanced Manufacturing Research Centre, Dublin City University, Dublin 9, Ireland
[a]neha.agarwal2@mail.dcu.ie, [b]gopinath.perumal@dcu.ie, [c]muhannad.ahmedobeidi@dcu.ie, [d]dermot.brabazon@dcu.ie

A Abstract

Nitinol is used for self-expandable stents used in biomedical applications considering their excellent properties of being superelastic and biocompatible. Minimally invasive implants need to be securely positioned in the human body with the property of being visible with the help of X-rays. Limited radiopacity of nitinol implants requires additional markers on the implants to facilitate accurate placement of the implant. This study explores the path of adding different concentrations of tungsten carbide (WC) to nickel-rich nitinol powder. Tests were conducted by compacting the mixed powders with a hydraulic press and then furnace sintering the green samples, with varying pressures and temperatures, to produce the solid parts. The mechanical properties of density and hardness of the sintered samples were measured and compared. An increase in hardness from 76 HV to 150 HV indicated that better mechanical properties could be achieved. Fully dense samples without any pores were obtained. These results show potential for the introduction of WC to nitinol for additively manufactured parts.

Keywords: powder alloying, radiopacity, compaction, sintering, hardness.

A.1 Introduction

Nitinol is a shape-memory alloy made of nickel and titanium, both of which are present in near-equal amounts. Recent advances in biomedical applications have been seen to be utilized as catheter tubes, guide wires, stone retrieval baskets, filters, needles, and stents [13,37,105,109]. Due to its excellent properties of shape memory alloy effect, superelasticity, high corrosion resistance, good biocompatibility, and good ductility, it is a desirable choice for implant applications [19,177,224]. However, nitinol poses the challenge of being radiolucent, which induces the challenge of the precise placement of

the device in the human body. To combat this challenge and enhance other properties, the alloying of nitinol was evaluated. Among many other options erbium (Er) [348], tantalum (Ta) [349], and tungsten carbide (WC) [350] are often combined with other metals to enhance the mechanical properties of the primary material. WC possesses many important features that make it desirable for use in stents such as its high hardness, resistance to corrosion, high density (when compared to NiTi), and biocompatibility. As reported by Mussatto [351], adding WC into stainless steel during the laser bed fusion process resulted in increased strength of the parts produced with a stronger crystallographic texture.

In this present study, we evaluate the possibility of the addition of WC in nickel-rich nitinol to investigate the hardness and density of the new composition. The samples have been produced by the compaction process of the powder using a hydraulic press with subsequent heat sintering to form solid circular disks. The addition of WC into NiTi for enhancing the mechanical property of hardness was evaluated. The addition of different materials in NiTi opens the possibility of assessing several different applications with desired functional properties. Small varying mass percentages of WC were added to NiTi to enhance the strength of the combined powder with a view to not significantly alter the shape memory properties of the produced NiTi composite part.

A.2 Materials and Methods

A.2.1 Powder Mixing and Compaction

Pre-alloyed nickel titanium powder was sourced from Fort Wayne Metals, Castlebar, Ireland with an elemental composition of 52.39 at.% Ni and 47.61 at.% Ti with a purity of 99.999%. The particle size distribution of NiTi powder is 12.3 μm (D_{10}), 27.4 μm (D_{50}) and 47.6 μm (D_{90}). A hydraulic press was used for the compaction process of the NiTi powder. The compaction parameters applied were the compaction pressure (ton), holding time (min), and varying powder mass to achieve highly compact powder to produce disc samples geometry of 20 mm diameter. Although the best results were achieved from the compaction of the pre-alloyed NiTi powder at 2.4 MPa, a holding time of 15 mins, and a NiTi powder mass of 2.4g; however, it was still not sufficiently compacted enough to continue onto the sintering process as shown in **Figure A- 1**.

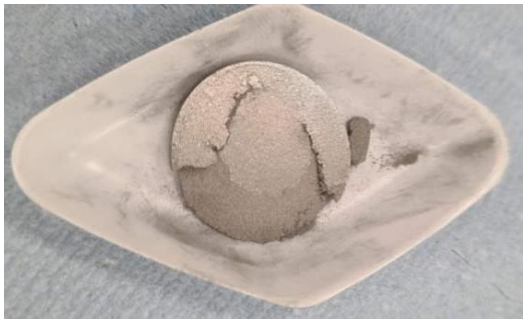

Figure A- 1: Pre-alloyed NiTi powder compacted at 22 tons, holding time of 15 mins and mass of 2.4 g.

Due to the failure of the achieving fully compact discs, separate nickel and titanium powders sourced from Fort Wayne Metals, Castlebar, Ireland was used with a purity of 99.996%. A Resodyn LabRam1 acoustic mixer was used to thoroughly mix the sample powder. A three-step mixing process was used with each step lasting 30 seconds with increased acceleration gravity (g) levels of 40g, 60g, and 70g in each step. These newly mixed samples of NiTi were then tested for compaction under different parametersand instant improvements to the samples post compaction were obtained. However, there were microcracks observed on the samples. A preliminary pilot test to investigate the optimum set of mixing ratios, it was found that the addition of water soluble 2% PVA (Polyvinyl Alcohol) to the powder mixture and compaction at a load of 25 tons, holding time of 15 mins, and the mass of the powder at 6.5g to achieve a significant and improved compaction results followed by efficient removal of the parts from the die as shown in **Figure A- 2**.

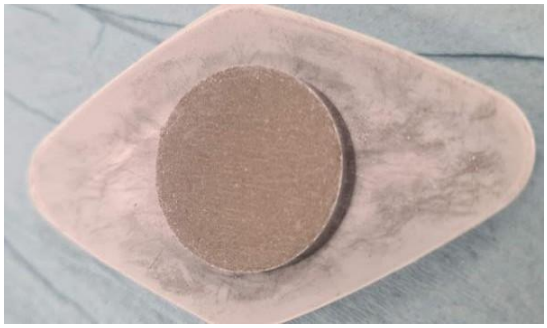

Figure A- 2: Self-mixed NiTi powder was compacted using the parameters of load 25 tons, hold time of 15 mins, mass of powder 6.5g and PVA added at 2% of the mass of the NiTi powder.

Once the parameters that are best suited for the compaction of NiTi was found, WC was mixed into the powdered samples at increasing mass percentages of 5%, 10%, 15% and 20% of the total mass of the powder mixed according to **Table A. 3**. These self-mixed

NiTi powders and WC were then compacted under the previously found parameters for compaction of the self-mixed NiTi powder.

Table A. 3: Varying masses of WC added to self-mixed NiTi powders for compaction.

Mass division of WC and NiTi		
WC %	**NiTi (g)**	**WC (g)**
0	40	0
5	38	2
10	36	4
15	34	6
20	32	8

A.2.2. Sintering

Sintering was done to each of the compacted samples with the use of a heat furnace. Due to the high melting point of NiTi, heat sintering method was employed to keep the purity of the samples post processing. Pre-testing was conducted for the heat sintering of the compacted samples by holding the samples inside the heat surface for 3 hours with a temperature 1200 ºC (as this was between the ideal sintering temperature between nickel (1091 ºC) and titanium (1251 ºC)). However, this resulted in the samples tested completely melted and incapable of any use. The samples were then sintered in steps until the heat furnace reached a temperature of 1000 ºC holding it for 3 hours before the heat furnace was cooled down in the same steps by which it was heated. **Figure A- 3** shows the sintering process used for the samples. The samples post sintering under these steps were seen to produce ideal samples.

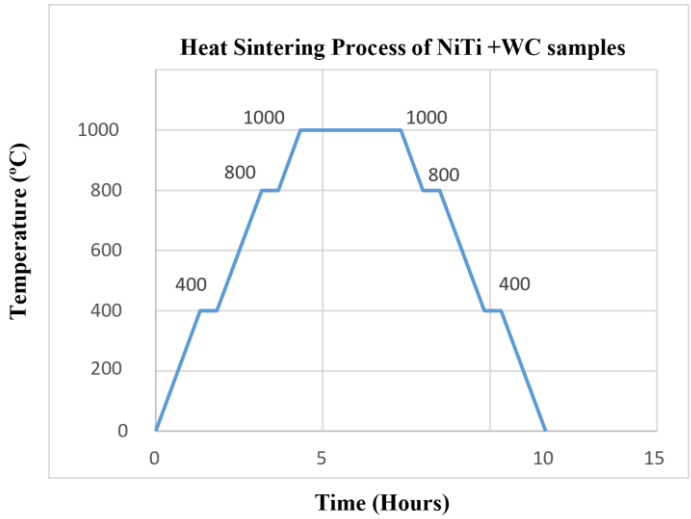

Figure A- 3: Sintering steps conducted until the heat furnace reached 1000 ºC with holding time for 3 hours before it was cooled down in steps.

A.2.3.Metallographic preparation of the samples

All the sintered samples were mounted in resin for ease of use during the grinding and polishing process of the surface. The samples were grinded using abrasive paper that went up in grit size value from P80 to P4000. Once all samples were grinded diamond polishing was done to the surface of the samples to achieve a smooth mirror-like finish on all samples to make them available for testing as shown in **Figure A- 4**. The samples were polished using diamond suspensions in decreasing number of particle sizes from 9µm, 6µm, 3µm and 1µm.

Figure A- 4: Polished sample surface of NiTi + 10% WC.

A.2.4. Characterization Techniques

Morphological characterization was conducted using a scanning electron microscope (SEM), Zeiss EVO LS-15, on all powders which comprised of pre-alloyed NiTi, self-mixed NiTi, and NiTi with varying amounts of WC. This inspection was conducted to analyze the even mixing of all powders before compaction. Energy dispersive X-ray spectroscopy (EDS), INCA, Oxford Instruments EDX system was used in combination with SEM to carry out an elemental analysis on all the samples being used. This technique helped to understand the composition of all powdered and

sintered samples by showing the average mass percentage value of each element present within each sample.

As there were many defects found within the topography of the sintered and polished samples it was almost impossible to see the composition of the material using optical microscopy, thus backscattered images were used to get the structural composition of the polished samples. This was done with the addition of the backscatter sensor to the SEM directly above the sample which detects backscattered electrons from the sample onto the sensor and produces high-quality images of the microstructure of the sample a small distance inside the sample being viewed. EDS was then used to map out the different elements present within the sample shown by each color contrast specific to a different element.

Vickers Hardness test was carried out on each of the samples to obtain a value for hardnesson each of these samples. A small indentation is made on each of the samples with a load of 0.98 N with a holding time of 20 secs. The average Vickers hardness was reported after 5 measurements were done on each sample. Density measurements were carried out on all the sintered samples using the Archimedes principle. The measurements were carried out using ethanol as fluid. Three measurements were conducted, and the average density has been reported.

A.3 Results and Discussion

A.3.1 Morphological characteristics of the powder samples

The SEM metallography images show clear structural difference between the NiTi particles and WC particles as shown in Error! Reference source not found. and **Figure A- 6**, respectively. The NiTi powder showed particles were circular and round consistently throughout the sample with little to no impurities or defects to the particles. On the other hand, WC was observed to have a much smaller particle size (ranging from 1-5 μm) and was very random in shape which is a commonly supplied form for this material [352].

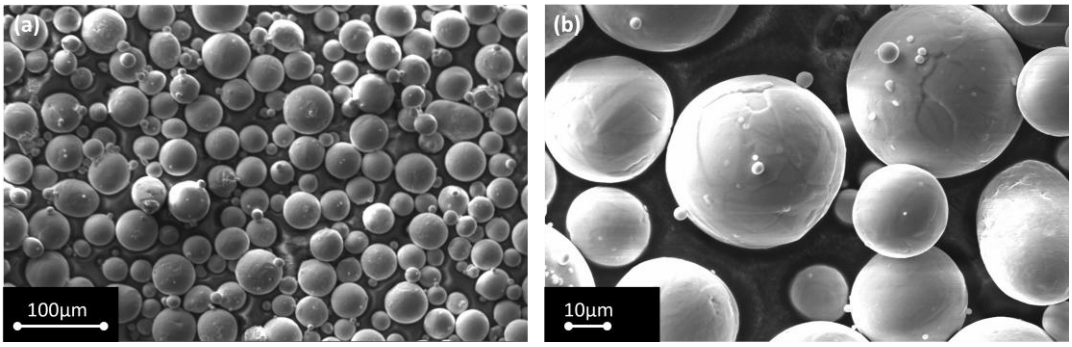

Figure A- 5: SEM image of self-mixed NiTi powder.

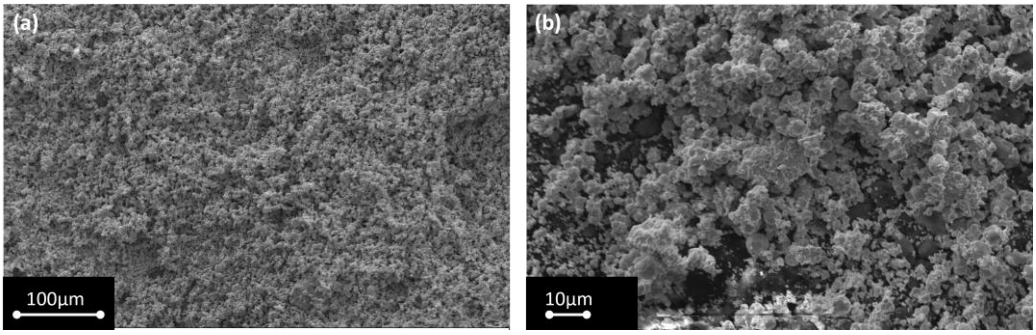

Figure A- 6: SEM image of WC powder.

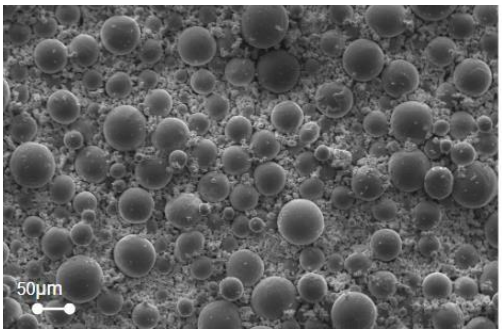

Figure A- 7: A constant and uniform mixing of both powders were observed of mixed NiTi + 10% WC powder.

As observed in **Figure A- 7**, all powders were found to be uniformly mixed with expected amounts of both NiTi and WC in all areas of the sample. EDS was conducted on all samples, and it was found that there was a steady increase in the WC in the average atomic mass percentage of the WC as more WC was added.

Backscattered scanning electron microscope images helped analyze the inner microstructure of each sample. The three distinct color contrasts were observed in the backscattered images of each of the samples as depicted by **Figure A- 8**.

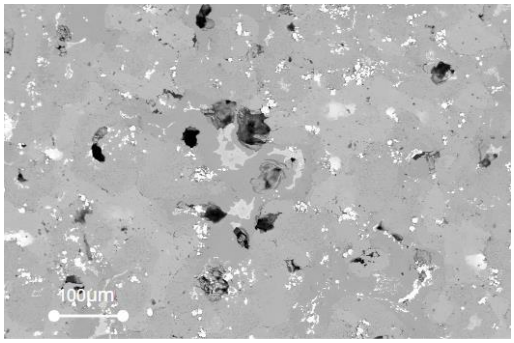

Figure A- 8: Backscattered scanning electron microscope image of NiTi + 10%WC.

A.3.2 Effect of addition of WC on the density of the samples

Due to the higher melting point of WC than that of NiTi, the WC particles would not form an alloy with NiTi after the sintering process. However, WC particles still retain all their properties post sintering which will increase mechanical properties such as hardness and density while being encapsulated in the ductile and biocompatible environment of the NiTi.

It was observed that there was a linear increase in the density of the samples with an increase in the WC percentage as shown in

Figure A- 9*:* . This is primarily because WC is a very dense material and as WC was not melted during the sintering process it still retains all its properties. Along with the reduction in the number of pores present throughout the sample, it also increased the density of the samples.

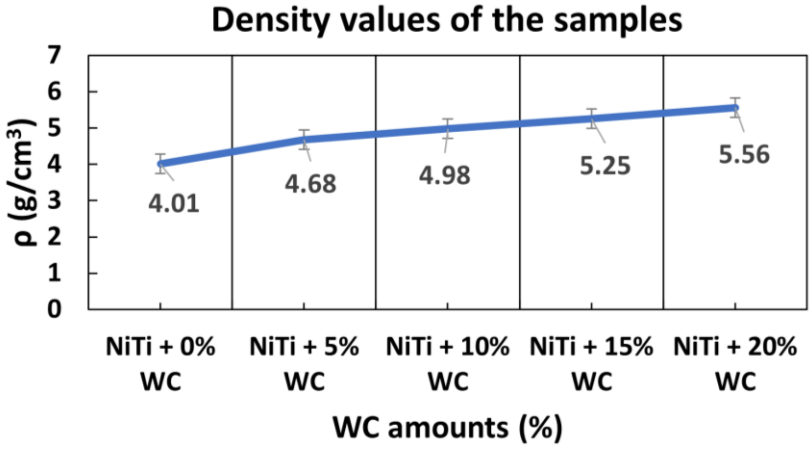

Figure A- 9: Density of the sintered samples after the compaction process with varying WC amounts.

A.3.3 Effect of addition of WC on the hardness values of the samples

A steady linear increase in the Vickers Hardness values was observed as the mass percentage of the WC powder present within the samples was increased as shown in

Figure A- 10. From analysis of all samples, it was seen that the sintered samples containing only NiTi had a lot of pores which resulted in the reduction of the hardness value of the sample. These pores were formed because of either the parameters used for the sintering process or due to the evaporation of the PVA from inside the sample leaving void spaces. The number of pores visible in the samples gradually decreased as the amount of WC increased. This is because the areas in which the pores were formed were filled with the WC powder which resulted in significantly fewer void spaces throughout the sample thereby increasing both the hardness and strength of the material.

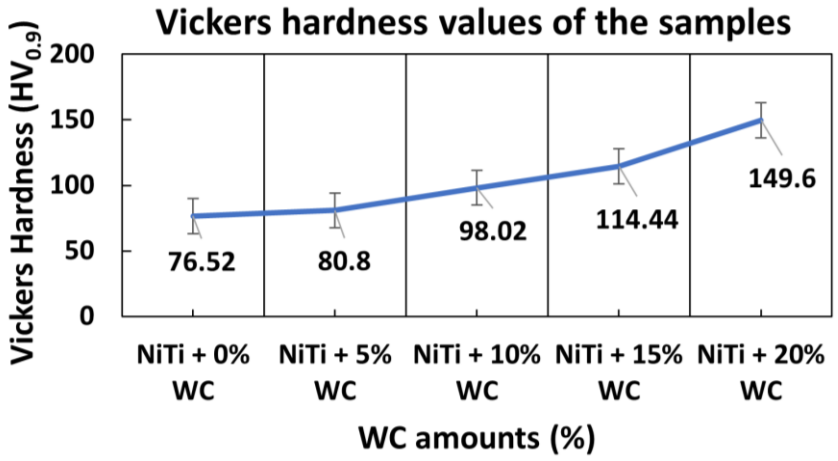

Figure A- 10: Vickers Hardness values was observed for all samples with varying WC %.

A.4 Conclusion

In this work, the advantages of adding tungsten carbide (WC) in different amounts to nickel-rich nitinol were investigated. Due to its extraordinarily high melting point, it was found that the WC powder did not entirely melt in any of the samples. The evaporation of PVA left gaps in the sample, but this powder-filled them and provided structural support for the NiTi resulting in fully dense solid samples. The sample's hardness increased with increasing amounts of WC. These are all extremely crucial elements to consider when creating any stent and will lower risk factors like restenosis and stent distortion. Further work will be carried out to evaluate the influence of addition of WC to NiTi on radiopacity and biocompatibility of the produced samples. As NiTi is still used as the primary element for the fabrication of the stent, it still inhibits all important properties such as shape memory, corrosion resistance, and biocompatibility along with the mechanical advantages of WC, making the addition of WC to NiTi stents a potential advantage for the fabrication of stents.

Appendix B: Conference paper 2

Effect of solution heat treatment of nitinol (Ni55%-Ti45%) manufactured via L-PBF

Neha Agarwal[1,2,3,*], Muhannad Ahmed Obeidi[1,2,3], Dermot Brabazon[1,2,3]

[1] School of Mechanical and Manufacturing Engineering, Dublin City University, Dublin, Ireland

[2]I-Form Advanced Manufacturing Research Centre, Dublin City University, Dublin, Ireland [3]Advanced Processing Technology Research Centre, Dublin City University, Dublin, Ireland

Karim Asal[4], Andrea Faraoni[4], Annalisa Pola[4]

[4]Mechanical and Industrial Engineering Dept., University of Brescia, Brescia, Italy

*Corresponding author: neha.agarwal2@mail.dcu.ie

B.1 Introduction

The properties of nitinol, an alloy of nickel and titanium, include its good biocompatibility, corrosion resistance, damping capacity, fatigue strength, superelasticity, and shape memory characteristics. With other conventional methods, it has been challenging to achieve high precision and accuracy of the produced parts; however, laser powder bed fusion (L-PBF) has provided a useful new route for the processing of nitinol [1]. While L-PBF offers many advantages, it also has drawbacks, including the potential for the formation of different phases and residual stress during rapid solidification. Post L-PBF heat treatment conditions aid in the generation of targeted stable phases. As reported by Lee et. al. [2], the mechanical properties and transformation temperatures of the manufactured nitinol samples were largely influenced by the heat treatment. Fan et. al. [3] showed an increase in the transformation temperatures by increasing the heat treatment temperatures after a solution heat treatment. Heat treatments that help in achieving the desired properties are two-step heat treatment processes [2,3]. This study investigates the feasibility of applying a single-step solution heat treatment to Ni-rich nitinol and reports its effects on density, transformation temperatures, microstructures and microhardness for intended applications.

B.2 Experimental Results

Nickel rich nitinol with a composition of 55%Ni was sourced as feedstock for the laser powder bed fusion (L-PBF), from Fort Wayne Metals Ireland, to fabricate cuboids of

dimensions 5 x 5 x 6 mm using a Aconity Mini 3D metal printer. The printer is equipped with a 200W fiber laser of wavelength 1068 nm. Cuboids with dimensions of 5 x 5 x 6 mm were fabricated with the process parameters as in **Table B. 1**.Layer thickness was maintained at 60 µm and laser spot size of 60 µm. After fabrication, solution heat treatment was performed on the samples using a Lenton box furnace under atmospheric conditions. Samples were treated at 800°C, 1000°C and 1200°C for varying times of 1, 3 and 5 hours respectively [4,5]. Density measurements were conducted according to ASTM standards [6] with microhardness measurements at 5 random locations on the sample [7]. Phase transformation temperatures were measured using a differential scanning calorimetry (DSC) with optical microscopy being used for microstructural characterisation. Kroll's reagent [8] was used to etch the samples and reveal the microstructures. Chemical composition was studied with the help of Energy Dispersive X-Ray Spectroscopy (EDX) equipped on a Zeiss Scanning Electron Microscope (SEM).

Table B. 1: Process parameters for fabrication of nitinol cuboids.

Laser Power (W)	**Scan Speed (mm/s)**	**Hatch Spacing (µm)**	**VED (J/mm^3)**
150	500	60	62.50

Samples heat treated at 800°C were found to be very close to that of the as-fabricated samples with density of 6.46 g/cm3. However, for the samples heat treated at 1000°C exhibited a slight decrease in the density values to an average of 6.08 g/cm3. Increase of time did not significantly affect the density values of the heat treated samples. It was also observed that samples heat treated at 1200°C showed an increase in density from 5.34 to 5.57 g/cm3 with an increase in holding time. However, it was much lower than the density values of as-built samples. Vickers microhardness results exhibited an increase in hardness values to an average of 408HV for samples heat treated at 800°C than the as fabricated samples with hardness of 356HV. It was noted that similar trends were observed for the hardness values treated at different temperatures and times. Nickel content of the samples heat treated for 3 hours at the varying temperatures was measured and reported. Samples heat treated at 800°C and 1000°C did not show significant changes in Ni content from the as-fabricated samples with a nickel content of 50.3 at.% before etching of the samples. However, samples treated at 1200°C reported higher nickel content. A general decrease in the Af temperature was observed for the heat treated samples from the as-fabricated samples (Af = -26°C) along with the other phase

transformation temperatures including Ms, Mf, and As. Samples exhibited an average decrease of 25 to 30°C when heat treated. No transformation temperatures results were obtained for the samples heat treated at 1200°C. Optical microscopy revealed the microstructures after the sample surface was etched using the Kroll's reagent. As-fabricated sample showed a checkerboard pattern according to the scanning strategy of 90° rotation employed during L-PBF. While samples treated for 3 hours at varying temperatures showed similar pattern and further analysis is needed to completely understand the microstructures.

B.3 Discussion

The L-PBF process parameters have an influence on the density, microstructures, transformation temperature and microhardness of the Ni-rich NiTi samples [8]. For the heat treated samples at 800°C and 1000°C irrespective of holding times, Ni evaporation during the L-PBF process and the restructuring of the NiTi matrix led to decrease in the Af when compared to the as-fabricated samples [5]. It is noted that even small variations in the Ni content can affect the transformation temperatures of NiTi samples, as this material is known to be highly sensitive [9]. Optical micrographs exhibited the presence of pores on the sample surface which was an effect of restructuring of the NiTi matrix which also resulted in an increase in the microhardness values. Samples treated at 1200°C need further in depth analysis to understand why it showed a higher Ni content. This increased Ni content could be due to the formation of a Ti-rich phase, possibly Ti2Ni.

B.4 Conclusions

The current study focused on the influence of process parameter and solution heat treatment on Ni-rich NiTi samples fabricated using the L-PBF technique. Solution treatment parameters were applied with varying temperatures (800°C, 1000°C, & 1200°C) and times (1h, 3h, & 5h). The phase transformation temperatures, density and microhardness were measured. All of the heat treated and L-PBF fabricated samples exhibited an austenitic finish temperature Af below the room temperature. Therefore, the samples should be superelastic in nature at room temperature. Heat treated samples exhibited a decrease of an average of 25 to 30°C in Af from the as-fabricated sample. Increased heat treatment time did not significantly affect the transformation temperature. Density values for samples treated at 800°C and 1000°C exhibited a slight decrease from as-fabricated (6.32 g/cm3) to a lowest of 6.04 g/cm3. However, a much lower density

was found for samples treated at 1200°C (at an average of 5.46 g/cm3). The microhardness of the heat treated samples slightly increased from 356HV to 446 HV for treatments up to 1000°C whereas samples treated at 1200°C showed hardness values up to 550HV.